Polarimetric Remote Sensing in the Visible to Near Infrared

by

James R. Shell II

B.S. Physics, United States Air Force Academy, 1992
M.S. Physics, Wright State University, 1995

A dissertation submitted in partial fulfillment of the
requirements for the degree of Doctor of Philosophy
in the Chester F. Carlson Center for Imaging Science
Rochester Institute of Technology

2005

Signature of the Author _____

Accepted by _____
Coordinator, Ph.D. Degree Program Date

CHESTER F. CARLSON CENTER FOR IMAGING SCIENCE
ROCHESTER INSTITUTE OF TECHNOLOGY
ROCHESTER, NEW YORK

CERTIFICATE OF APPROVAL

Ph.D. DEGREE DISSERTATION

The Ph.D. Degree Dissertation of James R. Shell II
has been examined and approved by the
dissertation committee as satisfactory for the
dissertation required for the
Ph.D. degree in Imaging Science

_____
Dr. John R. Schott, Dissertation Advisor

_____
Dr. Carl Salvaggio

_____
Dr. David W. Messinger

_____
Dr. Andrew Robinson

_____
Date

DISSERTATION RELEASE PERMISSION
ROCHESTER INSTITUTE OF TECHNOLOGY
CHESTER F. CARLSON CENTER FOR IMAGING SCIENCE

Title of Dissertation:
Polarimetric Remote Sensing in the Visible to Near Infrared

I, James R. Shell II, hereby grant permission to Wallace Memorial Library of R.I.T. to reproduce my thesis in whole or in part. Any reproduction will not be for commercial use or profit.

Signature _____
Date

Polarimetric Remote Sensing in the Visible to Near Infrared

by

James R. Shell II

Submitted to the
Chester F. Carlson Center for Imaging Science
in partial fulfillment of the requirements
for the Doctor of Philosophy Degree
at the Rochester Institute of Technology

Abstract

Polarization adds another dimension to the spatial intensity and spectral information typically acquired in remote sensing. Polarization imparted by surface reflections contains unique and discriminatory signatures which may augment spectral target-detection techniques. Benefits such as improving man-made object detection are often touted, as well as possible improvements to spectral algorithms used for detection and identification. However, virtually all efforts fail to cast polarimetric remote sensing within a cohesive framework in which *a priori* predictions of polarized radiance are made, as is done with spectral remote sensing techniques. This is due, in part, to the challenges of measuring and representing polarization signatures.

This research develops the governing radiometric equation for polarimetric remote sensing, illustrating the role of the polarimetric bidirectional reflectance distribution function (pBRDF). Using the governing radiometric equation as a basis, a technique for quantifying the pBRDF of *background* materials is presented. The measurement technique enables the generation of pBRDF as a function of the ground separation distance (GSD). Empirical data from employing the technique are fit to a pBRDF model. The model enables extrapolation of results to arbitrary illumination and viewing conditions throughout the visible to near infrared, all as a function of GSD.

A *target* material pBRDF model is also developed which enables the pBRDF representation of spatially homogeneous surfaces, typical of man-made materials. This model uses an unpolarized BRDF model as the basis, and generalizes the representation while enabling polarization. BRDF model parameters are determined from an existing database of BRDF measurements, which enables "polarization" of the database.

The quantification and understanding of target and background material polarization signatures is a prerequisite for exploring methods of fusing polarimetric and spectral information. This work advances this understanding and lays the foundation for spectral-polarimetric target detection techniques and algorithm development.

DISCLAIMER

The views expressed in this document are those of the author and do not reflect the official policy or position of the U. S. Air Force, Department of Defense, or the U. S. Government.

Acknowledgements

None of this would have been possible without the support and dedication of numerous people. I salute the faculty and staff of the Imaging Science Department and the Digital Imaging and Remote Sensing Group. I've been pushed harder and learned more beyond any expectation I had. After a few weeks in Roger Easton's linear math course, I quickly realized I was in for an interesting few years! Where do I start...I appreciate Lon Smith's willingness to loan me personal hardware. His creative engineering solutions enabled the polarimetric imaging system to be realized. Tim Gallagher was key in finding the right pieces of unusual hardware. Roger Easton patiently dealt with me while deconflicting our use of the SenSys camera system. The dedication demonstrated by Niek Sanders in implementing my algorithms into DIRSIG was unprecedented. Finally, John Schott consistently saw the forest for the trees, and his instruction provided a sensible and practical approach toward a science having many independent variables. Hats off to my research committee for providing valuable advice and for always being available.

Outside RIT there are equally many to thank. Julie Robinson of NASA Johnson digitized polarimetric images taken from 1980s U. S. Space Shuttle missions. Tom Caudill and Matt Fetrow of the Air Force Research Lab (AFRL) at Kirtland AFB dedicated time to helping me understand polarization phenomenology. Their willingness to share data and insights into modelling was also appreciated. Mike Metzler, the force behind the Maxwell-Beard BRDF model of the NEF Data System, entertained phone conversations helping me understand the history of the model and the current implementation. Joe Costantino of AFRL at Wright Patterson AFB readily provided data sets of BRDF measurements and material samples for me to work with. Carol May was also extremely helpful and responsive in providing material samples. Gary Stahl of General Dynamics went out of his way to provide and explain the Quick Look Sensor data sets.

The support of my family has been tremendous. My wife willingly moved to a place where snow is measured in "feet," and the whole family routine was adapted to accommodate my unusual work hours. Finally, I want to give glory to my Lord and Savior Jesus Christ, for through Him all things are possible. How exciting it has been to learn more about the intricacies of God's creation!

Contents

List of Figures

List of Tables

Nomenclature

Where practical, MKS units are used and often the dimensionality of units for a specific variable are given explicitly within enclosed brackets $[\cdots]$. Radiometric nomenclature is that established by the Commission Internationale de l'Eclairage (CIE). Radiometric values are spectral, or per unit of wavelength, though not always explicitly stated for brevity.

The following table provides a list of most variables used in this document. The variables are arranged alphabetically starting with Arabic characters, then Greek and finally symbols. Some quantities are used more than once, in which case the meaning may be understood from the context.

Table 1: List of globally used variables alphabetically arranged (Arabic, Greek, then symbols).

Symbol	Term	Units
a, b	f_{00} variability fit parameters	—
A	surface area	$\mathtt{m}^2$
$\mathtt{A}$	calibration panel image with solar and sky illumination	—
$\mathtt{B}$	calibration panel image of only sky illumination (shadow image)	—
c	speed of light	$\mathtt{m/s}$
c, d	DOP variability fit parameters	—
$\mathtt{C}$	measurement surface image with solar and sky illumination	—
d	fraction of diffuse sky to total irradiance	—
$\mathtt{D}$	measurement surface image of only sky illumination (shadow image)	—
DOP	degree of polarization	—
e, f	χ variability fit parameters	—
ΔE	the residual energy remaining from the difference between two sets of cross polarized images	—
E	irradiance	$\mathtt{W/m}^2$
E_d	diffuse sky irradiance on a target/ground	$\mathtt{W/m}^2$
E_s	exoatmospheric solar irradiance	$\mathtt{W/m}^2$
E_{fp}	irradiance on the focal plane	$\mathtt{W/m}^2$

$\vec{E}$	irradiance (Stokes)	$\mathtt{W/m^2}$
$\vec{\mathcal{E}}$	electric field vector	$\mathtt{V/m}$
$\mathcal{E}_{0x}$	maximum electric field amplitude along x-axis	$\mathtt{V/m}$
$\mathcal{E}_{0y}$	maximum electric field amplitude along y-axis	$\mathtt{V/m}$
$f_{\#\#}$	matrix elements (row major) of polarimetric BRDF, F_r	$\mathtt{sr^{-1}}$
f_{00}	pBRDF Mueller matrix element, equivalent to f_r	$\mathtt{sr^{-1}}$
f_{00}^p	polarized fraction of f_{00}	$\mathtt{sr^{-1}}$
f_{00}^u	unpolarized fraction of f_{00}	$\mathtt{sr^{-1}}$
f_1, f_2	Roujean BRDF model components	—
f_r	BRDF, equivalent to the f_{00} pBRDF element	$\mathtt{sr^{-1}}$
$\mathbf{F}_r$	polarimetric BRDF (matrix)	$\mathtt{sr^{-1}}$
GSD	ground separation or sample distance	$\mathtt{in}$
h	Planck's constant, 6.63×10^{-34}	$\mathtt{J\ s}$
$\mathtt{I_{xx}}$	image taken at polarization filter orientation of xx°	—
$\mathtt{k_0}, \mathtt{k_1}, \mathtt{k_2}$	Roujean BRDF model parameters	—
L	radiance	$\frac{\mathtt{W}}{\mathtt{sr\ m^2}}$
$\vec{L}$	radiance (Stokes)	$\frac{\mathtt{W}}{\mathtt{sr\ m^2}}$
L_d	ground-leaving radiance reflected from the *downwelled* skydome	$\frac{\mathtt{W}}{\mathtt{sr\ m^2}}$
$L_d^{\Omega_i}$	downwelled skydome radiance from incident solid angle Ω_i	$\frac{\mathtt{W}}{\mathtt{sr\ m^2}}$
L_r	radiance from direct solar *reflections*	$\frac{\mathtt{W}}{\mathtt{sr\ m^2}}$
L_s	total radiance reaching sensor of *solar* origin	$\frac{\mathtt{W}}{\mathtt{sr\ m^2}}$
L_u	radiance reaching sensor from *upwelled* atmospheric scattering	$\frac{\mathtt{W}}{\mathtt{sr\ m^2}}$
$\mathbf{M}$	Mueller matrix	use-dependent
n	real part of the index of refraction	—
$\tilde{n}_i$	complex index of refraction (incident medium)	—
$\tilde{n}_t$	complex index of refraction (transmitted medium)	—
$\hat{N}$	surface normal vector	—
$\mathtt{p_1} \cdots \mathtt{p_4}$	DOP polynomial fit coefficients	—
$\mathtt{pf_1} \cdots \mathtt{pf_4}$	ρ_p polynomial fit coefficients	—
R_F	Fresnel reflectance magnitude (total)	—
r_s	s-polarization reflectance coefficient	—
r_p	p-polarization reflectance coefficient	—
$\vec{S}$	Stokes vector	use-dependent
$\mathbf{T}$	transmissive Mueller matrix	—
α	absorptance	—
β	angle between the surface normal and θ_i or θ_r ($\xi/2$)	$\mathtt{rad}$ or $^\circ$
$\epsilon_0, \epsilon_1, \epsilon_2$	reflected downwelled sky Stokes vector elements	$\mathtt{sr^{-1}}$
ε_0	permittivity of free space	$\frac{\mathtt{C^2}}{\mathtt{N/m^2}}$
ξ	phase angle between Θ_i & Θ_r	$\mathtt{rad}$ or $^\circ$
λ	wavelength	$\mu\mathtt{m}$ or $\mathtt{nm}$
η	quantum efficiency	—

ν	E&M frequency	Hz or s^{-1}
Ω_i	incident solid angle	sr
Ω_r	reflected solid angle	sr
Θ_i	incident light direction (θ_i, ϕ_i)	
Θ_r	reflected light direction (θ_r, ϕ_r)	
θ_B	Brewster's angle	rad or °
θ_i	incident zenith angle	rad or °
θ_N	angle of the microfacet surface normal relative to the macrosurface	
θ_r	reflected zenith angle	rad or °
θ_t	transmission angle	rad or °
ϕ_i	incident azimuth angle	rad or °
ϕ_r	reflected azimuth angle	rad or °
ϕ	relative azimuth angle $(\phi_i - \phi_r)$	rad or °
Φ	flux	W
σ_{DOP}	the standard deviation of DOP	—
$\sigma_{f_{00}^{\%}}$	the percent (relative) standard deviation of f_{00}	—
$\sigma_{f_{00}}$	the standard deviation of f_{00}	sr^{-1}
σ_χ	the standard deviation of χ	rad or °
ρ	reflectance factor	—
ρ_{DHR}	directional hemispherical reflectance	—
ρ_{pol}	polarized reflectance factor	—
$\rho_{\mathcal{P}}$	Fresnel reflectance magnitude, $\mathcal{P}$ polarization	—
$\rho_{\mathcal{S}}$	Fresnel reflectance magnitude, $\mathcal{S}$ polarization	—
τ	transmittance	—
τ_i	atmospheric transmittance along solar to ground path	—
$\tau_{\mathcal{F}}$	Fresnel transmittance magnitude (total)	—
$\tau_{\mathcal{P}}$	Fresnel transmittance magnitude, $\mathcal{P}$ polarization	—
$\tau_{\mathcal{S}}$	Fresnel transmittance magnitude, $\mathcal{S}$ polarization	—
τ_{lens}	transmittance of a lens or lens assembly	—
τ_{pol}	transmittance—polarization filter	—
τ_{spec}	transmittance—spectral bandpass filter	—
τ_r	atmospheric transmittance along ground to sensor (reflected) path	—
χ	polarization orientation	rad or °
⊖	linear polarization filter at 0° (horizontal)	
⌀	linear polarization filter at 90° (vertical)	
⊘	linear polarization filter at +45°	
⦸	linear polarization filter at -45° (or +135°)	
⊛	identity (no) polarization filter	

Chapter 1

Introduction & Objectives

1.1 Introduction

Remote sensing has a myriad of applications in different disciplines. Broadly defined as the science of gaining information from a distance or without intimate contact, remote sensing has a critical daily role in such diverse areas as the prediction of tomorrow's weather, airport security and assessing bone fractures. Earth observation by aerial and space-based, or *overhead*, remote sensing provides benefits such as better management of agricultural resources, assistance in the discovery of petroleum reserves and monitoring of environmental conditions. The fusion of geographic data from overhead imaging systems into Geographic Information Systems (GIS) provides valuable information for planning, zoning and infrastructure growth. Overhead reconnaissance has been an essential part of strategic and tactical defense strategies as well.

Overhead remote sensing is based upon the detection and processing of electromagnetic energy. The energy may be that which naturally leaves the object (passive) or that reflected from the object by active illumination (*e.g.*, radar or lidar). Most often, an image or the 2-D spatial distribution of electromagnetic energy is the means to visually represent remote sensing data. Images acquired passively in the visible to near infrared (VNIR) region record the amplitude of energy of solar origin. The sensor-received radiance in the VNIR is composed of photons having their origin in reflectance off the ground by either direct solar radiance or downwelled sky radiance. Photons are also scattered in the atmosphere, and those directed along the ground to sensor path also contribute to the total scene radiance.

The amplitude of the energy may also be recorded as a function of the frequency, or wavelength of the radiation. Spectral imaging techniques have enabled imaging spectroscopy for material identification. Powerful spectral algorithms provide a means of identifying specific materials of interest or *targets* by analyzing image data cubes which may consist

of hundreds of bands of spectral data. Autonomous computer processing algorithms have provided the means of digesting large amounts of image data, identifying probable targets for closer examination by analysts and subsequent action.

The advances in spectral imaging and processing, while substantial, have largely ignored another property of electromagnetic radiation—the vector orientation of the transverse electric and magnetic fields, or *polarization*. Sunglasses are a common item which most people can associate with polarization. Polarized glasses improve the visual contrast by partially blocking glare, or specular glints, which have appreciable polarization. Prime examples of these reflections are those from windshields while driving, or the water surface when fishing. Imaging which records or quantifies the polarized nature of the electromagnetic radiation is termed *polarimetric imaging* and provides additional information not contained in simple amplitude or intensity imagery.

The fact that polarimetric remote sensing has value is not disputed. Polarimetric sensing has been routine for planetary science observations and space missions, but it was not until 1984 that space-based polarimetric images of the earth were acquired [1, 2]. A significant body of work has demonstrated increased image contrast and some ability to perform fundamental material classifications based on the polarimetric properties [3]. However, a systematic means of fusing polarimetric information with the richness of spectral data has not been developed.

Exploiting polarimetric signatures requires an understanding of the interaction of light and materials, including target materials, background (non-target) materials and the atmosphere. Polarimetric errors and error propagation must be understood. Polarimetric imaging systems need employment strategies which maximize the polarimetric information content given the solar and sensor positions.

A thorough examination of polarimetric remote sensing considers all elements of the *image chain*. The image chain approach is advocated by Schott and provides a systems engineering approach toward the acquisition and use of remotely sensed data [4]. Examining each element in the remote sensing process reveals the weakest "link" where further resource investment will maximize the end product, which is ultimately the ability to make a decision from the remotely sensed data. Large-scale elements of the image chain include input or acquisition, processing and finally output or display. This research heavily focuses on polarization phenomenology, or the means by which surfaces impart polarization.

The role of polarization in the imaging chain is illustrated by examining the governing equation for radiance reaching a remote sensor. This equation will be covered in more detail in Chapter 4, but it is briefly introduced here since it serves as the basis from which this investigation is launched. The total radiance in the visible to near infrared (VNIR)

portion of the spectrum (*i.e.* that of solar origin) reaching a sensor aperture (L_s) may be approximated as the sum of radiance values which have their origin in

1. solar *reflections* from the target, L_r
2. target-reflected *downwelled* radiance from the skydome, L_d
3. *upwelled* atmosphere radiance resulting from solar scatter in the atmosphere along the target to sensor path, L_u

More explicit expressions for L_r and L_d may be given by

$$L_r \propto \tau_r \, f_r \, \tau_i \, E_s \tag{1.1a}$$

$$L_d \propto \iint_{\Omega} \tau_r \, f_r \, L_d^{\Omega_i} \, d\Omega \, , \tag{1.1b}$$

where E_s is the exoatmospheric solar irradiance $\left[\frac{\mathtt{W}}{\mathtt{m}^2}\right]$, τ_i and τ_r are the atmospheric transmittance along the *incident* or sun-to-target path and *reflected* or ground-to-sensor path, f_r is the bidirectional reflectance distribution function (BRDF) and finally $L_d^{\Omega_i}$ in the integrand is the diffuse sky radiance over an infinitesimal solid angle, which must be integrated over the $\Omega = 2\pi$ [$\mathtt{sr}$] hemisphere. L_u is usually estimated from numerical algorithms which incorporate atmospheric scattering phase functions and absorption spectra. Therefore, the sensor-reaching radiance, L_s, is proportional to

$$L_s \propto \tau_r f_r \tau_i E_s + \iint_{\Omega} \tau_r f_r L_d^{\Omega_i} d\Omega + L_u \, . \tag{1.2}$$

As will be seen, the additional information from polarimetric remote sensing is by virtue of the BRDF, f_r, which describes the radiance distribution of reflected energy given the incident irradiance. Specifically, it is the more general *polarimetric* BRDF or pBRDF, which provides the polarized radiance distribution for arbitrary incident polarization states. All terms in equation 1.2 other than f_r effectively become uncertainties which must be estimated given the per-pixel spectral radiance received, L_s. The same is true for spectral, intensity-only remote sensing where spectral reflectance is proportional to f_r. The pBRDF for polarimetric imaging may be considered analogous to the spectral reflectance of a material for hyperspectral imaging—each provides unique signatures imparted to the reflected radiance. However, specification of the pBRDF function is significantly more complex than that of spectral reflectance or the BRDF.

Inclusion of the scalar or non-polarimetric BRDF in remote sensing is challenging unto itself, and is not widely used. Most often a simple reflectance factor is estimated under

the assumption that there is uniform reflectance in all directions. It is therefore beneficial to examine techniques for including the more simplistic scalar BRDF prior to investigating unique polarimetric signatures.

The quantification and representation of polarimetric BRDF is the core focus of this research effort. Establishing a coherent means of representing polarimetric BRDF is a prerequisite for answering application-oriented questions such as "How much better will my target detection algorithm perform with polarimetric information?"

Ultimately, it is this question that needs examining: what benefits are provided by polarimetry to target detection and classification algorithms? Fusion of polarimetric with spectral information should provide benefits over spectral-only data. Many spectral bands are highly correlated, as principal component analysis reveals, and polarimetric information provides additional discriminatory information which should improve target detection and identification. A means of maximizing polarization information must be explored by considering

1. algorithm employment methods and strategies (*e.g.*, in series or in parallel),

2. optimizing polarimetric spectral band selection and

3. optimal conditions for VNIR polarimetric image acquisition, such as solar and sensor angles.

Synthetically-generated imagery may be used to complete a parametric study of the polarimetric imaging benefits with respect to such algorithms. Experimental data will also be useful.

The results of this research provides the framework from which the exploration of polarimetric parameter space may begin. It will benefit and aid the design of future polarimetric remote sensing systems and the exploitation of the collected data. Informed system design decisions may be made by comparing trades between spectral versus polarimetric bands. If polarimetric bands are included, which spectral regions provide the most information—or should the polarimetry be panchromatic? Once the data is in hand, what are the algorithms and techniques that will maximize the signal to noise for target detection or identification?

1.2 Objectives

An overview of the objectives of this research are given below. They are adapted from those established at the time of the research proposal.

❶ Mature the governing radiometric equations to establish the framework for quantitative, reflective polarimetric remote sensing.

❷ Measure the pBRDF of background materials, to include their variability as a function of GSD.

(a) Materials such as grass, soil, aggregate and asphalt

(b) At two spectral bands, 550 ± 6 and 750 ± 12 nm

❸ Develop a means of representing background material pBRDF signatures.

(a) Generate the spectral pBRDF of background materials for any illumination and reflection geometry

(b) Incorporate the pBRDF variability as a function of GSD derived from the measurements

(c) Insure the pBRDF model is amenable to implementation in a synthetic image generation program, such as DIRSIG

❹ Develop a new pBRDF model suitable for homogeneous "target" materials.

(a) Semi-empirical model including volumetric scattering effects

(b) Model parameters derived from empirical data fits (*e.g.*, using Air Force Research Lab data)

(c) Enable "polarization" of the Nonconventional Exploitation Factors BRDF database

(d) Provide a means of estimating polarimetric signatures for materials for which pBRDF measurements have not been made

❺ Validate DIRSIG implementation of new pBRDF models and compare the results with those obtained from imaging experiments.

1.3 Scope

This effort considers *linear* polarization in the visible to near infrared (VNIR) spectral region, defined for this research as $\sim$ 400–2500 nm. Beyond 2500 nm atmospheric absorption is either appreciable or the photon flux from thermal emission becomes significant relative to that reflected. Circular polarization will not be investigated in detail. Several authors have indicated the magnitude of circular polarization imparted by most materials is insignificant [5, Ch. 10] and [6], especially when compared to noise sources in the imaging chain. Some

evidence suggests circular polarization may provide benefits for active polarimetry, *i.e.*, illumination with a source such as a laser. However, in the passive VNIR reflective region, the magnitude of circular polarization imparted is very low.

In all instances, the pBRDF of a surface will be assumed to have azimuthal symmetry. The added complexity of a fourth geometric degree of freedom is significant and not justified for the majority of materials.

This research does not address details of optical system design which enable multi-spectral polarimetric imaging. It is limited to predicting the radiance provided at the sensor aperture.

1.4 Dissertation Overview and Organization

The theoretical basis of polarimetric remote sensing is first covered in Chapter 2. Electromagnetic theory, to include optical scattering is reviewed. The theoretical background is followed by a history of polarimetric imaging and remote sensing (Chapter 3).

The results of this research effort are presented in Chapters 4–10. The governing equation for polarized radiance reaching a sensor aperture is developed in Chapter 4. A pBRDF measurement technique which quantifies the polarimetric signature and variability of background materials is developed in Chapter 5. The means of taking this raw data and producing results are discussed in Chapter 6, which also provides the for three materials: topsoil, asphalt and lawn grass. The means to model and represent the measured background materials is developed in Chapter 7. Finally, attention is turned toward homogeneous target materials (Chapter 8), where a new pBRDF model is proposed. These background and target pBRDF models are implemented into a synthetic image generation program, DIRSIG, discussed in Chapter 9. Finally, Chapter 10 provides some observations and recommendations for further work, to include approaches toward the development of spectral-polarimetric algorithms.

An attempt has been made to generate figures and plots suitable for black and white, however, color is used out of necessity in many of the figures. There is also considerable hyperlinking in the document, both internal and external, which provides easy navigation and additional information in the electronic version. An electronic version (Adobe PDF) may be requested from the Digital Imaging and Remote Sensing Group in the Imaging Science Department of RIT.

Chapter 2

Theory

In this chapter, the nature of "light" is explored, and its interaction with materials. First, the mathematical basis for discussing the propagation of light or more generally electromagnetic waves is presented. The means of representing polarized radiometry is also introduced. Next, optical scattering is examined in detail, as it is via this process that polarimetric signatures are imparted.

2.1 Electromagnetics

2.1.1 Electromagnetic Waves

Remote sensing is enabled by recording information from electromagnetic radiation. For passive remote sensing in the VNIR, this is radiation of solar origin which is reflected from a scene to form an image. The radiation reaching a sensor may be approximated by a plane wave given the aperture size of a remote sensing imaging system relative to the distance from the scene imaged. A generalized electromagnetic plane wave travelling in the z direction may be expressed as

$$\vec{\mathcal{E}}(z,t) = \vec{\mathcal{E}}_0 e^{i(\omega t - \vec{k}\cdot\vec{z}+\epsilon)} \ , \tag{2.1}$$

where $\vec{\mathcal{E}}$ is the magnitude and direction of the electric field [`Volts/m`] in the x-y plane as a function of position, z, and time, t. The propagation direction vector, $\vec{k}$, is given by $\frac{2\pi}{\lambda}$ where λ is the wavelength. The angular frequency, ω, is $\frac{2\pi\ c}{\lambda}$ where c is the speed of propagation of light in a vacuum. Finally, ϵ is the initial phase associated with the wave.

Using (2.1) as a basis, the available information content of an electromagnetic wave may be investigated. The quantity directly measured by sensors is the *irradiance*, E, or the

power per unit area [$\mathtt{W/m^2}$] incident upon a detector. The irradiance is equal to

$$E = \frac{c\ \varepsilon_0\ |\vec{\mathcal{E}}_0|^2}{2} \tag{2.2}$$

where ε_0 is the permittivity of free space equal to $\frac{10^7}{4\ \pi\ c^2}$ or $\sim 8.85 \times 10^{-12}\ \left[\frac{\mathtt{C^2}}{\mathtt{N \cdot m^2}}\right]$ in mks units.

For the VNIR region of the spectrum, the wavelength range of 400 $\mathtt{nm}$ to 2500 $\mathtt{nm}$ spans frequencies, ν, from $\approx 1.2 \times 10^{14}$ to 7.5×10^{14} Hz ($\nu_{\mathtt{2500nm}}$ to $\nu_{\mathtt{400nm}}$) given by

$$c = \lambda\nu \longrightarrow \nu = \frac{c}{\lambda}\ . \tag{2.3}$$

Clearly, in the VNIR, the oscillation frequency is such that many cycles are integrated with a conventional sensing system. Even at the lowest frequency of 1.2×10^{14} $\mathtt{Hz}$ for 2500 $\mathtt{nm}$ radiation, a "fast" sensor exposed over a microsecond or $T = 10^{-6}$ $\mathtt{s}$ integrates more than 1 billion cycles of the electromagnetic wave. Therefore, the modulus squared of the electric field vector used in the irradiance equation is given by the expectation value over the exposure time period (T) or

$$|\vec{\mathcal{E}}|^2 = \frac{1}{T}\int_0^T \vec{\mathcal{E}}^*(z,t)\vec{\mathcal{E}}(z,t)dt = \left\langle \vec{\mathcal{E}}^*(z,t)\vec{\mathcal{E}}(z,t) \right\rangle\ , \tag{2.4}$$

where $T \gg \nu^{-1}$ and * is the complex conjugate. The integration also makes the initial phase term, ϵ, insignificant. Note the irradiance recorded by a sensor does not retain the directional information of the electric field, such that $|\vec{\mathcal{E}}|^2 \rightarrow |\mathcal{E}|^2$.

From (2.1), it is seen that the frequency, ω, or "color" of the electromagnetic wave is another source of information content. This information is obtained by filtering or dispersing the energy into i spectral bands, and then recording the irradiance within that band, $\Delta\lambda_i$. Increasingly, hyperspectral imaging systems are being used in remote sensing to perform reflective spectroscopy. A hyperspectral system may have hundreds of bands across the visible to far infrared portion of the spectrum. Spectral resolutions on the order of $\Delta\lambda = 10$ $\mathtt{nm}$ are typical of such systems.

Finally, the direction of the electric field vector or the *polarization* is considered again. While a conventional solid state detector may not directly record the polarization, the electric field direction may be selectively filtered prior to reaching a sensor, just as spectral filtering is possible. Imaging which records the direction of the electric field vector, $|\vec{\mathcal{E}}|^2$, is termed *polarimetric imaging* and provides the final piece of information which may be

obtained from electromagnetic radiation—at least for passive, incoherent remote sensing.

Natural light is mostly randomly polarized where there is no net preference of the electric field vector. Solar irradiance is also randomly polarized, but reflection from surfaces and scattering by aerosols impart polarization. As will be seen, the polarization of reflected light is governed by the optical properties of the material reflecting the light. It is this phenomenology that may be exploited in polarimetric remote sensing to provide additional information.

2.1.2 Electromagnetic Waves at Discontinuities

The interaction of electromagnetic waves at discontinuities or the interface between two media is determined by the wave nature of the propagation and the boundary conditions imposed by Maxwell's equations. Expressions giving the direction of the transmitted and reflected energy and magnitude are desired.

2.1.2.1 Direction

The direction of the reflected and transmitted wave may be determined from the basic wave equation, without invoking any electromagnetic theory [7, pp. 65–67] [8, p. 365] [9, pp. 278–280]. The behavior of an electromagnetic wave in a medium is determined by the index of refraction, $\tilde{n}$. The index of refraction is given by

$$\tilde{n} = \sqrt{\frac{\varepsilon\ \mu}{\varepsilon_0\ \mu_0}}\ , \tag{2.5}$$

where ε is the *dielectric constant* and μ is the *permeability*. These respective values for free space are given by ε_0 and μ_0, which in turn determine the speed of light according to

$$c = \frac{1}{\sqrt{\varepsilon_0\ \mu_0}}\ . \tag{2.6}$$

From (2.6), it may be seen that the refractive index is the ratio of the velocity of the wave in free space to that in the medium. In general, $\tilde{n}$ is frequency-dependent and a complex number due to a generally complex dielectric constant. The real and imaginary components are given by

$$\tilde{n} = n + i\ \kappa\ . \tag{2.7}$$

From the law of reflectance, the reflection angle (θ_r) of a wave is equal to the incidence angle (θ_i), with both lying in the plane of incidence. The angle of the transmitted wave, θ_t,

is given by the familiar *Snell's law* or

$$\tilde{n}_i \sin\theta_i = \tilde{n}_t \sin\theta_t \ . \tag{2.8}$$

Consistent with the conservation of energy, the sum of the reflectance (ρ), absorptance (α) and transmittance (τ) must be unity. For absorptance to occur, a finite distance must be traversed in a medium. Since the present concern is only the infinitesimal interface between the two mediums, absorptance is zero and not considered. Therefore at the interface between two mediums, $\rho + \tau = 1$.

Snell's law provides insight into another phenomena which is of interest—total internal reflection. When $\tilde{n}_i > \tilde{n}_t$, an impossible refraction angle may result once the *critical angle* has been exceeded since $\sin\theta_t > 1$. The critical angle is defined as

$$\theta_c = \sin^{-1}\left(\frac{\tilde{n}_t}{\tilde{n}_i}\right) \ , \tag{2.9}$$

past which point total internal reflection occurs.

2.1.2.2 Magnitude

Having determined the direction of the reflected and transmitted wave, the magnitude of these components is investigated. The magnitude is a function of the indices of refraction and the incident wave angle and polarization; it is completely specified by the *Fresnel equations*.

Polarization will be discussed in detail below—for now it is noted that polarization may be separated into two orthogonal components relative to the plane of incidence. The component of the electric field perpendicular to the plane of incidence (and hence parallel to the material surface) is called s-polarization. The component parallel to the plane of incidence is termed p-polarization.

The Fresnel equations result from imposing boundary conditions from Maxwell's equations at the interface between two materials. The derivation of Fresnel equations may be found in most electromagnetic or optical textbooks [7, p. 68] [9, p. 280]. Without derivation, the Fresnel equations are presented, which determine the fractional amounts of the p- and s-polarized electric field components which are transmitted (t) and reflected (r). The

s-polarized reflectance and transmittance are

$$r_s = \frac{\mathcal{E}_s^r}{\mathcal{E}_s^i} = \frac{2\tilde{n}_i \cos\theta_i}{\tilde{n}_i \cos\theta_i + \frac{\mu_i}{\mu_t}\tilde{n}_t \cos\theta_t} \tag{2.10}$$

$$t_s = \frac{\mathcal{E}_s^t}{\mathcal{E}_s^i} = \frac{\tilde{n}_i \cos\theta_i - \frac{\mu_i}{\mu_t}\tilde{n}_t \cos\theta_t}{\tilde{n}_i \cos\theta_i + \frac{\mu_i}{\mu_t}\tilde{n}_t \cos\theta_t} \ . \tag{2.11}$$

Similarly, the p-polarization reflectance and transmittance are

$$r_p = \frac{\mathcal{E}_p^r}{\mathcal{E}_p^i} = \frac{2\tilde{n}_i\tilde{n}_t \cos\theta_i}{\frac{\mu_i}{\mu_t}\tilde{n}_t^2 \cos\theta_i + \tilde{n}_i\tilde{n}_t \cos\theta_t} \tag{2.12}$$

$$t_p = \frac{\mathcal{E}_p^t}{\mathcal{E}_p^i} = \frac{\frac{\mu_i}{\mu_t}\tilde{n}_t^2 \cos\theta_i - \tilde{n}_i\tilde{n}_t \cos\theta_t}{\frac{\mu_i}{\mu_t}\tilde{n}_t^2 \cos\theta_i + \tilde{n}_i\tilde{n}_t \cos\theta_t} \ . \tag{2.13}$$

The Fresnel equations may be cast in various forms. For instance, Snell's law may be used to express the equations in terms of θ_i without using θ_t. The result is a more complicated but also a more useful expression as it is in terms of the most immediate known values. The equations may be represented in this manner by the following substitution

$$\tilde{n}_t \cos\theta_r \longrightarrow \sqrt{\tilde{n}_t^2 - \tilde{n}_i^2 \sin^2\theta_i} \ . \tag{2.14}$$

The quantities of the Fresnel equations which are of most concern is the *energy* of the reflected and transmitted waves since it is this quantity which is detected. As shown by (2.2), the energy is proportional to the square of the electric field or the irradiance. However the expression for irradiance given by (2.2) is only explicitly true in a vacuum. The more general expression is

$$E = \frac{c\ \varepsilon\ |\vec{\mathcal{E}}_0|^2}{2\ \tilde{n}} \ , \tag{2.15}$$

where the dielectric constant of the medium replaces the free space constant and the actual velocity of the wave, given by $\frac{c}{\tilde{n}}$ replaces c. When the medium is air, then (2.2) is adequate since $\varepsilon \approx \varepsilon_0$ and $\tilde{n} \approx 1 + i0$. The energy reflected by the individual polarization components is therefore given by the square of the fraction of the electric field reflected (2.12, 2.10).

$$\rho_s = r_s^2 \qquad\qquad \rho_p = r_p^2 \tag{2.16}$$

The transmitted energy is given by (2.15) or from energy conservation considerations as

$$\tau_s = 1 - \rho_s \qquad\qquad \tau_p = 1 - \rho_p \tag{2.17}$$

Simplification of the Fresnel equations results by noting that most often the incident light is in air where $\tilde{n}_i \approx 1 + i0$, and that the permeability ratio for the two mediums is one ($\frac{\mu_i}{\mu_t} \approx 1$). With these assumptions, the Fresnel equations in terms of the reflected energy or ρ are given by

$$\rho_s(\theta_i) = \frac{(A - \cos\theta_i)^2 + B^2}{(A + \cos\theta_i)^2 + B^2} \tag{2.18}$$

$$\rho_p(\theta_i) = \rho_s(\theta_i)\left[\frac{(A - \sin\theta_i \tan\theta_i)^2 + B^2}{(A + \sin\theta_i \tan\theta_i)^2 + B^2}\right] , \tag{2.19}$$

where

$$A = \sqrt{\frac{\sqrt{C} + D}{2}} \tag{2.20}$$

$$B = \sqrt{\frac{\sqrt{C} - D}{2}} \tag{2.21}$$

$$C = 4n^2\kappa^2 + D^2 \tag{2.22}$$

$$D = n^2 - \kappa^2 - \sin^2\theta_i \tag{2.23}$$

using the notation of [10, p. 22]. These equations explicitly break the complex refractive index, $\tilde{n}$, into the real (n) and imaginary (κ) components. The total Fresnel reflectance, R_F, is simply the average of the individual ρ_s and ρ_p components or

$$R_F = \frac{\rho_s + \rho_p}{2} . \tag{2.24}$$

Figure 2.1 illustrates the Fresnel equations, where results are shown for typical glass ($\tilde{n}_t = 1.5 + 0i$) and for copper which, being a metal, has an appreciable κ value ($\tilde{n}_t = 0.405 + i2.95$). The incident light is in air, $\tilde{n}_i = 1 + i0$. Notice in Figure 2.1 that for the glass there is a point at which the p-component reflectance is zero. This condition occurs in dielectrics (*i.e.*, $\kappa = 0$) and corresponds to *Brewster's angle* given by

$$\theta_B = \tan^{-1}\left(\frac{\tilde{n}_t}{\tilde{n}_i}\right) . \tag{2.25}$$

At this angle the reflected radiance is completely polarized; this will become an important characteristic to be explored.

It is also of interest to observe that the Fresnel equations are not an explicit function of wavelength. The index of refraction, $\tilde{n}$, is wavelength dependent, but the index variation across the VNIR region for most materials is minimal. As a result, Fresnel reflectance and

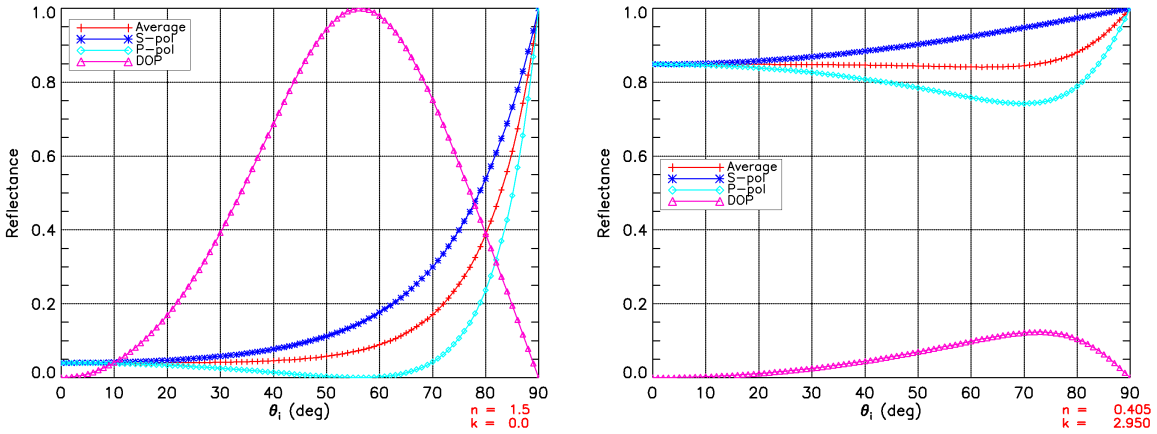

Figure 2.1: Polarized reflectance from a glass (*left*, $\tilde{n}_t = 1.5 + i0$) and copper (*right*, $\tilde{n}_t = 0.405 + i2.95$) as a function of θ_i. The incident light is in air.

transmittance are largely color neutral, meaning the spectral content of the reflected and transmitted energy is similar to that of the source.

2.1.3 Polarization and Polarization Calculus

2.1.3.1 Stokes Vectors

In order to quantify polarimetric radiometry, scalar flux values such as the irradiance, E, must be specified as a vector, $\vec{E}$, which contains the polarization information. A four element *Stokes* vector is traditionally used for this specification, which completely characterizes the polarization [11]. The first element of the Stokes vector (S_0) corresponds to standard scalar radiometric flux values (*e.g.*, radiance or irradiance). The second and third Stokes elements (S_1 and S_2) relate to linear polarization, and the fourth element, S_3 contains the circular polarization information.

The orientation of polarization is by convention defined relative to a reference plane, usually established as the surface under observation, such as the surface of the earth. As discussed in §2.1.2.2, the s-polarization or that which is orthogonal to the plane of incidence (parallel to the material surface) defines the $\chi = 0°$ orientation and the x-axis component of the electric field, $\mathcal{E}_x$. Similarly, the p-polarization component is defined as the $\chi = 90°$ or equivalently the $\chi = -90°$ orientation with the y-axis component of the electric field, $\mathcal{E}_y$.

The electromagnetic wave equation (2.1) may be rewritten in explicit terms of the or-

thogonal x- and y-components of the electric field vector as

$$\begin{aligned}\vec{\mathcal{E}}(z,t) &= \left(\mathcal{E}_x\hat{i} + \mathcal{E}_y\hat{j}\right) e^{i(\omega t - \vec{k}\cdot\vec{z})} \\ &= \left(\mathcal{E}_{0x}e^{i\delta_x}\hat{i} + \mathcal{E}_{0y}e^{i\delta_y}\hat{j}\right) e^{i(\omega t - \vec{k}\cdot\vec{z})} \ .\end{aligned} \tag{2.26}$$

The relative magnitudes and phases of $\mathcal{E}_x$ and $\mathcal{E}_y$ determine the net polarization of the electric field. For instance, if the magnitudes of $\mathcal{E}_x$ and $\mathcal{E}_y$ are equal ($\mathcal{E}_{0x} = \mathcal{E}_{0y}$) and the complex component or relative phase, δ between each is equal ($\delta = \delta_x - \delta_y = 0$) then the electric field oscillates in a single plane which is oriented at $\chi = \frac{\pi}{4}$ or 45° from the x-axis.

The Stokes vectors are defined by the electric field components in equation 2.26 according to

$$\begin{bmatrix} S_0 \\ S_1 \\ S_2 \\ S_3 \end{bmatrix} = \begin{bmatrix} \langle \mathcal{E}_x\mathcal{E}_x^* + \mathcal{E}_y\mathcal{E}_y^* \rangle \\ \langle \mathcal{E}_x\mathcal{E}_x^* - \mathcal{E}_y\mathcal{E}_y^* \rangle \\ \langle \mathcal{E}_x\mathcal{E}_y^* + \mathcal{E}_y\mathcal{E}_x^* \rangle \\ i\langle \mathcal{E}_x\mathcal{E}_y^* - \mathcal{E}_y\mathcal{E}_x^* \rangle \end{bmatrix} \tag{2.27}$$

using the complex electric field notation and

$$\begin{bmatrix} S_0 \\ S_1 \\ S_2 \\ S_3 \end{bmatrix} = \begin{bmatrix} \langle \mathcal{E}_{0x}^2 + \mathcal{E}_{0y}^2 \rangle \\ \langle \mathcal{E}_{0x}^2 - \mathcal{E}_{0y}^2 \rangle \\ \langle 2\mathcal{E}_{0x}\mathcal{E}_{0y}\cos\delta \rangle \\ \langle 2\mathcal{E}_{0x}\mathcal{E}_{0y}\sin\delta \rangle \end{bmatrix} \tag{2.28}$$

using the magnitude and relative phases of the $\mathcal{E}_x$ and $\mathcal{E}_y$ components. The Stokes parameters are often normalized by the S_0 value, resulting in S_1, S_2 and S_3 ranging from -1 to 1 or

$$\begin{bmatrix} S_0 \\ S_1 \\ S_2 \\ S_3 \end{bmatrix} = S_0 \begin{bmatrix} 1 \\ S_1/S_0 \\ S_2/S_0 \\ S_3/S_0 \end{bmatrix} \ . \tag{2.29}$$

A few examples are given to gain an understanding of the Stokes vectors. For instance, if all the electric field is in the $\mathcal{E}_{0x}$ component, or equivalently that there is complete s polarization, then $S_1 = 1$. If the electric field were completely contained in the $\mathcal{E}_{0y}$ component, or equivalently that there is complete p polarization, then $S_1 = -1$. If there is no relative phase difference between the $\mathcal{E}_{0x}$ and $\mathcal{E}_{0y}$ components, or $\delta = 0$, then there is no circular or elliptical polarization component making $S_3 = 0$. These relationships may be verified from (2.28). Examples of Stokes vectors are shown below, where the transpose (^{T})

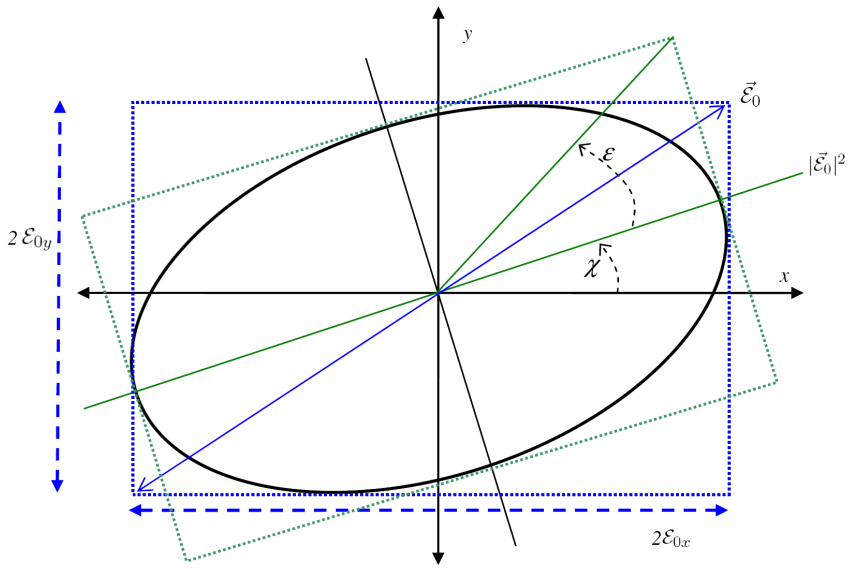

Figure 2.2: Polarization ellipse illustrating the linear polarization orientation, χ, and the ellipticity, ε.

of the vectors are used for compactness.

$[\ 1 \quad 0 \quad 0 \quad 0\ ]^T$	random
$[\ 1 \quad \pm 1 \quad 0 \quad 0\ ]^T$	$\chi = 0^\circ$ horizontal (+1) or $\chi = 90^\circ$ vertical (-1)
$[\ 1 \quad 0 \quad \pm 1 \quad 0\ ]^T$	$\chi = +45^\circ$(+1) or $\chi = 135^\circ$(-1)
$[\ 1 \quad 0 \quad 0 \quad \pm 1\ ]^T$	right-hand (+1) and left-hand (-1) circular

The most general case of polarization is elliptical polarization, or polarization where each of the Stokes vectors has some magnitude. The polarization ellipse is useful for illustrating polarization, as it traces out the location of the electric field vector around the axis of propagation, the $z-$axis. A polarization ellipse is presented in Figure 2.2 which illustrates the relationship between the two orthogonal electric field components and the variables used to define the Stokes vectors.

In terms of the polarization ellipse variables, the polarization orientation, χ, may be obtained from the electromagnetic wave as

$$\chi = \frac{1}{2}\tan^{-1}\left(\frac{2\mathcal{E}_x\mathcal{E}_y}{\mathcal{E}_x^2 - \mathcal{E}_y^2}\cos\delta\right) \ , \tag{2.30}$$

or directly from the Stokes parameters by

$$\chi = \frac{1}{2}\tan^{-1}\left(\frac{S_2}{S_1}\right) . \tag{2.31}$$

When there is no ellipticity $\varepsilon = 0$ and $S_3 = 0$ resulting in the polarization ellipse collapsing into a single plane of oscillation, or complete linear polarization.

Stokes parameters may also be defined relative to a detector output when ideal polarization filters are placed over the detector. This is perhaps the most intuitive means of expressing the parameters, and it is how they are typically derived in an imaging application. The nature of the filters will be discussed in more detail in §2.1.3.2. For now, it is sufficient to state that the intensity received through an ideal polarization filter oriented at $\theta = x^\circ$ relative to the $\chi = 0^\circ$ orientation is given by $I_{\mathtt{x}}$. Similarly, $I_{\mathtt{R}}$ and $I_{\mathtt{L}}$ are ideal right-hand and left-hand circular filters. Using this notation, the Stokes parameters are given by

$$\begin{bmatrix} S_0 \\ S_1 \\ S_2 \\ S_3 \end{bmatrix} = \begin{bmatrix} I \\ I_{\mathtt{0}} - I_{\mathtt{90}} \\ I_{\mathtt{45}} - I_{\mathtt{135}} \\ I_{\mathtt{R}} - I_{\mathtt{L}} \end{bmatrix} . \tag{2.32}$$

When there is no elliptical polarization ($S_3 = 0$), I may be determined by the sum of any two orthogonal linear polarization states such as $I_{\mathtt{0}} + I_{\mathtt{90}}$ or $I_{\mathtt{45}} + I_{\mathtt{135}}$.

Some polarization relationships and metrics may now be defined which are derived from the Stokes vectors. First, it is noted that $S_0 \leq \sqrt{S_1^2 + S_2^2 + S_3^2}$, with equality holding only for completely polarized light. The *degree of polarization* (DOP) and *degree of linear polarization* (DOLP) are given by

$$DOP = \frac{\sqrt{S_1^2 + S_2^2 + S_3^2}}{S_0} \tag{2.33}$$

$$DOLP = \frac{\sqrt{S_1^2 + S_2^2}}{S_0} . \tag{2.34}$$

Circular polarization will not be considered in detail, due to the small magnitude present in the VNIR from reflected solar radiation [5, p. 486]. This approximation results in $S_3 \simeq 0$ which makes $DOLP \simeq DOP$.[1]

Stokes vectors obey linear superposition. It is often helpful to represent radiance in terms of a completely polarized component and a randomly polarized component. This is

[1] Note that in this text, DOP is used as both an acronym and a variable. When appearing as a variable it is italicized.

easily accomplished by using DOP as the fractional component of complete polarization, such as

$$\begin{bmatrix} S_0 \\ S_1 \\ S_2 \\ S_3 \end{bmatrix} = DOP \begin{bmatrix} S_0 \\ S_1 \\ S_2 \\ S_3 \end{bmatrix} + (1 - DOP) \begin{bmatrix} S_0 \\ 0 \\ 0 \\ 0 \end{bmatrix} . \tag{2.35}$$

Finally, the effects of a rotating reference frame on the Stokes vectors is shown. As presented, the vectors are defined relative to $\theta = 0°$ corresponding to the horizontal reference position, usually a material surface. Rotation about the propagation vector will obviously change the Stokes vector—for instance s polarization becomes p polarization in a new reference frame rotated by $\theta = 90°$, or equivalently $+S_1$ becomes $-S_1$. The general relationship for the Stokes vector rotation is given by

$$\begin{aligned} \vec{S}(\theta) &= \mathbf{R}(\theta)\vec{S} \\ \begin{bmatrix} S_0 \\ S_1 \\ S_2 \\ S_3 \end{bmatrix}_{\theta°} &= \begin{bmatrix} 1 & 0 & 0 & 0 \\ 0 & \cos 2\theta & -\sin 2\theta & 0 \\ 0 & \sin 2\theta & \cos 2\theta & 0 \\ 0 & 0 & 0 & 1 \end{bmatrix} \begin{bmatrix} S_0 \\ S_1 \\ S_2 \\ S_3 \end{bmatrix} . \end{aligned} \tag{2.36}$$

It is important to note that this operation does not change the resulting DOP, only the relative magnitude between the S_1 and S_2 components. This geometry relative to an image alignment of θ is shown in Figure 2.3.

2.1.3.2 Mueller Matrices

Now that a means of representing polarized radiometry has been developed, a method of "transferring" the polarized radiance is needed. In general, transmittance and reflectance of radiance through or from a medium changes the magnitude and the polarization. The change resulting from reflectance was manifested in the Fresnel equations. One transfer function which completely describes the change in the radiant flux is the *Mueller matrix* [12]. The Mueller matrix, $\mathbf{M}$, provides the Stokes vector out given an incident Stokes vector,

$$\vec{S}_{out} = \mathbf{M}\ \vec{S}_{in} . \tag{2.37}$$

The unique reflectance properties of materials may be characterized by a Mueller matrix, which will become the focus for polarimetric remote sensing. This reflective Mueller matrix is the most generalized form of the *bidirectional reflectance distribution function* (BRDF),

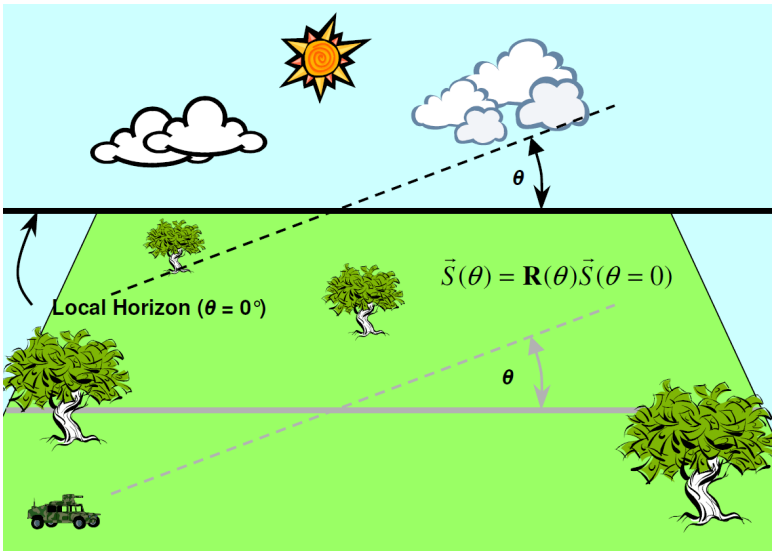

Figure 2.3: Geometry of imaging system alignment or the rotation of a given Stokes vector.

to be discussed in detail in §2.2.1.1. Equation 2.37 is given explicitly by

$$\begin{bmatrix} S_0 \\ S_1 \\ S_2 \\ S_3 \end{bmatrix}_{out} = \begin{bmatrix} m_{00} & m_{01} & m_{02} & m_{03} \\ m_{10} & m_{11} & m_{12} & m_{13} \\ m_{20} & m_{21} & m_{22} & m_{23} \\ m_{30} & m_{31} & m_{32} & m_{33} \end{bmatrix} \begin{bmatrix} S_0 \\ S_1 \\ S_2 \\ S_3 \end{bmatrix}_{in} . \tag{2.38}$$

Transmissive Mueller matrices will be represented by $\mathbf{T}$ and reflection Mueller matrices by $\mathbf{F}_r$ after BRDF notation. The units of a Mueller matrix are context-dependent. For instance, $\mathbf{T}$ is unitless, while $\mathbf{F}_r$ has units of $\mathtt{sr}^{-1}$ as does the BRDF function.

A few representative Mueller matrices for ideal transmissive polarization filters are provided in (2.39) and (2.40), which will be referenced when discussing polarimetric BRDF

measurements in §2.2.2.5.

$$\mathbf{T}_{\ominus} = \frac{1}{2}\begin{bmatrix} 1 & 1 & 0 & 0 \\ 1 & 1 & 0 & 0 \\ 0 & 0 & 0 & 0 \\ 0 & 0 & 0 & 0 \end{bmatrix} \qquad \mathbf{T}_{\oslash} = \frac{1}{2}\begin{bmatrix} 1 & -1 & 0 & 0 \\ -1 & 1 & 0 & 0 \\ 0 & 0 & 0 & 0 \\ 0 & 0 & 0 & 0 \end{bmatrix} \qquad \mathbf{T}_{\oslash} = \frac{1}{2}\begin{bmatrix} 1 & 0 & 1 & 0 \\ 0 & 0 & 0 & 0 \\ 1 & 0 & 1 & 0 \\ 0 & 0 & 0 & 0 \end{bmatrix} \tag{2.39}$$

$$\mathbf{T}_{\oslash} = \frac{1}{2}\begin{bmatrix} 1 & 0 & -1 & 0 \\ 0 & 0 & 0 & 0 \\ -1 & 0 & 1 & 0 \\ 0 & 0 & 0 & 0 \end{bmatrix} \qquad \mathbf{T}_{\circledast} = \begin{bmatrix} 1 & 0 & 0 & 0 \\ 0 & 1 & 0 & 0 \\ 0 & 0 & 1 & 0 \\ 0 & 0 & 0 & 1 \end{bmatrix} \qquad \mathbf{T}_{dep} = \begin{bmatrix} 1 & 0 & 0 & 0 \\ 0 & 0 & 0 & 0 \\ 0 & 0 & 0 & 0 \\ 0 & 0 & 0 & 0 \end{bmatrix} \tag{2.40}$$

The subscripts $\ominus$, $\oslash$, $\oslash$, and $\oslash$ represent the linear transmission orientation, θ, and are for horizontal, vertical, +45° and -45° (or +135°), respectively. A filter having no affect is the identity matrix, shown as $\mathbf{T}_{\circledast}$. A completely depolarizing filter is given by $\mathbf{T}_{dep}$. The general representation of a transmissive linear polarizing element oriented at angle θ is given by

$$\mathbf{T}_{\theta} = \frac{1}{2}\begin{bmatrix} 1 & \cos 2\theta & \sin 2\theta & 0 \\ \cos 2\theta & \cos^2 2\theta & \sin 2\theta \cos 2\theta & 0 \\ \sin 2\theta & \sin 2\theta \cos 2\theta & \sin^2 2\theta & 0 \\ 0 & 0 & 0 & 0 \end{bmatrix} . \tag{2.41}$$

Similar to the manner in which a Stokes vector may be decomposed into a completely polarized and randomly polarized component (2.35), a Mueller matrix may be decomposed into separate components [13]. This may prove useful in illustrating certain material properties.

Mueller matrices may also be cascaded as long as the order-dependent matrix multiplication is observed. For instance, the output of an incident Stokes vector which first passes through a horizontal polarization filter followed by a $\theta = 45°$ filter is represented as

$$\vec{S}_{out} = \mathbf{T}_{\oslash}\ \mathbf{T}_{\ominus}\ \vec{S}_{in} . \tag{2.42}$$

2.1.4 Electromagnetics Summary

From electromagnetic wave theory, the mechanism of polarization-induced reflectance has been presented. The law of reflection and refraction provided the direction of reflected and transmitted light, and the Fresnel equations provided the magnitude and polarization. The Fresnel equations only depend upon the incident angle (θ_i) and the index of refraction of the incident and reflected (or transmitted) mediums, $\tilde{n}_i$ and $\tilde{n}_t$.

Stokes vectors have been introduced as a suitable means of describing polarized radiance. Mueller matrices are shown to be a technique of propagating polarized radiance by transforming an incident Stokes vector into a resulting Stokes vector.

Having established the basic tools required to discuss polarized radiometry, the application of the Fresnel equations to real materials must now be addressed. Few materials are smooth at the macroscopic scale, so direct application of the Fresnel equations to realistic material surfaces is not possible. Optical scattering from materials is captured by the bidirectional distribution function (BRDF), which describes the geometric distribution of reflected energy from a surface. It is the main topic of discussion in §2.2.

2.2 Optical Scatter from Surfaces

Quantitative remote sensing in the VNIR is based upon measuring reflected solar energy from the earth. It is from these measurements and estimates of the surface "reflectance" that algorithms and quantitative techniques may be applied to derive information from remotely sensed light. Therefore, optical scatter or reflection phenomenology must be thoroughly understood, as this is the mechanism by which information unique to a specific material is translated into the reflected electromagnetic wave. This would seem to have been accomplished in §2.1.2.2 with the derivation of the Fresnel equations; however, real materials are significantly more complicated. This section examines optical scattering from surface reflections. Atmospheric optical scattering is also an important consideration as seen from equation 1.2, but will not be addressed until Chapter 4.

2.2.1 Reflection of Light

In the preceding example of Fresnel reflectance, the reflectance magnitude was completely determined based upon the optical properties of the materials and the angle of incidence. In addition, the reflected energy is only directed in the plane of incidence at the reflected angle, θ_r, where $\theta_r = \theta_i$ per the law of reflection. However, this is only true for perfectly planar or "smooth" surfaces which also have no internal scatter.

A quick look around is all it takes to realize that most surfaces are not perfect "mirror" surfaces,[2] and even mirror surfaces are not perfect. Also obvious is the fact that objects have color different than the illumination source, which is not accounted for by the Fresnel equations.

[2] An interesting thought experiment is to consider a world in which all surfaces were perfect mirror surfaces. In this world, only *sources* of illumination would be visible and no objects could be discerned!

Two effects are responsible for energy reflected or more generally energy scattered outside the $\theta_r = \theta_i$ reflectance angle. First, all materials have some level of surface roughness. This results in a distribution of localized surface normals which are oriented in multiple directions, similar to individual sequins on a dress. Therefore, the Fresnel reflectance is actually distributed around a reflection angle according to the "roughness" of the material. The second and usually more significant phenomena directing energy out of the $\theta_r = \theta_i$ scattering angle is *internal* or *volumetric scatter*. Once light has entered a material, multiple internal scattering results in distributing the energy around the hemisphere. The internal scattering sources are also responsible for color by selective spectral absorption. Figure 2.4 illustrates this complex interaction.

In Figure 2.4, several possible ray paths are noted. Incident irradiance, $\vec{E}_i$ may be reflected off the front surface of the material according to the local surface normal ($\hat{N}_i$) per the Fresnel reflection equation giving R_F (type A photons). Transmitted Fresnel irradiance, T_F, may then interact with a myriad of particles and molecules having selective absorption. After these single and multiple interactions, the energy may then re-emerge from the surface, again according to the Fresnel equations (type B photons). In most cases the incident medium is air, which results in the real part of the refractive index of the transmitted medium being greater than the incident medium or $n_t > n_i$. This in turn results in total internal reflection for upward scattered radiance exceeding the critical angle relative to the local surface normal (as most have experienced, only a small area of the sky is visible when looking up swimming underwater). Of course after re-emerging from the surface, additional interactions with adjacent facets may also occur (type C photons). Type C photons may also originate from secondary surface reflections, or two type A interactions. Therefore, the integration of the type A, B and C photons over a solid receiving angle and material surface area A determine the magnitude and polarization of the reflectance in a given direction.

A few important conclusions may be made. The multiple, random scattering centers within a material has the net effect of depolarizing the fraction of transmitted irradiance, T_F. This results in the diffuse component of scatter being highly randomly polarized. Also the scattered radiance from dark materials, or those which highly absorb T_F, have a higher relative Fresnel reflection component (which is polarized), R_F, since the magnitude of re-emerging scattered energy is low. This results in the degree of polarization (DOP) being inversely proportional to a material's reflectance. This has been termed the *Umov effect* [14] and is a phenomena which will be further investigated.

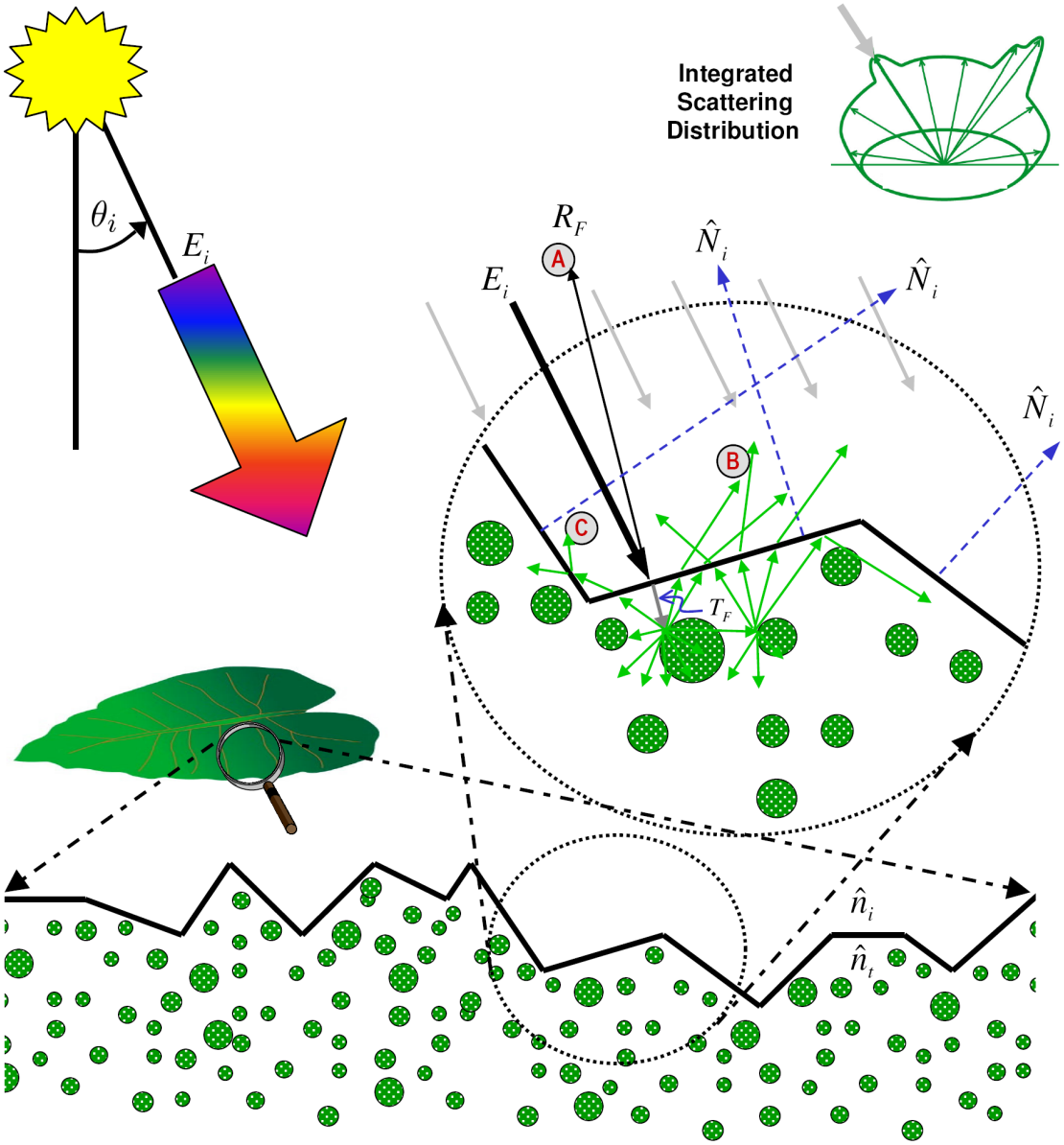

Figure 2.4: Detailed view of light scatter from material.

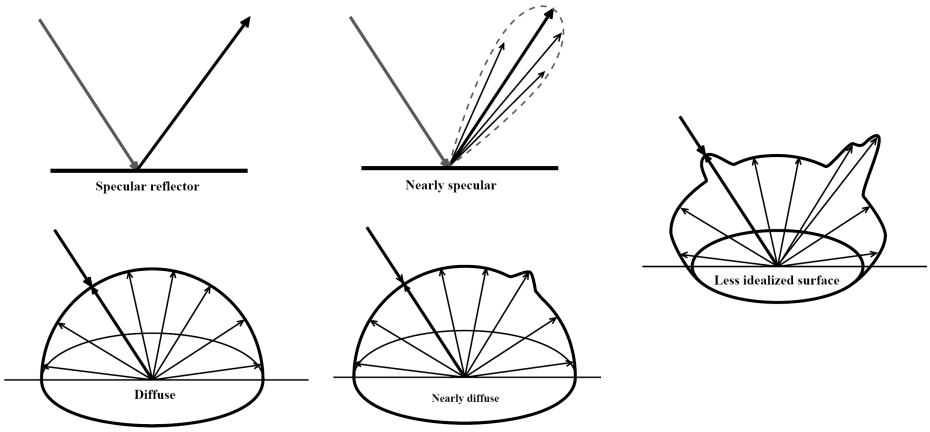

Figure 2.5: The radiance distribution for a range of BRDF examples (specular and diffuse, left) to the more realistic (right). From Schott [4, Fig. 4.7].

2.2.1.1 Bidirectional Reflectance Distribution Function (BRDF)

A means of characterizing this directional scatter is needed, which is the BRDF. BRDF may be thought of as quantitatively defining the qualitatively property of "shininess". A material may be described as being *diffuse* or *specular*; for example, a mirror is highly specular, and hence scatters minimal energy outside of the reflection angle. On the other hand, a projector screen is highly diffuse, where the apparent brightness (radiance) of the screen is the same regardless of viewing orientation. Examples of specular and diffuse scatter may be seen in Figure 2.5 where the geometric radiance distribution from different classes of objects is illustrated.

Specifically, BRDF quantifies the radiance scattered into all directions from a surface illuminated by a source in an arbitrary position above the hemisphere of the material. The BRDF is given by

$$f_r(\theta_i, \phi_i; \theta_r, \phi_r; \lambda) = \frac{dL_r(\theta_r, \phi_r)}{dE(\theta_i, \phi_i)} \ , \tag{2.43}$$

where L_r is the surface-leaving spectral radiance $\left[\frac{\mathtt{W}}{\mathtt{m}^2 \cdot \mathtt{sr} \cdot \mu\mathtt{m}}\right]$ and E is the spectral irradiance $\left[\frac{\mathtt{W}}{\mathtt{m}^2 \cdot \mu\mathtt{m}}\right]$ which results in BRDF having units of $\mathtt{sr}^{-1}$.

Half the battle in comprehending BRDF (and radiometry in general) is understanding the nomenclature and geometry. The nomenclature used is that recommended by Nicodemus [15, 16], which has subsequently been adopted by many authors. The National Bureau

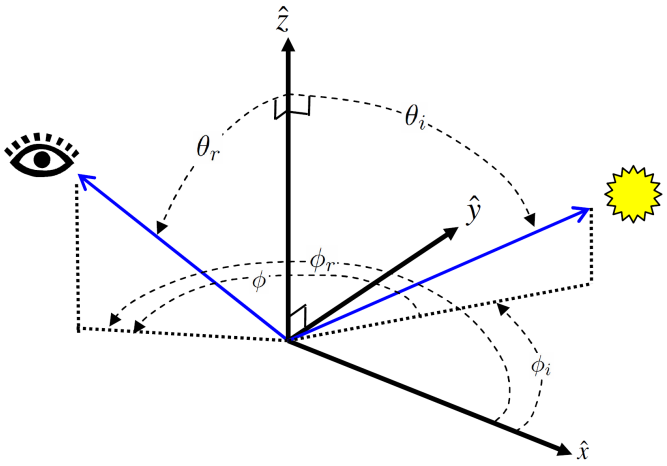

Figure 2.6: The BRDF geometry is uniquely specified by four angles corresponding to the source zenith and azimuth angles θ_i and ϕ_i and the reflected zenith and azimuth angles θ_r and ϕ_r. Most materials have azimuthal symmetry, in which case only a relative azimuth angle ϕ is required where $\phi = \phi_r - \phi_i$.

of Standards monograph by Nicodemus is a seminal document on BRDF [16].

The BRDF is a function of the incident angle, Θ_i, specified by the zenith and azimuth angles θ_i and ϕ_i; the reflected angle, Θ_r, similarly specified by zenith and azimuth angles θ_r and ϕ_r and finally the wavelength, λ. The zenith angles are defined relative to the local surface normal, which is $\theta_i = 0°$. Most materials have azimuthal or rotational symmetry about the surface normal. This reduces the degrees of freedom by one, enabling the azimuth angle to be characterized by only the difference between ϕ_i and ϕ_r, $\phi = \phi_r - \phi_i$. By convention, ϕ_i will be designated as $\phi = 0°$ and the reflected or scattering azimuth angle defined relative to this orientation, increasing counterclockwise as looking down on the surface. Forward scattering is therefore $\phi = 180°$. This reduces the BRDF specification for rotationally symmetric materials to a three-dimensional angular specification of $f_r(\theta_i; \theta_r, \phi; \lambda)$. The geometry is illustrated in Figure 2.6.

Note from Figure 2.6 that the source and detector occupy a solid angle, $d\omega$. BRDF is theoretically specified for a point source and detector, as well as an infinitesimal surface area, dA, but practical measurement considerations results in averaging over the source and detector solid angles ω_i and ω_s, and surface area A. The averaging is most critical when the BRDF varies greatly as a function of angle, such as is the case with a highly specular or mirror-like material around the scattered specular lobe.

BRDF is actually a subset of the more general bidirectional *scattering* distribution function (BSDF). Accompanying BRDF are the transmissive (BTDF) and volume (BVDF)

scattering functions which apply to materials having those scattering features [17]. The discussion will be limited to BRDF, but is worth noting that radiance contributions in what remote sensing ascribes to BRDF have elements from these other scattering sources (*e.g.*, vegetative canopies).

In general, man-made surfaces are likely to have a higher BRDF value in the forward scattering plane ($\phi = 180°$) near a reflectance angle equal to the incidence angle per the law of reflectance. However, this is generally not the case for natural surfaces with significant structure such as vegetation. The so-called "hot spot" is present in the backscattering direction of the illuminating source which may produce BRDF two to ten times that of a diffuse reflection angles. The source of the hot-spot is primarily due to no self-shadowing being visible when looking at a surface from the same orientation as the illumination angle. As the view angle moves away from the illumination position, self-shadowing by the material, such as from leaves of vegetation, result in decreased radiance. Coherent backscatter is also responsible for the hot spot phenomenon, but only dominates when the structure size of the material is on the order of the incident wavelength [18].

Reflectance, or the ratio of incident energy to that reflected, is only properly defined through the BRDF. This fact is often forgotten, as it is common to use a scalar value as a material's reflectance. Reflectance spectra "truth" databases typically only contain a scalar value as a function of wavelength. These values are actually the directional-hemispherical reflectance, ρ_{DHR}, which is the total reflectance for a specific angle of incidence [16, p. 11]. In terms of BRDF, ρ_{DHR} is given by

$$\rho_{DHR}(\theta_i, \phi_i) = \int_{2\pi} f_r(\theta_i, \phi_i; \theta_r, \phi_r; \lambda) \cos(\theta_r) \; d\Omega_r \; . \tag{2.44}$$

2.2.1.2 Polarimetric BRDF

Polarimetric BRDF, termed pBRDF, is the more generalized case of the scalar BRDF. In addition to quantifying the magnitude of the directional scattering, the polarization of the scattering is characterized. It is often overlooked that only the pBRDF correctly predicts the total reflectance magnitude when the incident irradiance is partially polarized. As described in §2.1.3, the radiometric quantities of equation (2.43) become Stokes vectors, and the BRDF becomes a Mueller matrix. The generalized polarimetric BRDF, $\mathbf{F}_r$, is thus represented as

$$\mathbf{F}_r(\theta_i, \phi_i; \theta_r, \phi_r; \lambda) = \frac{d\vec{L}_r(\theta_r, \phi_r)}{d\vec{E}(\theta_i, \phi_i)} \; . \tag{2.45}$$

Mueller matrix notation is most often used to describe transmissive mediums (such as

optics) which results in unitless Mueller matrices. Also, the matrix is frequently normalized such that the m_{00} element of $\mathbf{M}$ is 1 and the multiplicative constant dropped—this notation readily represents the medium's polarization characteristics at the expense of the losing absolute radiometric values. When representing BRDF using Mueller matrices, the matrix has units of $\mathtt{sr}^{-1}$ as expected, and multiplicative constants must be maintained. In this manner the f_{00} element of $\mathbf{F}_r$ remains equivalent to the scalar BRDF value such that

$$\rho_{DHR}(\theta_i, \phi_i) = \int_{2\pi} f_{00}(\theta_i, \phi_i; \theta_r, \phi_r; \lambda) \cos(\theta_r) \; d\Omega_r \; . \tag{2.46}$$

A good review of polarized BRDF representations is provided by Flynn [19].

Invoking the assumption that circular polarization is not present in a significant amount upon reflection from most natural surfaces [5, p. 486] reduces the Mueller matrix to a 3×3 matrix and the Stokes vector to a three element vector. With this reduction in dimensionality, (2.45) may be explicitly written as

$$\begin{bmatrix} L_0 \\ L_1 \\ L_2 \end{bmatrix} = \begin{bmatrix} f_{00} & f_{01} & f_{02} \\ f_{10} & f_{11} & f_{12} \\ f_{20} & f_{21} & f_{22} \end{bmatrix} \begin{bmatrix} E_0 \\ E_1 \\ E_2 \end{bmatrix} \; . \tag{2.47}$$

2.2.1.3 Reflectance Variability or Texture

The formal definition of BRDF requires the measurement of an infinitesimal surface area, dA, with an illumination source and detector that subtend an infinitesimal solid angle. It is obvious that each of these three areas must have a finite size for practical measurement purposes. It is actually *desirable* to have a surface area of sufficient size which adequately represents the material.

For example, consider characterizing the scatter from a "painted metal plate". Close inspection of the painted plate may reveal small defects such as paint bubbles or chips. If the BRDF measurement area were small and a defect occupied a significant fraction of the measurement area, it would significantly impact the scattering measurement. However, if a sufficiently large area of the plate were measured, the microscopic variability is averaged out, and a more accurate BRDF measurement results.

Local scattering variability within a material class is often called "texture", and may be quantified as the *bidirectional reflectance variance function* (BRVF) [20] or the bidirectional texture function, as it is commonly called in the computer graphics community [21]. Note

that this may be considered semantics—for the metal plate, one could also quantify the BRDF for "pristine paint," "paint bubbles" and "paint chips". From these three subclasses, the BRDF of the entire painted metal plate could be generated from a linear weighted combination of these surfaces.

Such approaches using fundamental material BRDF values quickly become impractical, since subclass divisions may be continued indefinitely; for instance, a subdivision of "paint chips" may be "paint chips with metal indentation", etc. The fundamental material approach toward constructing "macro" BRDF is also difficult with complex materials, such as a tree canopy which has significant transmittance and interaction among the leaves, ground, etc. The linear superposition of such complex objects becomes impossible with just BRDF data of the individual constituent materials. A BRDF measurement of a whole tree canopy is often more attractive.

Note that BRDF measurements of such macro materials enables averaging out local variabilities, but increases the responsibility on assigning adequate qualitative descriptors of the material. For instance, when pulling the BRDF of "grass" from a database of BRDF measurements, one would likely also want to know such parameters as the grass height, density of coverage or the amount of ground visible, the health of the grass, time of year, etc.

BRVF is a function of the surface area considered. If a remote sensing payload has a GSD of 1 `ft`, then there will essentially be no pixel-to-pixel variability due to BRDF when viewing the metal plate previously described. However, if the GSD is 1 `in`, then some pixel-to-pixel variability will likely be manifested from the material defects. Therefore, the BRVF may be defined as the BRDF probability density function given a measurement area, A.

$$BRVF(A) = p(f_r|A) \tag{2.48}$$

Often the BRVF distribution is unimodal and approximately Gaussian, in which case the variance is an adequate means of quantifying BRVF. It is also noted that the mean value of the BRVF is the BRDF.

BRVF has led to low-pass spatial filtering of high spatial resolution hyperspectral data cubes for target detection algorithms. If the target is resolved, then filtering down to the GSD of the projected target area may increase the signal to noise in detection algorithms due to the decreased background variability. Similarly, specular reflections from individual leaves in a tree canopy may have significant polarization imparted, but when integrated together at the level of a tree stand the net polarized radiance is not so easily determined.

2.2.2 BRDF Measurement

A means of quantifying the BRDF or more generally the pBRDF is needed to generate *a priori* BRDF databases of target and background materials which may be applied to algorithms. One means of generating the data is through BRDF models which may use physics-based principles to derive the directional reflectance—these will be discussed in §2.2.3. However, it will be seen that for practical purposes measurements are required as inputs for most BRDF models.

The key elements of any optical scatter measurement are the sample material or object to be measured, the illumination source and the detector. Most BRDF measurement devices employ one or more goniometric arms which provide angular positioning of the source and/or detector element. In some cases, the sample orientation may also be changed in order to achieve the full hemispherical range of source and detector orientations.

When high angular resolution is required to resolve the specular peak of mirror-like materials, the solid angle subtended by the detector may be minimized by increasing the material-to-detector distance or decreasing the detector size. For diffuse materials, the angular resolution is not as critical, since there are usually only modest changes in BRDF with reflection angle. The detector signal to noise can become an issue as one makes spectral BRDF measurements where a $\Delta\lambda$ of 10 nm may be desired, commensurate with the spectral bins of many hyperspectral sensors. Signal strength may also become problematic when measuring highly specular materials outside the specular lobe. However, in this circumstance the low signal is usually not of interest in remote sensing applications.

Commercial BRDF measurement systems have been developed and are available from at least two manufacturers. However, most measurement needs are satisfied with systems customized to the user's unique application. It is for this reason, in part, that very few BRDF databases exist. Measurements taken by a particular group often have inadequate material and experimental conditions described, and have tailored features which are not easily adaptable to a new user's interest.

Newer approaches in BRDF measurement often incorporate imaging techniques which enable the simultaneous sampling of multiple angles, greatly decreasing the required number of measurements. Imaging systems also readily enable characterization of the BRVF. However, many of the techniques are not polarization friendly. Other novel techniques have also been developed and will be briefly explored. The impetus for most of the newer measurement approaches are for improved rendering in computer animation and simulation, for which there is a significant commercial market.

Outdoor BRDF measurements are common for remote sensing due to the large spatial scales of the materials involved, as well as the inability to bring representative materials

into the lab, such as undisturbed live vegetation. Approaches toward outdoor BRDF measurements will be reviewed, as well as the means to handle some of the challenges outdoor measurements present.

Finally, the measurements required to capture the most general form of BRDF, the polarimetric BRDF will be reviewed. The foregoing measurement techniques may all be adapted to polarimetric measurements, with varying levels of complexity.

2.2.2.1 Conventional Laboratory Measurements

The most common and traditional means of measuring BRDF is to use an illumination source of small angular extent and a corresponding radiometer to measure the scattered radiance. Several means of acquiring the necessary source and detector angular sampling are invoked by using a goniometer. For most systems, it is easiest to fix the source position and vary the detector location to sample θ_r and ϕ_r. The incident angle, θ_i is sampled by moving the target sample, which is usually a relatively small, planar sample. In other circumstances where the detector system may be large, such as a spectrometer, the detector position is fixed and the source and material are moved to sample the hemisphere [22].

Illumination sources may either be lasers, or a broad-band source coupled with spectral filters at the source or detector to enable spectral measurements. Often the data acquisition process is automated, whereby the angular position of the detector and material is changed to cover the prescribed BRDF measurement sampling density. The number of required measurements is significant. For an isotropic material (no azimuth dependency) and sampling at 10° increments in both θ_i, θ_r and ϕ, the number of required measurements exceeds 1500 per spectral band: 9 for $0° \leq \theta_i \leq +80°$, 9 for $0° \leq \theta_r \leq +80°$ and 19 for $0° \leq \phi \leq +180°$ ($9 \times 9 \times 19$). If the material does not have azimuthal symmetry, an additional multiplier of 72 or more than 100,000 measurement per spectral band is required! This simple calculation illustrates the challenge in adequately measuring BRDF.

Lab measurements on materials of interest to remote sensing are particularly challenging. The heterogeneity or texture of most natural materials occurs at a spatial scale much larger than the typical sample size which is used in the laboratory. For this reason, natural materials are best measured over larger spatial scales and in their natural, undisturbed states by outdoor measurement techniques (§2.2.2.3). However, BRDF measurements of man-made materials, which often constitute "targets" in spectral detection algorithms, may be more accurately measured in the controlled lab environment. A review of BRDF lab measurements with a remote sensing perspective is provided by Sandmeier [23].

2.2.2.2 Camera-based Measurements

The use of focal planes to make BRDF measurements greatly increases measurement efficiency. Rather than having a single detector element, and hence a single bistatic angle for each measurement, multiple reflection angles may be simultaneously acquired by the individual focal place photosites. Several permutations on this concept may be employed. BRDF measurement techniques using focal planes may be categorized into three basic approaches: *i*) wide field of view (FOV) imaging to simultaneously sample many reflecting angles, *ii*) tailored optics imaging systems which uniquely samples the material (many variants) and *iii*) narrow FOV imaging used in a manner similar to a single element detector.

The wide FOV systems rely upon a large uniform material area for making measurements. Discrete scattering angles are obtained from each pixel of the imaging system, which enables an efficient, dense sampling of scattering angles for a single incident angle. Of course, spatial inhomogeneities in the material erroneously manifest themselves as a BRDF change so caution must be used. For pBRDF measurements using an optical system with polarization filters, the high incident angles make this approach challenging. A few outdoor systems make use of this measurement approach and will be addressed separately in §2.2.2.3.

The second basic imaging configuration, "tailored optics systems", encompasses a number of measurement concepts and are among the most creative. The overall approach is to re-image the material surface in a manner which enables efficient changes to the system, such as the incident angle of illumination and multiple viewing geometries. One such approach images an infinitesimal surface point [24, 25], and another employs a kaleidoscope which provides multiple discrete scattering angles while resolving the surface [26]. The most significant disadvantages of these systems are the limitations imposed upon the illuminating source and the sample size—outdoor measurements using the sun would be difficult. Also, since these systems use reflective optics having multiple reflections or varying reflectance angles, measuring the polarimetric BRDF is problematic due to the polarization dependency of the system.

Finally, a narrow FOV imaging system may be used, analogous in the manner of a single element detector. Implicit in this measurement technique is the ability to quantify BRVF from the image data. However, as with a single detector, many measurements or images must be acquired to cover the scattering hemisphere. Therefore, this technique must heavily rely upon BRDF models to inter/extrapolate the data. This technique is adaptable to both the lab and field. For field use, calibration and stray light mitigation are readily employed. Systems using this approach have not been noted in the literature, likely due to the inefficiency of hemispherical sampling. These three basic imaging approaches to BRDF

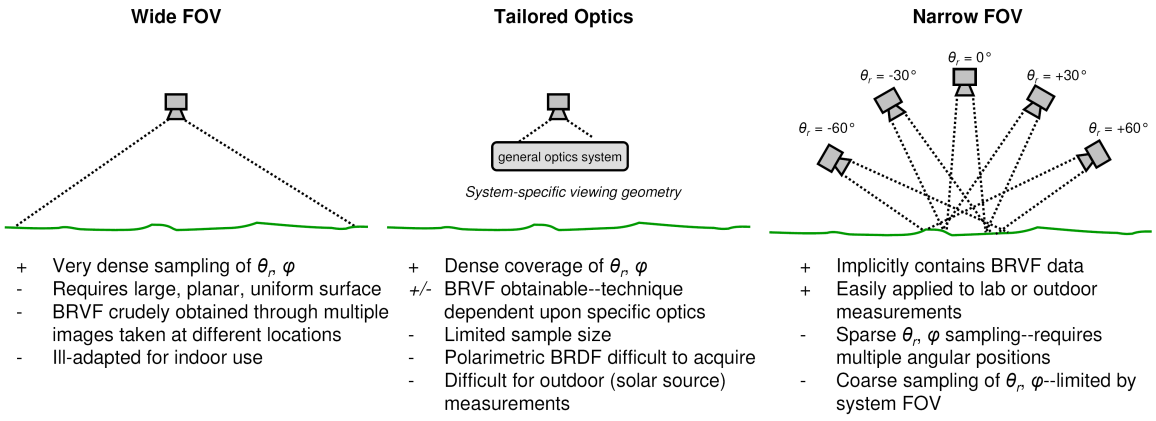

Figure 2.7: Three fundamental approaches toward focal-plane based BRDF measurements, along with their advantages (+) and disadvantages (-).

measurement, along with their relative merits are illustrated in Figure 2.7.

The following approaches are those of the "tailored optics systems," with the wide FOV systems addressed in the next section, §2.2.2.3. Discussion of the narrow FOV camera-based measurement will be postponed until §5.1, as it is this approach that will be used to characterize background pBRDF for this research effort.

A sampling of novel BRDF measurement techniques via imaging are briefly reviewed. Marschner reports a system which images an object of known shape, such as a sphere or a cone, covered with a desired material to be measured [27]. The shape of the object inherently provides the multiple viewing geometries rather than using optics. Viewing the object while having a single illumination source enables the direct measurement of a large number of incident and scattering angles with a single image. The technique is readily adaptable to pBRDF measurements, but only for a relatively small class of materials, such as painted surfaces. Measurement of background materials could not be accomplished using the technique.

Dana uses an off-axis parabolic mirror to image a single point on a material surface which provides multiple view angles [24, 25]. Multiple image points on the material surface are obtained by translating the parabolic mirror above the surface. The multiple image points enable BRVF or texture measurements. Again, this measurement concept is ill-adapted toward pBRDF measurement due to the high incident angles on the parabolic optic. A similar approach is also reported by Apel [28].

Finally, Han [26] images through a kaleidoscope which enables the simultaneous measurement of BRDF and BRVF. A tapered kaleidoscope having front-surface mirrors is used

to image a material, which creates a virtual sphere consisting of multiple, tapered facets corresponding to different viewing zenith angles of the object. The effect is equivalent to having multiple camera angles imaging the same surface area. A digital projector provides the light source and the incident illumination angles are controlled by selectively turning on groups of pixels in the digital projector. This is one of the most efficient measurement approaches, but again is not easily adapted for pBRDF measurements, nor is it very suitable for measurement of natural materials of large spatial extent.

2.2.2.3 Field Measurements

Portable BRDF devices suitable for outdoor measurements are attractive for a number of reasons. The use of portable devices arises out of necessity when measurements must be made which are extremely difficult, if not impossible to replicate in the lab. Natural materials may be heterogeneous over spatial extents significantly larger than what may be measured in the lab. Vegetation is a classic example of one such material, whether it is grass or a leaf canopy. Direct measurement of materials in their natural state and at larger spatial scales eliminates the requirement to scale-up individual material BRDFs which are often interactive, such as leaf transmittance and multiple leaf adjacency effects. Having the use of the sun as the source is advantageous as well. A good review of BRDF field measurements in the VNIR is given by Walthall [29].

Polarimetric BRDF field measurements also have an additional concern—the source must have a generator producing various polarization states. For practical reasons this is impossible. Placing an appropriate filter over the sun while making a measurement would be difficult and would require a large aperture filter, depending on the sample size being measured and the stand-off distance of the filter. As will be seen, having the ability to change only the analyzer polarization state results in quantifying the first column of the $\mathbf{F}_r$ scattering matrix.

An obvious challenge to outdoor measurements is cooperative weather and stray light. Good weather may eventually be found, but the downwelled sky radiance is always an error source in the measurements. In addition, the magnitude and distribution of this error source changes depending on local atmospheric conditions, such as extent of cloud cover. This error source obviously has a spectral dependence, as the blue sky testifies. A good discussion of outdoor measurement errors and minimization techniques is provided by Sandmeier [30] with some quantitative assessments provided by [31, 32]. A technique for minimizing this error will be discussed when addressing the approach toward background material pBRDF measurement in §5.1. Finally, the source zenith position is not easily adjustable.

In most circumstances, outdoor measurements are made over a sample size of area A

which is greater than that made with lab measurements. A sample area must be sufficiently large to average out high spatial frequency inhomogeneities or texture in the material, as discussed in §2.2.1.3. An indication of adequate sample size is when the resulting BRDF value is insensitive to changes in the sample area in the field of view (FOV) of the instrument, or $\frac{df_r}{dA} \rightarrow 0$.

A highly relevant challenge, though outside the scope of this treatment, is generating a sufficiently accurate and meaningful descriptive characterization of the material, which is critical for natural materials. It is by these descriptive labels that the material type will be selected and used in subsequent analysis, synthetic image generation, etc. A simple descriptor such as "Paint XYZ on Aluminum" is not sufficient when ascribing BRDF to inhomogeneous targets.[3] It is suggested that a robust meta-data set always accompany such measurements. This meta-data should include photographs of various viewing geometries of the sample, as well as detailed verbal descriptors.

A review is now provided of some field devices reported in the literature. Two fundamental designs may be used. A traditional "lab-like" system where the sensor is moved around a hemisphere above the target (mobile sensor design), or one in which the sensor does not translate, but acquires different view angles from the fixed position (immobile sensor design). With the latter type, the target area must be sufficiently uniform such that views of each area are representative of one another.

2.2.2.3.1 Mobile Sensor Designs The most direct approach toward field BRDF measurements is to emulate a laboratory setup by using a goniometer. With the illumination source (the sun) and target orientation on the ground fixed, the goniometer serves to move the detector to sampling positions throughout the hemisphere.

One such example of a system is FIGOS (field goniometer system) built by the Remote Sensing Lab of the University of Zürich [33, 34]. The system consists of a "zenith" arc of 2 `m` radius which rests on a circular frame of 4 `m` diameter—the azimuthal arc (Figure 2.8). A nearly identical goniometer, the Sandmeier Field Goniometer (SFG) was constructed by NASA Ames based upon the FIGOS design. However, this field goniometer is fully automated and the acquisition time for the same angular sampling scheme as FIGOS ($\Delta\theta_r = 15°, \Delta\phi_r = 30°$) is completed in less than 10 `min` [30]. Figure 2.8 pictures the SFG and FIGOS systems.

Another goniometer advertised as having outdoor measurement capability was constructed by ONERA in France. The target area is imaged with a bundle of 59 fiber optics

[3] Actually, adequately describing "simple" materials is very challenging also. Added to the description of "Paint XYZ on Aluminum" should also be information such as application method, surface condition and paint thickness—and again a picture doesn't hurt.

Figure 2.8: An example of field goniometers for BRDF measurements. FIGOS is shown on the left and the SFG system in the middle and right. From Sandmeier [30] (*left* and *right*) and Schill [35] (*middle*) with permission [36, 37].

and a fore optic [38, 39]. The fiber optics mixes the incident polarization of the scattered radiance, thus eliminating the polarization dependency of the diffraction grating in the spectrometer and making it suitable for pBRDF measurements.

The previous goniometer systems provide high angular precision and rapid sampling of the scattering hemisphere and are suitable for highly accurate characterization of field materials. However, both systems require significant support for transport and setup, which is exacerbated by having to time the weather conditions for suitable measurement periods. A much more simple measurement technique is often warranted which still provides meaningful BRDF data. Representing this other extreme are simple measurements made with a radiometer attached to a hand-held boom. The angular position of such a device may be estimated based on trigonometry of the height and distance from the measured area. Measurements of a only a few geometric positions provides an understanding of the BRDF anisotropy.

2.2.2.3.2 Immobile Sensor Designs An alternative approach to a sensor being repositioned around the hemisphere is a fixed sensor which changes the view angle over a large homogeneous measurement area. One such BRDF measurement device is PARABOLA (Portable Apparatus for Rapid Acquisition of Bidirectional Observations of Land and Atmosphere), which has been used in various forms by NASA-Goddard since the mid-1980s [40]. Such a sensor is often mounted high on a mast or a lift in order for the small FOV to image at an adequate GSD in an attempt to average out spatial inhomogeneities (Figure 2.9).

A similar device based upon this employment technique was designed and built by the Digital Imaging and Remote Sensing Laboratory at the Rochester Institute of Technology. The device uses a diffraction grating and a 2D CCD array which enables 10 nm sampling from

Figure 2.9: The Parabola III system showing the sensor, and the sensor mounted on a boom for field measurements. From NASA [41].

400–950 nm with a FOV of 1.72° × 0.06°, which was limited by the number of photosites on the focal plane. Using multiple scans, the effective FOV is increased to 1.72° × 1.6° [42]. As noted earlier, diffraction gratings are highly polarization sensitive, and for pBRDF measurements the incident radiance upon the diffraction grating should first be randomly polarized to provide consistent results.

An equivalent approach may be made with an imaging system. Rather than scanning a radiometer to acquire the multiple view angles, a wide FOV camera lens may be used. The University of Arizona uses such a system which assists in the vicarious radiance calibration of Landsat [43, 44, 45]. Linear CCDs may also be used to make a conical push-broom scan around the target area [46, 47].

2.2.2.4 Overhead BRDF Measurement

Finally, new payloads have enabled BRDF measurement from satellites and aircraft. In these instances the atmosphere provides an additional measurement uncertainty in deriving the surface-leaving radiance. One such instrument is POLDER (Polarization and Directionality of the Earth Reflectances) [48], which has a wide field of view (GSD of 6 km) and is flown on the ADEOS satellite [49]. Derivation of POLDER BRDF products is described in [50, 51]. Use of POLDER polarization data and additional details on the system is further discussed in §10.2.3.

Similar data is provided by NASA's MODIS (Moderate Resolution Imaging Spectroradiometer) instruments, flown on Terra (EOS AM-1) and Aqua (EOS PM-1), having a GSD of 250-1000 m depending upon the spectral band [52]. MODIS scans ±55° thus enabling multiple angular views with successive passes. Initial BRDF products from the instrument

were available in the year 2000 [53]. The Terra satellite also hosts NASA's MISR (Multi-angle Imaging SpectroRadiometer) payload which provides BRDF data using 4 spectral bands to acquire 9 angular views spaced in the along-track direction [54].

2.2.2.5 Polarimetric BRDF Measurement

As noted in §2.2.1.2, one quantifies the reflective BRDF Mueller matrix, $\mathbf{F}_r$, in making polarimetric BRDF measurements per equation (2.45). In polarimetric BRDF measurements, the scattered or reflected Stokes radiance vector, $\vec{L}$, must be quantified such that

$$\vec{L}(\theta_r, \phi) = \mathbf{F}_r(\theta_i, \phi, \theta_r)\vec{E}(\theta_i) \ . \tag{2.49}$$

However, without the use of any polarization filtering, the detector only measures the magnitude of the irradiance and radiance as in the case of the scalar BRDF or

$$L_0(\theta_r, \phi) = f_{00}(\theta_i, \phi, \theta_r)E_0(\theta_i) \ , \tag{2.50}$$

where the "0" subscript denotes the first element of the Stokes vector, which is the total flux and f_{00} is the upper left element of the BRDF matrix equivalent to the scalar BRDF, f_r.

Clearly, additional measurements are needed to characterize the other 15 elements of the BRDF matrix. When considering linear polarization, this requirement is reduced to determining the remaining 8 elements of the 3×3 BRDF matrix. These additional elements of the array may be determined by linear combinations of incident irradiance polarization states, $\vec{E}$, and received polarization radiance states, $\vec{L}$.

The most generalized means of acquiring the matrix elements is through presenting multiple incident polarization states, and measuring the output for each incident state, thus building a system of linear equations. The polarization filters which create incident polarization states are termed *generators* while those which filter the output are called *analyzers*. The presentation of i incident polarization states onto the sample and their polarized radiance measurements may be represented as

$$\mathbf{F}_r \left[\ \vec{E}_1\vec{E}_2\cdots\vec{E}_{i-1}\vec{E}_i \ \right] = \left[\ \vec{L}_1\vec{L}_2\cdots\vec{L}_{i-1}\vec{L}_i \ \right] \ , \tag{2.51}$$

where $\left[\ \vec{E}_1\vec{E}_2\cdots\vec{E}_{i-1}\vec{E}_i \ \right]$ is a $4 \times i$ matrix consisting of irradiance column Stokes vectors and $\left[\ \vec{L}_1\vec{L}_2\cdots\vec{L}_{i-1}\vec{L}_i \ \right]$ is the equivalent radiance representation. Rewriting these terms

as matrix quantities $\mathbf{E}$ and $\mathbf{L}$, the new expression is

$$\mathbf{F}_r\mathbf{E} = \mathbf{L} \tag{2.52}$$

where it is seen that

$$\mathbf{F}_r = \mathbf{L}\ \mathbf{E}^{-1}\ . \tag{2.53}$$

However, inversion of $\mathbf{E}$ is only possible when it is a nonsingular square matrix. For the general case where $i > 4$, the pseudoinverse of $\mathbf{E}$ is sought, $\mathbf{E}^{\#}$, which provides a least squares estimate in the presence of random noise. The pseudoinverse is given by

$$\mathbf{E}^{\#} = \mathbf{E}^T \left(\mathbf{E}\mathbf{E}^T\right)^{-1}\ , \tag{2.54}$$

where T is the transpose of the matrix. The Mueller matrix is therefore solved by

$$\mathbf{F}_r = \mathbf{L}\ \mathbf{E}^{\#}\ . \tag{2.55}$$

In this manner the full BRDF Mueller matrix may be determined for each permutation of θ_i, θ_r, ϕ and λ as one would measure the scalar BRDF.

For practical measurement considerations, one would like an efficient set of input and output polarization states to minimize the number of measurements. The equation describing this measurement setup is given as

$$\vec{L} = \mathbf{T}_A\ \mathbf{F}_r\ \mathbf{T}_G\ \vec{E}\ , \tag{2.56}$$

where $\mathbf{T}_G$ is the transmissive generator filter over the source and $\mathbf{T}_A$ is the transmissive analyzer filter over the detector. Note that the generator and analyzer Mueller matrices have no units, but the BRDF Mueller matrix $\mathbf{F}_r$ has BRDF units, $\mathtt{sr}^{-1}$ (*cf.* §2.2.1.2).

Referencing the polarization filters provided by equation (2.39), a simple example is constructed for generator and analyzer linear horizontal filters. The equation is given by

$$\vec{L} = \mathbf{T}_{\ominus}\ \mathbf{F}_r\ \mathbf{T}_{\ominus}\ \vec{E} \tag{2.57}$$

or explicitly as

$$\begin{bmatrix} L_0 \\ L_1 \\ L_2 \end{bmatrix} = \frac{1}{2}\begin{bmatrix} 1 & 1 & 0 \\ 1 & 1 & 0 \\ 0 & 0 & 0 \end{bmatrix}\begin{bmatrix} f_{00} & f_{01} & f_{02} \\ f_{10} & f_{11} & f_{12} \\ f_{20} & f_{21} & f_{22} \end{bmatrix}\frac{1}{2}\begin{bmatrix} 1 & 1 & 0 \\ 1 & 1 & 0 \\ 0 & 0 & 0 \end{bmatrix}\begin{bmatrix} E_0 \\ E_1 \\ E_2 \end{bmatrix} \tag{2.58}$$

which reduces to

$$\begin{bmatrix} L_0 \\ L_1 \\ L_2 \end{bmatrix} = \frac{1}{4} \begin{bmatrix} (f_{00} + f_{01} + f_{10} + f_{11})\,(E_0 + E_1) \\ (f_{00} + f_{01} + f_{10} + f_{11})\,(E_0 + E_1) \\ 0 \end{bmatrix} \quad . \tag{2.59}$$

However, as always it is only the first Stokes component that the detector will be measuring. If the original source is highly randomly polarized, then $E_1 \ll E_0$ and the measurement yields

$$L_0 = \frac{(f_{00} + f_{01} + f_{10} + f_{11})\,E_0}{4} \quad . \tag{2.60}$$

In a similar manner, other permutations of generator and analyzer polarization states produce additional linear combinations of the Mueller matrix elements. A summary of such combinations is provided by Bicket [55]. To quantify the 3×3 subset of $\mathbf{F}_r$ which relates to linear polarization, a total of 9 measurement permutations is required which include the three generator and analyzer states of horizontal, $+45°$ and no (or random) polarization. These states are represented symbolically as $\ominus$, $\oslash$ and $\circledast$, respectively. Using this symbolic representation, equation 2.60 may be recast as

$$\ominus\,\ominus = \frac{L}{E_0} = \frac{f_{00} + f_{01} + f_{10} + f_{11}}{4} \tag{2.61}$$

where the first "$\ominus$" represents the generator state, and the second "$\ominus$" is the polarization of the analyzer. Using this notation, the Mueller matrix elements may be shown to equal

$$f_{00} = \circledast\circledast \tag{2.62a}$$
$$f_{01} = 2\ominus\circledast - \circledast\circledast \tag{2.62b}$$
$$f_{02} = 2\oslash\circledast - \circledast\circledast \tag{2.62c}$$
$$f_{10} = 2\circledast\ominus - \circledast\circledast \tag{2.62d}$$
$$f_{11} = 4\ominus\ominus - 2\circledast\ominus - 2\ominus\circledast + \circledast\circledast \tag{2.62e}$$
$$f_{12} = 4\oslash\ominus - 2\circledast\ominus - 2\oslash\circledast + \circledast\circledast \tag{2.62f}$$
$$f_{20} = 2\circledast\oslash - \circledast\circledast \tag{2.62g}$$
$$f_{21} = 4\ominus\oslash - 2\circledast\oslash - 2\ominus\circledast + \circledast\circledast \tag{2.62h}$$
$$f_{22} = 4\oslash\oslash - 2\circledast\oslash - 2\oslash\circledast + \circledast\,\circledast \quad . \tag{2.62i}$$

Often the symmetry of the material results in $f_{01} = f_{10}$, $f_{02} = f_{20}$ and $f_{12} = -f_{21}$.

Careful error analysis must also accompany this measurement process. Errors may be

introduced from several factors. The illuminating source may have some inherent polarization and the detector may have a polarization-dependent response. Some errors are always present from polarization filters, which are not perfect. All filters have a finite extinction coefficient, or the transmittance along one polarization axis relative to the other axis. This amounts to some leakage of the opposite polarization state which becomes an error source. This leakage is also spectrally-dependent. Finally, the fidelity of filter alignment results in an error source. Propagation of Mueller matrix element errors has been addressed by several authors [56, 57, 58, 59, 60].

2.2.2.6 BRDF Databases

There are few BRDF databases, and no known polarimetric BRDF databases. A brief synopsis of some scalar-only BRDF databases are given. The Columbia-Utrecht Reflectance and Texture (CUReT) Database supports computer graphics rendering and as such the spectral data is limited to RGB channels. It contains more than 60 different materials, with measurements for each consisting of more than 200 incident and scattering angle combinations—all the data is internet accessible [21, 61]. Cornell also has a similar database, having fewer materials but higher spectral fidelity [62]. Numerous spacecraft and optical component BRDF data are consolidated in SOLEXIS^{TM}, a database assembled from many independent private sources [63]. Finally, Surface Optics Corporation maintains a small BRDF database available for purchase [64].

The database of most interest in this research is contained in the Nonconventional Exploitation Factors (NEF) Data System. The NEF provides BRDF signatures of more than 400 materials via a modified Maxwell-Beard BRDF model [10], but is limited in distribution and not publicly available. Access has been gained to the raw measurements which are used to derive the Maxwell-Beard model parameters. The measurement protocol for acquiring the data is that recommended by Maxwell [65], discussed in detail in §2.2.3.3.2. These raw measurements contain *pp*, *ss* and *sp* BRDF measurements, where the first letter indicates the incident polarization state, and the second the sensed stated. Laser sources from the UV to LWIR are used to obtain the scattering in the plane of incidence. Spectral interpolation is accomplished by a high spectral resolution DHR measurement, where it is assumed that the spectral BRDF change with orientation is a slowly varying function [10]. Materials covered in the NEF are grouped into twelve general categories which include asphalt, brick, camouflage, composite, concrete, fabric, water, metal, paint, rubber, soil and wood. The database has been employed in rendering computer graphics [66, 67] as part of a project by the National Institute of Standards and Technology [68]. The availability of the raw data used to derive the Maxwell-Beard model parameters provides the motivation for enabling

the polarization of this and other similar BRDF models.

2.2.3 BRDF Models: Target Materials

As has been seen, an infinite number of measurements is required to fully quantify BRDF. The difficulty in making and managing BRDF datasets necessitates the use of BRDF models. BRDF models are motivated from several factors:

1. *Compactness*: Individual material data sets with high angular and spectral sampling may easily exceed 100 `MB`, and if a scene is considered which contains hundreds of materials, the volume of data is unmanageable. A BRDF model provides a concise means of storing the data.

2. *Interpolation*: Often only sparse hemispherical sampling has been measured for samples, in which case a means of inter- or extrapolating the measured values is required.

3. *Prediction*: No BRDF measurements have been made for a material, but the physical attributes of the material are known which enable prediction of the BRDF.

4. *Information Extraction*: In fields such as remote sensing and semiconductor processing, BRDF models may be linked to physical attributes such as leaf area index which provide target information.

Virtually all BRDF models satisfy the need for compactness, and most provide some means of interpolation. Models providing prediction without any measured data are first-principles, physics based and are attractive since empirical data is not needed. Many models are prediction models which use a modest amount of empirical data, to which some constants or parameters are fit. Finally, models which provide information extraction are usually tailored to a specific target classes of interest, such as erectophile vegetation or conifer forests.

There are seemingly an infinite number of BRDF models, derived from many researcher's dissatisfaction with attempting to apply existing models to their specific interest area. Surprisingly, the computer graphics community has made substantial contributions to the field as processing power has enabled three-dimensional rendering of objects. Of course, there is a significant commercial market for these applications which continues to drive development.

The BRDF models covered in this section are limited to those for *homogeneous* materials. That is, models which describe a highly uniform surface that is common with man made materials which have minimal texture. Thus they are suitable for describing surfaces which

are often *target materials* in spectral algorithms. *Heterogeneous* material BRDF models, such as those commonly used in remote sensing for complex vegetation canopies are very distinct from the homogeneous material models. These models may be used to describe *background materials* in spectral algorithms, which may generally be referred to as *clutter*. It is rare to find a remote sensing publication which references homogeneous or target material BRDF models common to the optics and radiometry community. Historically, the GSD of remote sensing systems has necessitated the use of background material BRDF models which mixes many material classes within a pixel. Discussion of background material BRDF models is postponed until §2.2.4.

BRDF models may be classified in a number of ways. One classification is based upon the treatment of the optics. *Geometric optics models* are in general more approachable, but the underlying ray model assumptions break down as surface roughness dimensions decrease and become proportional to or less than the wavelength. Models based on *physical optics* provide a much more thorough treatment through field equations, but result in complicated expressions.

BRDF models may also be classified as *physical* or *empirical*. Physical models rely upon first-principle physics of electromagnetic energy and material interactions, and require inputs such as surface roughness parameters and the complex index of refraction. Empirical models rely solely upon measured BRDF values, while *semi-empirical* models incorporate some measured data, but may have significant elements of physics-based principles. These *semi-empirical* models are perhaps the most common and versatile.

Many BRDF models divide a surface into microfacets, for which the distribution of the individual microfacet normals drives the specular and diffuse scattering contributions, as previously discussed (*cf.* Figure 2.4). These models heavily rely on spherical trigonometry to relate the local microfacet coordinate system to the material surface coordinate system.

Recently, polarized BRDF (pBRDF) models have been developed which predict the polarized radiance as discussed in §2.2.1.2. Such models are a prerequisite to the quantitative analysis of polarimetric images in remote sensing. The polarized models are usually enabled by using the Mueller matrix representation of the microfacet reflections. Two of the pBRDF models reported in the literature have been enabled by adapting an existing BRDF model to include polarization effects.

Finally, the question of required accuracy must be addressed. A systems engineering approach to this question is appropriate, as the required accuracy of any BRDF model depends upon the specific application, as well as the magnitudes of other radiometric errors present in the remote sensing imaging chain. It is suggested that the accuracy of many of the models discussed below is more than sufficient in remote sensing applications. Consider a

spectral target detection algorithm. An assumption must be made regarding the orientation of the target relative to the local horizon. The most obvious assumption is that the target is on level ground. However, deviations of $\pm 20^\circ$ are not difficult to consider (*e.g.*, the slope of the front of a vehicle, a vehicle on a modest hill, etc.).

2.2.3.1 Early BRDF Models

Though often not considered a BRDF model, the Lambertian assumption ascribes a constant BRDF for all incident and reflecting geometries [69]. It is simply

$$f_r = \frac{\rho}{\pi} \tag{2.63}$$

where ρ is the reflectance. This is the traditional treatment of reflectance in remote sensing.

One of the earliest variable BRDF models was proposed by Minnaert in 1941 to account for darkening near the lunar limb [70]. It is represented by

$$f_r = \frac{\rho \left(\cos\theta_r \cos\theta_i\right)^{k-1}}{\pi} \tag{2.64}$$

where k is the "limb darkening" parameter. Note for $k = 1$, it is equivalent to Lambert's BRDF.

Astronomical observations have motivated significant BRDF work. In particular, physical explanations of the "hot spot" effect for planetary bodies was sought. Analysis was also performed in attempts to better understand the surface of the moon in preparation of the Apollo lunar landings. Toward this end, Hapke developed what is known as the Hapke/Lommel-Seeliger BRDF model which accounted for opposition effects [71]. This work concluded that the lunar surface was composed of fine, compacted dust. The model would later form part of the basis of the popular semi-empirical model by Maxwell-Beard.

2.2.3.2 Empirical Models

The most straightforward means of producing BRDF data for all incident and scattering angles is simply by interpolation of empirical data, which may be viewed by some as circumventing a BRDF model altogether. Here, no physical basis of the scattering is considered, and the only inputs are the empirical measurements. This approach is attractive due to the simplicity.

Such an approach has been used by the University of Zurich's Remote Sensing Laboratories for outdoor measurements using the BRDF measurement system described in §2.2.2.3 [33, 34]. An example of fitting BRDF data for lawn grass is shown in Figure

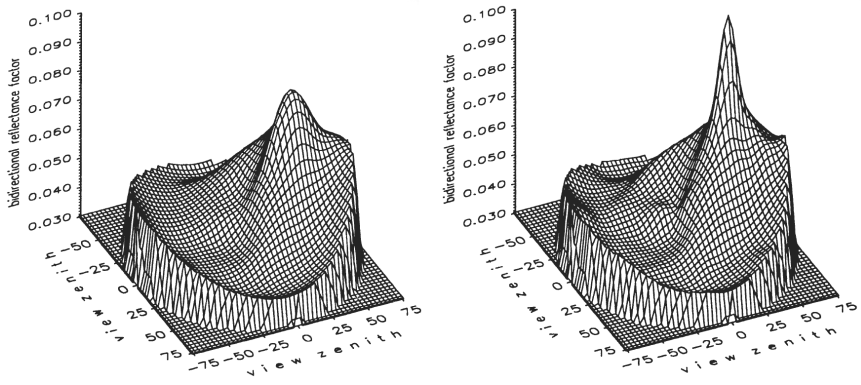

Figure 2.10: BRDF data for grass at 600 nm interpolated using spherical Delaunay triangulation with ∼70 measurements (left) and ∼400 measurements (right). Data acquired with the FIGOS system (*cf.* §2.2.2.3.1). (With permission from Sandmeier [36, 72]).

2.10 at 600 nm for an incident solar angle of $\theta_i = 35°$. Here, interpolation is accomplished by spherical Delaunay triangulation, with the left figure having a sampling of $\Delta\theta_r = 15°; \Delta\phi = 30°$ (∼70 measurements) and the right figure having a ∼sixfold increase in sampling at $\Delta\theta_r = 5°; \Delta\phi = 15°$ (∼400 measurements). While there is a marked change in the peak magnitude around the "hot spot" or retroreflection position, the other angular positions in the coarser sampling appear to have only minor variations.

Interpolation of measured data is highly accurate so long as measurements are made with reasonable sampling densities. The accuracy increases as the geometric sampling density increases, but at the expense of massive data storage requirements (*cf.* §2.2.2.1). Measured BRDF values may be decomposed into appropriate basis functions having spherical or circular symmetry, greatly reducing the storage requirements for measured data sets.

Spherical harmonics may be used as a basis set to represent an arbitrary BRDF, analogous to the manner in which a Fourier series may be used to represent a function. However, a significant number of coefficients may be required for accurate representation, and "ringing" may be present from series truncation [73]. As an alternative to spherical harmonics, the hemisphere may be projected onto a single plane and Zernike polynomials used [74]. In a similar manner, spherical wavelets may also be used [75]. Other ideas for efficient representation include transforming BRDF variables by taking advantage of symmetries to reduce the number of required basis function coefficients [76].

2.2.3.3 Semi-empirical Models

2.2.3.3.1 Torrance-Sparrow In 1967 Torrance and Sparrow presented one of the first BRDF models to capture such phenomena as the off-specular peak, as well as providing good predictions as $\theta_r \rightarrow 90°$ [77]. The Torrance-Sparrow (T-S) model is developed on the basis of geometrical optics, and as such it requires the RMS surface roughness, σ_m, to be comparable to or greater than the wavelength considered ($\sigma_m/\lambda \gtrsim 1.0$). As with many BRDF models, the contributions of individual microfacet reflections to the overall material BRDF is considered. Each microfacet of area A_f is treated as a specular surface, for which the surface normal angular positions, α, are distributed according to a gaussian probability distribution, $P(\alpha)$. The diffuse BRDF component of the BRDF arises from multiple microfacet reflections or internal scattering. Therefore, the reflected radiance, L_r may be expressed as the sum of the specular and diffuse components

$$L_r = L_{r,s} + L_{r,d} \ , \tag{2.65}$$

with the diffuse component given in terms of the incident radiance, L_i, by

$$L_{r,d} = aL_i \cos\theta_i \tag{2.66}$$

where a is a constant.

The specular reflection is obtained by considering the Fresnel reflection, F, off each microfacet, *cf.* (2.10) and (2.12). The significant advancement made by the T-S model was the introduction of a *geometric attenuation factor*, G, which enables *masking* and *shadowing*. Masking is the blockage of specular reflections by adjacent microfacets while shadowing is the blockage of the illumination source onto a microfacet by adjacent microfacets. The resulting BRDF from the T-S model is given as

$$f_r = \frac{F(\theta_i^{'}, \hat{n})\, A_f\, G(\theta_{i,p}, \theta_{r,p})\, P(\alpha)}{4\, \cos\theta_i\, \cos\theta_r} + \frac{a}{d\omega_i} \ , \tag{2.67}$$

where the second term is the diffuse component and the primed coordinate system is relevant to the microfacet normal. The $\theta_{X,p}$ coordinates result from projections of θ_i and θ_r onto the plane determined by the facet and surface normals.

So what parameters are required for producing T-S BRDF predictions? To obtain the Fresnel reflectance, $\tilde{n}$ is required. A roughness parameter, c, which relates the distribution of facet slopes relevant to the normal plane is required. Note that c is contained in $P(\alpha)$,

$$P(\alpha) = c\ e^{-c^2\alpha^2} \ . \tag{2.68}$$

T-S used a value of $c = 0.05$ which was justified based on fitting the data to experimentally-determined BRDF. While T-S makes use of first principles to model the BRDF, it nonetheless requires a parameter which they fit to experimental data.

2.2.3.3.2 Maxwell-Beard The development of the Maxwell-Beard (M-B) BRDF model was originally motivated for use on painted surfaces [65]. The model development emphasizes BRDF prediction from IR laser sources (1–4 $\mu\mathtt{m}$) with varying polarization states. As with the Torrance-Sparrow model, separate specular and diffuse contributions to the BRDF are considered, which Maxwell and Beard term *surface* and *volume* contributions.

With the surface model, only single reflections from the microfacet surface are considered. The distribution of the microfacets are obtained through a "zero angle" bistatic scan (ZBS) in which the detector and illumination source are co-located, or as close to the same position without subtending each other. The surface normals of each microfacet are defined as being oriented in the (θ_N, ϕ_N) direction. The measured signal of the ZBS scan may then be related to the density of microfacets which fall within the detector solid angle, giving a density of $\Xi(\theta_N, \phi_N)$ which has units of $\mathtt{sr}^{-1}$. Reflection from the microfacets is given by the Fresnel reflectance, (2.10) and (2.12).

In terms of these experimentally-measured parameters, the surface model component of the BRDF may be expressed as

$$f_{r_{\mathtt{surf}}}(\theta_i, \phi_i; \theta_r, \phi_r) = \frac{R_F(\beta)}{R_F(0)} \frac{f_{ZBS}(\theta_N) \cos^2 \theta_N}{\cos\theta_i \cos\theta_r} \tag{2.69}$$

where R_F is the Fresnel reflectance, expressed in terms of half the angle between the source and receiver, where 2β is the bistatic angle or angle between the source and receiver. $f_{ZBS}(\theta_N)$ is the BRDF from the ZBS scan through the zenith position (*i.e.*, $-90^\circ \leq \theta_i = \theta_r \leq 90^\circ$). It is given by

$$f_{ZBS}(\theta_N) = \frac{R_F(0)\Xi(\theta_N, \phi_N)}{4\cos\theta_i \cos\theta_r} \tag{2.70}$$

from which the microfacet density function is obtained.

All information needed for (2.69) is experimentally obtained. However, the Fresnel reflectance requires the complex index of refraction, $\tilde{n}$, of the material. M-B assumed the surfaces were dielectrics, a reasonable assumption for the paint samples they were modelling, which makes $k \approx 0$ or $\tilde{n} \approx n$. A value of n in their study was estimated as $n = 1.65$ and was based upon experience with paint samples [65, §7.2, p. 56]. As an alternative, M-B indicate the value of n may be calculated based upon Brewster's angle, θ_B, or the angle of

incidence where the p-polarization component is minimum.

Using (2.69), M-B derived what the in-plane BRDF should be with a fixed incident angle. Systematic variations were found which were attributed to shadowing and masking of the microfacets, previously addressed in the Torrance-Sparrow model discussion. However, M-B developed their own empirically-derived function to account for shadowing and obscuration (SO), which they found superior to the Torrance-Sparrow function. The SO function has two free parameters, τ and Ω [65, p. 10] and is given by

$$SO(\tau,\Omega) = \frac{1+\frac{\theta_N}{\Omega}\ e^{-2\beta/\tau}}{1+\frac{\theta_N}{\Omega}} \left(\frac{1}{1+\frac{\phi_N}{\Omega}\frac{\theta_i}{\Omega}}\right) , \tag{2.71}$$

where ϕ_N is a "factor calculated from the geometry, which adjusts the fall-off rate of the shadowing and obscuration function in the forward-scattered direction" [65, p. 10]. With this modification, the M-B surface BRDF is given by

$$f_{r_{\mathtt{surf}}}(\theta_i,\phi_i;\theta_r,\phi_r) = \frac{R_F(\beta)}{R_F(0)} \frac{f_r(\theta_N)\cos^2\theta_N}{\cos\theta_i\cos\theta_r}\ SO(\tau,\Omega)\ . \tag{2.72}$$

Maxwell and Beard then develop a volume component of the model. The non-Lambertian volume component development was motivated by experimental observation that the diffuse scatter component was in fact not Lambertian, both from the angular dependency and the lack of complete depolarization. The non-Lambertian volume component accounts for subsurface scatter, or the type B and C photons in Figure 2.4. Derivation of this volume component considers the exponential loss via scattering of energy as the light propagates into the medium, as well as the exponential loss of energy as the light propagates back to the surface. It is assumed there is no net transmission of energy through the surface, and absorption in the medium is not explicitly considered. Given these considerations, the parametric volume component of the BRDF is given as

$$f_{r_{\mathtt{vol}}} = \frac{2\ \rho_V f(\beta)\ g(\theta_N)}{\cos\theta_i + \cos\theta_r}\ , \tag{2.73}$$

where $f(\beta)$ and $g(\theta_{\hat{N}})$ collectively include the β and θ_N dependencies, and are treated as free parameters for adjustment based upon the empirical data. However, the computer model implemented by M-B kept $f(\beta) = g(\theta_N) = 1$, and simply cite these parameters may provide flexibility in future model development [65, p. 57]. ρ_V is a constant which may be seen to equal $f_{r_{\mathtt{vol}}}$ when $\theta_i = \theta_r = 0°$ and with $f(\beta) = g(\theta_{\hat{N}}) = 1$. ρ_V is experimentally obtained by measuring the BRDF at $\theta_i = \theta_r = 0°$ with the incident light polarized orthogonal to the detector filter [65, pp. 16, 57].

The complete M-B BRDF model is given by the sum of the surface and volume components, or

$$\begin{aligned} f_r(\theta_i, \phi_i; \theta_r, \phi_r) &= f_{r_{\texttt{surf}}} + f_{r_{\texttt{vol}}} \\ &= \frac{R_F(\beta)}{R_F(0)} \frac{f_{ZBS}(\theta_N) \cos^2 \theta_N}{\cos\theta_i \cos\theta_r} + 2\frac{\rho_V f(\beta) g(\theta_N)}{\cos\theta_i + \cos\theta_r} \ . \end{aligned} \tag{2.74}$$

So how is the model implemented? The monostatic scan is necessary for determining the microfacet surface normal distribution function. For the microfacet Fresnel reflectance, an estimate of $\tilde{n}$ is required which may be estimated based upon Brewster's angle derived from experimental data. Using these as inputs, three parameters are fit to empirically-measured BRDF: two which model the shadowing and obscuration, τ and Ω; and one which gives the volume component of the scatter, ρ_V. Values of these parameters used in the M-B paper for a green and tan paint were $\tau = 15$, $\Omega = 40$ and $\rho_V = 0.007$ and 0.05.

The Nonconventional Exploitation Factors Data System (NEFDS) (§2.2.2.6) uses a modified version of the M-B model [10, pp. 21–27]. The *SO* function is simplified and does not include the term in parentheses in (2.71). The volume scattering parameters, $f(\beta)$ and $g(\theta_N)$ are also dropped. However, the NEF version allows the simultaneous inclusion of a Lambertian (ρ_D) as well as the non-Lambertian volume component of scatter. These modifications result in a form of the Maxwell-Beard model given by

$$f_r(\theta_i, \phi_i; \theta_r, \phi_r) = \frac{R_F(\beta)}{R_F(0)} \frac{f_{ZBS}(\theta_N) \cos^2 \theta_N}{\cos\theta_i \cos\theta_r} \left(\frac{1 + \frac{\theta_N}{\Omega}\ e^{-2\beta/\tau}}{1 + \frac{\theta_N}{\Omega}} \right) + \rho_D + \frac{2\rho_V}{\cos\theta_i + \cos\theta_r} \ . \tag{2.75}$$

The Maxwell-Beard model is addressed in more detail in Chapter 8 as part of the target material pBRDF model development.

2.2.3.3.3 Sandford-Robertson The Sandford-Robertson (S-R) BRDF model has its origins in infrared signature prediction for aircraft. Though developed for IR emittance, Kirchoff's law enables the application to reflected energy as well since $\varepsilon_0 = 1 - \rho_h$. The model is presented as given by Conant [78] and Jafolla [79], since the original document by Sandford is not easily acquired [80]. The model serves as the BRDF model for the SPIRITS image generation and radiometry code, to be discussed in §4.4.

The model uses four parameters:

ρ_d, strength of the diffuse reflectance,

ε, the hemispherical-averaged emittance or equivalently, $1 - \rho_h$,

b, the rate of emittance decrease toward grazing-angle, and

e, the width of the specular lobe.

Like the previous models, the BRDF is composed of specular and diffuse components.

From Kirchhoff's law, the hemispherical reflectance from a direction θ equals

$$\begin{aligned} \rho_h(\theta) &= 1 - \varepsilon(\theta) \\ &= \rho_{hs}(\theta) + \rho_{hd}(\theta) \ , \end{aligned} \tag{2.76}$$

which S-R divide into specular and diffuse components, $\rho_{hs}(\theta)$ and $\rho_{hd}(\theta)$. The diffuse hemispherical reflectance is represented by

$$\rho_{hd}(\theta_i) = \rho_d \frac{g(\theta_i, b)}{G(b)} \tag{2.77}$$

where ρ_d is one of the model parameters controlling the strength of the diffuse reflectance. The $g(\theta_i, b)$ function approximates Fresnel reflectance behavior or the grazing angle reflectance dependence and is given by

$$g(\theta_i, b) = \frac{1}{1 + b^2 \tan^2 \theta_i} \tag{2.78}$$

The $G(b)$ function in (2.77) is a normalization factor for the angular distribution of the energy and is given by

$$G(b) = \frac{1}{1-b} \left[1 + \frac{b^2}{1-b^2} \log(b^2) \right] \ . \tag{2.79}$$

Based upon these expressions, the S-R diffuse BRDF component, f_d, is given by

$$f_d(\theta_i, \phi_i; \theta_r, \phi_r) = \frac{\rho_d}{\pi} \frac{g(\theta_i, b) g(\theta_r, b)}{G^2(b)} \ . \tag{2.80}$$

The specular portion of the BRDF is constrained by energy conservation of the hemispherical reflectance according to (2.76), such that $\rho_{hs}(\theta_i) = \rho_h(\theta_i) - \rho_{hd}(\theta_i)$. The specular BRDF component, f_s, is given as

$$f_s(\theta_i, \phi_i; \theta_r, \phi_r) = \frac{\rho_{hs}(\theta_i)}{4\pi} \frac{h(\beta)}{H(\theta_i, e) \cos \theta_r} \ , \tag{2.81}$$

where β is the angle between the local surface normal and the incident angle (the same as that for the Maxwell-Beard model). The function $h(\beta)$ describes the distribution of a

surface of ellipsoids with eccentricity, e (another R-S model parameter) and is given by

$$h(\beta) = \left(e^2 \cos^2 \beta + \sin^2 \beta\right)^{-2} \ . \tag{2.82}$$

The $H(\theta_i)$ function provides the energy conservation normalization, such that the integral of the BRDF is equal to the hemispherical specular reflectance. It is represented as

$$H(\theta_i, e) = \frac{1}{2e^2} \left\{ (1 - e^2) \cos\theta + \frac{2e^2 + (1 - e^2)^2 \cos^2 \theta}{\sqrt{(1 - e^2)^2 \cos^2 \theta + 4e^2}} \right\} \ . \tag{2.83}$$

The full expression for the S-R BRDF is therefore

$$\begin{aligned} f_r(\theta_i, \phi_i; \theta_r, \phi_r) &= f_s(\theta_i, \phi_i; \theta_r, \phi_r) + f_s(\theta_i, \phi_i; \theta_r, \phi_r) \\ &= \frac{\rho_{hs}(\theta_i)}{4\pi} \frac{h(\beta)}{H(\theta_i, e) \cos\theta_r} + \frac{\rho_d}{\pi} \frac{g(\theta_i, b) g(\theta_r, b)}{G^2(b)} \ . \end{aligned} \tag{2.84}$$

2.2.3.4 Physical Models

A physical BRDF model based upon first-principles is now reviewed. Many physical models have their origin in wave-based or physical optics and are approached via Kirchhoff scalar diffraction theory. Discussion of scalar diffraction is beyond the scope of this document, but a thorough treatment of the topic as applied to rough surfaces is available from Beckmann [81]. Discussion of physical BRDF models will be limited to the popular He model [82]. Like many other models, the He model has its roots in computer graphics.

The He BRDF model is a physical optics treatment of surface scatter which uses many of the same concepts as the semi-empirical models such as shadowing and masking. The model is developed from Beckmann's general formulation [81], with the following inclusions: *i*) the vector form of Kirchoff diffraction, thereby enabling polarization; *ii*) a surface roughness averaging scheme using a joint probability distribution function which includes height, slope, and two spatial points; *iii*) incorporation of an effective roughness due to illumination angle and *iv*) a geometrical shadowing factor.

He's BRDF model is presented as a summation of three different components, using He's notation as: specular-diffuse (sp), directional-diffuse (dd) and uniform-diffuse (ud), which may be given by

$$f_r = f_{r_{sp}} + f_{r_{dd}} + f_{r_{ud}} \ . \tag{2.85}$$

The sp component is due to the specular reflection by the mean surface orientation. The dd component is from diffraction by the surface roughness, analogous to the geometric optical

treatment of the microfacet distributions. These first two contributions result from first surface (Fresnel) reflectance. Finally, the *ud* component is a constant which results from multiple scattering internal to the material.

Each of these components is represented as follows using previously defined variables where possible:

$$f_{r_{sp}} = R_F \cdot e^{-g} \cdot S \cdot \delta(\theta_i - \theta_r) \ , \tag{2.86}$$

$$f_{r_{dd}} = \frac{\mathcal{F}\left(\hat{n}_b, \hat{n}_b, \vec{p}\right) \cdot S}{\cos\theta_i \cdot \cos\theta_r} \cdot \frac{\tau^2}{16\pi} \cdot \sum_{m=1}^{\infty} \frac{g^m \cdot e^{-g}}{m! \cdot m} \cdot \texttt{exp}\left[-\frac{(k\ v_{xy}\ \tau)^2}{4m}\right] \ , \tag{2.87}$$

$$f_{r_{ud}} = \alpha(\lambda) \ , \tag{2.88}$$

where S is a shadowing function, g is a function of the effective surface roughness (σ) given by

$$g = \left[\left(\frac{2\pi\sigma}{\lambda}\right)(\cos\theta_i + \cos\theta_r)\right]^2 \ . \tag{2.89}$$

The delta function ensures the *sp* component is zero outside the specular reflection angle for the mean surface (per Snell's law). $\mathcal{F}$ is a function dependent upon R_F (equation 2.24) and $\vec{p}$, the incident polarization state. k is the wavenumber ($\frac{2\pi}{\lambda}$),[4] v_{xy} is a function dependent upon the illumination and reflection angles and finally τ is the surface roughness autocorrelation length. The explicit representations of S, $\mathcal{F}$, τ and v_{xy} are not given here.

As a surface becomes perfectly smooth, $g \to 0$ and $S \to 1$, so there is no attenuation of the *sp* component. Likewise, it is seen that the *dd* component contribution is zero as $g \to 0$, as expected. Finally, the free parameter $\alpha(\lambda)$ representing the isotropic (Lambertian) component of scatter may be set out of energy conservation considerations, by using measurements of ρ_{DHR} for instance.

The fundamental parameters required for the He BRDF model are therefore the index of refraction $\tilde{n}(\lambda)$, surface roughness σ, surface roughness autocorrelation length τ and for practical purposes ρ_{DHR}. So even for a highly physical BRDF model, the empirical quantity ρ_{DHR} is used.

He's model has been criticized as being slow due to the series in (2.87) which may require many terms to converge under some conditions. To address this, He later provided a means of pre-computing a look up table with minimal accuracy sacrificed [83].

[4] N.B. the original paper contains an error in the expression for $f_{r_{dd}}$ (Eqs 7 and 78 in [82]) and does not include k in the exponent.

2.2.4 BRDF Models: Background Materials

Remote sensing BRDF models are specifically tailored for heterogeneous materials. Natural surfaces and landcover contain significant variability, which is difficult to capture with homogeneous material BRDF models (§2.2.3). The spatial resolution (GSD) of satellite-based remote sensing platforms has historically been limited to 10s of m (*e.g.*, Landsat). For most regions of the earth, this results in a per-pixel radiance value due to the integration of many unidentified landcover features. It is from this perspective that remote sensing BRDF models have been developed. A special issue of *Remote Sensing Reviews* (Vol. 18, 2000) provides several articles of interest, which originated from papers and discussions at the International Forum on BRDF held in December 1998.

Remote sensing BRDF models serve many functions. One purpose is the normalization of radiance from multi-angle views. It is standard practice to normalize oblique angle data to that of nadir viewing. This enables improved comparisons to other data sets of the same region. BRDF models are also instrumental in deriving surface DHR, or the albedo, for input to climatology models and modelling the planet's thermal exchange. Finally, as with homogeneous BRDF models, model parameters may be linked to extracting information from the scene such as leaf area index (LAI) or leaf area distribution. Often, remote sensing models must be used to approximate a full hemispherical BRDF representation when only a few measurements are made, such as with a single pass of POLDER or a few passes of an off-nadir viewing payload like MODIS.

The general situation considered is a vegetative canopy region over a ground material. The canopy may have varying crown and leaf orientations, analogous to microfacet surface variations in target material model. However, leafy materials have significant transmittance and multiple interactions which complicate the radiometry. The vegetative canopy may also have varying spacing or areal density. A heavily forested region may have the entire surface covered by tree crowns, with little ground visible, while other areas may have sparse trees allowing the ground to drive the signature. New commercial satellites now provide high resolution (GSD $\sim$ 1 m) imagery such as IKONOS and QuickBird, enabling resolution of surface features which provide *a priori* knowledge of the land cover type such as "trees" or "grass."

As with target material BRDF models, a range of empirical to physical models have been developed. Full empirical models are often not useful for satellite-derived observations, since the geometric sampling density is very sparse. Physical models provide radiometric modelling of the surface and enable extraction of parameters having physical significance. Finally, semi-empirical models provide a hybrid approach from which fits to empirical data provide some physical basis for the BRDF. Good reviews of remote sensing BRDF models

are provided in an extensive treatment by Goel [84] which was summarized and updated in [85]. Additional overviews of BRDF models are given by Strahler [86] and [87]. Finally, a recent book provides excellent coverage of models and measurement techniques, and also provides a database [88].

The discussion will be limited to semi-empirical models, which are often composed of a summation of linear contributions expressed as

$$f_r(\theta_i, \theta_r, \phi) = \sum_n a_n \mathtt{k_n}(\theta_i, \theta_r, \phi) \tag{2.90}$$

where n typically ranges from 2 to 10. Many models have $n = 3$ parameters with the $\mathtt{k_n}$ terms consisting of isotropic, surface and volumetric functions. The $\mathtt{k_n}$ contributions are called *kernels* from which these models are also called kernel-driven or kernel-based models [87]. The kernels provide different geometric expressions for a particular type of BRDF contribution. Detailed examination of a particular BRDF model by Roujean provides further details on the kernel representation.

The semi-empirical Roujean BRDF model [89] is a kernel-based model and has maintained popularity due to its versatility and accuracy for modelling a number of land cover types. The BRDF is quantified by a geometric and volumetric scattering component. The geometric scattering component models randomly placed vertical, opaque "long-wall protrusions" on a flat horizontal plane [89]. Both the protrusions and the background plane are assumed to be Lambertian surfaces. Increasing zenith angle illumination produces increased shadowing of the background plane according to the protrusion height. However, the protrusions are distributed such that mutual shadowing of one protrusion onto another is not considered.

The volumetric component models randomly placed facets which absorb and scatter radiation according to a simple radiative transfer model. The facet distribution is treated as isotropic, with a specified density. Several assumptions are made in deriving the volumetric term—only single scattering is considered and the facet reflectance and transmittance are treated as being equal. This last assumption is a gross one, but was necessary to reduce the number of free parameters in the model to three.

All scattering results from the geometric and volumetric components, which are considered independent. The resulting BRDF model, is given by

$$\rho(\theta_i, \theta_r, \phi) = \mathtt{k_0} + \mathtt{k_1} f_1(\theta_i, \theta_r, \phi) + \mathtt{k_2} f_2(\theta_i, \theta_r, \phi) \tag{2.91}$$

where ρ is the reflectance factor. The geometric scattering results from $\mathtt{k_0} + \mathtt{k_1} f_1$ and the

volumetric scattering is contained in $\mathtt{k}_2 f_2$. The standard means of implementing the model is such that the magnitude of the k_n parameters returns the reflectance factor, scaled from 0–100. The equivalent BRDF is obtained by a simple scale factor, or

$$f_r = \frac{\rho}{100\ \pi}\ . \tag{2.92}$$

The f_1 function is derived from geometric considerations of the protrusion placement and without further derivation is given by

$$f_1 = \frac{1}{2\pi}[(\pi - \phi)\cos\phi + \sin\phi]\tan\theta_i \tan\theta_r - \frac{1}{\pi}\left(\tan\theta_i + \tan\theta_r + \sqrt{\tan^2\theta_i + \tan^2\theta_r - 2\tan\theta_i\tan\theta_r\cos\phi}\right)\ . \tag{2.93}$$

The f_2 function has its origin in a simple radiometry model, which includes some of the previously mentioned assumptions. It is given by

$$f_2 = \frac{2}{3\pi}\frac{(\pi - 2\xi)\cos\xi + 2\sin\xi}{\cos\theta_i + \cos\theta_r} - \frac{1}{3}\ , \tag{2.94}$$

where ξ is the scattering angle between the incident and scattering directions defined by

$$\cos\xi = \cos\theta_i\cos\theta_r + \sin\theta_i\sin\theta_r\cos\phi\ . \tag{2.95}$$

Roujean's convention is for $0° \leq \phi \leq 180°$ and $0° \leq \theta_r \leq 90°$, where the backscattering orientation is $\phi = 0°$. The full derivation of these functions is lengthy, to which the reader may reference [89].

The free parameters, $\mathtt{k}_0$, $\mathtt{k}_1$ and $\mathtt{k}_2$ have some physical significance. $\mathtt{k}_0$ correlates to an isotropic Lambertian contribution and is equivalent to the reflectance when $\theta_i = \theta_r = 0°$. $\mathtt{k}_1$ is related to the protrusion height, length and width while $\mathtt{k}_2$ is related to the facet reflectance and area (*e.g.*, canopy leaf reflectance and coverage, or leaf area index). The Roujean model was implemented with parameters from Roujean's paper, successfully replicating the results for a "wheat field" (Figure 2.11).

2.2.5 Model Performance

It was earlier observed that the proliferation of BRDF models was in part due to the dissatisfaction of researchers with their performance. That being said, how well do the models perform? Some examples are present in the literature which provide some insight, though they are perhaps negatively biased in that most focus on a new model which provides

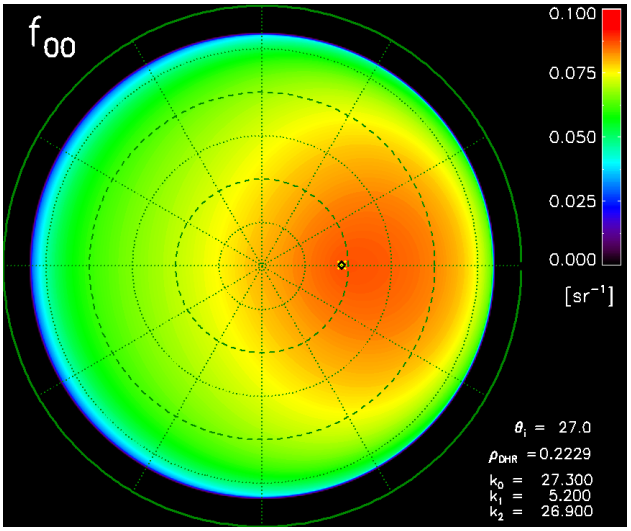

Figure 2.11: Roujean model results fit to empirical data for a wheat field in the visible for $\theta_i = 27°$, where the magnitude is in terms of BRDF or $\mathtt{sr}^{-}\mathtt{1}$. This replicates the results in [89, Fig. 7, p. 20,463]. The peak reflectance is noted at the "hot spot" or retro-reflection location. Parameter values are $\mathtt{k}_0 = 27.3$, $\mathtt{k}_1 = 5.2$ and $\mathtt{k}_2 = 26.9$.

an improved fit relative to "classical" models. The manner in which data is fit to a model is also a topic of discussion unto itself. Typical approaches are to derive model parameters which minimize the least square error of the fit, but algorithms which do so are subject to localized minimums. Some have used visual inspection of the fit, which may be appropriate when accuracy around one particular scattering geometry is desired.

The performance of various target material BRDF models was investigated by Culpepper [90] for glossy white and black paints and mill-finished aluminum. These materials are relatively specular with the BRDF spanning 3–4 orders of magnitude. Culpepper limited the measurements to the plane of incidence and desired a model to fit all the measured data to within 10%. However, differences from a factor of 2 to a factor of 10 were present with all the models at some point over the $-90° \leq \theta_r \leq 90°$ scan. Culpepper resorted to empirical interpolation to obtain the required accuracy. Perhaps it should have been anticipated that models would be challenged in achieving the desired accuracy given the dynamic BRDF range of specular materials. Other publications also present measured data which has been fit to BRDF models [91] to include the Sandford-Robertson model [92].

The performance of several remote sensing or background material BRDF models is reported by Boucher [39] and Hautecoeur [93]. Boucher made measurements on sand, "dry" grass, and "green" grass at 600 and 800 $\mathtt{nm}$. Significant in this work is the quantification of model performance for different azimuth sampling densities. The Roujean model [89]

provided one of the best performances, and had minimal errors for all the materials at both wavelengths when at least 25 hemispherical samples were acquired (for a single θ_i value). The Roujean model also provided good performance when measurements were limited to only three azimuth planes: $\phi = 0°$ (or 180°), 60° and 120°. Roujean's model was also commended by Hautecoeur [93], having the best performance of the semi-empirical models surveyed.

2.2.6 Polarimetric BRDF Models

Polarimetric BRDF (pBRDF) models are required for predicting the reflected polarized radiance given an incident irradiance having arbitrary polarization. There has been minimal development of pBRDF models. As with the scalar or intensity-only conventional BRDF models, a distinction is made between homogeneous (target) materials and inhomogeneous (background) materials.

For target materials, polarized versions of scalar BRDF target models have been created by incorporating the Fresnel reflectance contributions from the micro-facet surface representation. The Mueller matrix for each micro-facet is considered and related back to the global, macro geometry, and a superposition of the individual microfacet polarized radiance contributions are made. Background material pBRDF models have been developed which crudely approximates landcover classes.

2.2.6.1 Target Material pBRDF Models

A late 1990's industry survey concluded that no existing pBRDF model represented pBRDF signatures with the required fidelity [94]. However, some historical scalar BRDF models such as He's provides an intrinsic means of modelling polarization.

Like He's model, a new physical optics model by Duncan also provides polarization information [95]. Other historical scalar BRDF models derive polarized reflectance values as an intermediary to calculating the scalar radiant intensity, L or the L_0 Stokes vector component. However, few efforts have been made toward implementing fully polarized versions of these models.

Recently, Priest provided a general polarized formulation for a microfacet BRDF model [96, 97]. The microfacets are represented as a two-dimensional Gaussian distribution function, from which the polarized radiance may be calculated. A polarized version of the Sandford-Robertson BRDF model has been developed by Conant [78], where the volumetric scattering component is considered to be completely depolarizing. Finally, a polarized variant of the Torrance-Sparrow BRDF model has been reported by Fetrow [98]. Meyers

implemented a hybrid model using the Priest microfacet specular reflectance, and the volumetric scattering component of the Torrance-Sparrow model [99]. The OPTASM BRDF model also supports polarimetric calculations [94, 100, 92], though details behind the polarized implementation are lacking.

In pBRDF models, it is common to assume that the volumetric scattering is completely depolarizing (*cf.* type B photons in Figure 2.4). However, as reported by Ellis, this assumption is shown to be inaccurate [101]. Thus a model which includes a polarized contribution from this scattering source is desired.

2.2.6.2 Background Material pBRDF Models

Even fewer pBRDF models for background materials exist. The only effort appears to be a parameterized model which supports the POLDER mission (discussed in more detail in §3.2.2.2. Data collected over large, homogeneous land areas was analyzed to produce two expressions for the pBRDF of landcover. pBRDF representations for general "vegetation" [102] and "soil" [103] classes have been developed. The models are used as a linear combination with the relative weighting based upon a normalized difference vegetation index (NDVI) calculation [51].

The models are given by

$$\rho_p^{veg} = \frac{F_p(\alpha)}{4(\cos\theta_i + \cos\theta_r)} \ , \tag{2.96}$$

$$\rho_p^{soil} = \frac{F_p(\alpha)}{4\cos\theta_i \cos\theta_r} \ , \tag{2.97}$$

where α is the incident angle, $\alpha = (\pi - \gamma)/2$ where γ is given by

$$\cos\gamma = -\cos\theta_i \cos\theta_r - \sin\theta_i \sin\theta_r \cos\phi \ . \tag{2.98}$$

$F_p(\alpha)$ is the polarized fraction of the Fresnel reflectance given by

$$F_p(\alpha) = \frac{1}{2}\left[\left(\frac{\hat{n}\cos\alpha_t - \cos\alpha}{\hat{n}\cos\alpha_t + \cos\alpha}\right)^2 - \left(\frac{\hat{n}\cos\alpha - \cos\alpha_t}{\hat{n}\cos\alpha + \cos\alpha_t}\right)^2\right] \ , \tag{2.99}$$

where α_t is the transmitted angle solved via Snell's law.

This model provides a baseline by which the pBRDF of natural materials may be represented—however, only at a GSD which integrates out the BRDF variability. For this reason even if it were highly accurate it is inadequate. Existing scalar BRDF models for background materials, such as Roujean's, are not amenable to a polarized adaptation. A

viable background pBRDF representation will likely be stochastic in nature due to the high variability of these materials at GSDs of interest (GSD ≈ 1 `ft`).

2.2.7 BRDF Summary

The direction and magnitude of optical scattering from surfaces is defined by the BRDF. The most generalized form of the BRDF is the polarized BRDF and is represented as a Mueller matrix, which contains all the scattering information. The variability or texture of a surface may be characterized by the bidirectional variance function (BRVF), which is necessary for inhomogeneous materials such as natural surfaces. It is through the BRDF that material-dependent polarization signatures are imparted which may be exploited in remote sensing.

Many measurement techniques have been developed to quantify BRDF. Polarimetric BRDF measurements add another degree of difficulty to an already challenging characterization. BRDF models serve to compactly represent a complex BRDF through a reduced number of parameters. BRDF models may also provide BRDF predictions based upon physical properties of the materials. Few BRDF models have been developed which provide a full polarimetric treatment. It is appropriate to divide BRDF models into those which represent homogeneous (target) materials and inhomogeneous (background) materials.

By having polarimetric BRDF data and/or models, it is possible to predict polarimetric signatures. The origin of VNIR radiance at an aperture of a remote sensing system must be explored in detail, which will serve to highlight the importance of the polarimetric BRDF function, $\mathbf{F}_r$. The governing equation for polarized radiance reaching a sensor aperture is presented in Chapter 4.

Chapter 3

Prior Work & Advancements

A review of polarimetric imaging is now made in order to establish the current state of the art from which advances may be made. Use of polarization is by no means limited to remote sensing, and a review of current applications being developed and explored in other disciplines provides insight into potential means of applying those techniques to remote sensing problems. The historical use of polarization in remote sensing will be reviewed, along with current developments toward target detection and classification. Novel means of dealing with polarization calculus are discussed, followed by techniques developed for presenting polarization information to the human visual system. Techniques of presentation to the human visual system provide no additional qualitative analysis or information content, but are useful for visualizing and discussing polarization phenomenology. Finally, polarimetric optical systems are briefly commented on.

3.1 Imaging Polarimetry Across Disciplines

A literature search on electromagnetic polarization returns results which are generally germane to *i*) astronomical imaging, *ii*) biological and medical imaging, *iii*) machine or computer vision or *iv*) remote sensing. Each of the first three categories may be defined as remote sensing in the broadest sense, but each has its own body of literature. A brief review of polarimetric imaging in these fields is warranted in an effort to identify synergy with overhead remote sensing.

Other fields also have significant polarization research and applications efforts. Telecommunication efforts are concentrated on maintaining polarization states in optical fibers, as a further attempt to increase the bandwidth akin to dense wave division multiplexing. To some extent, polarimetric remote sensing may be considered ellipsometry, but with very poorly controlled conditions! Ellipsometry is typically limited to measurement and char-

acterization of optical thin films. At the opposite extreme of overhead remote sensing, polarimetric microscopy derives information at the micro scale which is not obtainable with intensity-only images [104].

3.1.1 Machine Vision & Artificial Intelligence

Polarimetric imaging has been used as a means to derive additional information from objects for "machine" vision. Wolff demonstrated a technique of separating conductive materials from dielectrics based upon the higher DOP imparted by dielectric materials. An application of this system for autonomous circuit board inspection is suggested [105]. Further work by Wolff developed polarization techniques to determine whether edges in images were a result of one object occluding another, or an inherent feature on an object [106]. A means of estimating surface normal orientation is also presented in the same work and an improved polarization imaging system for these applications is shown in [107]. Techniques to remove specular reflections based upon polarization have also been developed for image recovery [108].

3.1.2 Astronomy

The astronomical and planetary science community is responsible for generation of the first BRDF model, and routinely uses polarimetric sensing of planetary bodies and satellites. This early history will be covered as part of the review of the polarimetric remote sensing review (§3.2). Recent instrumentation advances have enabled optical polarimetric imaging at the 0.001% level which has served to invigorate the field. Dedicated conferences on the subject are now established [109].

For planetary bodies and satellites without atmospheres, polarimetry enables derivation of the physical composition of the surface—examples of such efforts will be discussed in §3.2. For planetary atmospheres, polarimetry is routinely used to determine cloud, aerosol and particulate structure.

3.1.3 Medical

Polarimetric medical imaging and medical imaging in general is motivated by the desire to make non-invasive diagnosis. Optical spectralpolarimetric imaging has been demonstrated for subsurface tissue imaging, at depths up to 1 `cm`, which is otherwise not achievable with intensity-only methods [110]. Mueller matrix imaging techniques have also shown promise for material discrimination, such as between cancerous and non-cancerous cells [111]. Other promising non-imaging applications include the monitoring of glucose levels, which imparts

polarization due to the chiral molecular structure of glucose. Polarization is also proving useful for studying blood circulation [112]. The use of biometric information for security applications has also motivated the use polarization to verify identities, such as fingerprint verification [113].

3.1.4 Remote Sensing

The use of passive polarimetric imaging in remote sensing will be reviewed in detail in the rest of this chapter, but it is worth noting other uses of polarization in remote sensing. The two most significant areas both use active imaging methods in which an illumination source is supplied. Significant polarization techniques in synthetic aperture radar have been enabled and the prospects of active laser illumination in the optical frequency regime are also being explored. It's worth noting that the signal returned by active systems returns that of a monostatic angular BRDF, or the co-location of source and receiver ($\theta_i = \theta_r$, to within the propagation time difference). For radio frequencies, this is often called the radar cross section, and is simply a subset of the generalized BRDF.

3.1.4.1 Synthetic Aperture Radar

Synthetic aperture radar or SAR has been used to provide "all-weather" imaging due to the fact that water vapor (clouds) are highly transmissive in the radio frequency regime. The surface of Venus was mapped using SAR and an accurate digital elevation model (DEM) of the Earth's surface has been provided by a SAR mission on the U.S. Space Shuttle. The use of polarimetric SAR has long been acknowledged as a means of obtaining additional and discriminatory information from targets or backgrounds [114, 115].

As with optical polarimetry, illumination and receive states of two orthogonal polarization components are used. In the parlance of SAR, the s-polarization is "H" for horizontal and the p-polarization state is termed "V" for vertical. Scattering matrices or the Mueller matrices describing the scattering are used to obtain discriminatory information from targets [116]. As with optical polarimetry, BRDF models have been developed for varying materials, though significant simplification of the models is possible since $\theta_i = \theta_r$. One such model is that for bare, rough soil over the 1–100 `GHz` range [117].

In the RF regime, λ is often much greater than the surface roughness parameters considered in optical BRDF models, in which case models based on the ray approach of geometric optics fails. The other significant difference are the dielectric constants of materials at SAR frequencies. Rather than characterizing materials in terms of the index of refraction,

materials are characterized by their *impedance*, Z, having units of Ohms and expressed by

$$Z = \sqrt{\frac{\mu}{\varepsilon}} \,. \tag{3.1}$$

As seen from (2.5), information equivalent to $\tilde{n}$ is contained in Z. The impedance mis-match (or equivalently the difference in the refractive index) of dielectric materials at microwave frequencies is not as great as that in the optical regime, which enables significant transmission into materials. This is the basis of ground penetrating radar.

3.1.4.2 Active Optical Imaging

Active optical imaging in remote sensing is usually via light detection and ranging (LIDAR) with laser sources. Polarimetric LIDAR is not as advanced as polarimetric SAR due in part to a lack of appropriate laser sources. VNIR LIDAR systems typically operate at 532 `nm` or 1064 `nm` using a Nd:YAG laser. Achieving spectral diversity with sufficient power is very challenging. As with polarimetric SAR, the ability to control the polarization of the incident and received radiation enables recovery of the full polarimetric BRDF matrix ($\mathbf{F}_r$), which is not possible with passive polarimetric remote sensing.

3.2 Polarimetric Remote Sensing

3.2.1 Early Uses of Polarization in Remote Sensing

In 1929, Lyot published the results of polarization measurements of the moon, enabled by a polarimeter of his own design [118]. Lyot found the DOP to be phase angle (ξ) dependent, and that for $0° \leq \xi \leq 23.5°$ the lunar polarization was predominantly p-polarization or parallel to the earth-sun-moon scattering plane. Emulating this result in the lab with a variety of substances, he concluded the lunar surface was covered with small grains [119]. Further investigations in the late 1950's and early 1960's corroborated and refined this prediction of the lunar surface. Dollfus completed many studies of lunar polarization [120, 121, 119] and Hapke [71] formulated an early BRDF model which predicted "fine, loosely compacted dust" for the lunar surface.

The use of polarimetric imaging for terrestrial remote sensing began in earnest in the late 1960's. A spectral dependence on polarization was noted by Chen when making pBRDF measurements of white and desert sand, soil and water [122]. Egan began a prolific career with a 1970 publication on crop identification using polarization [3, Ch. 11]. Burns reports the use of a system to detect and monitor the oceans for oil pollution [123]. A 1976

high-altitude balloon flight made linear polarization measurement in the visible and near infrared, producing some of the first polarization measurements of the earth's atmosphere and demonstrated the ability to distinguish between clouds composed of liquid water or ice [124]. A seminal paper by Walraven demonstrated derivation of Stokes images using linear polarization filters and the generation of images showing the DOP and polarization phase angles [6]. Walraven demonstrated improved contrast and noted the additional information obtained through polarization images. It's of interest to note Walraven's words in the abstract:

> "The polarization of reflected radiation can provide useful information which could be used in remote sensing applications to help distinguish different natural surfaces with similar spectral signatures. Yet the use of polarization has been almost completely neglected in remote sensing applications partially because of the lack of understanding of the information contained in the polarization field."

This statement rings as true today as it did when published in 1977. As will be seen, most work in polarimetric remote sensing stops at the point of presenting "pretty pictures" which provide contrast improvement, or enhanced detection of "man made materials".

3.2.2 Space-based Missions

To date, there have only been two space-based payloads which have provided polarimetric imaging of the earth. A series of Space Shuttle missions was completed in the mid-1980's and recently two French payloads flew on the Japanese ADEOS satellites.

3.2.2.1 Space Shuttle

The U.S. Space Shuttle completed a series of six missions in 1984 and 1985 which provided some 1000 polarized images of the earth. The experiment used two bore-sighted Hasselblad 500 EL/M 70-mm format cameras with linear polarization filters oriented 90° with respect to one another. Film used in these missions was either black and white or Ektachrome 5036. Mission specialists were instructed to rotate the camera such that a maximum intensity image (I_{max}) was acquired for one camera, which resulted in the minimum intensity image (I_{min}) in the cross-polarized camera.

Development of the film was done under identical conditions for each image pair to maintain the best inter-frame relative exposure densities. However, quantitative analysis of the imagery is challenging, given the non-linear response of the film, the shuttle window's polarization effects and the uncertainty in the alignment when the images were taken. The

I_{max} and I_{min} images have been used to derive an approximation to the DOP according to

$$DOP = \frac{I_{max} - I_{min}}{I_{max} + I_{min}} , \tag{3.2}$$

where it is noted that $-1.0 \leq DOP \leq 1.0$. Negative values are possible since an individual pixel in the I_{min} image may have a value greater than the corresponding I_{max} image, in which case the polarization orientation is reversed.

Preliminary results from this experiment were reported by Coulson [1]. The experiments served as an impetus for a NASA workshop to discuss some of the findings and provide future direction of polarimetric remote sensing [125]. Signal to noise or contrast enhancement for various surface features are reported by Whitehead [2]. Further quantitative analysis of the imagery was completed by Egan for the Hawaiian islands [126][3, Ch. 20] and for farm crop identification [127][3, Ch. 11]. An attempt to provide better calibration of the images is discussed by Roger [128] as is further analysis of various images. Israel noted a distinct variation in the polarization between barren land and the ocean from varying view angles with the shuttle images [129]. Additional and similar findings are found in [130] [131]. The shuttle images are further discussed in §10.2.4, where the initial examination of some images is discussed.

3.2.2.2 POLDER

As previously mentioned in §2.2.2.4, the POLDER mission also acquired overhead polarization images of the earth. The Polarization and Directionality of the Earth's Reflectance (POLDER) instrument was developed by the French Space Agency and was operational on both the Japanese ADEOS and ADEOS-2 satellites in sun-synchronous 796 km orbits. The along-track and cross-track FOVs are ±43° and ±51° which is imaged onto a Si-based CCD of 242 × 272 resulting in a nadir GSD of some 6 × 7 km. These characteristics enable up to 12 multi-angle images of a point during a single pass—successive passes enable a reasonable sampling to construct BRDF as previously discussed in §2.2.2.4. POLDER has eight spectral bands, from 443–910 nm. Three of the bands, 443, 670 and 865 nm are polarized and have spectral bandwidths of 20, 20 and 40 nm, respectively. The polarized bands are limited to linear polarization which are acquired at three orientations: 0°, 60° and 120° [49].

A sample of POLDER imagery is shown in Figure 3.1, where the RGB bands have been encoded from the 865, 670 and 443 nm bands, respectively. The left image in each of the four sets shown is the total radiance, while the right image is the DOP image. Examination of Figure 3.1 illustrates some polarization phenomenology. The DOP images are predominantly blue, as expected from the polarization-dependent Rayleigh scattering.

Solar "glitter" from the sea surface is also seen to be highly polarized. The backscatter direction, $\theta_r = \theta_i$ is seen to provide the minimum DOP.

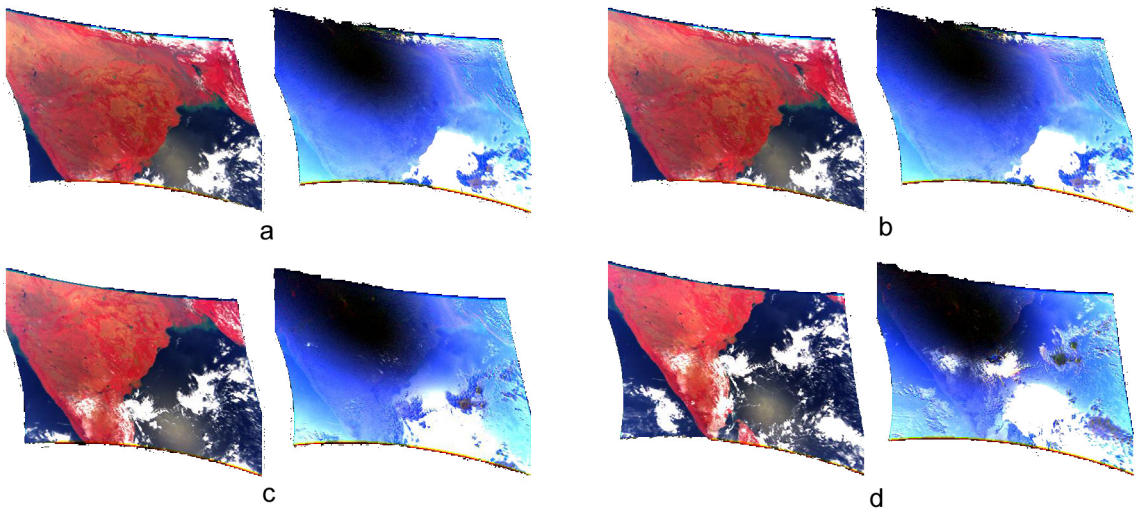

Figure 3.1: Four sets of POLDER images over India from a single pass, sequenced a → d. The RGB channels correspond to 865, 670 and 443 nm with the left image in each set the total radiance and the right image DOP. Courtesy of [132] with permission.

Using POLDER data, the polarized BRDF was empirically determined for four land classes: forest, shrubland, low vegetation and desert [51]. The GSD used for this characterization was 19×19 km^2, therefore requiring large uniform cover areas. A sample of this data in the principal plane for forest and desert is shown in Figure 3.2. The magnitude of the data shown here is for that of the s-polarization. The significant tail in the distribution in the forest data at the high forward scattering geometry is attributable to sparse areas of water inundation. The polarized reflectance throughout the hemisphere for forest and desert land classes is shown in Figure 3.3, which also includes three incident angles. Also shown is the fit to a pBRDF model, as described in §2.2.6.

Additional analysis of land surface polarization from POLDER data is given by Anjun, where the polarization effects of vegetation, bare soil and water land classes were characterized. Atmospheric polarization correction parameters were applied to all three POLDER polarization bands, but the final analysis was limited to the 865 nm band to minimize atmospheric scattering effects. As anticipated, a monotonic increase in the DOLP was seen as the relative azimuth scattering angle approached 180° [133].

These data indicate there is a gross polarization effect from land cover. Higher spatial resolution would enable derivation of the polarimetric BRDF variance (or BRVF), which

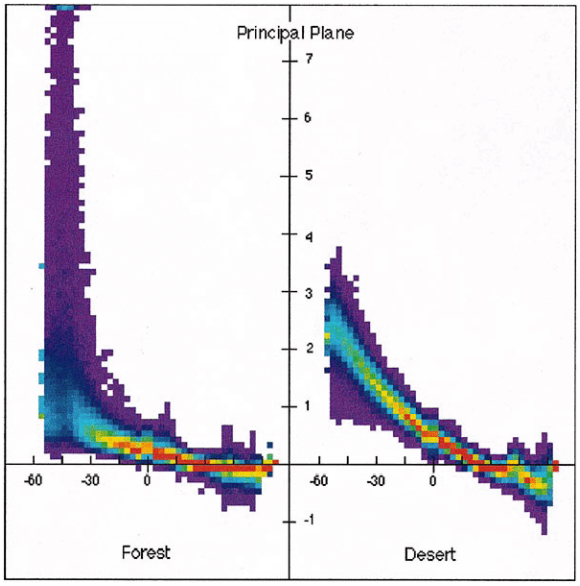

Figure 3.2: Polarimetric BRDF of "forest" and "desert" land classes in the principal plane at 865 nm with $40° \leq \theta_i \leq 45°$. Forward scattering is represented by negative θ_r values (x-axis) and backward scattering by positive θ_r. The colors indicate the density histogram for a given θ_r [51]. With permission from IEEE, ©1999 IEEE.

would likely become significant when sampled down to the $GSD = 1$ m level. This exemplifies the type of data needed to approximate polarimetric background signatures.

3.2.3 Polarized Reflectance Measurements

In order to predict the polarized radiance reflected from a material, it is necessary to characterize the pBRDF of that material (*cf.* §2.45). Relatively few references may be found on pBRDF material measurements where the full scattering matrix is quantified. A less general case of pBRDF is often measured, called here the polarized reflectance. These measurements are usually limited to incident random polarization, and hemispherical sampling is typically performed only in the plane of incidence.

3.2.3.1 Natural materials

Soils and sand Chen performed some of the first polarimetric scattering experiments on soil, "desert" sand, "white" sand and water in an effort to characterize their properties and provide insight into the scattering mechanisms, which at the time (1968) did not have a strong theoretical basis. Discrete wavelengths of 0.3975, 0.5000 and 0.6050 μm were used and the DOP was measured over a range of θ_r in the plane of incidence. For all four materials,

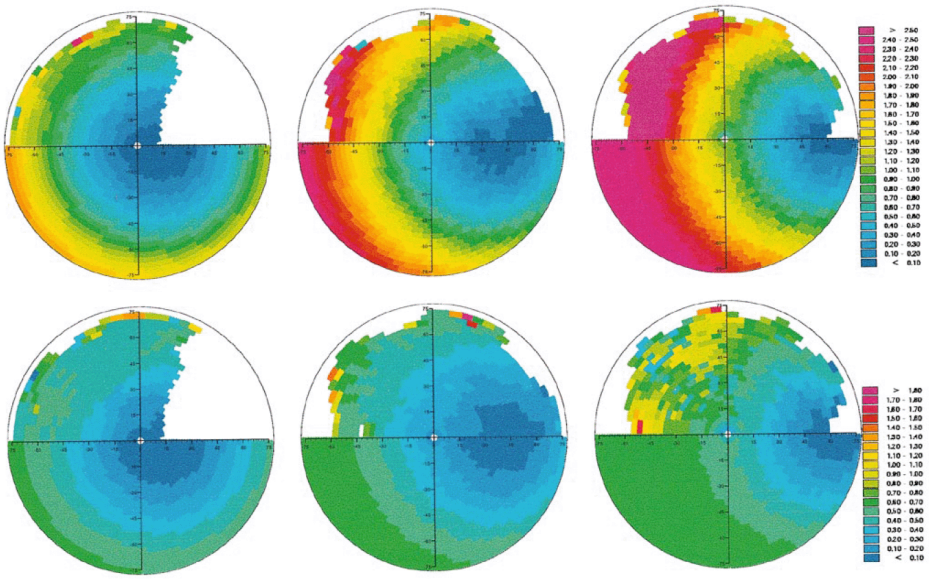

Figure 3.3: The hemispherical polarimetric BRDF of "desert" (top) and "forest" (bottom) land classes at 865 nm for three ranges of θ_i: $10° \leq \theta_i \leq 15°$, $35° \leq \theta_i \leq 40°$ and $60° \leq \theta_i \leq 65°$ (left to right). Isotropic, or azimuthal symmetry is assumed; the top half of each diagram is the empirically determined pBRDF, and that on the bottom is a fit to a pBRDF model. Not clearly visible is the magnitude scale, ranging from < 0.10 to > 2.50 for the desert (top) and < 0.10 to > 1.80 for the forest (bottom) [51]. With permission from IEEE, ©1999 IEEE.

the "negative" polarization branch or p-polarization resulted near the angle of incidence, which was $\theta_i = 53°$. As anticipated, the water had the highest DOP which peaked at > 0.80 around $\theta_i = \theta_r$. The soil DOP approaches a maximum for all three wavelengths at $\theta_r \approx 40°$, with DOP maximums of 0.18, 0.11 and 0.07 with decreasing wavelength. The "desert" sand is similar, but with the maximum DOP occurring at $\theta_r \approx 65°$. Finally, the "white" sand DOP continually increases with θ_r to a maximum of 0.13 and 0.18 at 0.3975 and 0.6050 μm at $\theta_r = 80°$, the highest scattering angle measured. Chen also made these measurement using different incident polarization states.

Soils and mineral polarized reflectance have also been measured by Gibbs who concluded that volumetric scattering contributed to a higher level of depolarization, evident from translucent soil particles such as quartz and gypsum sand. Opaque soil particles result in a lower depolarization [134, 135].

Vegetation The polarized reflectance of vegetation has received considerable attention. Most of the investigations are motivated to support the agricultural applications of remote sensing [136, Ch. 14].

The phenomenology of polarization by vegetation is thoroughly discussed by Herman. Leaf reflectance in the context of leaf morphology is presented, to include surface and interior or volume scattering by leaves. Polarization from leaves is primarily due to reflectance off the epicuticular wax [137].

Vanderbilt has completed several studies on vegetation [138, 139] concentrating on agricultural crops such as wheat [140], oats [141] and sorghum [142]. Vanderbilt provides a more thorough treatment than most researchers of the radiant sources in a vegetation canopy. The sky light, transmitted radiance through leaves, and diffuse scatter from leaves are all considered secondary sources. A semi-quantitative technique of delineating the origin of polarized reflectance is developed, distinguishing between direct solar specular reflections and specular reflections from the diffuse sky and light transmitted through the canopy [141].

Vanderbilt concludes that practically all polarized radiance from the canopy may be attributed to direct solar specular reflectance [141, p. 460]. Vanderbilt advocates spectral polarimetric imaging of vegetation canopies to provide insight into their radiative transport. In particular, sensing in the red (where there is high absorptance from chlorophyll) maximizes the polarization information [141]. In some instances, the polarized radiance may degrade the biochemistry information of the canopy [142]. This conclusion is not surprising, as the volumetric (diffuse) scatter from leaves provides the spectral information on the leaf interior. As previously discussed, polarized reflectance is color neutral, largely providing information limited to the leaf surface morphology.

Rondeaux acquired polarimetric images of corn and soybean crops at 550, 630 and 790 nm at varying solar angles. Data from the soybeans were taken during water-stressed conditions and after heavy rainfall. The soybean DOP was lower under water-stressed conditions which is attributed to a leaf inclination change due to "droopy" leaves. It is important to note that this change was not discernable using intensity-only data. Corn measurements were made before and after tasseling. Rondeaux develops a polarized reflectance model applicable to vegetation incorporating a leaf distribution function which may be used for planophile and erectophile vegetation [102]. Duggin has also imaged agricultural crops and noted the polarization variability of vegetation in the NIR, red and green spectral regions [143].

3.2.3.2 Target materials

The pBRDF measurements of paints corresponding to the colors of Federal Standard paints is reported by [144]. Flat, semi-gloss and gloss paints were used to provide a range of surface roughness. The DOP is measured as a function of wavelength from 0.65–1.0 μm and as a function of phase angle, ξ. The findings are consistent with that expected from Fresnel reflectance and Umov's effect (§2.2.1)—a higher DOP is observed in highly absorbing

materials. For $\theta_i = \theta_r = 45°$ in the plane of incidence, the DOP ranges from ≈ 0.02 to 0.18 for flat white and flat black paints, respectively. When scanned over varying incident angles, the DOP reached a maximum of 0.45 at $\theta_i \approx 82°$ for the flat black paint and 0.07 at $\theta_i \approx 87°$ for the flat white paint.

3.2.4 Object Classification and Detection

There is a significant body of literature on spectral polarimetric imaging. Most of the research demonstrates the improved contrast which may be obtained with proper spectral and polarization selection. Minimal attempts have been made to integrate the fundamental phenomenology responsible for these effects. That is, an end-to-end simulation using *a priori* $\mathbf{F}_r$ knowledge in conjunction with a governing radiometric equation has not been noted. A brief discussion is given on some relevant target-detection and/or classification efforts using polarization.

Hyperspectral polarimetric images in the VNIR of plants and painted metal plates are reported by Gupta toward target detection and identification efforts by the U.S. Army Research Lab. For indoor lab measurements, a phase angle of 105° was found to provide the best polarimetric differentiation between targets. Outdoor tests were completed under varying weather conditions and at ranges from 100 `m` to 20 `km`. The 100 `m` tests attempted to compare the lab results with those which included diffuse sky illumination. As anticipated, data taken on clear days provided a much higher polarization signature than data on an overcast day [145]. Gupta has also demonstrated the increased polarization of man-made objects to include cars and asphalt [146].

Cheng of the Jet Propulsion Lab has also reported results from hyperspectral polarimetric imaging. Cheng notes the effects of aerosols in outdoor imaging, which for the particular imaging scenario, resulted in an increased DOP with distance [147]. Data was also collected on inactive landmines, cement blocks and plastic pipes placed in backgrounds of a field of iceplants and dirt [148]. Cheng notes the value of combining spectral and polarimetric signatures, but states that there needs to be an understanding of the phenomenology to take advantage of the information.

Denes demonstrates the increased polarization of a surrogate military vehicle compared to that of a vegetation background [149]. Measurements on green painted metals, green vegetation and camouflaged netting were completed by Katkovsky where the maximum contrast in intensity and DOP were quantified. DOP was noted to be highly dependent upon the phase angle, and the polarization orientation was found to be highly independent of phase angle. The polarization orientation change primarily resulted from the orientation of the observation plane relative to the incident plane [150]. An analysis of spectral-polarimetric

imagery of camouflaged military equipment from 0.51–0.77 μm was completed by Sturgeon, who concluded the spectral data was useful in distinguishing the equipment from the background. However, she found that the camouflaged netting had a polarization signature similar to trees, the background in which such netting is frequently found [151].

The polarimetric signatures of landmines were reported by Howe who includes separate results for VIS, NIR and MWIR measurements. Surprisingly, a circular polarization component was found to provide a discriminating signature. The circular polarization signature may be attributed to the diffuse sky linear polarization component incident upon the metal, which in turn imparts some ellipticity [152].

Results of passive polarization measurements in the SWIR of the sky, automobiles, trees, water, a roof and other objects throughout a day are reported by Miller [153]. The improved categorization of painted metal plates using polarization information in conjunction with spectral is noted in [154].

Petri contemplated reducing the dimensionality of hyperspectral cubes for target detection based upon polarization signatures [155]. This work directly addresses the information content of the two imaging domains, and is where further phenomenology-driven work should be completed.

The most significant effort found to date toward the fusion of spectral and polarization signatures is discussed by Mayer, *et al.* [156] of the Naval Research Lab. Detection of camouflaged targets using the RX spectral algorithm [157] demonstrated that false detections were largely uncorrelated between the spectral and polarimetric imaging modalities. ROC curves produced by the study demonstrated increased target detection performance. The study was somewhat limited by sensor noise and spatial registration accuracy.

3.3 Visual Representation

Different means of visualizing polarization data and images are useful for human consumption, though they have no affect on information content or algorithm performance. Stokes images are a direct means of presenting the Stokes vector data. Perhaps a more visually appealing technique is to use the hue, saturation and value (HSV) color space which may be used to encode the polarization information [158]. In this manner the hue correlates to the orientation (χ), the saturation with DOP and value the intensity image (S_0). Examples of Stokes and HSV-encoded images are presented in §10.2.1.

3.4 Instrumentation

This research is focused on the radiance reaching a sensor aperture, and as such will not delve into details of imaging polarimeters. However, it is worthwhile to briefly comment on the technology, which is a required input into the imaging chain. Imaging polarimeters have two fundamental designs. The system may be one which uses multiple apertures with each aperture providing unique polarization filtering, or a single aperture which provides the same filtering but via sequentially changing the polarization filters. The multiple aperture systems have the advantage of simultaneous image acquisition, which is important for accurately capturing the Stokes vectors for scene elements where there is movement (*e.g.*, blowing grass in the wind) or changing illumination conditions. However, the use of multiple focal planes results in the spatial mis-registration of the images, which must first be registered; any residual registration error is translated in errors in the determined Stokes vectors. The single aperture system typically results in better spatially-registered images, but the time required to acquire the images result in errors from any temporal changes in the scene.

3.5 History Summary

It has long been recognized that polarized radiometry provides more information than intensity-only sensing. Many disciplines have found polarimetric imaging to be valuable. The use of polarimetric remote sensing of the earth is still in its infancy with the first space-based polarized images of the earth being acquired in the mid-1980s. Several studies have pointed to the promise of polarimetric imaging.

However, a cohesive framework which provides an end-to-end prediction of polarimetric signatures based upon the governing polarized radiance equation has not been established. Most studies are primarily limited to visual observations of increased contrast, with some noting synergism with spectral imaging.

Methods of visualizing polarimetric information are not important for polarimetric algorithms, but are required to present the information to human analysts. These visualization techniques provide an improved contextual basis for analyzing polarized imagery which may be useful to guide algorithm development. Finally, the development of polarimetric imaging systems was briefly discussed to gain an appreciation of the system limitations and their contribution of a polarimetric error budget.

Chapter 4

Governing Radiometric Equation

Having reviewed electromagnetic theory and the phenomenology of optical scattering from materials, it is now appropriate to consider the net radiance received at an overhead sensor aperture. The net radiance equation or "governing" equation was briefly discussed in the Introduction (1.2), but a thorough investigation is now warranted. As previously stated, one attempts to derive as accurate an estimate as possible of the reflectance factor, or specifically the BRDF and more generally the polarimetric BRDF $\mathbf{F}_r$ at the particular solar-ground-sensor geometry in question. All other terms in the governing equation essentially add uncertainty in the $\mathbf{F}_r$ estimate. The better the uncertainties are characterized and quantified, the better an estimate of the polarized BRDF may be made.

4.1 Governing Radiometric Equations

4.1.1 Governing S_0 Equation

The impact BRDF has on the radiance reaching a sensor aperture may be understood if the radiance contributions are examined in some detail. The total radiance in the visible to near infrared (VNIR) portion of the spectrum (*i.e.* that of solar origin) reaching a sensor aperture (L_s) may be approximated as the sum of three radiance sources:

1. direct solar *reflections* from the target, L_r
2. *upwelled* atmosphere radiance resulting from solar scatter along the target-to-sensor path, L_u
3. target-reflected *downwelled* radiance from the skydome, L_d

The order of the radiance terms above is that of typically decreasing magnitude, though the ground or target reflectance and atmospheric conditions greatly influence their relative

values (*cf.* Fig. 4.12, Tbl. 4.1 of [4]). These radiance terms are functions of the incident and reflected zenith angles, θ_i, θ_r and reflected azimuth angle ϕ.

An expression for the radiance from the direct solar reflection, L_r, is obtained by first considering the exoatmospheric solar irradiance, E_s, which propagates through the atmosphere along the solar-to-target path having a transmittance of τ_i. When incident upon a surface, it is then reflected, and again attenuated by the atmosphere along the ground-to-sensor atmospheric path by τ_r. Often the reflectance is considered Lambertian, or isotropic, such that a reflectance factor is used as an approximation to what is properly the bidirectional reflectance distribution function (BRDF), f_r. Assembling these terms, L_r may therefore be expressed as

$$L_r = \tau_r(\theta_r)\ f_r(\theta_i, \theta_r, \phi)\ \cos\theta_i\ \tau_i(\theta_i)\ E_s(\theta_i)\ . \tag{4.1}$$

Care must be used with the coordinate systems in (4.1). BRDF is defined relative to the material surface normal, which generally is not coincident with the zenith direction. This requires conversion of the coordinate systems such that the local surface normal and local earth system are common. However, for purposes of illustrating the radiative transport, we only consider zenith facing materials such that (4.1) is adequate.[1]

In a similar fashion, target-reflected radiance from the sky, L_d may be derived. The downwelled radiance distributed over the entire sky hemisphere, $L_d^{\Omega_i}$, is integrated to sum irradiance contributions onto the target across the sky, which is modified by the cosine of the incident angle upon the surface normal. As before, each of these irradiance contributions is then reflected by the surface BRDF, which is then attenuated by the target-to-sensor atmospheric transmittance as before. Replacing the BRDF by an isotropic reflectance factor greatly simplifies the expression, as the reflectance factor may be placed outside the integral. However, the more stringent BRDF must be retained as it is essential to polarimetry. An appropriate expression for L_d is therefore

$$L_d = \tau_r(\theta_r) \iint\limits_{\Omega_i} f_r(\theta_i, \theta_r, \phi)\ \cos\theta_i\ L_d^{\Omega_i}(\theta_i, \phi)\ d\Omega_i\ , \tag{4.2}$$

where $d\Omega_i = \sin\theta_i\ d\theta_i d\phi$.

A representation for the upwelled atmospheric radiance, L_u will not be attempted, as it is rather complex and usually approximated by atmospheric scattering codes such as MODTRAN, as is the downwelled sky radiance component ($L_d^{\Omega_i}$) in equation 4.2. The

[1] Secondary illumination from adjacent surfaces and shadowing are also important, but are considered secondary effects and not necessary for this discussion.

upwelled radiance is given simply to show the geometry dependence as

$$L_u = L_u(\theta_r, \phi) \ . \tag{4.3}$$

The atmospheric factors impacting these terms will be discussed separately in §4.2.

Note that the BRDF plays a direct role in L_r and L_d. For a completely diffuse or Lambertian target, the BRDF function in equations 4.1 and 4.2 is not directional and may be replaced with $f_r = \frac{\rho}{\pi}$, or that of a Lambertian surface. This approach does not require knowledge of the illumination-target-sensor geometry for calculating L_r and L_d, other than the incorporation of the atmospheric attenuation, τ. Therefore the Lambertian assumption greatly simplifies the equations and is the usual approach taken in radiometric remote sensing. With this assumption, the Lambertian ρ becomes a *reflectance factor* which one attempts to derive from the sensor-reaching radiance. Under the Lambertian assumption, ρ is easily obtained. Replacement of f_r by ρ in the governing equation results in

$$\begin{aligned} L_s &= L_r + L_d + L_u & (4.4) \\ &= \tau_r \, \frac{\rho}{\pi} \, \cos\theta_i \, \tau_i \, E_s \ + \ \tau_r \, \frac{\rho}{\pi} \iint\limits_{\Omega_i} \cos\theta_i \, L_d^{\Omega_i} \, d\Omega_i \ + \ L_u \ , & (4.5) \end{aligned}$$

where it is seen that $\frac{\rho}{\pi}$ may be pulled out of the L_d integral since it is a constant. The integrated downwelled radiance may be collectively represented as a diffuse irradiance term or E_d. With this substitution, (4.4) becomes

$$L_s = \tau_r \, \frac{\rho}{\pi} \, \cos\theta_i \, \tau_i E_s \ + \ \tau_r \, \frac{\rho}{\pi} \, E_d \ + \ L_u \ . \tag{4.6}$$

From (4.6), ρ is solved for as

$$\rho = \frac{\pi \ (L_s - L_u)}{\tau_r(\cos\theta_i \ \tau_i \ E_s + E_d)} \ . \tag{4.7}$$

In this manner, retrieval of ρ via (4.7) from remotely sensed data serves as the measured spectral reflectance factor which may be compared with known "truth" data from material spectral reflectance libraries.

However, what if the actual BRDF of the material or f_r were known—how would that knowledge be used? Simplification of the equations is complicated by the inclusion of f_r in the L_d integral. However, f_r in the L_d integral may be reasonably approximated as $\frac{\rho}{\pi}$ by considering the behavior of the L_d contribution. First, the magnitude contributed by L_d to the total sensor radiance is often low, especially as one moves toward the red to NIR

spectral region. Second, the downwelled sky radiance often has a semi-uniform radiance distribution, with the exception of scattered clouds. If the sky radiance distribution were truly uniform, then f_r in the L_d integral could truly be replaced by $\frac{\rho}{\pi}$, even if f_r were that of a "mirror" surface due to the BRDF reciprocity relationship, or $f_r(\Theta_i, \Theta_r) = f_r(\Theta_r, \Theta_i)$. Given that most materials may be approximated as Lambertian, and that the L_d magnitude is often relatively low, it is suggested that f_r may be reasonably approximated as $\frac{\rho}{\pi}$ in the L_d integral.

It now becomes possible to approximate the f_r from the L_r sensor contribution as

$$f_r = \frac{L_s - \tau_r \ \frac{\rho}{\pi} \ E_d - L_u}{\tau_r \ \cos\theta_i \ \tau_i \ E_s} \ . \tag{4.8}$$

From (4.8) it is seen that the L_d contribution is subtracted as a constant bias to f_r, just as the upwelled L_u radiance component is.

Further scrutiny of equation 4.8 presents another issue—given an observed pixel radiance, it is not possible to relate the target surface normal coordinate system to the global system. For land cover classes (*i.e.*, background materials) this is not a significant issue, since the surface normal of the material often coincides with the global surface normal (*i.e.*, level terrain). Generally, the specific geographic region being imaged is known, in which case it is possible to apply digital elevation map (DEM) data to obtain an improved knowledge of the local surface slopes. However, this consideration is beyond the scope of this treatment. For target materials, the surface normal orientation ambiguity is a more significant issue. Key considerations for the treatment are whether the target is imaged at a sub pixel or resolved resolution.

The objective of quantitative spectral remote sensing may be summarized as the task of obtaining as accurate an estimate as possible of the spectral BRDF of the individual image pixel. That is, solving for f_r (and hence ρ for the solar-target-sensor geometry) given the aperture-reaching radiance, L_s. Once this is accomplished, an array of spectral algorithms may be employed [159] such as matched filters based upon spectral BRDF libraries of materials. Such algorithms provide autonomous classification of land cover to potentially include species of vegetation. It has been reported that BRDF has a more important role in improving spectral classification algorithms than does hyperspectral resolution for some scenarios [160].

Some qualitative comments on the impact of incorporating BRDF, rather than making the Lambertian assumption, may be made. One general result may be a reduction in the target radiance relative to the background radiance. The source of this change results from many "target" materials being man-made, which typically are more specular than the

natural, background materials. Of course when the target normal vector lies in the same plane as the sun-to-target and target-to-sensor vector, the inverse may easily occur if the target observation angle is near the specular lobe or θ_r is $\sim \theta_i$. From these effects one should expect decreased target detection algorithm performance as the BRDF difference between the background and target material increases. If one had truly Lambertian targets and background materials, no performance degradation is incurred.

4.1.2 Governing Polarized Radiance Equation

Having examined the impact of the scalar or intensity-only BRDF, it is now appropriate to investigate the more general polarimetric BRDF (pBRDF) and the polarized version of the terms constituting the governing radiance equation (4.1–4.3).

Transforming (4.1–4.3) into the polarized representation is accomplished using the Mueller-Stokes formalism commonly used in polarized radiometry. In brief, all radiometric flux values are replaced by Stokes vectors and "transfer" functions such as atmospheric transmittance and reflectance (BRDF) are replaced by Mueller matrices.

Prior to making these substitutions, some simplifications are appropriate. First, the exoatmospheric solar irradiance may be considered randomly polarized, so only the scalar magnitude (or first Stokes component) of the direct solar irradiance need be considered. Second, the atmospheric transmittance values in (4.1–4.3) all represent forward scattering, which retains the incident polarization. Therefore, the scalar values for τ_i and τ_r may be used without resorting to a Mueller matrix representation. Equations 4.1–4.3 therefore become

$$\vec{L}_r = \tau_r(\theta_r)\ \mathbf{F}_r(\theta_i, \theta_r, \phi)\ \tau_i(\theta_i)\ \cos\theta_i\ E_s(\theta_i) \tag{4.9}$$

$$\vec{L}_d = \tau_r(\theta_r) \iint_{\Omega_i} \mathbf{F}_r(\theta_i, \theta_r, \phi)\ \cos\theta_i\ \vec{L}_d^{\Omega_i}(\theta_i, \phi_i)\ d\Omega_i \tag{4.10}$$

$$\vec{L}_u = \vec{L}_u(\theta_r, \phi_r) \tag{4.11}$$

where $\mathbf{F}_r$ is now the polarimetric BRDF (pBRDF). Some knowledge of the upwelled polarized radiance ($\vec{L}_u$) along the target and sensor may be gained from Rayleigh scattering theory and other sources such as Coulson [161] and Chandrasekhar [162]. However, knowledge of the polarized downwelled radiance, $\vec{L}_d^{\Omega_i}$ is more problematic since this term often has a high spatial variability, *e.g.*, varying cloud cover.

The total polarized radiance reaching a sensor aperture is then

$$\vec{L}_s = \vec{L}_r + \vec{L}_d + \vec{L}_u\ . \tag{4.12}$$

Atmospheric scattering, generally proportional to λ^{-4}, results in $\vec{L}_d$ and $\vec{L}_u$ having relatively large magnitudes at shorter wavelengths compared to $\vec{L}_r$, especially from orbital altitudes. Atmospheric polarimetric remote sensing uses this phenomena to minimize ground reflected polarization signatures to better extract atmospheric water vapor and aerosol properties [50].

Similarly, for polarimetric remote sensing of land features one wants the magnitude of the direct solar reflected radiance to be large compared to the reflected radiance from the downwelled sky and upwelled atmospheric scattering, *i.e.*, $\vec{L}_r > \vec{L}_d, \vec{L}_u$. This provides optimal conditions for estimating the polarimetric BRDF, $\mathbf{F}_r$. Exploiting polarimetric signatures in a manner analogous to spectral signatures requires estimating $\mathbf{F}_r$ given the polarized radiance reaching the aperture, $\vec{L}_s$.

Estimating $\mathbf{F}_r$ given the radiance at the sensor aperture proceeds as

$$\vec{L}_r = \vec{L}_s - \vec{L}_d - \vec{L}_u \tag{4.13}$$

$$\tau_r \ \mathbf{F}_r \ \tau_i \ \cos\theta_i \ E_s = \vec{L}_s - \tau_r \iint\limits_{\Omega_i} \mathbf{F}_r \ \cos\theta_i \ \vec{L}_d^{\Omega_i} \ d\Omega_i - \vec{L}_u \ . \tag{4.14}$$

Since the exoatmospheric irradiance is randomly polarized, only the first column of the pBRDF Mueller matrix is of concern in the $\vec{L}_r$ expression. In fact, overhead polarimetric remote sensing may only retrieve the first column of the polarimetric BRDF matrix. (Solving for other matrix elements requires illumination by varying polarization states). With this consideration (4.14) may be expressed as

$$\tau_r \begin{bmatrix} f_{00} \\ f_{10} \\ f_{20} \end{bmatrix} \tau_i \ \cos\theta_i \ E_s = \vec{L}_s - \tau_r \iint\limits_{\Omega_i} \mathbf{F}_r \ \cos\theta_i \ \vec{L}_d^{\Omega_i} \ d\Omega_i - \vec{L}_u \tag{4.15}$$

with the first column of the pBRDF given by

$$\begin{bmatrix} f_{00} \\ f_{10} \\ f_{20} \end{bmatrix} = \frac{\vec{L}_s - \tau_r \iint_{\Omega_i} \mathbf{F}_r \ \cos\theta_i \ \vec{L}_d^{\Omega_i} \ d\Omega_i' - \vec{L}_u}{\tau_r \ \cos\theta_i \ \tau_i \ E_s} \ , \tag{4.16}$$

which is analogous to (4.8) representing the intensity-only case.

Solving for $\mathbf{F}_r$ is complicated by its inclusion in the integral of the $\vec{L}_d$ term, which also contains the highly spatially variable and generally ill-known downwelled radiance component, $\vec{L}_d^{\Omega_i}$. However, under nominal sky conditions, the magnitude of the direct solar irradiance for $\lambda > 600$ nm is five times that of the integrated sky-dome irradiance, increasing

to 10x for $\lambda > 1000$ nm. This makes it reasonable to approximate the polarized radiance contribution of the downwelled sky radiance as an error term.

$$\begin{bmatrix} f_{00} \\ f_{10} \\ f_{20} \end{bmatrix} = \frac{\vec{L}_s - \vec{L}_u}{\tau_r \ \tau_i \ \cos\theta_i \ E_s} - \frac{\tau_r \iint_{\Omega_i} \mathbf{F}_r \ \cos\theta_i \ \vec{L}_d^{\Omega_i} \ d\Omega_i}{\tau_r \ \tau_i \ \cos\theta_i \ E_s} \tag{4.17}$$

$$= \frac{\vec{L}_s - \vec{L}_u}{\tau_r \ \tau_i \ \cos\theta_i \ E_s} - \begin{bmatrix} \epsilon_0 \\ \epsilon_1 \\ \epsilon_2 \end{bmatrix} . \tag{4.18}$$

Therefore, polarimetric remote sensing may recover the first column of polarimetric BRDF Mueller matrix to within the error resulting from downwelled sky radiance, presented as

$$\begin{bmatrix} f_{00} + \epsilon_0 \\ f_{10} + \epsilon_1 \\ f_{20} + \epsilon_2 \end{bmatrix} = \frac{\vec{L}_s - \vec{L}_u}{\tau_r \ \tau_i \ \cos\theta_i \ E_s} . \tag{4.19}$$

Note that ϵ_0 is always positive, and while termed an "error" may be approximated with some certainty. For diffuse surfaces the ratio of $\frac{\epsilon_0}{f_{00}}$ is equivalent to the ratio of the downwelled sky irradiance to the direct solar irradiance. The linear polarization terms ϵ_1 and ϵ_2 may either be positive or negative and represent the polarization resulting from the downwelled sky radiance.

4.2 Atmospheric Effects

It is now necessary to further examine the effects of the atmosphere in more detail. Specifically, the downwelled and upwelled radiance components, $\vec{L}_d$ and $\vec{L}_u$, must be considered. For intensity-only remote sensing, $\vec{L}_d$ or equivalently L_{0_d} provides additional signal (reflectance) from the target. This is particularly true when the Lambertian reflectance approximation is considered. However, in polarimetric remote sensing, this term is a source of uncertainty, as the $\vec{L}_d$ polarization is dependent upon the geometric location in the skydome.

Upwelled radiance, $\vec{L}_u$, or the solar energy which is scattered in the atmosphere in the direction toward the sensor is an additive term which increases the uncertainty in both intensity and polarimetric remote sensing. It must be subtracted from the sensor-reaching radiance when recovering the reflectance factor or the first column of the pBRDF Mueller matrix (equation 4.19). For intensity-only remote sensing, it serves as a contrast reduction term. The effects of $\vec{L}_u$ in polarimetric remote sensing are more complex, since the upwelled

radiance is in general polarized.

4.2.1 Atmospheric Propagation

Conservation of energy is observed with radiance in the atmosphere, as with any other medium. Atmospheric transmittance along the incident or solar-to-target path, τ_i and along the reflected or target-to-sensor path, τ_r were previously introduced as factors which attenuate the energy along that path. From the conservation of energy, it is noted that

$$\tau = 1 - \rho - \alpha \ , \tag{4.20}$$

where ρ is reflectance and α is absorptance. τ may be expressed in terms of the optical depth, δ as

$$\tau = e^{-\delta} = e^{-(\delta_s + \delta_\alpha)} \ , \tag{4.21}$$

where δ_s and δ_α are the optical depths for the scattered (reflected) and absorbed components. Generally α results in photons being lost from thermal energy conversion in atmospheric constituents. It is the reflectance or scattering which is of most interest here, as it is these photons which are responsible for the $\vec{L}_u$ and $\vec{L}_d$ components.

Atmospheric scattering is fundamentally governed by the interaction of electromagnetic energy with molecules and particles. Solutions for the interaction of electromagnetic waves with these molecules and particles are complex and governed by Maxwell's equations. It's convenient to approximate the scattering effect based upon the size of the scattering center relative to the wavelength of incident radiation. *Rayleigh scatter* results from interaction with molecules or particles which are small in comparison to λ. *Mie* or *aerosol scattering* theory applies to particles whose size is on the same order as that of λ, and finally *nonselective scattering* results from particles which are large compared to λ. Using these three categorizations, δ_s may be represented as the sum of these individual scattering terms, which results in atmospheric transmittance expressed as

$$\tau = e^{-\delta} = e^{-(\delta_r + \delta_a + \delta_{ns} + \delta_\alpha)} \tag{4.22}$$

where the δ_r, δ_a and δ_{ns} are the optical depths resulting from the Rayleigh, aerosol and nonselective scattering, respectively [4, §3.4.2.2]. This expression provides an understanding of the source of atmospheric losses, but does not provide information on the direction of scatter—other than out of the propagation direction along which τ is determined.

The direction of the scatter and in particular the polarization of the scatter must be determined to quantify $\vec{L}_d$ and $\vec{L}_u$. This information is captured by the *phase function* of

the scattering. Each of the three scattering components and their phase functions are now examined in more detail.

4.2.2 Rayleigh Scatter

Rayleigh scattering applies when the particle size is small relative to the wavelength, or $\frac{2\pi a}{\lambda} \ll 1$ where a is the radius of a spherical scatterer [163]. Coulson indicates that $\frac{a}{\lambda} \leq 0.03$ is required to meet the small-particle criterion [5, §4.3.1]. Rayleigh scatter answers why the sky is blue, since the magnitude of the scattering is proportional to λ^{-4}. (Actually the "blue" is also a result of the spectral response of the human eye, combined with the λ-dependent scattering dependency). This also explains the red color associated with a sunrise and sunset, since the long solar path length through the atmosphere preferentially scatters the blue out of the propagation path. Rayleigh scatter is independent of particle size, which significantly simplifies the mathematical description.

First, it is noted the Rayleigh optical depth δ_r may be expressed in terms of the Rayleigh scattering coefficient, β_r, which is the magnitude of scatter per unit length of propagation, z.

$$\delta_r = \beta_r \; z \tag{4.23}$$

Without further derivation, β_r is shown to be equal to

$$\beta_r = \frac{32 \; \pi^3 \; (\hat{n}(\lambda) - 1)^2}{3 \; \lambda^4 \; m} \quad \left[\mathtt{m}^{-1}\right] \tag{4.24}$$

where $\hat{n}(\lambda)$ is the complex index of refraction and m is the *number density* or molecules per cubic meter. From the scattering coefficient β_r, the attenuation along the propagation direction is therefore determined as a function of the wavelength, refractive index and density.

The scattering out of the propagation path, $\beta_r(\theta)$ may be expressed in terms of the scattering coefficient and a phase function $p(\theta)$ which provides the angular distribution of the scattering.

$$\beta_r(\theta) = \frac{\beta_r}{4\pi} p(\theta) \tag{4.25}$$

The Rayleigh phase function for randomly oriented particles is [163]

$$p(\theta) = \frac{y + \cos^2 \theta}{y + 1/3} \tag{4.26}$$

with y being a sphericity or molecular anisotropy parameter typically ranging from 1–13, with $y = 1$ for spherical scatterers. The Rayleigh scattering function for incident randomly

Table 4.1: Maximum DOP for the Rayleigh atmosphere [5, Fig. 4.5] and fraction of skylight irradiance [164].

λ (μm)	DOP_{max}	d_{sky}
0.3120	0.55	—
0.3715	0.72	0.47
0.4365	0.82	0.38
0.5460	0.91	0.28
0.8090	0.97	0.18

polarized radiance and $y = 1$ is given by [4, §3.4.2.1]

$$\beta_r(\theta) = \frac{8\pi^2\ (n(\lambda) - 1)^2}{3\lambda^4\ m} \left[\frac{3}{4}\left(1 + \cos^2\theta\right)\right] \tag{4.27}$$

Furthermore, the DOP is given by equation 4.28 where it is seen for spherical scatters ($y = 1$) that the radiance becomes completely polarized as $\theta \to 90°$ or $DOP = 1$ for $\theta = 90°$ [163].

$$DOP = \frac{1 - \cos^2\theta}{y + \cos^2\theta} \tag{4.28}$$

The maximum DOP is always at $\theta = 90°$ and for this reason, the sky has a maximum DOP in an arc 90° from the sun, with the polarization composed of the $\mathcal{S}$-polarization. The location of maximum polarization is easily verified by viewing the sky $\vec{L}_d$ radiance in different Θ_i locations with a linear polarization filter. Of course, the same is true for the upwelled $\vec{L}_u$ component as will be seen from overhead polarization images (*cf.* Figure 3.1). From equation 4.28, it is also seen that $DOP_{max} = y^{-1}$.

The polarization of the scattered radiance is understood if the scattering geometry of dipole radiation is visualized. Incident randomly polarized radiance scattered in the forward direction continues to be randomly polarized. However, in accordance with equation 4.28 the polarization increases with scattering angle.

Based upon Rayleigh scattering theory, Chandrasekhar derived expressions using a "discrete ordinate method" for the polarized radiance leaving the top and bottom of the atmosphere [162], or $\vec{L}_u$ and $\vec{L}_d$, respectively. From these expressions, Coulson published tables of calculated results [161].

Although the magnitude of skylight decreases with increasing λ per the λ^{-4} scattering dependency, the DOP actually increases with λ. This is due to multiple scattering which has the effect of depolarizing shorter wavelengths. The maximum DOP for a nominal atmosphere as a function of wavelength is given in Table 4.1, which also includes the typical fraction of the diffuse sky irradiance, d_{sky}, relative to the total.

While the skylight polarization is predominantly s-polarization, there is a negative polarization branch, or p-polarization (polarization direction radially oriented with respect to the sun) observed near the solar point. Multiple Rayleigh scattering has been shown as a probable source of the negative polarization branch [5, §4.7], which is similar to the phenomenology responsible for similar observations of particulate surfaces such as the moon (*cf.* §3.2.1).

4.2.3 Aerosol and Nonselective Scatter

As the scattering center size increases to the same order as that of the wavelength, Rayleigh scattering theory breaks down and aerosol scattering theory must be used. Aerosol scattering is often treated by Mie scattering theory and is predominantly in the forward direction, which retains the initial radiance polarization. Therefore the magnitude of $\vec{L}_d$ and $\vec{L}_u$ which results from scattering away from the propagation direction is inherently low. Therefore, the polarization from aerosol scattering may be treated as a first-order correction to Rayleigh scattering [5, §4.5.1].

Nonselective scattering may be treated by geometric optics due to the large particle sizes. The net polarization effects from aerosol and nonselective scatter are low in comparison to Rayleigh scatter.

4.2.4 Polarized Atmospheric Calibration

Given the polarization of $\vec{L}_d$ and $\vec{L}_u$, a means of estimating these parameters is needed such that $\vec{L}_r$ and specifically $\mathbf{F}_r$ may be retrieved given $\vec{L}_s$ (equation 4.14).

The magnitude or L_0 component of $\vec{L}_u$ is frequently estimated using atmospheric propagation computer codes such as MODTRAN [165, 166]. Recently, polarized versions of MODTRAN have been developed and may also be used to estimate the polarized atmosphere radiance [3, Ch. 31]. An alternate technique is the use of the "Coulson tables" which provides estimates of the Rayleigh scattering polarization component [161].

Interestingly, some have proposed using the land-reflected polarization signature ($\vec{L}_r$ and $\vec{L}_d$) to derive the atmospheric contribution, $\vec{L}_u$. At an adequate GSD and over uniform land cover regions, the $\vec{L}_r + \vec{L}_d$ component may be treated as relatively constant or as "truth" data [103]. The land-reflected radiance components are then derived by applying polarimetric BRDF land cover models such as that discussed in §2.2.6.2 [167].

4.3 Spatial Scale

One of the first considerations made in the application of BRDF data to remote sensing is determining over what spatial extent are the data required? Recall the painted metal plate and the bidirectional reflectance variance function (BRVF). Can the payload resolve the individual paint bubbles and flakes? If it can't, then the integrated BRDF for the painted metal plate is appropriate. If individual features of the plate may be resolved, then a more appropriate BRDF should be considered. For remote sensing and imaging in general, the spatial resolution of the BRDF must be at least as small as the sensor GSD.

In general, the radiance reaching a single detector element will not result from a homogeneous material, but rather from a collection of many homogeneous materials with many different geometric orientations. For example, consider a 10×10 m section of a soybean field. The sensor-reaching radiance from this section will be due to multiple homogeneous materials such as leaves, dirt and rocks. Of course these "homogeneous" materials really aren't—leaves may be decomposed into the vein and flesh areas, dirt into different organic materials, silicates, etc. This process may be continued *ad nauseam*.

For many overhead systems, the BRDF of multiple materials are integrated, as the GSD is on the order of 10s of m or greater. However, higher resolution systems often have GSDs of the same scale as many natural objects, such as individual trees, shrubs and leaves. For target detection applications, the reflectance truth data or BRDF data should be for an appropriate spatial scale which characterizes the key identifying materials for that target. Additional fidelity may be obtained by also characterizing the background directional reflectance at the same GSD.

The spatial scaling of BRDF values from individual "fundamental" material measurements and geometries (*e.g.*, a leaf canopy) is challenging and an active area of research [168]. Large area BRDF measurements which integrate multiple materials may be more effective than attempting to scale single material measurements, whose radiance contributions are often not linear.

4.4 Synthetic Image Generation

Synthetic image generation (SIG) programs have enabled the theoretical analysis of remote sensing algorithms and payload performance. This is completed at a minimal cost compared to field campaigns, and has proven beneficial for exercising many parameters which would not be feasible with experiments. SIG programs, unlike computer graphics programs and animations, place a premium on maintaining high radiometric accuracy. Essential to

SIG programs is the inclusion of a radiometrically correct atmosphere, which is often calculated by well-established atmospheric radiation propagation programs such as MODTRAN. The Digital Imaging and Remote Sensing Image Generation (DIRSIG) model [169] at the Rochester Institute of Technology's Center for Imaging Science is one such example and renders scenes with a spectral coverage from 0.3 to 14 μm [170, 171].

Incorporating realistic background spatial and spectral signatures (*i.e.*, non-target materials) into SIG models is challenging. Early efforts resulted in background materials being unrealistically spectrally pristine, thus artificially enhancing the performance of spectral detection algorithms. An array of "mapping" approaches have been developed which provide varying levels of realism to individual material facets. These approaches include texture, mixture and reflectance maps ([172], [173, Ch. 4]).[2] These mapping functions are analogous to including the BRVF which results from the natural variability within a material "class."

Separate from the material maps, BRDF models may also be implemented for facets in the synthetic scene. The use of polarimetric BRDF models with the Mueller matrix formalism enables the analysis and comparison of polarization information content versus spectral information. DIRSIG was recently upgraded to include a polarimetric BRDF model based upon a modified Torrance-Sparrow BRDF model [97] which is detailed by Meyers [99]. Other SIG programs such as IRMA and SPIRITS (Spectral and Inband Radiometric Imaging of Targets and Scenes) have also incorporated polarimetric signatures.

IRMA calculates the BRDF Mueller matrix based upon the Fresnel reflectance given the complex index of refraction, and simply adds the diffuse reflectance to the f_{00} element (equivalent to adding the scalar BRDF). As an alternative, IRMA allows the manual entry of Mueller matrix data for $\sim$10 different scattering angles [94].

The SPIRITS SIG code is owned by the U.S. Government and a polarized version, called "POLAR", was produced in 1986. When first developed, POLAR implemented polarized BRDF based upon the Maxwell-Beard model, distinct from the Sandford-Robertson BRDF model which is used with the unpolarized, SPIRITS, code [174]. However, the POLAR BRDF model failed to couple the specular and diffuse BRDF components, and was limited to dielectric materials. In the late 1990's, the POLAR code was supplanted by a new version of SPIRITS which incorporated a polarized Sandford-Robertson BRDF model [78, 94]. However, the polarized version of SPIRITS is difficult to obtain, and it is thought that the U.S. Government may not hold the data rights to the polarization module [175].

The availability of polarimetric BRDF data continues to be a bottleneck in simulating polarimetric imaging through SIG. While there is some pBRDF data on homogeneous materials, appropriate background polarimetric signatures is lacking. The background materials

[2] http://dirsig.cis.rit.edu/doc/maps.pdf

are typically natural, heterogeneous materials such as vegetation and soils.

4.5 Environmental Impacts to BRDF

Once BRDF data and models are in place for employment in spectral algorithms, the job is only partially complete. More often than not, the BRDF characterization for a material does not represent that material in the field. Weathering alters the optical properties via UV "washing," oxidation, surface abrasions, etc. Also, the material may be covered by dust, dirt or other particulates. This effect has also been termed "contamination" of the material. A cursory examination of these effects have been made by Thomas [176] and Lukesh [177] where only the scalar BRDF is considered.

In principle, polarimetry has the potential to provide a unique means of modelling degradation of materials in the field. It is hypothesized that a surface covered by contaminants may be represented using the Mueller matrix formalism. The effect of the contaminants may be represented as a transmissive Mueller matrix, $\mathbf{T}_{cont}$, which when coupled with the pristine surface BRDF could be represented as

$$\vec{L} = \mathbf{T}_{cont}\mathbf{F}_r\mathbf{T}_{cont}\vec{E} \tag{4.29}$$

with the optical path incident on the material first encountering the contaminant, scattered by the BRDF, then altered by passing again through the contaminant. With a thin and relatively sparse layer of contamination such as dust, the $\mathbf{T}_{cont}$ matrix may be relatively constant over a wide range of illumination angles.

4.6 Summary

The governing radiometric equation for polarized radiance reaching a sensor aperture has been developed (4.9-4.11). The inclusion of BRDF in two terms of the governing equation resulted in an under-determined equation (4.19). Downwelled and upwelled atmospheric radiance was shown to be polarized through different scattering mechanisms. Techniques for predicting these terms include computer models such as MODTRAN and look-up tables based upon atmospheric turbidity.

Physics-based synthetic imagery has proven valuable in exercising algorithms which would otherwise be cost-prohibitive using experimental data sets. A robust synthetic image generation (SIG) program which provides polarimetric signatures for different classes of materials is lacking. Maturation of a polarimetric SIG tool will enable the parameter space between spectral and/or polarimetric algorithms to be explored.

Finally, it is emphasized that passive remote sensing may only recover the first column of the pBRDF Mueller matrix, to within some residual uncertainty due to the reflected downwelled and upwelled sky radiance along the target to sensor path. However, prior to employing governing polarimetric radiance equation 4.19, a means to quantify $\mathbf{F}_r$ for materials is needed—this establishes the focus for the rest of this research.

Chapter 5

Polarimetric BRDF Measurement Approach

With the governing equation for polarimetric remote sensing in hand (equation 4.19), it becomes possible to devise a measurement technique which quantifies the f_{00}, f_{10}, f_{20} and $\epsilon_0, \epsilon_1, \epsilon_2$ contributions that a remote sensor would measure. The essential component is the polarimetric BRDF, or the f_{00}, f_{10}, f_{20} elements of the pBRDF Mueller matrix. Given the polarimetric BRDF elements, the ϵ_x or sky contribution may be determined for varying sky conditions.

First the experimental technique is reviewed. Next, details of the specific imaging system used with the technique are discussed. Finally, an analysis of different error contributions is presented, establishing estimates for the measurement uncertainties.

5.1 Polarimetric BRDF Measurement Technique

Ideally, BRDF measurements are made in a lab environment with an illumination source subtending a minimal angle relative to the measurement surface and with careful control and minimization of stray light. However, many materials such as vegetation do not lend themselves to easy indoor measurements due to alteration of their natural state or simply from their physical size (*e.g.*, a tree canopy). Outdoor BRDF measurements of such materials becomes a necessity, and many approaches have been successfully employed [40, 29, 34, 30]. Wide field of view (FOV) imaging systems, as discussed in §2.2.2.2, may be used which efficiently enable the simultaneous measurement of multiple scattering angles [45, 26, 25].

This approach uses relatively narrow FOV ($\approx 10^\circ$) imaging to make BRDF measurements, as shown previously in Figure 2.7. Each image pixel is approximately at the same scattering angle as that at the center of the image, such that the average radiance across the focal plane enables determination of the BRDF. Such an approach limits the scattering angle resolution to the FOV, but this is not a concern for most natural surfaces which are

not appreciably specular and hence do not have rapid BRDF changes over the 10° FOV of the system. The impetus for this technique is the ability to quantify the BRDF variability or BRVF as discussed in §2.2.1.3. Multiple scattering angles are sampled by repositioning the camera in the hemisphere above the measurement surface.

This technique may be used at any distance from the measurement surface—the only prerequisite is that the total surface area imaged or ground FOV (GFOV) is large enough that it adequately integrates the spatial variability or inhomogeneities of the material. For instance, a GFOV of 1 foot may be adequate for grass, asphalt and aggregate; but measurements of tree canopies and shrubs would require a larger GFOV. For easy field use not requiring elevated platforms or other positioning devices, an operating distance of around six feet is appropriate, providing a GFOV of approximately 1 foot. Details of the measurement approach follow, which was also published in [178].

5.1.1 BRDF Measurement

A successful technique for outdoor BRDF measurements may be developed by considering the radiance contributions to a sensor as discussed in §4.1.1. It is first noted that imaging surfaces at a short range results in negligible atmospheric scattering along the surface-to-sensor path, such that $\vec{L}_u$ may be approximated as zero. Therefore an outdoor measurement of a surface is composed of the $\vec{L}_r + \vec{L}_d$ radiance components. This "normal" image will be referred to as image `C` (Figure 5.2).

The reflected downwelled sky radiance, $\vec{L}_d$ is a stray light source for the purpose of a BRDF measurement. However, it may be directly measured and eliminated via an image subtraction technique. This is possible by imaging the area of interest while occluding just the sun and having the area shadowed. In this manner a "shadow" image is an $\vec{L}_d$ measurement. The shadow image is termed image `D`. In this manner it is seen that the $\vec{L}_r$ radiance needed to determine the BRDF is given according to

$$\vec{L}_r \propto \mathtt{C} - \mathtt{D} \;=\; (\vec{L}_r + \vec{L}_d) - (\vec{L}_d)\ . \tag{5.1}$$

Following the development of the governing radiometric equations as presented by equation (4.19), it is noted that the shadow image is equivalent to $\vec{\epsilon}$. The error term shown in (4.19) is therefore eliminated by the "shadow" image. This is significant, as comparison of the `C` and `C` − `D` data quantifies the change in the Stokes radiance which results from the downwelled sky.

5.1.2 Radiance Calibration

The "digital counts" recorded by the imaging system may be normalized into absolute BRDF values by use of a calibration target having a known reflectance factor. Spectralon has a highly Lambertian, approximately angular-invariant BRDF of $\frac{\rho}{\pi}$, with a randomly polarized reflectance of $\rho \geq 0.97$ across most of the VNIR spectrum [179]. As with the surface being measured, images of the calibration target are taken both in sun and in shadow, images `A` and `B`, respectively.

When acquiring multiple images over a short time period such that the atmospheric conditions and solar zenith position (θ_i) do not change appreciably, the BRDF may be determined by the ratio of the known calibration target BRDF to that of the unknown surface or

$$\frac{L_r^{cal}}{L_r^{sur}} = \frac{\frac{\rho}{\pi}}{f_r} \longrightarrow f_r = \frac{\rho}{\pi}\frac{L_r^{sur}}{L_r^{cal}} \ . \tag{5.2}$$

In terms of the digital counts of the pixels in each of the four images, `A` through `D`, the BRDF is

$$f_r = \frac{\rho}{\pi}\left[\frac{\mathtt{C}-\mathtt{D}}{\mathtt{A}-\mathtt{B}}\right] \ . \tag{5.3}$$

When imaging a calibration target such that it occupies the full FOV, this technique also self-corrects for the so called "lens falloff" irradiance reduction away from the center of the focal plane.

5.1.3 Polarimetric BRDF

The polarized radiance leaving the surface may be quantified as a Stokes vector using well-established approaches [55, 180]. In this implementation, images are acquired under four different linear polarization filter orientations relative to the horizon: 0°, 45°, 90° and 135°. This enables derivation of the Stokes parameters according to

$$\begin{bmatrix} S_0 \\ S_1 \\ S_2 \end{bmatrix} = \begin{bmatrix} \frac{I_0+I_{90}+I_{45}+I_{135}}{2} \\ I_0 - I_{90} \\ I_{45} - I_{135} \end{bmatrix} \tag{5.4}$$

where $I_{\mathtt{xx}}$ represents an image acquired with the polarization filter set at `xx`°. It is noted that the first Stokes component is derived using an average of both sets of cross-polarized images.

In terms of the images using the calibration target, it is seen from (5.3) and (5.4) that

the polarimetric BRDF is therefore

$$\begin{bmatrix} f_{00} \\ f_{10} \\ f_{20} \end{bmatrix} = \frac{\rho}{\pi \left[(\mathtt{A}_{\perp} + \mathtt{A}_{\parallel}) - (\mathtt{B}_{\perp} + \mathtt{B}_{\parallel}) \right]} \times \begin{bmatrix} \frac{1}{2} \left[(\mathtt{C}_0 - \mathtt{D}_0) + (\mathtt{C}_{90} - \mathtt{D}_{90}) + (\mathtt{C}_{45} - \mathtt{D}_{45}) + (\mathtt{C}_{135} - \mathtt{D}_{135}) \right] \\ (\mathtt{C}_0 - \mathtt{D}_0) - (\mathtt{C}_{90} - \mathtt{D}_{90}) \\ (\mathtt{C}_{45} - \mathtt{D}_{45}) - (\mathtt{C}_{135} - \mathtt{D}_{135}) \end{bmatrix}, \tag{5.5}$$

where the $\perp$ and $\parallel$ subscripts on the calibration target images indicate two orthogonal polarization orientations, normally taken at 0° and 90°. In theory, a single calibration image could be doubled and equal the calibration target BRDF since the radiance is unpolarized. However, in practice it is found that the calibration panel does impart some minor polarization, thus requiring the acquisition of two cross-polarized images to properly calibrate the system. (The calibration panel will be addressed in more detail in §5.3.4.1). The fact that all images are acquired with the polarization filter in place conveniently eliminates any polarization filter transmittance dependency from the calculations.

To summarize, for each hemispherical scattering position, a total of 8 images are acquired of the measurement surface, 4 polarization orientations with 2 illumination conditions (full sun and shadow). A minimum of 4 calibration target images must be taken, a set of cross-polarized images in sun and in shadow. Therefore a data set at one scattering position at a single spectral band is composed of 12 images. The image-wide average pBRDF is determined according to 5.5 by averaging the digital count values in each image. In this manner, image-to-image spatial registration is not critical. However, spatial registration of the images is required to obtain an accurate pixel-wise polarimetric image and to fully exploit the polarimetric variability or pBRVF behavior.

5.1.4 BRDF Probability Distribution (BRVF) Calculation

Thus far, only the average digital count values over the entire image have been considered in deriving the BRDF. However, the impetus for this technique is the ability to quantify the BRDF variability, or BRVF discussed in §2.2.1.3. The variability is obviously a function of the GSD, as a larger GSD results in greater averaging of texture within a pixel, and hence decreased pixel-to-pixel variability within a single material class.

The high-resolution images acquired with the BRDF measurement system may be used to generate the BRVF given the specified GSD of a remote sensing sensor. Generating the BRVF is accomplished by convolving the image, $f[x, y]$, with a convolution kernel $h[x, y]$

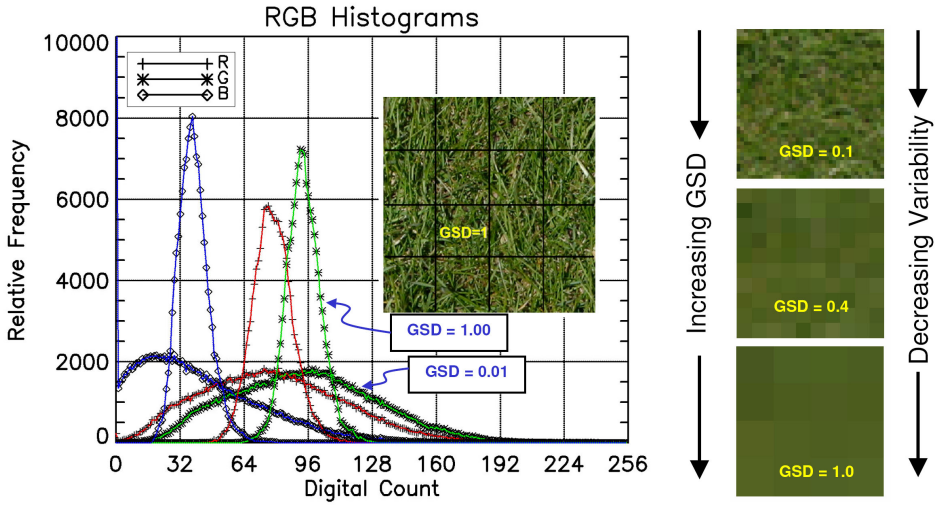

Figure 5.1: The RGB BRDF distributions or BRVF for a "grass" measurement. Histograms are shown for the full image resolution and at an arbitrarily defined "GSD = 1". The averaging of the texture as a function of GSD is illustrated at right.

sized to the GSD of interest. The result is a low-pass filtered image, $g[x, y]$ with the spatial texture representative of the GSD of $h[x, y]$. This is presented mathematically as

$$g[x, y] = \frac{1}{X^2} \sum_{i=0}^{m-1} \sum_{j=0}^{n-1} f[x, y]\ h[x - i, y - j] \tag{5.6}$$

where X^2 is a weighting factor such that the average magnitude of $g[x, y]$ is that of the original image, $f[x, y]$. Ideally $h[x, y]$ is the point spread function of the remote sensing platform in question, but for quick processing a simple function with a unit magnitude and square spatial extent is used (termed a `RECT` function by some [181]). Figure 5.1 illustrates the effect using a simple color (RGB) image of "grass" taken with a commercial digital camera.

Unlike the image-wide polarimetric BRDF determination, the accuracy of the BRVF depends upon the degree of the spatial registration of the four sets of polarized `C` and `D` images. When the size of the convolution kernel is commensurate with the spatial registration accuracy, significant errors result. The same is true of movement of measurement surfaces while acquiring the four polarization orientations, *e.g.* grass blowing in the wind. This requires the `C` and `D` image sets to be spatially registered prior to performing BRVF calculations. The spatial registration technique will be further discussed in §6.1.2 with spatial registration error analysis provided in §5.3.2.

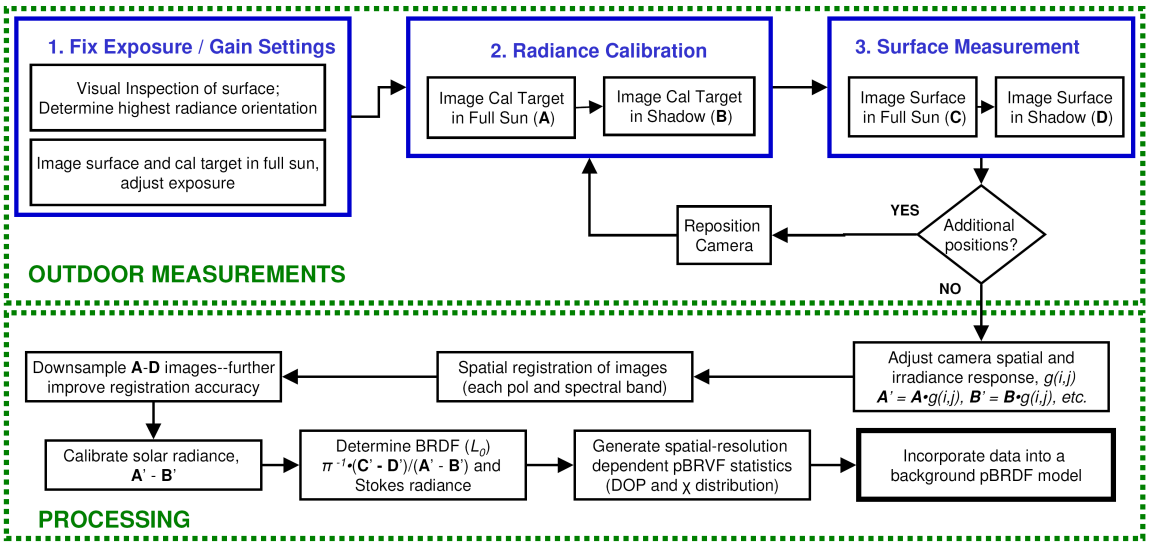

Figure 5.2: Measurement and process flow for making polarimetric BRDF and BRVF measurements with the camera system.

A summary of the general measurement steps for this technique is presented as Figure 5.2, which also provides some of the calibration and processing steps discussed later. Depending on the polarimetric imaging system used to make the measurements, this process should be modified accordingly, such as spectral filter changes, etc.

5.2 Imaging System Description & Characterization

The imaging system consists of a SenSys 1602E camera having a 1536×1024 thermoelectric-cooled, 12-bit silicon CCD with a response nonlinearity $\leq 0.5\%$ [182]. A filter wheel located between the lens and the CCD is used to mount 25 mm diameter spectral band-pass filters. The spectral filter wheel housing accepts a standard F-mount lens, to which a Nikon 50 mm, f/1.8 lens was used. The resulting FOV is 14.6° along the x-axis or horizontal dimension of the array and 9.7° along the y-axis or vertical dimension of the array. The resulting pixel-level FOV or IFOV is 0.1658 mrad. A linear polarization filter is used external to the lens, and mounted on an optics post in a precision rotary mount. The camera assembly and polarization filter mount are affixed to a common optics board, which is then mounted on a tripod. An overview of the system is shown in Figure 5.3 and a view of the spectral filter mount is shown in Figure 5.4. Three spectral filters were used with the system: 550 ± 5 nm, 650 ± 5 nm and 750 ± 12.5 nm (Omega Optical® 550BP10, 650BP10 and 750DF25). (The 650 nm filter was not used until the end of the research). The transmittance of each

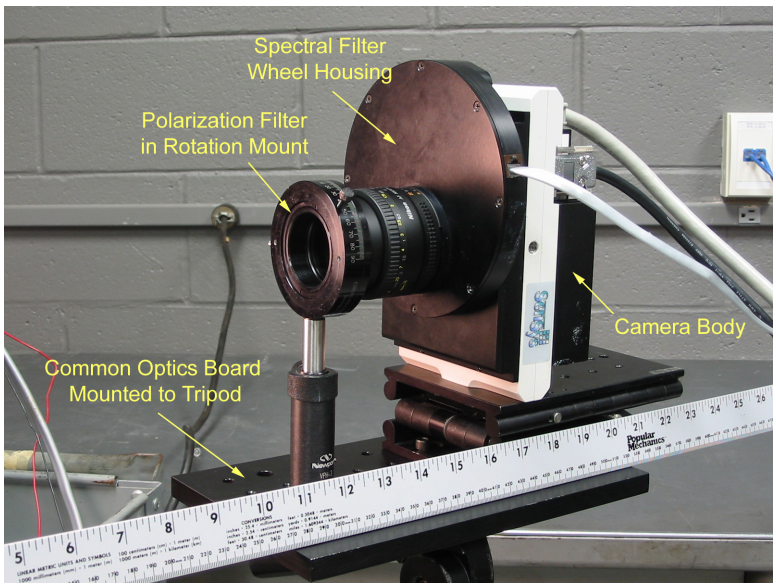

Figure 5.3: The assembled imaging system mounted on a tripod.

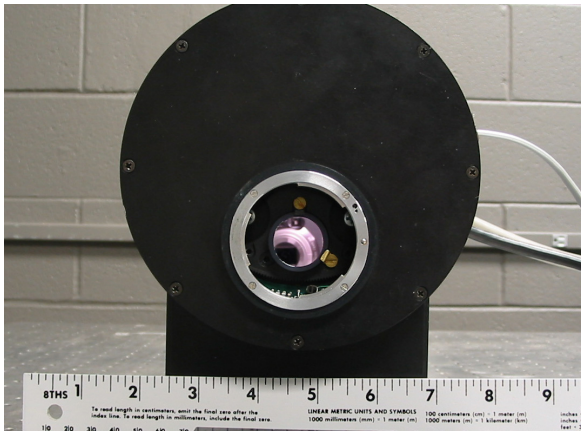

Figure 5.4: Looking down the optical axis with the lens removed showing the 550 `nm` spectral filter mounted in the filter wheel.

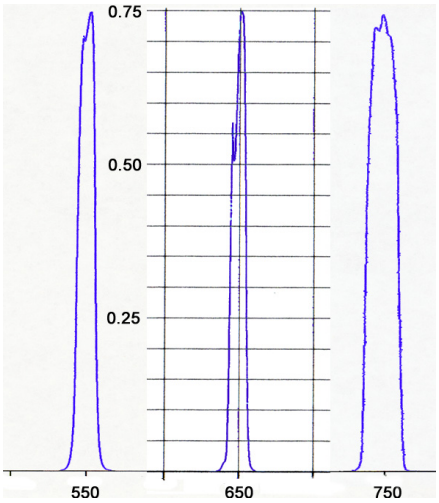

Figure 5.5: The transmittance of the spectral filters is shown, as measured by the manufacturer.

of the three filters is shown in Figure 5.5. A spectral band farther into the NIR would have been preferred, but the polarization filter contrast drops substantially beyond 800 nm. The polarization filter is an inexpensive optical grade glass filter having a cross-polarized transmission of 0.15% (Edmund Industrial Optics®, Stock No. H52-557).

Prior to using the system for pBRDF measurements, it is important to gain confidence of the system performance in a lab environment. Toward that end, a series of tests were conducted which characterized *i*) the focal plane irradiance profile, *ii*) the noise and repeatability of the system and *iii*) images of known polarization behavior. Each of these is reviewed. A discussion of the measurement uncertainties is presented in §5.3.

5.2.1 Focal Plane Irradiance Profile

All imaging systems using a planar focal plane (or imaging media such as film) have a natural taper in the focal plane irradiance away from the center of the array. This is commonly referred to as "lens falloff" [4, p. 71]. If it were possible to make the A and B images in which the calibration target completely covered the FOV of the image, then this characterization is not required as division by these images according to (5.5) would self-correct the falloff behavior. However, in practice a full FOV image is not practical and spatial imperfections in the calibration target do not make this a viable approach. It is therefore necessary to understand and quantify the focal plane irradiance profile for this system.

An integrating sphere was used providing uniform radiance across the FOV of the camera (Figure 5.6). Images were acquired at varying aperture settings, ranging from f/1.8 to

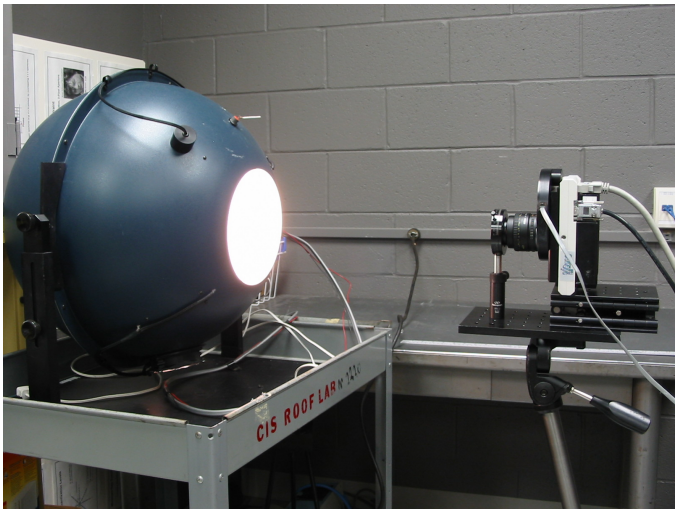

Figure 5.6: An integrating sphere was used to characterize the focal plane irradiance across the field of view of the camera.

f/16.0 in order to understand the lens falloff as a function of aperture setting. The resulting images were analyzed by considering the irradiance (or digital counts) as a function of radius from the center of the CCD. The normalized response of the focal plane was then determined for varied aperture settings as a function of radius from the center of the CCD. By circumscribing bands of pixels centered about the focal plane, the entire CCD was characterized by the mean and standard deviation of the response as a function of radius. Figure 5.7 presents the results for varied aperture settings.

At f/5.6 and slower the response is similar; a drop of approximately 10% is seen at the corners of the CCD relative to the center. At f/4.0 the reduction at the corners is approximately 15%, growing to 20% and over 35% at f/2.8 and f/1.8, respectively. It is presumed that the lens incorporates vignetting in the optical design which reduces aberrations at higher field angles for faster aperture settings. For the pBRDF measurements, there is adequate radiance such that the aperture is stopped down to f/11.0, which also provides a good depth of focus.

5.2.2 Dark Noise Properties

Each image acquired in the measurement has a "dark image" subtracted from it or the digital counts which result from other than photons interacting with the focal plane. The consistency of the dark images in part establishes the level of repeatability the system may achieve. Figure 5.8 illustrates the dark image properties via comparison of two dark images

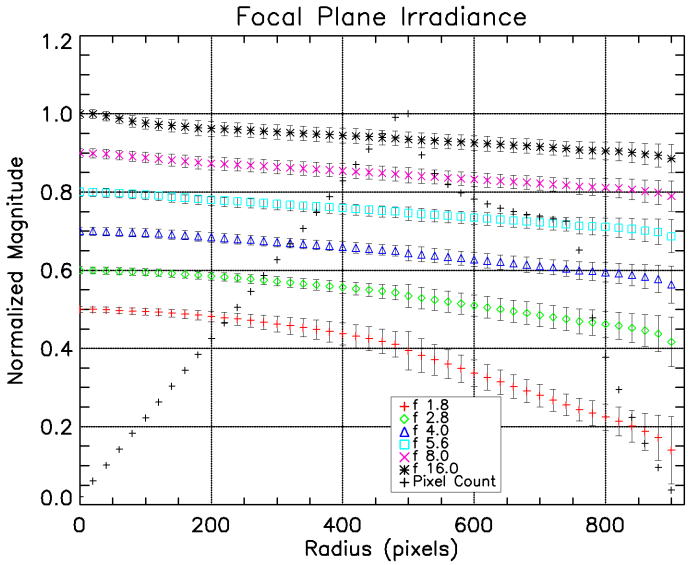

Figure 5.7: Focal plane irradiance as a function of f/stop and FOV. Note that each data series has been offset by 0.1 for greater visibility. The error bars represent one standard deviation.

acquired under the same gain setting and exposure time. The data indicate a very good dark image repeatability, and as such there is minimal impact to the results. As seen from Figure 5.8, the maximum variance in the dark image is on the order of 2.5 digital counts, or a standard deviation of ≈ 1.58. This represents a noise level of $\frac{1.58}{2048}$ or less than 0.08% for a signal at half the camera's dynamic range.

5.2.3 Test Images

A short experiment acquired a series of "test" images in which the overall polarimetric behavior is known. The test setup (Figure 5.9) included a Spectralon panel as the background which presumably has a $DOP \approx 0$. A black terry cloth covered box was used as a stand to place objects. Lighting was ambient room lighting provided by overhead fluorescent lights, with no special consideration other than keeping the illumination conditions constant between successive images.

The first experiment imaged a linear polarization filter positioned such that the Spectralon was visible through most of the filter. Analysis of the polarization filter imaging results will prove helpful when the measurement uncertainties are considered in detail. Obviously, one would expect $DOP \approx 1.0$ through the filter. The raw images taken at 0°, 45°, 90° and 135° are shown in Figure 5.10. The effects of the linear filter are readily apparent.

Now, the Stokes and resulting DOP images are shown derived from the raw images

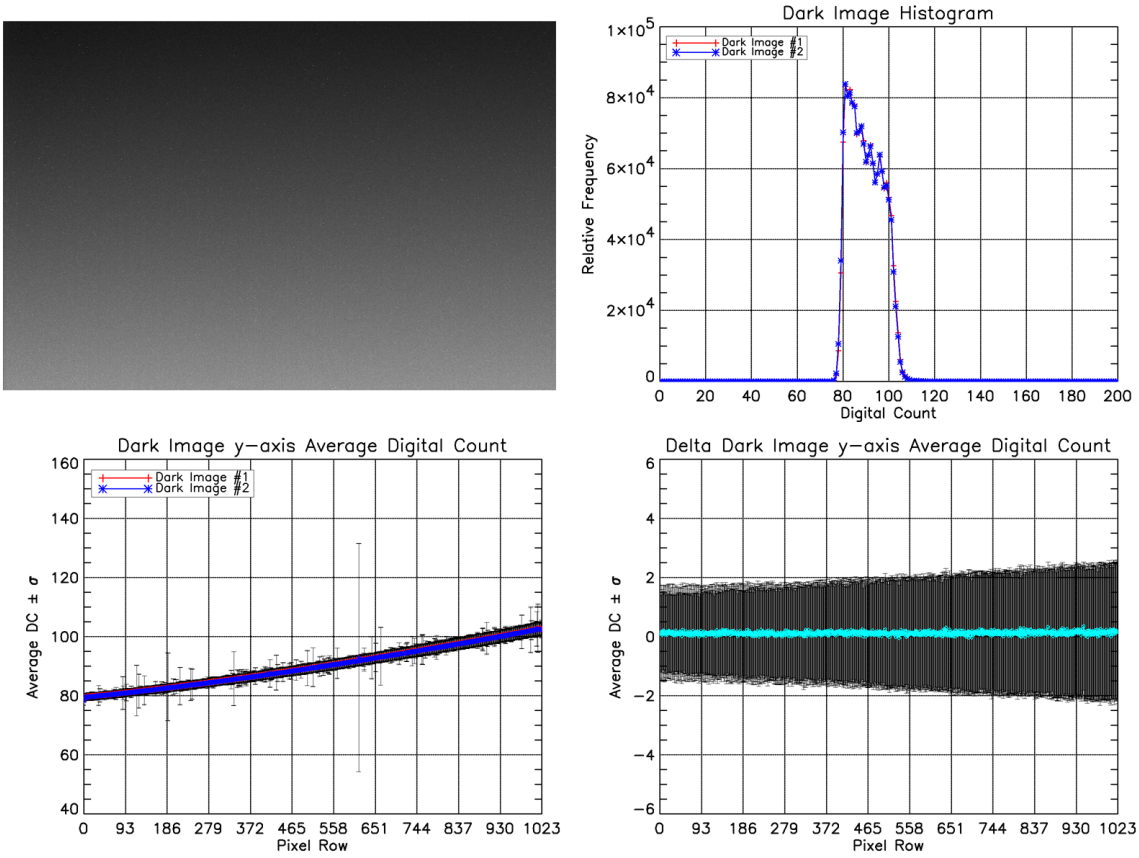

Figure 5.8: *Top left*: A dark image exemplifies the readout direction of the CCD, as noise signal is shown to accumulate along the bottom of this image—this image scaled significantly to enable visualization of the dark noise. *Top right*: Virtually identical histograms result from two dark images taken under the same gain setting and exposure time. *Bottom left*: Similar repeatability is seen when examining the average and variance of the two images along the y-axis. *Bottom right*: The y-axis average and variance of the difference between two dark images taken with identical gain settings and exposure times.

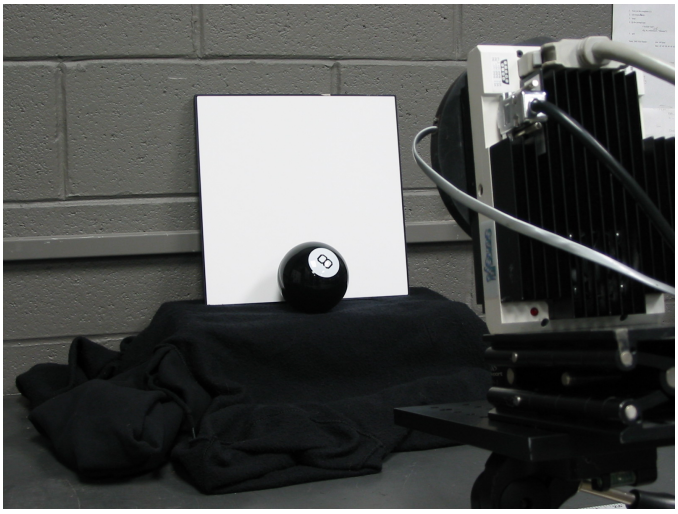

Figure 5.9: The setup for acquiring the test images includes a 1 `ft` × 1 `ft` Spectralon panel in the background and a stand covered with black terry cloth.

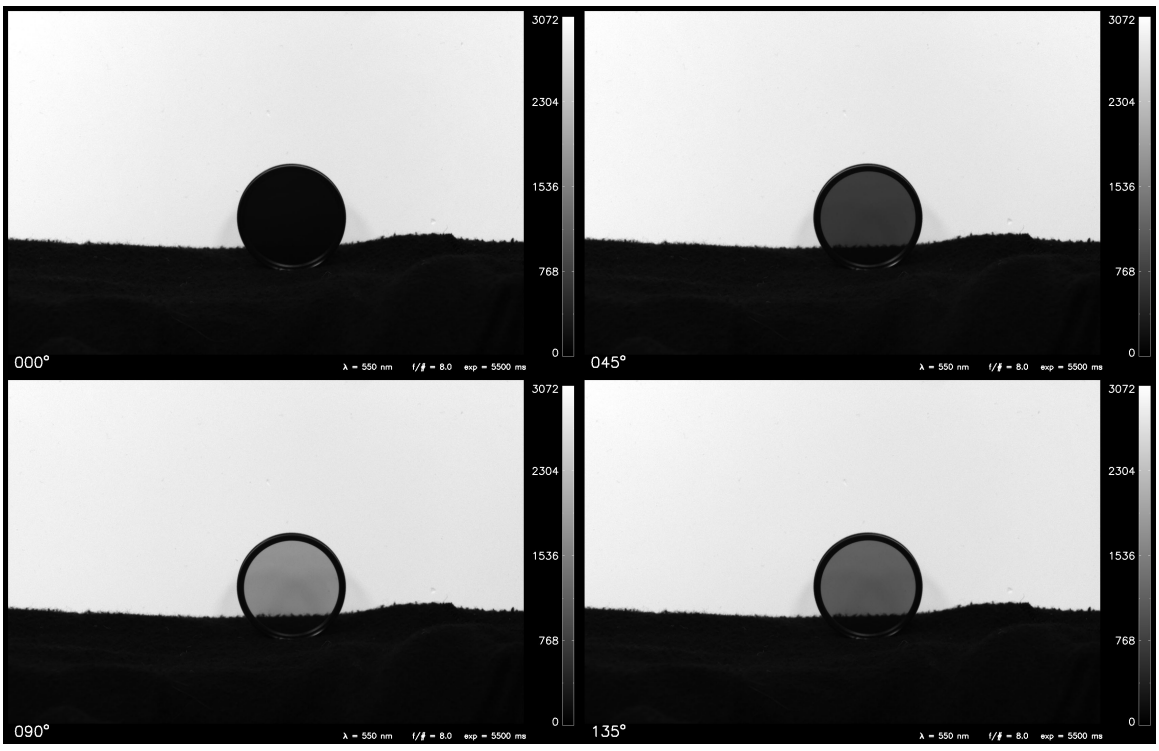

Figure 5.10: The raw images acquired of the linear polarization filter against a Spectralon panel. 000° (*top left*), 045° (*top right*), 090° (*bottom left*) and 135° (*bottom right*).

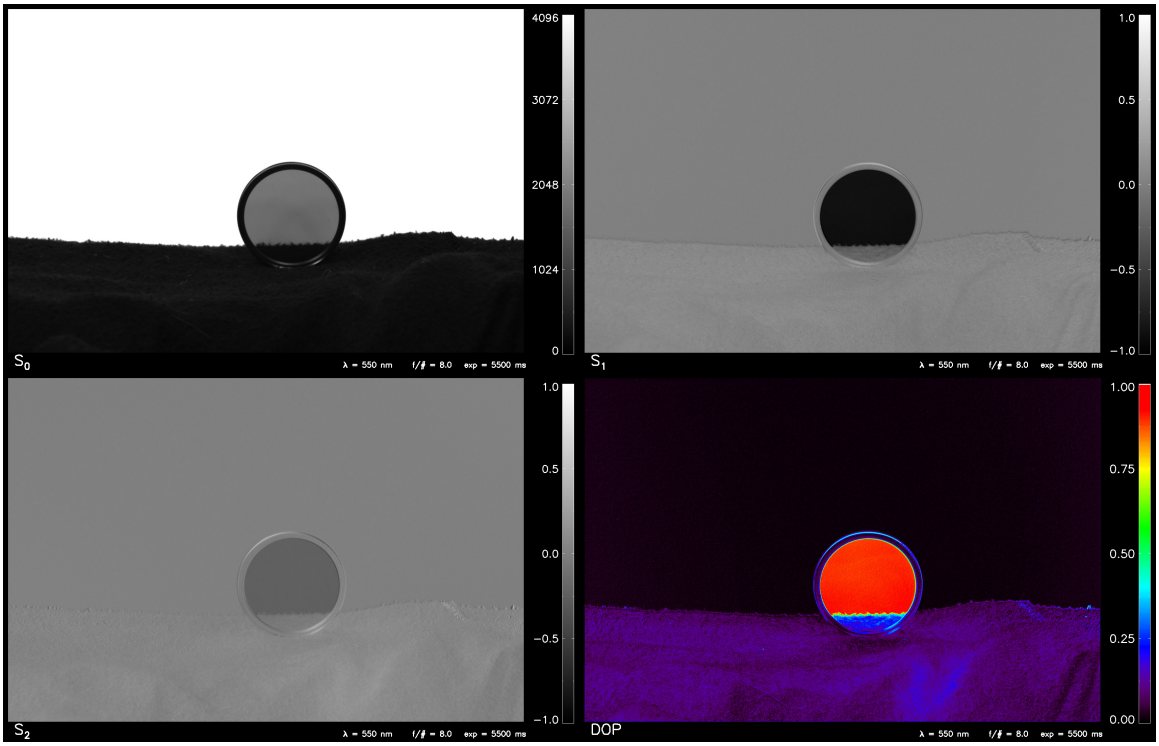

Figure 5.11: The Stokes and DOP images derived from the raw images (Figure 5.10). S_0 (*top left*), S_1 (*top right*), S_2 (*bottom left*) and DOP (*bottom right*).

(Figure 5.11). Perhaps the first thing to note is that the DOP for the filter is determined as ~ 0.9, not ~ 1.0 as expected. However, it must be remembered that front-surface reflections off the polarization filter are also in the image. Given the view angle of the camera to the filter, this front-surface reflectance is highly unpolarized and therefore $DOP \approx 0.9$ for the filter region is acceptable.

Second, it is noted that the Spectralon polarization signature appears negligible when viewed over the dynamic range of $0.0 \leq DOP \leq 1.0$ in Figure 5.11. This result is satisfying. Next, the black terry cloth cover is considered, where an appreciable amount of polarization is noted (≈ 0.15). This is not surprising given how absorbing or dark the material is (*i.e.*, Umov's effect). Finally, the terry cloth behind the filter is seen to have a $DOP \approx 0.25$. As with the Spectralon seen through the filter, one would expect $DOP \approx 1.0$, but now the relative magnitude of the front surface reflectance is quite appreciable relative to the signal transmitted through the polarization filter. So this polarization magnitude is reasonable as well.

The DOP data is further scrutinized by examining the DOP magnitude of the polar-

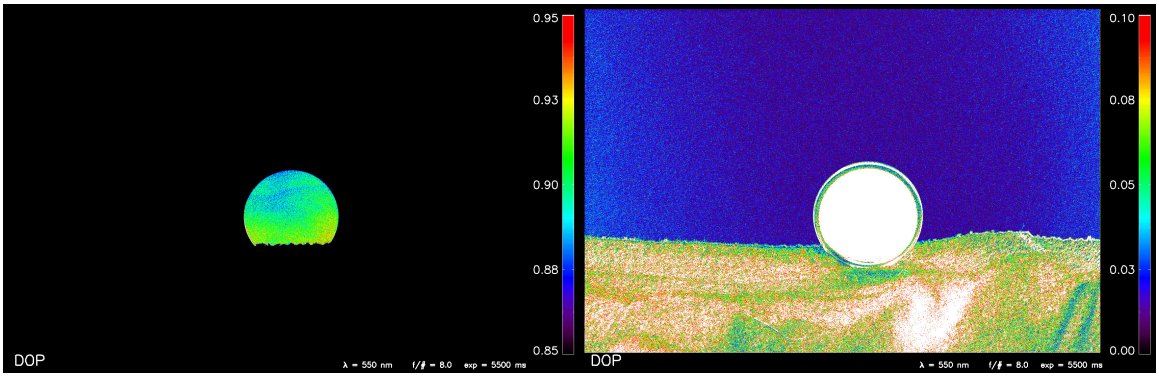

Figure 5.12: The *DOP* image shown in Figure 5.11 for two narrow ranges, 0.85–0.95 (*left*) and 0.0–0.1 (*right*).

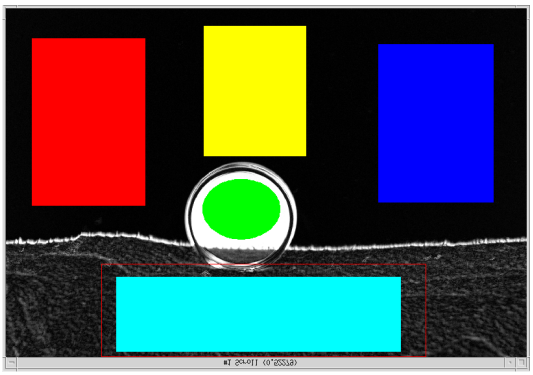

Figure 5.13: Regions over which the average and standard deviation of the *DOP* are taken as given in Table 5.1.

ization filter and Spectralon panel. This is facilitated by narrowing the *DOP* range to $0.85 \leq DOP \leq 0.95$ and $0.0 \leq DOP \leq 0.1$ for the filter and panel, respectively (Figure 5.12). Seen in this manner, the filter is noted to have $DOP \approx 0.90$. The *DOP* variability within the filter area may be attributed to filter alignment errors when acquiring the original images (to be discussed in §5.3.1.2), or to a spatial variation in the front surface reflectance magnitude previously discussed. Examination of the Spectralon panel signature is more troubling—it appears that the *DOP* averages ≈ 0.02; further examination of this result is warranted and will be addressed in §5.3.4.1. Surface imperfections in the panel are also highlighted. A statistical analysis of the *DOP* for various regions is presented in Table 5.1, with the specific regions shown in Figure 5.13.

Finally, the polarization orientation χ is examined. Figure 5.14 presents these results and also provides a focused range around the filter orientation angle. Examination of the

Table 5.1: *DOP* for various regions in the polarization filter image as depicted in Figure 5.13.

Region	**# pixels**	*DOP*
Filter (green)	32,000	0.8987 ± 0.0120
Black cloth (cyan)	184,000	0.1045 ± 0.0340
Spectralon (left, red)	165,000	0.0172 ± 0.0086
Spectralon (middle, yellow)	115,000	0.0136 ± 0.0071
Spectralon (right, blue)	159,000	0.0187 ± 0.0088

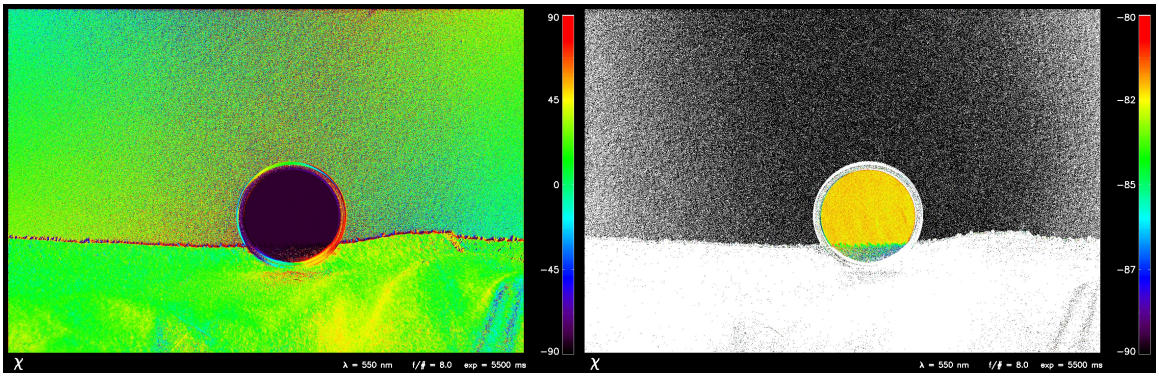

Figure 5.14: Polarization orientation (χ) images covering the full range of $-90 \leq \chi \leq 90°$ (*left*) and a narrow range of $-90 \leq \chi \leq -80°$ (*right*).

filter region shows $\chi = -82.229 \pm 0.305°$. (No care was taken to position the filter to be imaged in any particular polarization orientation). This almost insignificant variability may be attributed to the small FOV change across the area of the filter ($\approx 3°$).

One additional data set is presented for a "Magic 8-ball" (Figure 5.15). The ball is well-suited for an imaging test since it has a highly smooth, specular surface, including regions of black and white which have very low and very high diffuse (randomly polarized) scatter. In addition, the curvature of the ball provides multiple specular view angles. The *DOP* image provides a pleasing result—reflectance from the Spectralon panel off the edges of the ball provide a *DOP* commensurate with that expected from Fresnel reflectance, with a peak magnitude reached near Brewster's angle. The abrupt decrease in the *DOP* going toward the center of the ball occurs at the transition where the specular reflectance is from the relatively dark wall, rather than the Spectralon. This results in a larger fraction of the total radiance coming from other illumination sources, which was a lower *DOP*.

Perhaps the most interesting result from the "8-ball" image is the polarization orientation or χ information. As anticipated, the polarization orientation from the dark regions is parallel or *s*-polarized relative to the spherical surface (Figure 5.16). However, there is a reversal of 90° over the white region of the 8-ball; with the exception of the white region

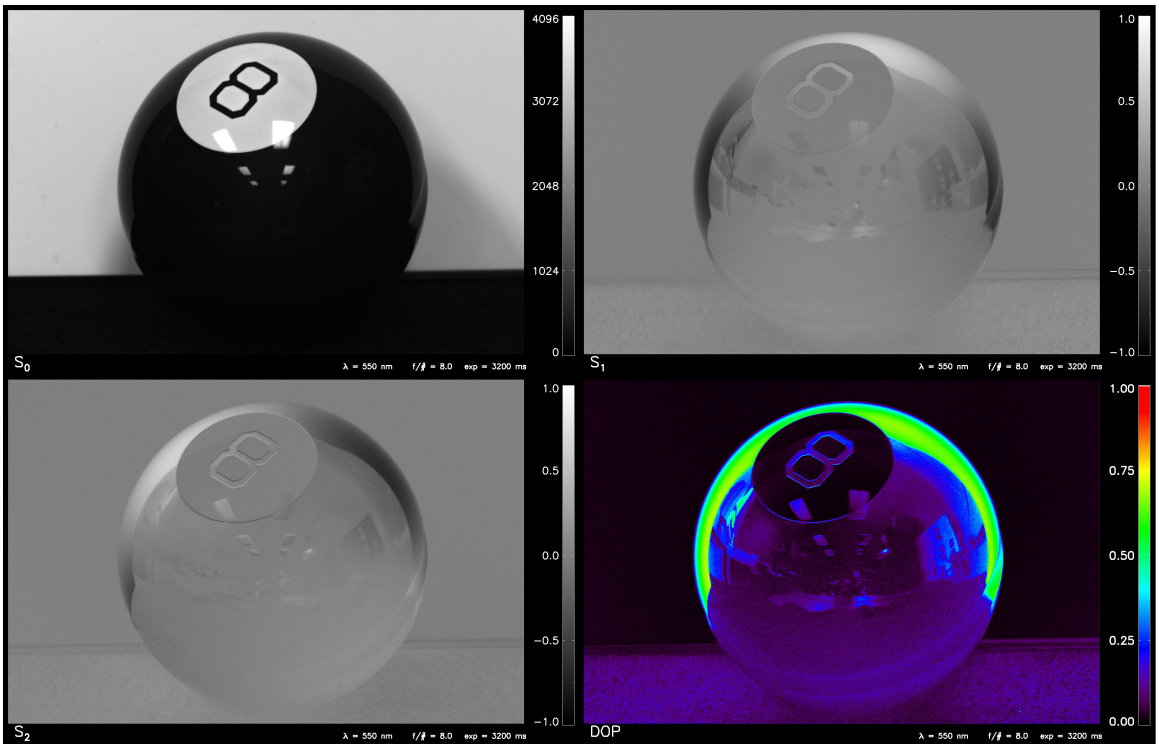

Figure 5.15: The Stokes and DOP images of a "Magic 8-ball". S_0 (*top left*), S_1 (*top right*), S_2 (*bottom left*) and DOP (*bottom right*).

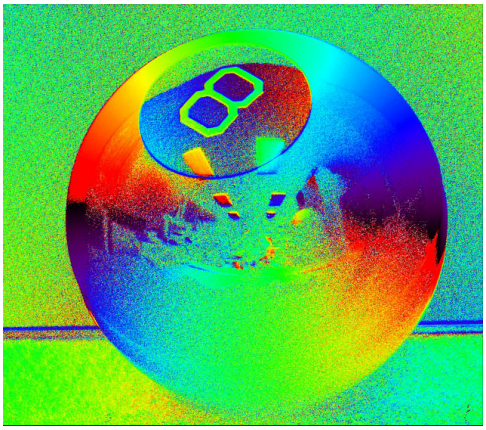

Figure 5.16: The polarization angle information from "8-ball" image. Green corresponds to $\chi = 0°$ while the red-black transition is the transition point from $\chi = 90°$ to $-90°$.

toward the outer edge of the ball, which has a high specular reflection from the Spectralon panel. It is hypothesized that this polarization angle reversal is from volumetric scatter which is p-polarized via Fresnel transmittance back through the surface.

5.3 Measurement Error Analysis

Experimental results only have significance if the uncertainties associated with them are known. There are several error sources in polarimetric imaging, some of which are unique to this specific technique. The error sources from using this imaging system configuration are discussed in this section. The uncertainty may be divided into those which are attributed to *i*) polarization filters, *ii*) spatial registration accuracy, *iii*) the time difference in acquiring successive images, *iv*) the radiance calibration process, *v*) inherent errors from the imaging system and finally *vi*) angular positioning errors.

The distinction between precision and accuracy is important. Precision refers to the ability of the measurement system to make repeatable measurements, while accuracy refers to the ability of the system to match known truth values [4, §4.6.2]. A variety of error terms are defined and quantified, culminating with the propagation of these uncertainties to the values of interest using the appropriate governing equations in §5.3.7.

5.3.1 Polarization Filter-Related Errors

There are three primary errors introduced from the polarization filters. Two are from the alignment of the filters, while the last is from the finite filter contrast or extinction ratio.

The first alignment error is the filter orientation position relative to the local horizon, or the reference frame for determining the polarization orientation χ. This is referred to as "reference frame" error since χ and hence the Stokes vectors are defined relative to the horizon in the scene being imaged. Any filter misalignment about the optical axis relative to the reference frame introduces error. The second and more critical alignment error is the accuracy with which the filter positions are set to their prescribed orientations of 0°, 45°, 90° and 135°.

5.3.1.1 Reference Frame Error

The reference frame error is systematic and fully correctible via a simple rotation operation. This error is termed ϵ_{rot}. Reference frame errors *do not impact the measured DOP* and are therefore not deemed as critical. The impact of a poor χ determination results in an error in the relative ratios of the S_1 and S_2 Stokes components. The Stokes vector determined from the camera measurements at a θ_{hor} orientation relative to the absolute reference frame may be corrected for the misalignment by application of the Stokes vector rotation matrix (equation 2.36) by an amount equal to $-\theta_{hor}$.

The challenge is determination of θ_{hor} for each repositioning of the camera. Alignment of the camera to the horizon is made by use of a "bubble" level located on the tripod mount. The accuracy of this alignment is estimated to be within ±5° based upon imaging experiments of a water surface having a known polarization orientation. However, there is an additional degree of freedom from positioning the polarization filter within the rotation mount. Alignment of the polarization filter within the mount was performed manually by visual observations made by rotating the filter while viewing a polarized source—the filter did not have the polarization direction marked. This manual alignment is estimated to have only been performed to within ±10°.

The net result is that the χ orientation may be determined directly from the polarization phenomenology with a much greater accuracy than is possible from the uncertainties present in the experimental set-up. This is possible by treating the polarization as that which results solely from front surface microfacet scatter, which is further discussed in Chapter 8. This results in a loss of the ability to capture subtle polarization phenomenology from polarized volumetric scattering contributions. Capturing these subtle effects is estimated to require an absolute alignment error of less than a few degrees.

5.3.1.2 Filter Positioning Error

Errors resulting from the relative filter alignment accuracy between the four images is rather complex. This error is applicable to many polarimetric imaging systems, including those having multiple, co-aligned cameras, and one would think that a similar uncertainty analysis would be in the literature. However, no such analysis was found and therefore a detailed analysis was completed.

First, the linear polarization components of the Mueller matrix for the transmittance through an ideal linear polarizer positioned at orientation θ is recalled from equation 2.41 as

$$\mathbf{T}_\theta = \frac{1}{2}\begin{bmatrix} 1 & \cos 2\theta & \sin 2\theta \\ \cos 2\theta & \cos^2 2\theta & \sin 2\theta \cos 2\theta \\ \sin 2\theta & \sin 2\theta \cos 2\theta & \sin^2 2\theta \end{bmatrix} . \tag{5.7}$$

It has also been shown (equation 5.5) that the incident Stokes vector may be measured by the following combination of images,

$$\begin{bmatrix} S_0 \\ S_1 \\ S_2 \end{bmatrix} = \begin{bmatrix} \frac{I_0+I_{90}+I_{45}+I_{135}}{2} \\ I_0 - I_{90} \\ I_{45} - I_{135} \end{bmatrix} . \tag{5.8}$$

In explicit terms of the incident Stokes vector, $\vec{S}_{in}$, and linear polarization filters, (5.8) may be expressed as

$$\begin{bmatrix} S_0 \\ S_1 \\ S_2 \end{bmatrix} = \begin{bmatrix} \frac{T_0+T_{90}+T_{45}+T_{135}}{2}\vec{S}_{in} \\ (T_0 - T_{90})\vec{S}_{in} \\ (T_{45} - T_{135})\vec{S}_{in} \end{bmatrix} . \tag{5.9}$$

A filter alignment error, ϵ, having a zero mean and normally distributed will be considered in conjunction with the combination of images necessary to produce a Stokes vector. It is necessary to consider four independent alignment errors, one associated with each filter positioning. The individual error terms will be annotated as ϵ_{xx} where xx° is the angle associated with that particular filter position.

5.3.1.2.1 S_1 and S_2 components The "action" of the filters in (5.9) upon $\vec{S}_{in}$ is considered. The action is simply to provide the right linear combination such that the Stokes vector component desired to be measured is "brought up to" the S_0 component on the output, in order to be sensed by a detector. For instance, the S_1 component in terms of the

filters in (5.9) (without considering error) is

$$S_1 = \frac{1}{2}\left\{\begin{bmatrix} 1 & 1 & 0 \\ 1 & 1 & 0 \\ 0 & 0 & 0 \end{bmatrix} - \begin{bmatrix} 1 & -1 & 0 \\ -1 & 1 & 0 \\ 0 & 0 & 0 \end{bmatrix}\right\}\begin{bmatrix} S_{0_{in}} \\ S_{1_{in}} \\ S_{2_{in}} \end{bmatrix} \tag{5.10}$$

$$= \begin{bmatrix} 0 & 1 & 0 \\ 1 & 0 & 0 \\ 0 & 0 & 0 \end{bmatrix}\begin{bmatrix} S_{0_{in}} \\ S_{1_{in}} \\ S_{2_{in}} \end{bmatrix} = \begin{bmatrix} S_{1_{in}} \\ S_{0_{in}} \\ 0 \end{bmatrix} . \tag{5.11}$$

Not shown in (5.10) is the fact that the detection process only measures the S_0 component of whatever radiance is incident, which is equivalent to a "detection" Mueller matrix of all zeros with the exception of the 00 matrix element. Seen in this manner, it is noted that determination of the $\vec{S}_{in}$ components only depends upon the first row of the $T_{\mathtt{xx}}$ matrices, or those that are responsible for the magnitude of the resultant S_0.

Expressions for the measured S_1 and S_2 components in (5.9) are now given in terms of the top row of the appropriate $T_{\mathtt{xx}}$ matrix combinations. From (5.7) and (5.9) it may be shown that

$$S_1 = \frac{1}{2}\left\{S_{1_{in}}\left[\cos(0+2\epsilon_0) - \cos(\pi+2\epsilon_{90})\right] + S_{2_{in}}\left[\sin(0+2\epsilon_0) - \sin(\pi+2\epsilon_{90})\right]\right\} \tag{5.12}$$

and

$$S_2 = \frac{1}{2}\left\{S_{1_{in}}\left[\cos\left(\frac{\pi}{2}+2\epsilon_{45}\right) - \cos\left(\frac{3\pi}{2}+2\epsilon_{135}\right)\right]\right\} + \frac{1}{2}\left\{S_{2_{in}}\left[\sin\left(\frac{\pi}{2}+2\epsilon_{45}\right) - \sin\left(\frac{3\pi}{2}+2\epsilon_{135}\right)\right]\right\} \tag{5.13}$$

where the measured S_1 and S_2 components are

$$S_1 = S_{1_{in}} + \epsilon_{1_{tot}} \tag{5.14}$$

$$S_2 = S_{2_{in}} + \epsilon_{2_{tot}} . \tag{5.15}$$

Equations (5.12–5.13) may be simplified via trig identities by noting that

$$\cos(0+\alpha) - \cos(\pi+\beta) = \cos(\alpha) + \cos(\beta) \tag{5.16}$$

$$\sin(0+\alpha) - \sin(\pi+\beta) = \sin(\alpha) + \sin(\beta) . \tag{5.17}$$

By use of (5.16, 5.17), the measured S_1 and S_2 values of (5.12, 5.13) are simplified to

$$S_1 = S_{1_{in}} + \epsilon_{1_{tot}} = \frac{1}{2}\Big\{S_{1_{in}}\left[\cos(2\epsilon_0) + \cos(2\epsilon_{90})\right] + S_{2_{in}}\left[\sin(2\epsilon_0) + \sin(2\epsilon_{90})\right]\Big\} \tag{5.18}$$

$$S_2 = S_{2_{in}} \pm \epsilon_{2_{tot}} = \frac{1}{2}\Big\{S_{2_{in}}\left[\cos(2\epsilon_{45}) + \cos(2\epsilon_{135})\right] - S_{1_{in}}\left[\sin(2\epsilon_{45}) + \sin(2\epsilon_{135})\right]\Big\} \ . \tag{5.19}$$

So qualitatively, inspection of (5.18) and (5.19) show that the error in the measured Stokes vectors are proportional to the magnitude of that particular Stokes component, which is reduced by the cosine of the alignment errors in the two filters. The alternate Stokes component, or that not being measured, is added as an error term, with the magnitude dependent upon the individual signs of the alignment errors. The sensitivity of the S_1 and S_2 errors to the alignment errors is highly linear for small amounts of error. This may be seen by noting that for small values of ϵ, $\sin(\epsilon) \approx \epsilon$ and $\cos(\epsilon) \approx 1 - \epsilon$.

This result is intuitively satisfying, but extracting more meaning and understanding is challenging since the errors are expressed in terms of S_1 and S_2. For instance, $S_{1_{in}}$ and $S_{2_{in}}$ are constrained with respect to one another by the fact that the degree of polarization (DOP) is less than or equal to one, or for a normalized Stokes vector, $DOP = \sqrt{S_{1_{in}}^2 + S_{2_{in}}^2} \leq 1$. An alternate representation of the error may be made in terms of the degree of polarization (*i.e.*, the $S_{1_{in}}$ and $S_{2_{in}}$ magnitudes) and the polarization orientation, χ (*i.e.*, the relative magnitudes of the incident Stokes components). Expressions for $S_{1_{in}}$ and $S_{2_{in}}$ must first be developed as functions of χ and DOP.

The polarization orientation and the degree of polarization are given by

$$\chi = \frac{1}{2}\tan^{-1}\left[\frac{S_2}{S_1}\right] \qquad\qquad DOP = \sqrt{S_1^2 + S_2^2}\ , \tag{5.20}$$

from which S_1 and S_2 may be expressed in terms of χ and DOP as

$$S_1 = \left(\frac{DOP^2}{1 + \tan^2(2\chi)}\right)^{\frac{1}{2}} \qquad \begin{cases} + & \text{if } -\frac{\pi}{4} \leq \chi \leq \frac{\pi}{4}, \\ - & \text{if } -\frac{\pi}{2} \leq \chi < -\frac{\pi}{4} \text{ or } \frac{\pi}{4} < \chi \leq \frac{\pi}{2} \end{cases} \tag{5.21}$$

$$S_2 = \left(\frac{DOP^2\tan^2(2\chi)}{1 + \tan^2(2\chi)}\right)^{\frac{1}{2}} \qquad \begin{cases} + & \text{if } 0 \leq \chi \leq \frac{\pi}{2}, \\ - & \text{if } -\frac{\pi}{2} \leq \chi < 0\ . \end{cases} \tag{5.22}$$

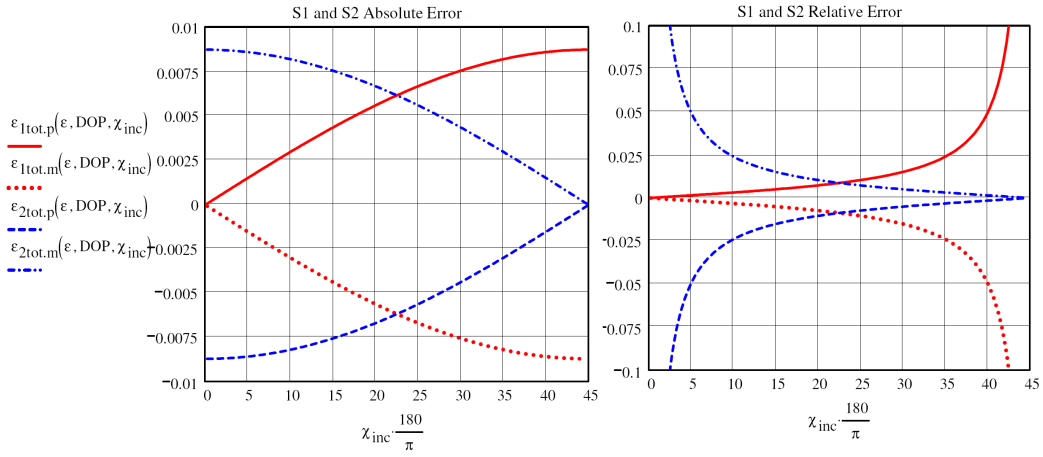

Figure 5.17: The absolute (*left*) and relative (*right*) or percent error in the S_1 (red) and S_2 (blue) Stokes components as a function of χ for $\epsilon_{xx} = \pm 0.25°$.

Substituting these Stokes component expressions into (5.18–5.19) results in

$$S_1 = \frac{1}{2}\left\{\left(\frac{DOP^2}{1+\tan^2(2\chi)}\right)^{\frac{1}{2}}\left[\cos(2\epsilon_0)+\cos(2\epsilon_{90})\right]\right\}+ \frac{1}{2}\left\{\left(\frac{DOP^2\tan^2(2\chi)}{1+\tan^2(2\chi)}\right)^{\frac{1}{2}}\left[\sin(2\epsilon_0)+\sin(2\epsilon_{90})\right]\right\} \quad (5.23)$$

and

$$S_2 = \frac{1}{2}\left\{\left(\frac{DOP^2\tan^2(2\chi)}{1+\tan^2(2\chi)}\right)^{\frac{1}{2}}\left[\cos(2\epsilon_{45})+\cos(2\epsilon_{135})\right]\right\}- \frac{1}{2}\left\{\left(\frac{DOP^2}{1+\tan^2(2\chi)}\right)^{\frac{1}{2}}\left[\sin(2\epsilon_{45})+\sin(2\epsilon_{135})\right]\right\}. \quad (5.24)$$

The S_1 and S_2 errors may now be investigated as functions of DOP and χ. Examination of (5.23–5.24) reveals that the magnitude of both Stokes component errors increase linearly with DOP for a given χ. This results in the relative Stokes component error (*i.e.*, percent error) being constant as a function of DOP. The errors as a function of χ are more interesting. The absolute and relative errors as a function of χ for $DOP = 1$ are shown in Figure 5.17. Having obtained the equations for the S_1 and S_2 error, it is now necessary to consider the error in the total radiance or S_0 components.

5.3.1.2.2 S_0 **component** It has been proposed to measure S_0 by averaging two orthogonal linear polarization states, as seen in (5.9). Recalling that only the top row of the transmittance matrix (5.7) must be considered, the addition of the two sets of orthogonal filters results in values for S_0 given by

$$S_0^{(0+90)} = S_{0_{in}} + \frac{S_{1_{in}}}{2}\left[\cos(0+2\epsilon_0) + \cos(\pi + 2\epsilon_{90})\right] + \frac{S_{2_{in}}}{2}\left[\sin(0+2\epsilon_0) + \sin(\pi+2\epsilon_{90})\right] \quad (5.25)$$

and

$$S_0^{(45+135)} = S_{0_{in}} + \frac{S_{1_{in}}}{2}\left[\cos\left(\frac{3\pi}{2}+2\epsilon_{45}\right) + \cos\left(\frac{\pi}{2}+2\epsilon_{135}\right)\right] + \frac{S_{2_{in}}}{2}\left[\sin\left(\frac{3\pi}{2}+2\epsilon_{45}\right) + \sin\left(\frac{\pi}{2}+2\epsilon_{135}\right)\right] \quad (5.26)$$

where ϵ_{xx} is the zero mean, normally distributed error in the alignment of the filter at xx°.

Using trigonometric identities as before, (5.25) and (5.26) may be simplified to

$$S_0^{(0+90)} = S_{0_{in}} + \frac{S_{1_{in}}}{2}\left[\cos(2\epsilon_0) - \cos(2\epsilon_{90})\right] + \frac{S_{2_{in}}}{2}\left[\sin(2\epsilon_0) - \sin(2\epsilon_{90})\right] \quad (5.27)$$

$$S_0^{(45+135)} = S_{0_{in}} + \frac{S_{1_{in}}}{2}\left[\sin(2\epsilon_{135}) - \sin(2\epsilon_{45})\right] + \frac{S_{2_{in}}}{2}\left[\cos(2\epsilon_{45}) - \cos(2\epsilon_{135})\right]\ . \quad (5.28)$$

Inspection of (5.27) and (5.28) demonstrate some anticipated results. When all the error terms are zero, S_0 is determined with zero error. Furthermore, when the same amount of error is present in a set of measurements, no matter how large, S_0 is determined with zero error (via the even and odd properties of the cosine and sine). This is satisfying since the same amount of error in each of the two filters still results in orientations orthogonal to one another. Furthermore, as the magnitude of the linear Stokes components goes to zero, the error in S_0 goes to zero; this relationship is also intuitive since with random polarization, changing the filter orientation has no effect on the transmitted radiance.

Noting that the final determination of S_0 is by averaging (5.27) and (5.28), the resulting measurement of S_0 is

$$S_0 = S_{0_{in}} + \frac{S_{1_{in}}}{4}\Big\{\left[\cos(2\epsilon_0) - \cos(2\epsilon_{90})\right] + \left[\sin(2\epsilon_{135}) - \sin(2\epsilon_{45})\right]\Big\} + \frac{S_{2_{in}}}{4}\Big\{\left[\cos(2\epsilon_{45}) - \cos(2\epsilon_{135})\right] + \left[\sin(2\epsilon_0) - \sin(2\epsilon_{90})\right]\Big\}\ . \quad (5.29)$$

To better understand the resulting error, numerical simulations of equations 5.18–5.19

Table 5.2: Errors resulting in the measured Stokes vector, DOP and χ for a filter alignment error of $\epsilon_{xx} = 0 \pm 0.25°$ for three incident polarization angles: $\chi = 0$, $\frac{\pi}{8}$ and $\frac{\pi}{4}$. The data is generated numerically from 10^6 simulations. Histograms of the $\chi = 0$ case are shown in Figure 5.18.

χ	**Quantity**	**Truth**	**Mean**	$\pm 2\sigma$
0	S_0	1.00000	1.00000	+0.00616, -0.00617
	S_1	1.00000	0.99996	+0.00004, -0.00012
	S_2	0.00000	0.00001	+0.01236, -0.01235
	DOP	1.00000	0.99999	+0.00620, -0.00615
	χ	0.00000	0.00014°	+0.35344°, -0.35344°
$\frac{\pi}{8}$	S_0	1.00000	1.00000	+0.00616, -0.00617
	S_1	0.70711	0.70708	+0.00870, -0.00876
	S_2	0.70711	0.70708	+0.00868, -0.00876
	DOP	1.00000	0.99998	+0.01068, -0.01065
	χ	22.50000°	22.49990°	+0.25030°, -0.24990°
$\frac{\pi}{4}$	S_0	1.00000	1.00000	+0.00616, -0.00617
	S_1	0.00000	-0.00001	+0.01234, -0.01233
	S_2	1.00000	0.99996	+0.00004, -0.00613
	DOP	1.00000	0.99999	+0.00620, -0.00613
	χ	45.00000°	45.00026°	+0.35315°, -0.35340°

and 5.29 were implemented to determine the measured Stokes vector given $\vec{S}_{in}$ and $\epsilon_{xx} = 0 \pm 0.25°$. Since the error is perhaps best understood in terms of χ, three different values of χ were used: 0, $\frac{\pi}{8}$ and $\frac{\pi}{4}$; $DOP = 1.0$ was used in all instances (recall the error scales directly with DOP). Symmetry of the Stokes components makes the domain of $0 \leq \chi \leq \frac{\pi}{4}$ adequate. Table 5.2 provides the mean and $\pm 2\sigma$ values resulting from the simulation using 10^6 measurements. Histograms of the data for $\chi = 0°$ are presented in Figure 5.18. This filter positioning error will be referred to as the ϵ_{fil} contribution.

5.3.1.3 Finite Filter Contrast Error

All linear polarization filters allow some transmission of the polarization state they are intended to block. The result is that some of the orthogonal polarization state is added to the measurement. The derivation of this error begins by again considering the equation for an ideal linear polarization filter, (5.7).

The result of the cross-polarization transmittance, $\tau_{\otimes}$, is to have a $\mathbf{T}_{\theta+\frac{\pi}{2}}$ contribution of $\tau_{\otimes}$ magnitude to the $\mathbf{T}_{\theta}$ measurement. Considering only the first row of the $\mathbf{T}_{\theta}$ matrix, the effective $\mathbf{T}_{\theta}$ with cross-polarization leakage ($\mathbf{T}_{\theta}^{\tau_{\otimes}}$) is

$$\mathbf{T}_{\theta}^{\tau_{\otimes}} = \frac{1}{2}\left[\begin{array}{cc} 1+\tau_{\otimes} & \cos(2\theta)+\tau_{\otimes}\cos(2[\theta+\frac{\pi}{2}]) \quad \sin(2\theta)+\tau_{\otimes}\sin(2[\theta+\frac{\pi}{2}]) \end{array}\right] \tag{5.30}$$

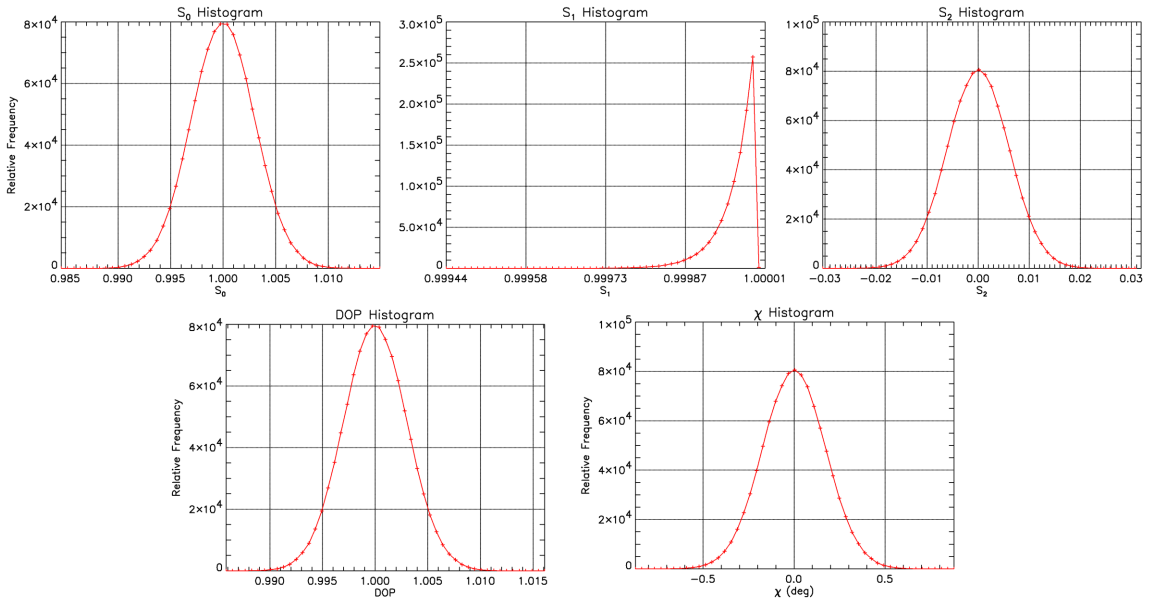

Figure 5.18: Histograms of the measured Stokes vector (*top*) and *DOP* and χ (*bottom left* and *right*) given an incident Stokes vector of [1.0 1.0 0.0] with the estimated filter alignment error of $\epsilon_{xx} = 0 \pm 0.25°$. 10^6 iterations numerically simulated equations 5.18, 5.19 and 5.29.

which is simplified to

$$\mathbf{T}_\theta^{\tau_\otimes} = \frac{1}{2}\begin{bmatrix} 1+\tau_\otimes & (1-\tau_\otimes)\cos(2\theta) & (1-\tau_\otimes)\sin(2\theta) \end{bmatrix} . \tag{5.31}$$

The result of (5.31) on the incident Stokes vector, $\vec{S}_{in}$ is therefore

$$\mathbf{T}_\theta^{\tau_\otimes}\vec{S}_{in} = \frac{1}{2}\begin{bmatrix} (1+\tau_\otimes)S_{0_{in}} & (1-\tau_\otimes)\cos(2\theta)S_{1_{in}} & (1-\tau_\otimes)\sin(2\theta)S_{2_{in}} \end{bmatrix} . \tag{5.32}$$

The effect on the measured Stokes vectors is obtained by considering the right linear combination of $\mathbf{T}_\theta^{\tau_\otimes}$ matrices to obtain the Stokes components (*i.e.*, (5.9)).

$$\begin{aligned} S_1 &= (\mathbf{T}_0^{\tau_\otimes} - \mathbf{T}_{90}^{\tau_\otimes})\vec{S}_{in} \\ &= \frac{1}{2}\Big\{0S_{0_{in}} + (1-\tau_\otimes)S_{1_{in}}[\cos(0)-\cos(180)] + (1-\tau_\otimes)S_{2_{in}}[\sin(0)-\sin(180)]\Big\} \\ &= (1-\tau_\otimes)S_{1_{in}} \end{aligned} \tag{5.33}$$

and similarly for S_2

$$\begin{aligned} S_2 &= (\mathbf{T}_{45}^{\tau_\otimes} - \mathbf{T}_{135}^{\tau_\otimes})\vec{S}_{in} \\ &= (1-\tau_\otimes)S_{2_{in}} \ . \end{aligned} \tag{5.34}$$

One could have likely guessed at these results. The magnitude of the measured linear Stokes components is reduced by the amount of cross-polarization leakage.

Now the effects of cross-polarization leakage on the determination of S_0 is assessed. Via a similar process as that above, the measured S_0 component is overestimated by the amount of $\tau_\otimes$,

$$S_0 = (1+\tau_\otimes)S_{0_{in}} \ . \tag{5.35}$$

However, when the calibration target is imaged, the same bias is also present. Upon division of the measurement surface images by the calibration target signature to convert the digital counts into units of [$\mathtt{sr}^{-1}$], this error self-corrects (see equation 5.5).

Finally, the effects upon χ and DOP are considered. Since the measured S_1 and S_2 components are reduced by the same amounts, there is no net effect upon the χ determination. However, the leakage errors in the Stokes components do impact the DOP. This is seen by

$$\begin{aligned} DOP &= \frac{\sqrt{[(1-\tau_\otimes)S_{1in}]^2 + [(1-\tau_\otimes)S_{2in}]^2}}{(1+\tau_\otimes)S_{0_{in}}} \\ &= \frac{\sqrt{(1-\tau_\otimes)^2(S_{1in}^2 + S_{2in}^2)}}{(1+\tau_\otimes)S_{0_{in}}} \\ &= \left(\frac{1-\tau_\otimes}{1+\tau_\otimes}\right) DOP_{in} \ . \end{aligned} \tag{5.36}$$

So what is the net impact for the measurement system in question? Per the polarization filter manufacturer $\tau_\otimes$ at 550 $\mathtt{nm}$ is estimated to be 0.015. Reliable data is not available at 750 $\mathtt{nm}$, where the filter performance starts to degrade. An experiment was therefore devised which provides an estimate of $\tau_\otimes$ at 750 $\mathtt{nm}$.

A sauce pan with a dark interior was filled with water and placed in front of a Spectralon panel. The Spectralon panel was illuminated with a quartz halogen lamp, and the water surface imaged at an angle such that a high reflectance was obtained from the Spectralon in the background. With this scenario, all of the radiance from the water surface has its origin from the randomly polarized reflectance off the Spectralon panel. The only additional radiance contributions could be from internal reflections off the sauce pan interior. However,

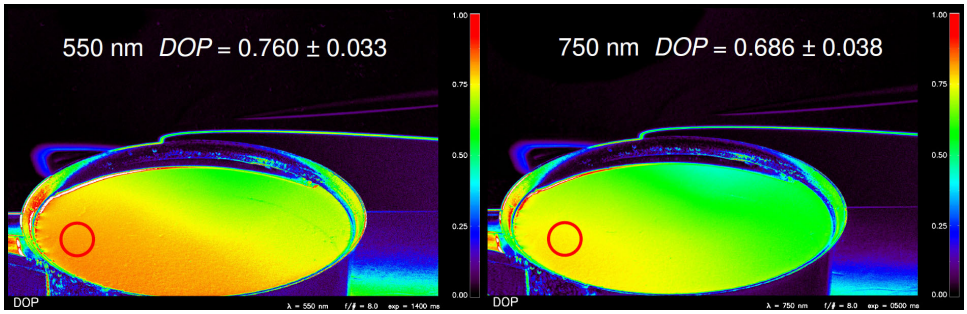

Figure 5.19: The *DOP* measurement of water made at 550 nm (*left*) and 750 nm (*right*). The common region measured between the two images is shown by the red circle.

these are estimated to be minimal, as the surface is black and the intensity of the Spectralon panel illumination was significant compared to any illumination upon the pan interior.

The refractive index of water is nearly constant between 550 and 750 nm, with the real part approximately 1.334 at 550 nm and 1.329 at 750 nm [183, p. 33]. This results in the water surface having a *DOP* which is identical at 550 and 750 nm. Using this as the truth data, the *DOP* at 550 nm is compared to that at 750 nm. From the *DOP* data, common regions were selected and analyzed. The measured *DOP* at 550 nm was 0.760 ± 0.033 and at 750 nm 0.686 ± 0.038, as shown in Figure 5.19.

Having the measured water DOP (DOP_m), the known $\tau_\otimes$ at 550 nm and the relationship on how $\tau_\otimes$ impacts the true *DOP* (equation 5.37) enables derivation of $\tau_\otimes$ at 750 nm. This is seen by noting that

$$\begin{aligned} DOP_{in} &= \left(\frac{1+\tau_\otimes(550)}{1-\tau_\otimes(550)}\right) DOP_m(550) \\ &= \left(\frac{1+\tau_\otimes(750)}{1-\tau_\otimes(750)}\right) DOP_m(750) \ , \end{aligned} \tag{5.37}$$

from which it is easily shown that

$$\tau_\otimes(750) = \frac{x-1}{x+1} \tag{5.38}$$

where

$$x = \left(\frac{1+\tau_\otimes(550)}{1-\tau_\otimes(550)}\right) \frac{DOP_m(550)}{DOP_m(750)} \ , \tag{5.39}$$

resulting in $\tau_\otimes(750) \approx 0.067$.

Returning to equation 5.37, the net impact on the measured DOP may now be determined. At 550 nm the measured *DOP* is only 0.970 that which is actually incident. At 750

nm, the measured DOP is only 0.874 that of the incident polarization. Since these errors are systematic, they are compensated for when processing the data. The finite filter contrast error is termed the ϵ_τ error.

5.3.2 Spatial Registration Errors

The measured Stokes vector is dependent upon the linear combination of the four polarization images acquired at a single scattering orientation. The accuracy of the pixel-level data is dependent upon the degree to which the eight images of the material surface are spatially registered. Often the Stokes and DOP imagery derived from multiple-aperture polarimetric imaging systems appear to highlight the edges in a scene, which is the result of poor spatial registration. A detailed investigation of these effects would include consideration of the point spread function (PSF) of the optics and the sampling density of the detectors relative to this PSF, or the "Q"-value [184]. However, a much simpler approach will be taken in an effort to quickly bound the magnitude of the spatial registration error. The PSF of the system will be considered to be a perfect RECT function, or an idealized case such that projection of the CCD onto the ground is made up of contiguous samples with no overlap.

The rotation of the polarization filter introduces some spatial misregistration among the sets of four images. The polarization mount has some lateral "play", resulting in a shift of the filter normal relative to the optical axis of the system. The net result is a translation of the images acquired at the different polarization orientations. An algorithm provides a correction to this mis-registration, which is further discussed in §6.1.2. The registration algorithm results in images with a maximum residual mis-registration estimated to be ≤ 1 pixel.

The measurement data provides an inherent means to estimate the residual spatial mis-registration of the images after correction by the spatial registration algorithm. Each set of the orthogonal polarization images should produce the total radiance when summed. That is, $\mathtt{I}_{00} + \mathtt{I}_{90} = \mathtt{I}_{45} + \mathtt{I}_{135}$. A metric will be used, termed the "delta energy" or ΔE which is simply the difference between these two sets of images. The metric is therefore given by

$$\Delta E = (\mathtt{I}_{00} + \mathtt{I}_{90}) - (\mathtt{I}_{45} + \mathtt{I}_{135}) \ . \tag{5.40}$$

Ideally $\Delta E = 0$, and any residual value is the result of *i*) residual spatial mis-registration of the images, *ii*) movement between successive images *iii*) changes in the illumination conditions between successive images or *iv*) noise characteristics of the system.

ΔE images and statistics are generated and analyzed as a function of the GSD convolution size. As GSD increases, ΔE decreases until a lower threshold is reached. This

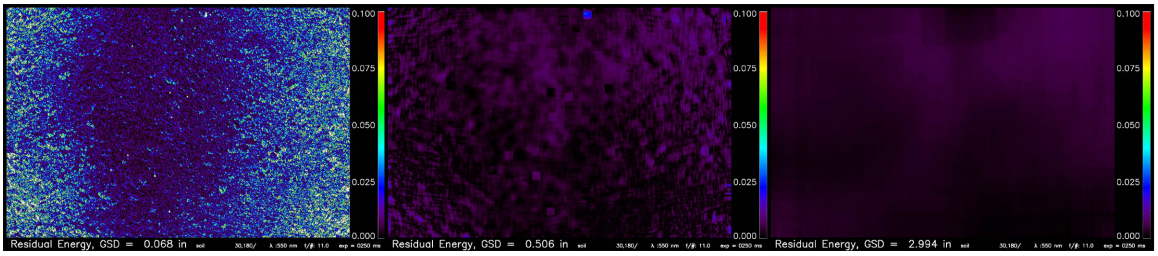

Figure 5.20: The ΔE images are shown from one of the topsoil measurements for $GSD = 0.068, 0.506, 2.994$ `in`, left to right. The magnitude is fixed at 0.1 (10%) for all images and the image wide average ΔE is 0.0165, 0.0036 and 0.0032, respectively. (Data set: 550 `nm`, $\theta_i = 23.3°$, $\theta_r = 30°$ and $\phi = 180°$).

lower threshold provides an estimate of the irradiance change between successive images, another source of error later discussed. The ΔE data are therefore a critical quality metric to consider when analyzing the data. An example of ΔE data is shown in Figure 5.20, which demonstrates the improvement with increasing GSD size.

If there are gross mis-registration errors, then construction of the f_{00} image from the eight independent images produces a blurred image in comparison to the individual raw images. The lowest GSD value for which the variablity data is generated is $GSD = 0.5$ `in`, which for the notional stand-off distance corresponds to ≈ 35 pixels or $X = 35$. Therefore, a mis-registration of 1 pixel represents at most an area coverage difference of $\frac{1}{35}$ or 2.9%. The resulting error magnitude from this area coverage difference is a function of the average relative difference between the pixels which are contained in the base image but not in the misregistered image, and the converse, or the pixels contained in the misregistered image but not the base image. A more realistic maximum error is half the area coverage difference, from which the misregistration error may be approximated as

$$\epsilon_{reg}^{\%} = \frac{0.5}{X} \ , \tag{5.41}$$

where $\epsilon_r^{\%}$ is the percentage error for a given pixel between two successive images which have been convolved with a $X \times X$ pixel-sized convolution kernel.

5.3.3 Sequential Imaging Related Errors

As previously discussed, the imaging system requires twelve images to produce a result for a single camera orientation. Ideally, these images would be made simultaneously, such that the illumination conditions are identical. In practice, it usually takes $\approx$ 2.5 minutes to acquire the eight measurement surface or `C` and `D` images. The calibration panel images are

often acquired at a time different by several minutes from the surface measurement images. All this contributes to error when determining the pBRDF per equation 5.5. This error is collectively referred to as ϵ_t after the *time* difference between the images.

5.3.3.1 Changing Solar Angle, θ_i

The duration required to make the eight measurement surface images or the `C` and `D` images is first considered. The solar motion during this 2–3 minute time period results in a change in the incident irradiance on the material surface, according to $\cos(\theta_i)$. For example, on May 20th in Rochester, New York, the solar incident angle at 3:00 PM (standard time) is $\theta_i = 42.7°$ and changes to $\theta_i = 43.2°$ by 3:03 PM. This represents a worst-case scenario, as an attempt was made to make measurements between ±2 hours relative to the "solar" noon. These incident angles results in the cosine of the incident irradiance being 0.81% higher at 3:00 PM than that at 3:03 PM as seen by

$$\frac{\cos(42.7°) - \cos(43.2°)}{\cos(42.7°)} = 0.00809 \ .$$

The resulting error may be understood by analyzing the hypothetical results from imaging a completely depolarizing Lambertian surface. The measurement process was such that images were acquired in the following order: I_{00}, I_{135}, I_{90} then I_{45}. Presuming the images are equally spaced in time, and treating the 0.81% irradiance change as linear, then the magnitude of the I_{xx} images normalized to the first image may be given by

$$I'_{00} = 1.0000 \qquad I'_{135} = 0.9973 \qquad I'_{90} = 0.9946 \qquad I'_{45} = 0.9919 \ , \tag{5.42}$$

where the $'$ notation is used to indicate the normalized images. The known results of the images should be a $DOP = 0.0$ with the resulting normalized Stokes vector measured as $\begin{bmatrix} 1 \\ 0 \\ 0 \end{bmatrix}$. However, after equation 5.4, the measurement results in

$$\begin{bmatrix} S_0 \\ S_1 \\ S_2 \end{bmatrix} = \begin{bmatrix} \frac{I'_0 + I'_{90} + I'_{45} + I'_{135}}{2} \\ I'_0 - I'_{90} \\ I'_{45} - I'_{135} \end{bmatrix} = \begin{bmatrix} \frac{1.0000 + 0.9946 + 0.9919 + 0.9973}{2} \\ 1.0000 - 0.9946 \\ 0.9919 - 0.9973 \end{bmatrix} \tag{5.43}$$

$$= \begin{bmatrix} 1.9919 \\ 0.0054 \\ -0.0054 \end{bmatrix} . \tag{5.44}$$

This is normalized to $\begin{bmatrix} 1 \\ 0.0027 \\ -0.0027 \end{bmatrix}$, with a resulting $DOP = 0.0038$ and polarization angle of $\chi = -45°$. Prior to solar noon, this error reverses itself resulting in a negative S_1 component and positive S_2 component, with $\chi = -45°$. The net S_0 or total intensity error is 0.4%, or half the irradiance change during the measurement period.

Therefore an estimate of the error from the changing solar position is given as

$$\epsilon_{\theta_i}^{\%} = 0.27\% \ , \tag{5.45}$$

where this error is applied to the S_1 and S_2 Stokes components.

The preceding analysis helps bound the problem, but the resulting error from specular highlights in the image may be greater. For instance, a blade of grass at the right orientation may have a significant specular component from the sun, and the percentage variance in intensity between the images from solar movement would be greater than that from a Lambertian surface. However, these effects manifest themselves in the ΔE imagery as discussed in §5.3.2 and may be considered when analyzing the data.

5.3.3.2 Atmospheric Changes

Just as cosine irradiance effects impact the measurements, changing atmospheric conditions may result in considerable measurement error. The culprit is most often high, thin cirrus clouds, which during the 2–3 minute measurement period may alter the incident solar irradiance. On all but the clearest of days this effect can impact the measurements. Often the change is not visually perceptible, but data analysis can quickly reveal the impact.

Significant irradiance changes are readily apparent in the ΔE imagery. Rather than the ΔE images having high frequency content indicative of spatial mis-registration, a global irradiance change results in a global residual ΔE magnitude. This magnitude does not decrease as the convolution kernel size is increased.

An example of this error is shown during a "mulch" measurement. High cirrus clouds were present, resulting in significant variability in the irradiance during a 2–3 minute measurement window. Although the spatial registration among the eight images is good as demonstrated by a "sharp" f_{00} image created from the eight `C` and `D` images, the ΔE metric asymptotically decreases to a still very high average value of 0.057 with increasing GSD. Figure 5.21 illustrates the effect.

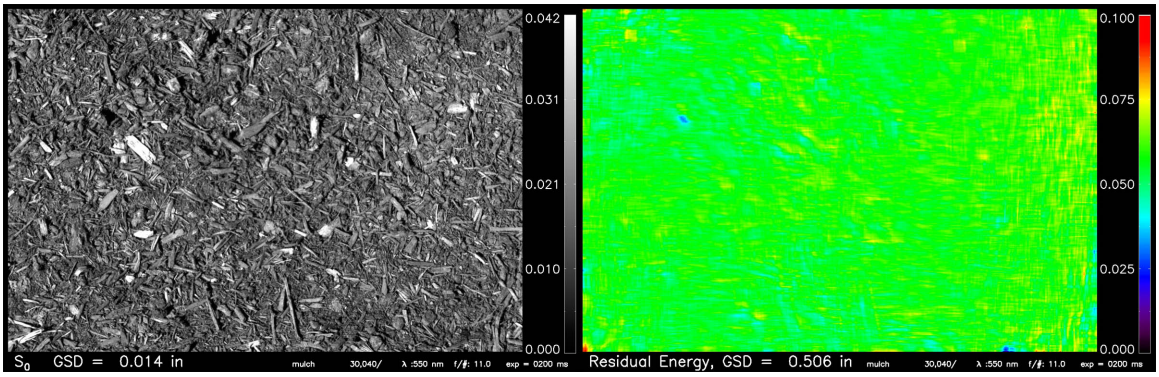

Figure 5.21: Although a high degree of spatial registration was achieved for this "mulch" measurement (*left*), high cirrus clouds resulted in an irradiance change during the measurement sequence as shown from the ΔE data at $GSD = 0.5$ `in` which has a mean of 0.05752. (Data set: 550 `nm`, $\theta_r = 30°$ and $\phi = 40°$).

5.3.4 Radiance Calibration Error

5.3.4.1 Calibration Panel Characterization

Ideally, the calibration panel is completely Lambertian, having a constant BRDF at all illumination and viewing orientations equal to $\frac{\rho}{\pi}$ with $DOP = 0.0$. Pristine Spectralon is very close to this specification for all but highly grazing illumination and viewing angles [179]. However, the panel used for these measurements has been reconditioned to remove surface blemishes via a wet sanding process. It has been reported that such reconditioning of the surface may introduce some degree of specularity into the panel, resulting in a departure from an ideal Lambertian surface. The polarization signature noted in Figure 5.12 provides some evidence of probable specular behavior.

A simple laboratory experiment was constructed to obtain in-plane BRDF estimates of the calibration panel. These are only estimates, as the illumination source did not provide uniform irradiance on the sample. The distance of the source to the measured illuminated region was also relatively small, resulting in varying incident angles across the field of view of the camera. The configuration was such that the mean illumination angle was $\theta_i \approx 50°$ and measurements were made at $\theta_r \approx -35°, 0°$ and $41°$, where the negative angle is a backscattering orientation. The results are shown in Table 5.3 and unfortunately indicate a significant variance in the BRDF and DOP for these three viewing orientations.

This quick experiment warranted further investigation into the panel's behavior and suitability as a calibration standard. This was accomplished by obtaining a second "pristine" calibration panel, which is believed to have never been resurfaced and has been carefully

Table 5.3: The BRDF and DOP measured for $\theta_i = 50°$ for three different θ_r positions. Significant deviation from Lambertian behavior is noted.

θ_r	$S_0 \pm \sigma$ **(DC)**	$DOP \pm \sigma$
$-35°$	5458 ± 256	0.019 ± 0.009
$0°$	5663 ± 332	0.018 ± 0.009
$41°$	6759 ± 329	0.075 ± 0.021

Table 5.4: Comparison between the pristine Spectralon calibration panel to the field panel. The total digital counts (DC) and standard deviation, along with the DOP are examined for a "forward" scattering case where $\phi = 180°$ and a "side" scattering case where $\phi = 90°$. In both instances the data is for 750 nm with $\theta_r = 30°$.

Panel	$DC \pm \sigma$	DOP
$\phi = 180°$		
Pristine	5629 ± 47.0	0.0286
Field	5796 ± 60.8	0.0593
$\phi = 90°$		
Pristine	5484 ± 51.6	0.0283
Field	5235 ± 43.3	0.0326

handled. An outdoor experiment with the panels was completed in order to have uniform, unpolarized, incident irradiance. The panels were placed adjacent to one another and imaged in a "forward" scattering or $\phi = 180°$ and a "side" or $\phi = 90°$ orientation. The resurfaced Spectralon panel is referred to as the "field" panel.

The results of the experiment at 750 nm are shown in Table 5.4. It is interesting to note that the relative total intensity or digital counts between the two panels reverses between the two orientations. The field panel has a higher forward scattering result, which is consistent with the specular nature previously noted. The pristine panel has a signature which is more constant with viewing condition, or as one expects, a more Lambertian behavior. It is further noted that these two orientations were taken only five minutes apart, so cosine irradiance changes are insignificant compared to the DC magnitude change (*cf.* §5.3.3.1).

The total intensity and DOP images for the forward scattering orientation are shown in Figure 5.22. In the DOP image of the field panel, the sanding marks from refinishing the surface are visible. As noted from Table 5.4, the DOP signature of the pristine panel is lower in both orientations and does not exhibit pronounced polarization in the forward scattering orientation. However, even the pristine panel has a much higher than anticipated DOP.

The results of these measurements necessitated the use of a careful protocol to obtain accurate absolute radiance levels when using the field panel. The first requirement is that

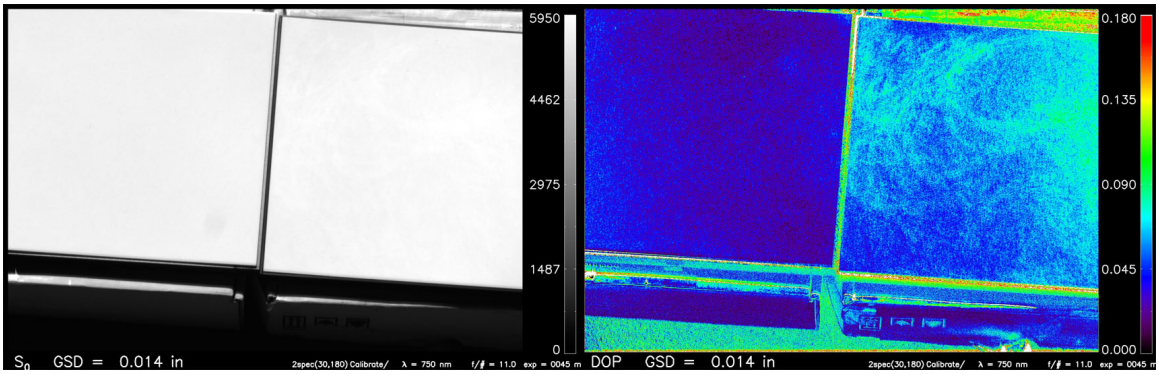

Figure 5.22: The total intensity (DC) and *DOP* images for the "pristine" and "field" calibration panels. Shown is the forward or $\phi = 180°$ scattering orientation at 750 nm. In each image, the pristine panel is on the left, and the field panel on the right.

two orthogonal polarization filter orientations be acquired to determined the total intensity, since the panel polarization would bias the results obtained with a single filter position. This is the origin of the two $\mathtt{A}_\perp, \mathtt{A}_\parallel$ and $\mathtt{B}_\perp, \mathtt{B}_\parallel$ orthogonal calibration images required in equation 5.5. The second requirement is for the calibration images to all be made with the panel in a $\phi = 90°$ position. In this manner, a consistent signature is achieved.

Finally, the magnitude of ρ to use in equation 5.5 is estimated. This is approached by considering the DC of the pristine panel from both orientations, which is an average of $DC = 5556.5$. This magnitude is considered to be the Lambertian signature from the pristine panel, which has $\rho_{DHR} \approx 0.985$ [179]. Having established this correlation between the pristine panel DC and ρ, the effective ρ for the field panel is determined by the ratio of the field panel digital counts in the $\phi = 90°$ orientation compared to the average of the pristine panel, which is known to have $\rho \approx 0.985$. The field panel ρ is therefore estimated as $\rho = \frac{5235}{5556.5}\ 0.985 \approx 0.93$. Therefore a $\rho = 0.93$ is used in equation 5.5 when processing the data.

5.3.4.2 Calibration Panel Measurement Time Difference

Since the calibration panel must be imaged at a $\phi = 90°$ orientation to achieve a consistent radiance magnitude, the camera must be repositioned between the calibration and surface measurement. This repositioning of course takes time, and as previously seen solar movement during this time impacts the measurement accuracy.

In practice, it was found that it was best to provide a time correction to the calibration images. In fact, for stable atmospheric conditions, a calibration image was found to not be required for each measurement orientation. The correction to the digital counts of

the calibration panel (DC) is made by a ratio of the cosines of the incident angle when the calibration panel was imaged ($\theta_{i_{cal}}$) relative to the incident angle of when the surface is imaged ($\theta_{i_{sur}}$). This results in the digital counts which is used for the total radiance calibration, DC_{cal}, given by

$$DC_{cal} = \frac{\cos(\theta_{i_{sur}})}{\cos(\theta_{i_{cal}})}\ DC\ . \tag{5.46}$$

So when a surface measurement uses a calibration made at a time when the sun is higher (θ_i lower), the DC_{cal} is decreased by the appropriate amount, with the converse being true. In this manner, calibration images were used which were taken at a time up to 30 minutes different than that of the measurement surface images.

5.3.4.3 Calibration Panel Measurement Variability

An additional error source not yet discussed is that of the calibration panel positioning; that is, how close to zenith is the normal of the calibration panel? Deviations away from the zenith angle toward the sun result in a higher radiance level, as deviation away from the sun results in a lower radiance level. Placement of the calibration panel on the ground was not accompanied by a panel orientation measurements (*e.g.*, use of a level), and it is estimated that the surface normal deviation from the zenith angle was $< \pm 10°$. The radiance error resulting from this angle error is a function of θ_i. In a scenario where $\theta_i = 35°$ and the panel alignment is off the zenith 10° toward the sun, the resulting radiance error is approximately 10%.

Examination of the calibration panel measurement data perhaps provides the best insight into estimating the overall radiance calibration error. A series of panel measurements is examined, and the data normalized to an equivalent $\theta_i = 0°$ digital count (DC) by dividing by $\cos(\theta_i)$ at the time of the measurement. The cosine-normalized data should be in good agreement, with the exception of the additional atmospheric path-length and hence increased τ_i attenuation. Table 5.5 presents one set of data, where it is seen that the standard deviation of the cosine-normalized data is approximately ±5% that of the mean. It is also noted from the data that there is an overall decrease in the cosine-normalized DC with increasing θ_i, implying increased τ_i attenuation. The data are also plotted as a function of θ_i in Figure 5.23. From these data, it is estimated that the overall radiance calibration error is on the order of ± 5%. There may be additional systematic error resulting from the $\rho = 0.93$ estimate made due to the non-Lambertian behavior of the panel. However, this systematic error is not as offensive as it does not impact the measurement of the anisotropic BRDF "shape".

The net radiance calibration error ϵ_{cal} may therefore be given as the sum of an indepen-

Table 5.5: The raw and cosine-corrected calibration panel measurements. These data are from a May 5, 2005, data collection.

θ_i [°]	DC	normalized DC
28.4	6022.6	6846.6
31.1	5840.2	6820.5
33.3	5296.6	6337.2
35.4	5208.9	6390.3
39.0	4754.3	6117.6
43.9	4623.6	6416.7
46.4	4220.9	6120.6
Mean $\pm\sigma$		6435.6 $\pm$297.1

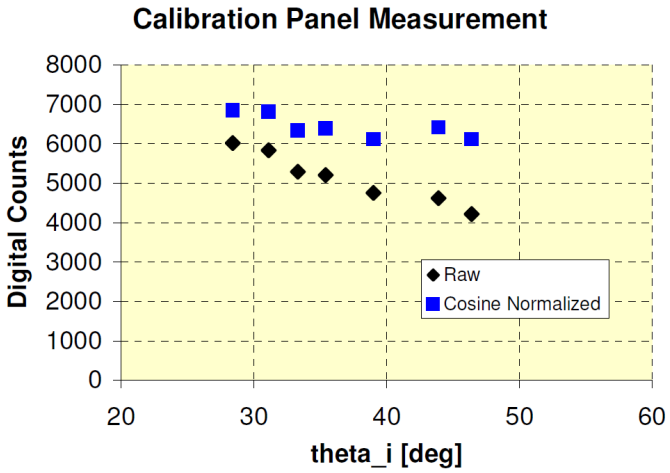

Figure 5.23: The raw and cosine-normalized digital counts of the calibration panel.

dent error of approximately 5% to which an error bias of approximately 2% may be added from the effective reflectance estimate of 0.93 from the panel.

5.3.5 Inherent Imaging System Errors

All systems are subject to "photon" noise, or the noise due to the Poisson-distributed arrival of photons [185]. This noise is proportional to the square root of the total number of photons received. A quick estimate of the photon noise is made by considering the full well capacity of a photosite in the SenSys camera CCD, along with the quantum efficiency. At a gain setting of "2", the manufacturer reports a full well electron capacity of 89,000. The quantum efficiency is approximately 0.5 at 550 and 750 `nm`, and around 0.6 at 650 `nm`. For the purposes of this calculation, a quantum efficiency of 0.5 will be considered for all three bands.

Given the 12-bit dynamic range, there are ≈ 21.73 electrons per digital count value, or ≈ 43.5 photons per digital count given the quantum efficiency of 0.5. The photon noise as a percentage of the total number of photons is therefore

$$\epsilon_p^{\%} = \frac{\sqrt{43.5\ DC}}{43.5\ DC} = (43.5\ DC)^{-\frac{1}{2}}\ , \tag{5.47}$$

with the absolute uncertainty in terms of DC (ϵ_p) given by

$$\epsilon_p = \epsilon_p^{\%}\ DC\ . \tag{5.48}$$

When $DC = 1$, the photon noise is 15.2%. At 10% of the dynamic range, or $DC = 400$, the noise is around 0.8%. Once half the dynamic range is reached or $DC = 2000$, the photon noise diminishes to 0.34%.

The inherent detector noise is very low, and given by the manufacturer as 20 electrons out of the full well of 89,000, or approximately one digital count for the 12-bit camera. This is in good agreement with the dark image characterization previously shown where the repeatability was within ± 2 digital counts.

Collectively, the photon and dark noise are referred to as the *inherent* noise, or ϵ_{inh}. In absolute error terms, ϵ_{inh} may be shown to be

$$\epsilon_{inh} = \left(2^2 + \left[\frac{DC}{\sqrt{43.5\ DC}}\right]^2\right)^{\frac{1}{2}}\ [\mathtt{DC}]\ , \tag{5.49}$$

when the photon and dark noise are considered independent.

It is furthermore noted that the DC magnitude of the shadow images (`B` and `D` images)

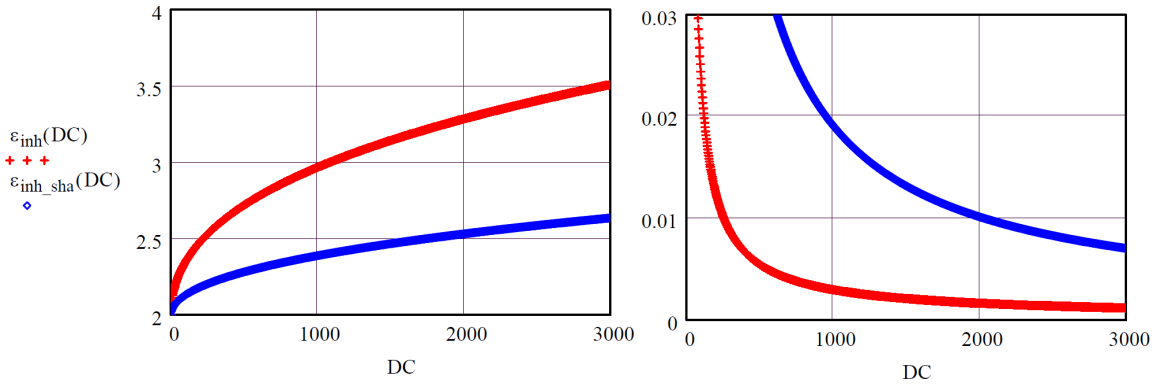

Figure 5.24: The inherent detector noise as a function of the digital count value of the "sun" or `C` image. The absolute DC error is shown *left*, while the relative or percentage error is shown *right*. The sun images (red data) have a higher absolute error, but lower relative error compared to the shadow or `D` images (blue).

are typically $\frac{1}{8}$ that of the sun images (`A` and `C` images), due to the same exposure length being used to acquire both sets of images, and the relative magnitude of the downwelled sky irradiance compared to the direct solar irradiance. This simplification enables expression of the shadow image inherent errors, $\epsilon_{inh(shadow)}$, in terms of the total illumination image DC values, given by

$$\epsilon_{inh(\mathtt{D})} = \left(4 + \left[\frac{\frac{DC}{8}}{\sqrt{43.5\ \frac{DC}{8}}}\right]^2\right)^{\frac{1}{2}} [\mathtt{DC}]\ . \tag{5.50}$$

The relative or percentage error is determined by division of (5.49) or (5.50) by the DC magnitude. The inherent percentage error of the sun and shadow images as a function of the sun image DC magnitude is shown in Figure 5.24. Typically the mean exposure level for the sun image is such that $DC > 2000$, resulting in a sun image inherent error of $< 0.2\%$ and a shadow image inherent error of $< 1.0\%$.

Finally, all imaging systems have some level of polarization sensitivity. A thorough characterization of a system would result in a spectrally-dependent transmission Mueller matrix for each photosite in the array. This is difficult to accomplish and certainly not feasible for this instrument. The fact that many have successfully implemented polarimetric imaging using a standard camera and optics attests to the fact that the polarization bias in these systems is not too substantial. Limiting the FOV helps avoid high incident angles, which result in the differential transmittance of incident polarized radiance. The polarization sensitivity of a very similar lens was characterized in [186, §2.6].

5.3.6 Angular Position Errors

The final error considered is that of the geometry of the measurements, that is the incident solar angle θ_i and scattering angles θ_r and ϕ. The reported incident solar angles are highly accurate and are taken directly from standard tables providing the solar position as a function of time, latitude and longitude. They are given in the measurement data at a resolution of 0.1°.

Indoor tests with the tripod and mount were completed which resulted in standard settings for configuring the camera in reflection angle orientations of $\theta_r = 0$, 30, or 45°. These preset configurations maintained the same distance from the camera to the center of optical axis on the measurement surface. The estimated accuracy of θ_r is approximately $\sigma = \pm 5°$.

Finally, the azimuth angle was measured with the help of a hula hoop and a plumb line. The hoop was marked in even increments of 45°. The hoop is placed around the surface being measured, and is large enough to stay out of the FOV during measurements. First, the hoop is rotated such that marks on the hoop opposite one another (180° away) are lined up toward the camera aperture. With the camera pointing at the center of the measurement area, a plumb line was used. The shadow of the plumb line string was made to bisect the center of the hoop. In this manner, the point at which the shadow crosses the hoop can be noted relative to the angular markings on the hoop, which are aligned toward the camera. The accuracy of this technique is estimated to be $\sigma = \pm 10°$.

Impacting all these uncertainties is the orientation of the measurement surface. Care was taken to make measurements of non-sloping surfaces. It is also reminded that the system FOV results in a changing θ_r and ϕ for every pixel in the image. With a 15° horizontal FOV, ϕ increases by 7.5° at the left edge of a frame with a corresponding decrease at the right edge. Similarly, with a vertical FOV of 10°, θ_r at the top of the image is increased by 5° with a corresponding decrease at the bottom of the frame.

5.3.7 Error Propagation

The errors are now propagated, following the equations necessary to derive the net uncertainty values of interest. The principal equation under consideration is (5.5); however, it is not readily apparent how the error terms developed in the previous sections apply. First, the total error in the f_{00}, f_{10} and f_{20} pBRDF components is determined. These errors may be quantified in terms of the raw digital count (DC) values measured by the focal plane.

Based upon the pBRDF component errors, uncertainties in values derived from them such as DOP and χ may be quantified. The conversion from DC to absolute BRDF levels

invokes an additional uncertainty which must be considered, namely the radiance calibration error discussed in §5.3.4. This only impacts the magnitude scale, and has no effect on the DOP and χ determination, as these quantities result from the ratio of DC magnitudes.

5.3.7.1 pBRDF Component Errors

In order to determine the uncertainty in the f_{00}, f_{10} and f_{20} pBRDF components, it is first necessary to consider the governing equation of measured quantities from which they are derived. The pBRDF components result from the difference between the "sun" and "shadow" images, images $\mathtt{C}$ and $\mathtt{D}$, respectively (*cf.* equation 5.5). In terms of digital count values, without considering the radiance calibration, the f_{xx} BRDF components from equation 5.5 are given by

$$\begin{bmatrix} f_{00} \\ f_{10} \\ f_{20} \end{bmatrix} = \begin{bmatrix} \frac{1}{2}\left[(\mathtt{C_0}-\mathtt{D_0})+(\mathtt{C_{90}}-\mathtt{D_{90}})+(\mathtt{C_{45}}-\mathtt{D_{45}})+(\mathtt{C_{135}}-\mathtt{D_{135}})\right] \\ (\mathtt{C_0}-\mathtt{D_0})-(\mathtt{C_{90}}-\mathtt{D_{90}}) \\ (\mathtt{C_{45}}-\mathtt{D_{45}})-(\mathtt{C_{135}}-\mathtt{D_{135}}) \end{bmatrix}, \tag{5.51}$$

which for the purposes of the error analysis is rearranged as

$$\begin{bmatrix} f_{00} \\ f_{10} \\ f_{20} \end{bmatrix} = \begin{bmatrix} \frac{1}{2}\left[(\mathtt{C_0}+\mathtt{C_{90}}+\mathtt{C_{45}}+\mathtt{C_{135}})-(\mathtt{D_0}+\mathtt{D_{90}}+\mathtt{D_{45}}+\mathtt{D_{135}})\right] \\ (\mathtt{C_0}-\mathtt{C_{90}})-(\mathtt{D_0}-\mathtt{D_{90}}) \\ (\mathtt{C_{45}}-\mathtt{C_{135}})-(\mathtt{D_{45}}-\mathtt{D_{135}}) \end{bmatrix}. \tag{5.52}$$

Basic rules of error propagation are observed for proper treatment of the uncertainties. Unless otherwise noted, the individual error sources previously discussed are considered independent. Given this, the uncertainty from a sum or a difference is propagated by the addition of the absolute error amount (*i.e.*, $\mathtt{DC}$ units) in quadrature. Similarly, the uncertainty associated with the product of terms is propagated by summing their relative or percent errors in quadrature [187, §3.3]. This technique is used to derive the net f_{xx} errors.

Determination of the resulting f_{00}, f_{10} and f_{20} errors proceeds by first quantifying the errors present in the individual $\mathtt{C_{xx}}$ and $\mathtt{D_{xx}}$ images used to form the pBRDF quantities per equation 5.52. The errors under consideration are the inherent image errors (ϵ_{inh}, §5.3.5), the spatial registration error ($\epsilon^{\%}_{reg}$, §5.3.2) and the sequential imaging error due to changes in θ_i ($\epsilon^{\%}_{\theta_i}$, §5.3.3).

An assumption is made regarding the average DC magnitude of the $\mathtt{C}$ and $\mathtt{D}$ images. The exposure of the imaging system was set such that on average, the $\mathtt{C}$ images have a mean DC value of approximately 2000, or about half the dynamic range of the system. The same

exposure setting was used for the corresponding shadow images (D images) which usually resulted in a DC magnitude of $\frac{1}{8}$ that of the C images, or approximately $DC = 250$ (this ratio is related to the magnitude of the downwelled sky radiance relative to the direct solar irradiance).

Inherent error With these ground rules in place, the inherent C image error is shown from (5.50) to be

$$\begin{aligned} \epsilon_{inh}(\mathtt{C}) &= \left(2^2 + \left[\frac{2000}{\sqrt{43.5\ 2000}}\right]^2\right)^{\frac{1}{2}} \\ &\approx 3.28\ [\mathtt{DC}]\ , \end{aligned} \tag{5.53}$$

which is a percentage error of $\frac{3.28}{2000}$ or 0.164%. Similarly, the inherent shadow image D is shown to have an error of

$$\begin{aligned} \epsilon_{inh}(\mathtt{D}) &= \left(2^2 + \left[\frac{250}{\sqrt{43.5\ 250}}\right]^2\right)^{\frac{1}{2}} \\ &\approx 2.52\ [\mathtt{DC}]\ . \end{aligned} \tag{5.54}$$

which is a percentage error of $\frac{2.52}{250}$ or 1.01% and as expected is substantially higher than the C image error, as earlier depicted in Figure 5.24.

The total inherent error for the f_{00} component results from the summation of the inherent errors from four C images as well as that from four D images (*c.f.* §5.3.5). The total f_{00} inherent error is therefore

$$\begin{aligned} \epsilon_{inh}(f_{00}) &= \sqrt{4 \cdot 3.28^2 + 4 \cdot 2.52^2} \\ &= 8.27\ [\mathtt{DC}]\ . \end{aligned} \tag{5.55}$$

Similarly, the inherent error for the f_{10} and f_{20} components result from the summation of the inherent errors from two C images and two D images, giving

$$\begin{aligned} \epsilon_{inh}(f_{10}) = \epsilon_{inh}(f_{20}) &= \sqrt{2 \cdot 3.28^2 + 2 \cdot 2.52^2} \\ &= 5.85\ [\mathtt{DC}]\ . \end{aligned} \tag{5.56}$$

Note that relative magnitude of f_{00} compared to f_{10} and f_{20} is usually such that the percentage error in the f_{00} is lower in spite of a higher DC error magnitude.

Spatial registration error Next, the spatial registration errors from §5.3.2 are considered. For the f_{00} component, there are three registration error possibilities among the four C images, and similarly three among the four D images. The error between the C and D images is considered negligible, as no "touch" adjustments were made between these images. The registration error expressed in equation 5.41 is a relative or percentage error term, which is converted to the absolute error by multiplication with DC. The resulting registration error for the f_{00} component is thus

$$\begin{aligned}\epsilon_{reg}(f_{00}) &= \sqrt{3 \cdot \left[\frac{0.5}{X} \cdot DC(\texttt{C})\right]^2 + 3 \cdot \left[\frac{0.5}{X} \cdot DC(\texttt{D})\right]^2} \\ &= \sqrt{3 \cdot \left[\frac{0.5}{X} \cdot 2000\right]^2 + 3 \cdot \left[\frac{0.5}{X} \cdot 250\right]^2} \\ &\approx \frac{1746}{X}\ [\texttt{DC}]\ .\end{aligned} \tag{5.57}$$

The registration error for the f_{10} and f_{20} elements is only among a single set of C and D images or

$$\begin{aligned}\epsilon_{reg}(f_{10}) = \epsilon_{reg}(f_{20}) &= \sqrt{\left[\frac{0.5}{X} \cdot DC(\texttt{C})\right]^2 + \left[\frac{0.5}{X} \cdot DC(\texttt{D})\right]^2} \\ &= \sqrt{\left[\frac{0.5}{X} \cdot 2000\right]^2 + \left[\frac{0.5}{X} \cdot 250\right]^2} \\ &\approx \frac{1008}{X}\ [\texttt{DC}]\ .\end{aligned} \tag{5.58}$$

At $GSD = 0.5$ in, or the lowest processed, the resulting error is approximately 50 DC, considering $X = 35$ pixels. For a mean value of 2000 for the C images and 250 for the D images, the resulting f_{00} magnitude is 3500 DC. This results in an error of $\frac{50}{3500}$ or 1.43%.

Sequential imaging error Finally, the sequential imaging error from §5.3.3 is considered. It is assumed that post-processing and the ΔE data highlights errors resulting from unacceptable atmospheric changes. Therefore, the concern is limited to the changing θ_i incidence angle error. This error could be treated as a systematic error based upon the time of the day of the acquisition, but for simplicity is included as an error term applied to all conditions. Recall that the f_{10} and f_{20} error magnitude is $\epsilon_{\theta_i}(f_{10}) = 0.27\%$ and the f_{00} error magnitude is $\epsilon_{\theta_i}(f_{00}) = 0.4\%$. This error is the net result of the C or "sun" image combinations, as the shadow or D images obviously do not include direct solar illumination. Presuming an average C magnitude of $DC = 2000$, the resulting error in terms of DC is $\epsilon_{\theta_i}(f_{10}) \approx 5.4$ DC

and $\epsilon_{\theta_i}(f_{00}) \approx 8.0$ DC.

pBRDF component error summary The error terms necessary to derive the f_{00}, f_{10} and f_{20} uncertainties are now summarized. Relevant error sources include the relative polarization filter error ϵ_{fil}, as well as the inherent, spatial registration and sequential imaging error sources recently discussed. In terms of DC values, the f_{00} error is considered to be $\epsilon_{fil}(f_{00}) = 3500 \cdot 0.3\% \approx 10.5$ DC and the f_{10} (and equivalently f_{20}) error is considered as $\epsilon_{fil}(f_{10}) = 1750 \cdot 0.43\% \approx 7.5$ DC (*cf.* 1-σ values from Table 5.2 for $\chi = \frac{\pi}{8}$).

Considering these four error sources, the f_{00} total error is

$$\begin{aligned} \epsilon(f_{00}) &= \sqrt{\epsilon_{inh}(f_{00})^2 + \epsilon_{reg}(f_{00})^2 + \epsilon_{\theta_i}(f_{00})^2 + \epsilon_{fil}(f_{00})^2} \\ &= \sqrt{8.27^2 + \left(\frac{1746}{X}\right)^2 + 8.0^2 + 10.5^2} \ , \end{aligned} \tag{5.59}$$

with the f_{10}/f_{20} error

$$\begin{aligned} \epsilon(f_{10}) = \epsilon(f_{20}) &= \sqrt{\epsilon_{inh}(f_{10})^2 + \epsilon_{reg}(f_{10})^2 + \epsilon_{\theta_i}(f_{10})^2 + \epsilon_{fil}(f_{10})} \\ &= \sqrt{5.85^2 + \left(\frac{1008}{X}\right)^2 + 5.4^2 + 7.5^2} \ . \end{aligned} \tag{5.60}$$

It is readily apparent that the spatial registration accuracy is the driver. Considering the normal resolution of 70 pixels/in, equations (5.59) and (5.60) may be stated explicitly in terms of GSD (in units of inches) as

$$\begin{aligned} \epsilon(f_{00}) &= \sqrt{8.27^2 + \left(\frac{24.9}{GSD}\right)^2 + 8.0^2 + 10.5^2} \quad [\text{DC}] \\ \epsilon(f_{10}) = \epsilon(f_{20}) &= \sqrt{5.85^2 + \left(\frac{14.4}{GSD}\right)^2 + 5.4^2 + 7.5^2} \quad [\text{DC}] \ . \end{aligned} \tag{5.61}$$

The digital count error as a function of GSD is shown in Figure 5.25, where the rapid error decrease with increasing GSD is apparent.

5.3.7.2 *DOP* Error

Having quantified the individual f_{00}, f_{10} and f_{20} errors, it is now possible to propagate these uncertainties to the *DOP* and χ calculations. Recall that *DOP* from the measurements is

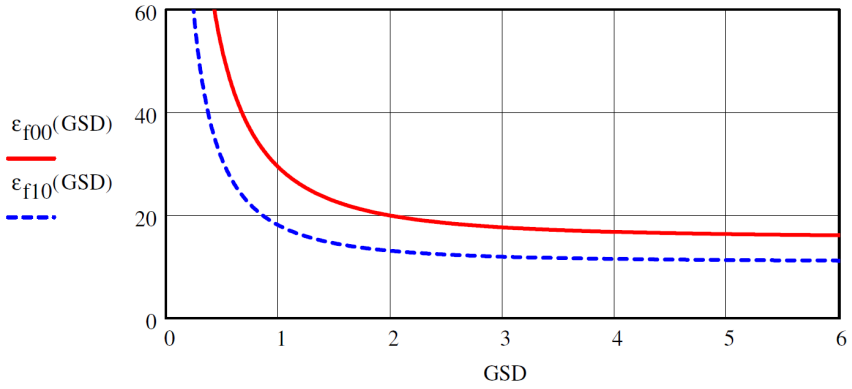

Figure 5.25: The digital count (DC) error of f_{00} (solid, red) and f_{10} and f_{20} (dashed, blue) pBRDF components as a function of GSD in inches.

given from the pBRDF component elements as

$$DOP = \frac{\sqrt{f_{10}^2 + f_{20}^2}}{f_{00}} \ , \tag{5.62}$$

while χ is determined by

$$\chi = \frac{1}{2} \tan^{-1} \left[\frac{f_{20}}{f_{10}} \right] \ . \tag{5.63}$$

The net error of a dependent variable (such as DOP or χ) given a governing equation may be determined by the quadrature summation of the partial derivative of dependent variable with respect to the independent variable(s) multiplied by the error of the independent variable [4, eq. 4.71]. Mathematically, for DOP the net error (ϵ_{DOP}) is expressed as

$$\epsilon_{DOP} = \left[\left(\frac{\delta DOP}{\delta f_{00}} \epsilon_{f_{00}} \right)^2 + \left(\frac{\delta DOP}{\delta f_{10}} \epsilon_{f_{10}} \right)^2 + \left(\frac{\delta DOP}{\delta f_{20}} \epsilon_{f_{20}} \right)^2 \right]^{\frac{1}{2}} \ , \tag{5.64}$$

which may be shown to equal

$$\epsilon_{DOP} = \left[\left(\frac{-\sqrt{f_{10}^2 + f_{20}^2}}{f_{00}^2} \epsilon_{f_{00}} \right)^2 + \left(\frac{f_{10}}{f_{00}\sqrt{f_{10}^2 + f_{20}^2}} \epsilon_{f_{10}} \right)^2 + \left(\frac{f_{20}}{f_{00}\sqrt{f_{10}^2 + f_{20}^2}} \epsilon_{f_{20}} \right)^2 \right]^{\frac{1}{2}} \ . \tag{5.65}$$

One could erroneously be led to the conclusion that for $DOP = 0$, which requires $f_{10} = f_{20} = 0.0$, that the total error is zero when directly applying (5.65). However,

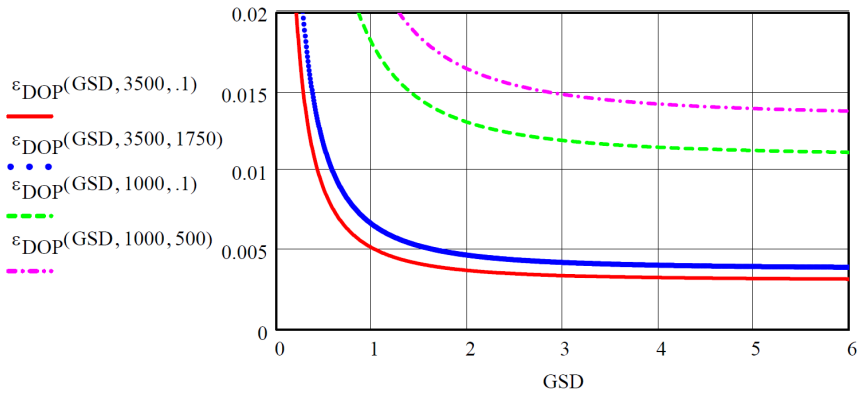

Figure 5.26: Estimates of the DOP measurement error for four scenarios are given as a function of GSD. The four scenarios shown are: high signal, $DOP = 0.0$ (red); high signal, $DOP = 0.5$ (blue); low signal, $DOP = 0.0$ (green) and low signal, $DOP = 0.5$ (magenta).

the limiting behavior as f_{10} and $f_{20} \rightarrow 0$ is not for $\epsilon_{DOP} \rightarrow 0$. Four different cases will be analyzed: *i*) high signal with zero DOP, *ii*) high signal with high DOP, *iii*) low signal with zero DOP and *iv*) low signal with high DOP. The high signal case considers a "normal" camera setting, where the average f_{00} DC magnitude is 3500 counts. The low signal case is for an f_{00} DC magnitude of 1000. Finally, "high" DOP is $DOP = 0.5$. The results of these four cases, as a function of GSD, are shown in Figure 5.26.

Some of the values from Figure 5.26 for $GSD = 0.5$ `in` are now considered. For the high signal, $DOP = 0.0$ case, the resulting error is $\epsilon_{DOP} = 0.0088$. This value is consistent with the observational results of the measurements—that is, rarely is a consistent DOP less than 0.01 obtained for an image. At the 1-σ level, the DOP "floor" is around 0.009. For the high signal, $DOP = 0.5$ case, the resulting error is $\epsilon_{DOP} = 0.0115$, or a percentage error of only 2.3%. The errors increase appreciably with a lower signal. With an f_{00} DC magnitude of only 1000 (which corresponds to a raw image DC of 500, or only $\frac{1}{8}$ the dynamic range of the camera), ϵ_{DOP} for the $DOP = 0.0$ case increases to $\epsilon_{DOP} = 0.031$, establishing a relatively high DOP "floor". For the low signal, $DOP = 0.5$ case, $\epsilon_{DOP} = 0.04$ or a relative error of 8%.

It is reminded that the DOP errors portrayed in Figure 5.26 and discussed here are not all inclusive. In particular, the estimate for the finite polarization filter contrast (*cf.* §5.3.1.3) has an additional uncertainty which manifests itself as a consistent DOP bias.

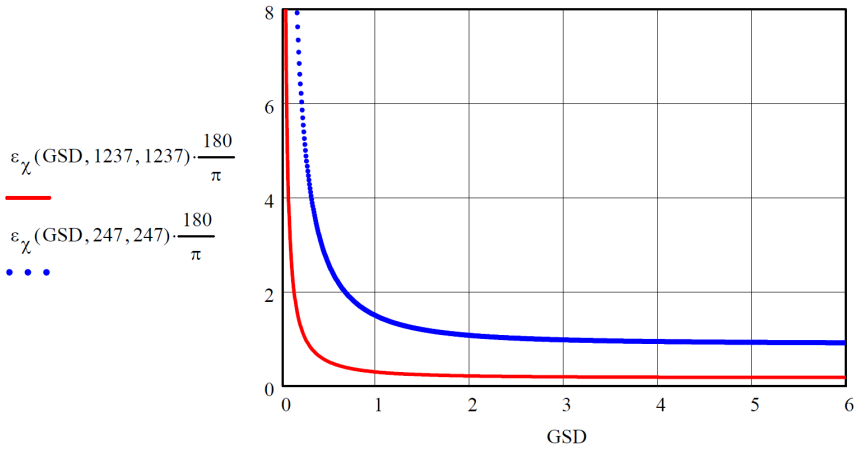

Figure 5.27: Estimates of the χ measurement error in degrees as a function of GSD. χ error estimates are given for $DOP = 0.5$ (red) and $DOP = 0.1$ (blue).

5.3.7.3 χ Error

Following the same development path as that taken for the DOP error, the polarization angle error ϵ_χ equation is given by

$$\epsilon_\chi = \left[\left(\frac{\delta\chi}{\delta f_{10}} \epsilon_{f_{10}} \right)^2 + \left(\frac{\delta\chi}{\delta f_{20}} \epsilon_{f_{20}} \right)^2 \right]^{\frac{1}{2}} , \tag{5.66}$$

which is equal to

$$\epsilon_\chi = \left\{ \left[\frac{-f_{20}}{2f_{10}^2 \left(1 + \frac{f_{20}^2}{f_{10}^2}\right)} \epsilon_{f_{10}} \right]^2 + \left[\frac{1}{2f_{10} \left(1 + \frac{f_{20}^2}{f_{10}^2}\right)} \epsilon_{f_{20}} \right]^2 \right\}^{\frac{1}{2}} . \tag{5.67}$$

As with the DOP error, the polarization angle error ϵ_χ is examined as a function of GSD. It is insightful to relate the χ error to the measured DOP. However, ϵ_χ is not a function of f_{00}, but only depends on the magnitudes of the f_{10} and f_{20} components. The notional scenario is considered where the f_{00} DC magnitude is 3500, and ϵ_χ analyzed for cases where $DOP = 0.5$ and $DOP = 0.1$. For both cases, the f_{10} and f_{20} magnitudes are evenly distributed (which is equivalent to a mean $\chi = 22.5°$), with the magnitudes adjusted to give the correct DOP magnitude. For the $DOP = 0.5$ case, the magnitudes are 1237 DC and for the $DOP = 0.1$ case the magnitudes are 247 DC. The results are shown in Figure 5.27.

As with the *DOP* error analysis, these results do not include all sources of χ error. Most significantly, the large bias resulting from the poorly defined reference frame of the camera is not included. Therefore, the results in Figure 5.27 provide a good estimate of χ precision, but not the accuracy.

5.3.7.4 Radiance Calibration Error

Finally the radiance calibration of the data is addressed. As seen from equation 5.5, the additional variables having uncertainties are the `A` and `B` calibration panel images and the estimated Lambertian reflectance factor, ρ. The same inherent image errors are present in the `A` and `B` images, although at reduced levels. This is attributed to a typical exposure setting which results in an average image DC magnitude which is 1.5 times that of the average target material magnitude. Furthermore, there are no spatial registration issues to contend with, as an average of a central grouping of pixels is used to derive the DC calibration value.

The net result is that most of the calibration uncertainty is due to the approximation of the ρ quantity as discussed in §5.3.4. Another contending factor is the positioning of the panel surface normal relative to the zenith position. The final estimate of the radiance calibration precision is on the order of 5%, with an accuracy or bias estimate on the order of 2% as given in §5.3.4.3. The radiance calibration accuracy is supported in part by favorable comparison of the pBRDF measurement-derived reflectance factor estimate to that of field spectrometer measurements, to be presented in Chapter 7 in §7.4.

5.3.7.5 Error Summary

A number of assumptions and approximations have been made toward producing an estimate of the system uncertainty. Uncertainties in polarimetric imaging are complex, and a function of the spatial frequency content of the scene in question. A more thorough uncertainty analysis may be obtained by numerical simulation of all error components, similar to that completed with the filter alignment error in §5.3.1.2. Although the derivation of the net system error involved many approximations, the results are corroborated by experimental observations from the system.

5.4 Summary

The experimental technique to quantify the pBRDF of background materials, to include their variability as a function of GSD has been presented. A shadow subtraction technique

enables elimination of the downwelled sky radiance, enabling quantification of the first column of pBRDF Mueller matrix. The imaging system used for the measurements has been characterized and the lens falloff and dark noise properties quantified. Test images with the system demonstrate anticipated results, which builds confidence in the system performance. A variety of uncertainties have been discussed and quantified.

Chapter 6

Measurement Results

Having obtained raw data from the measurement technique described in Chapter 5, it is necessary to process the data to provide meaningful results. The processing algorithms may be divided into two steps. A "pre-processing" step provides spatial registration of the raw images and radiometric corrections, such as for the lens-falloff. This data is then used by the polarimetric BRDF algorithm which provides final results by implementing equation 5.5. Finally, the measurement results for three materials are presented: topsoil, lawn grass and asphalt.

6.1 Raw Data Pre-Processing

A set of calculations are only required once with the raw data, and are collectively termed "pre-processing" steps. The pre-processing performs two primary functions: *i*) determining the correct digital count (DC) value to equate to the known $\frac{\rho}{\pi}$ BRDF for absolute radiance calibration and *ii*) spatial registration, lens falloff and dark noise correction of the `A`, `B`, `C` and `D` image sets (Figure 5.2). An overview of the pre-processing steps are shown in Figure 6.1, which is a good reference for the following discussion.

6.1.1 Radiance Calibration

The radiance calibration is performed with the two sets of orthogonally polarized `A` and `B` images. This digital count determination is made independent of the other calculations, and the results written out to an ASCII text file. It is completed without any spatial registration being performed. The only preliminary processing to the `A` and `B` images are dark image subtraction and lens falloff correction.

The mean value is determined for the `A` (sun + sky), `B` (sky or shadow image) and `A` − `B`

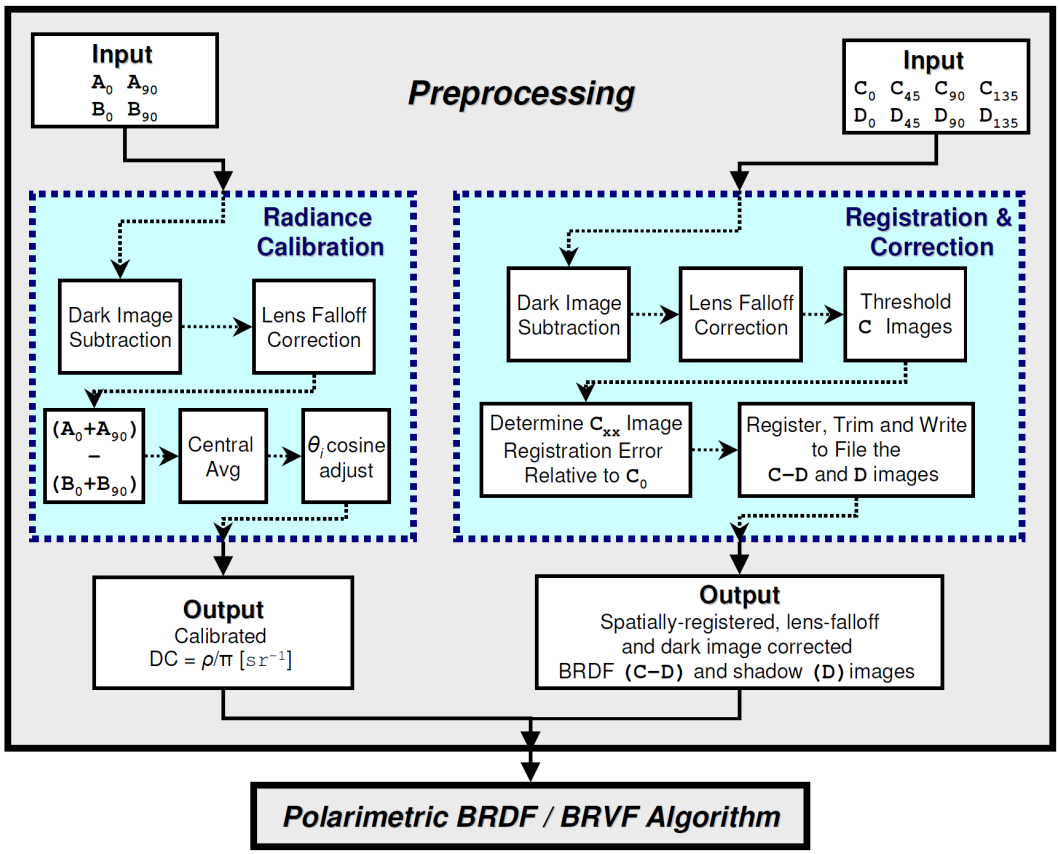

Figure 6.1: The preprocessing algorithms are only performed once per data set, per spectral band. The two major components are the radiance calibration and spatial registration.

(sun-only or BRDF) images. To arrive at a single DC value, the average of only 100 pixels is used—those comprising the central 10×10 area. A check is made to ensure that a pixel-to-pixel variability threshold is not exceeded. This provides a means to detect debris which may blow onto the panel (or in one case an ant which crawled onto the panel). The output of the routine provides the DC values for the three illumination conditions of interest: full sun and sky illumination, sky-only illumination and sun-only illumination. Also computed is the fraction of the total radiance which is attributed to the sky, or the L_d component of L_s. The difference between the cross-polarized images is also reported. The output of one such calibration is shown below, where the first line contains meta data.

```
Data Set Information Data/20050520_Soil/ Calibrate/ cal4(30,270) 750 11.0 0010
Average Digital Count (Sun + Sky, Shadow, Sun)
  4683.4268   554.1308  4129.2964
Sky Radiance Fraction
     0.1183
Percent Variance (Sun+Sky, Shadow, Sun)
     0.0095     0.0131     0.0101
Delta of 000-090 (average, variance)
    -0.0165    -0.4250
```

Therefore for this example the BRDF is known to be $4129.3 = \frac{\rho}{\pi} = \frac{0.93}{\pi}[\mathtt{sr}^{-1}]$, recalling the origin of $\rho = 0.93$ from §5.3.4.1. A further adjustment to this DC value is made by considering the time difference between the calibration image and surface measurement image, and resulting θ_i difference. This cosine correction was previously shown in equation 5.46.

6.1.2 Spatial Registration

Spatial registration of the eight `C` and `D` images for a given measurement is critical to obtain accurate results, in particular for the DOP determination (*cf.* §5.3.2). The images are typically mis-registered a maximum of ten pixels, which results from the rotation of the polarization filter whose surface normal is slightly mis-aligned to the optical axis of the system. Thus, the mis-registration may be treated as purely translational, such that no scaling or rotational effects need be considered.

The spatial registration technique employed invokes a cross-correlation of the images in the frequency domain, where spatial displacement corresponds to a phase shift. For example, given the $\mathtt{C}_0$ and $\mathtt{C}_{90}$ images, the shift between the images in terms of the x and

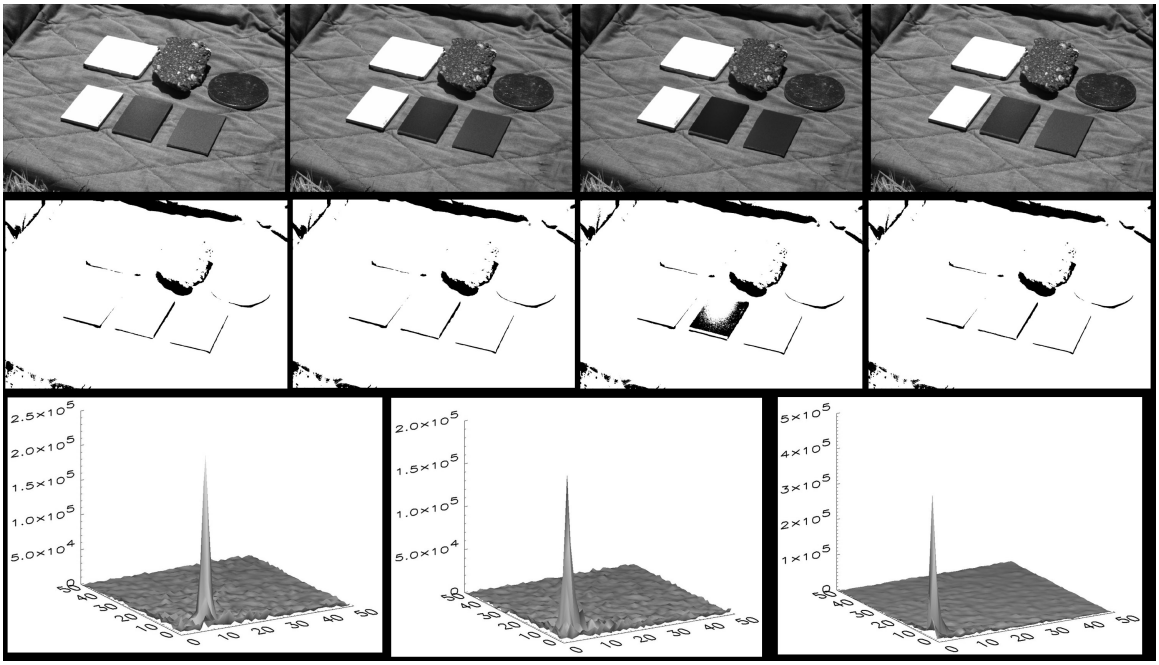

Figure 6.2: The spatial registration algorithm first takes the raw $\mathtt{C_0}$, $\mathtt{C_{45}}$, $\mathtt{C_{90}}$ and $\mathtt{C_{135}}$ images (*top row*, left to right), and converts them to binary images (*middle row*). For the conversion illustrated, a threshold of $\frac{1}{6}$ the maximum among all images was used. The correlation magnitude of the binary images to the "base" $\mathtt{C_0}$ binary image is shown on the bottom row, where the x and y-axis correspond to pixel displacement (*cf.* equation 6.1). Note that the axes have been limited to 50 pixels.

y coordinates x_0 and y_0 may be given as [188]

$$[x_0, y_0] = \mathtt{MAX}\left[\mathcal{F}^{-1}\left\{\frac{\mathcal{F}(\mathtt{C_0})\mathcal{F}^*(\mathtt{C_{90}})}{|\mathcal{F}(\mathtt{C_0})\mathcal{F}(\mathtt{C_{90}})|}\right\}\right] , \tag{6.1}$$

where $\mathcal{F}$ is the Fourier transform, $\mathcal{F}^{-1}$ is the inverse Fourier transform and $*$ is the complex conjugate. As implemented, a total of nine discrete Fourier transforms and inverse transforms are required for each image set. On a PC with a 1 GHz class processor, this is easily completed in under two minutes.

When this method was first implemented, it was unsuccessful due to the contrast changes resulting from the different polarization filter orientations. However, the technique succeeded once the images were converted to binary (two-tone) images. Optimal thresholds for the binary conversion were generally found to be between $\frac{1}{6}$ to $\frac{1}{4}$ the maximum value among the images. This is due to specular highlights having the highest degree of polarization, and hence the most variability. The spatial registration technique was found to provide an accuracy on the order of a pixel or less. Figure 6.2 illustrates the procedure.

The mis-registration calculation was only performed on the C images. Since the shadow (D) image was made immediately after the C image without any changes which may disturb the camera, it may be assumed that the D and C images for a given polarization orientation are already registered. In registering the C images, the $\mathtt{C}_0$ image was arbitrarily selected as the "base" image, and the registration routine provided Δx and Δy coordinates for the $\mathtt{C}_{45}$, $\mathtt{C}_{90}$ and $\mathtt{C}_{135}$ images relative to the $\mathtt{C}_0$ image. Similarly, these same Δx and Δy coordinates are provided to all the D images.

After determining the displacements of all the images relative to the base image, the images are trimmed such that only the common regions in all images remain. This operation may be thought of as a logical AND among all images. After the trimming operation, the set of four $\mathtt{C}-\mathtt{D}$ or "BRDF" images and four D or "sky" images are written out to individual files. Henceforth, the BRDF or $\mathtt{C}-\mathtt{D}$ images will be referred to as the E images. Prior to performing the spatial registration, a dark image subtraction is made, followed by the lens fall-off correction. Therefore the images written out at this stage are registered, trimmed and corrected for the lens fall-off and dark noise. This provides a set of images still in terms of digital counts, though they are no longer integer values due to the lens fall-off correction.

It would seem logical to go ahead and perform the DC to $\mathtt{sr}^{-1}$ conversion and write these images out to files. However, as noted earlier, some of the error terms are dependent upon the DC magnitude. Retention of the DC magnitudes in the preprocessed data enables further error analysis without consulting the raw data files.

6.2 Polarimetric BRDF and Variability Determination

After the preprocessing, the four BRDF images from which f_{00}, f_{10} and f_{20} or $\vec{f}$ are determined and the four sky images from which ϵ_0, ϵ_1 and ϵ_2 or $\vec{\epsilon}$ are determined are suitable for analysis. The first operation is a conversion of the images from digital counts into BRDF units of $[\mathtt{sr}^{-1}]$, which is completed by dividing by the digital count calibration and multiplication with $\frac{0.93}{\pi}$ per equation 5.3.

From these images which are now calibrated to units of $[\mathtt{sr}^{-1}]$, images $\vec{f}$ and $\vec{\epsilon}$ elements are calculated. From equations 5.4 and 5.5 it is seen that

$$\begin{bmatrix} f_{00} \\ f_{10} \\ f_{20} \end{bmatrix} = \begin{bmatrix} \frac{1}{2}\left[\mathtt{E}'_0 + \mathtt{E}'_{90} + \mathtt{E}'_{45} + \mathtt{E}'_{135}\right]/(1+\tau_\otimes) \\ (\mathtt{E}'_0 - \mathtt{E}'_{90})/(1-\tau_\otimes) \\ (\mathtt{E}'_{45} - \mathtt{E}'_{135})/(1-\tau_\otimes) \end{bmatrix}, \tag{6.2}$$

where the $'$ indicates the images which are in terms of $[\mathtt{sr}^{-1}]$, and it is reiterated that

$\mathtt{E}'_{\mathtt{xx}} = \mathtt{C}'_{\mathtt{xx}} - \mathtt{D}'_{\mathtt{xx}}$. It is also seen in (6.2) that the error resulting from the cross-polarized leakage, $\tau_{\otimes}$, is corrected for as discussed in §5.3.1.3 and shown in equations 5.33–5.35. Similarly, $\vec{\epsilon}$ is given by

$$\begin{bmatrix} \epsilon_0 \\ \epsilon_1 \\ \epsilon_2 \end{bmatrix} = \begin{bmatrix} \frac{1}{2}\left[\mathtt{D}'_0 + \mathtt{D}'_{90} + \mathtt{D}'_{45} + \mathtt{D}'_{135}\right]/(1+\tau_{\otimes}) \\ (\mathtt{D}'_0 - \mathtt{D}'_{90})/(1-\tau_{\otimes}) \\ (\mathtt{D}'_{45} - \mathtt{D}'_{135})/(1-\tau_{\otimes}) \end{bmatrix} . \tag{6.3}$$

The details of the variability determination are now described using (6.2) and (6.3) as the basis. Figure 6.3 provides an overview of the processing algorithm, and may be referenced in the subsequent discussion.

6.2.1 Variability Computation

The $\vec{f}$ and $\vec{\epsilon}$ elements may be used to develop the variability statistics by varying the size of a convolution kernel, $h[x, y]$ per equation 5.6. The observation is made that the mean value of the $\vec{f}$ and $\vec{\epsilon}$ elements do not change, regardless of the GSD of interest. That is, varying the size of $h[x, y]$ has no impact on the mean values, due to the linear convolution operation.

In practice, the variability is determined by convolving the individual $\mathtt{E}'_{\mathtt{xx}}$ and $\mathtt{D}'_{\mathtt{xx}}$ images which serve as inputs to $\vec{f}$ and $\vec{\epsilon}$ elements per (6.2) and (6.3). By linearity of the convolution operation, the same results may be more efficiently obtained by direct convolution of the $\vec{f}$ and $\vec{\epsilon}$ elements. However, this more efficient technique is not used as it does not enable calculation of the ΔE data at varying GSD sizes, which requires the four individual polarization images (equation 5.40). It is seen that in terms of the $\mathtt{E}'_{\mathtt{xx}}$ images that $\Delta E(GSD)$ is given by

$$\Delta E(GSD) = [\mathtt{E}'_0(GSD) + \mathtt{E}'_{90}(GSD)] - [\mathtt{E}'_{45}(GSD) + \mathtt{E}'_{135}(GSD)] . \tag{6.4}$$

Using a simple `RECT` function, the eight convolutions required for each GSD of interest is completed in approximately 30 `sec` on a PC with a 1 `GHz`-class processor.[1]

The variability statistics are therefore taken directly from $\vec{f}(GSD)$ and $\vec{\epsilon}(GSD)$ where the appropriate GSD has been used to filter the $\mathtt{E}'_{\mathtt{xx}}$ and $\mathtt{D}'_{\mathtt{xx}}$ images. The variability is quantified by the standard deviation of the data. This is a suitable metric for much of the data, which has a pseudo-Gaussian distribution. An additional input not yet mentioned

[1] This was implemented in IDL using the "SMOOTH" function. In other programming languages, or for other than `RECT` convolution kernels, it may likely be more efficient to perform this low-pass filtering in the frequency domain.

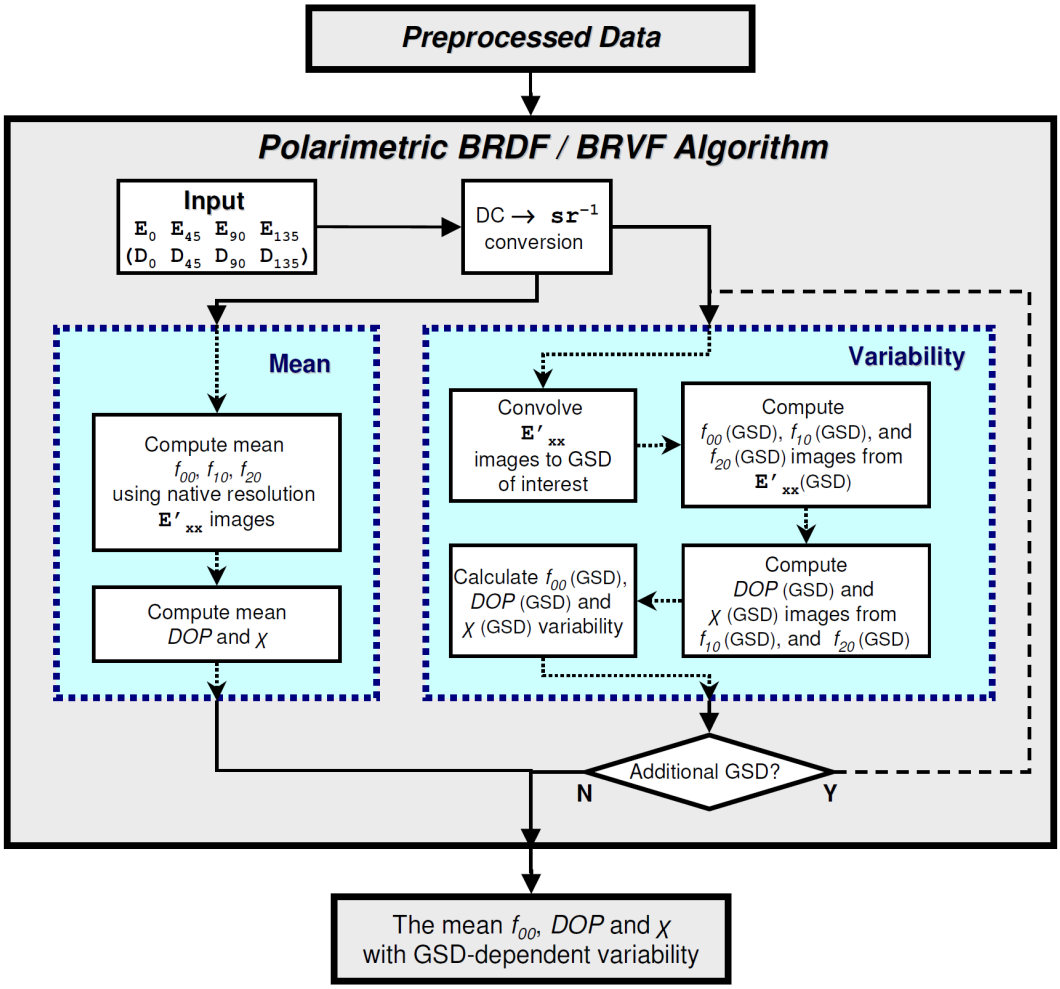

Figure 6.3: The preprocessed data from Figure 6.1 is provided as an input to the pBRDF and BRVF algorithms shown here. These algorithms provide the pBRDF mean variability. The processing is identical for either the BRDF ($\mathtt{E}'_{\mathtt{xx}}$) or downwelled sky ($\mathtt{D}'_{\mathtt{xx}}$) data.

is the ground instantaneous FOV or the appropriate conversion factor relating a single pixel to the corresponding ground distance. The "standard" configuration of the system for the $\theta_r = 30°$ and $45°$ measurements used a standoff distance of approximately 80.4 `in`., resulting in a ground resolution of 73.14 pixels per inch. For the $\theta_r = 0°$ measurements, the standard standoff distance had to be reduced to approximately 68 `in`. in order to provide easy access to the polarization filter, which resulted in 87.15 pixels per inch. Other unique measurement orientations, in particular those made at high phase angles, had a significantly larger standoff distance with a correspondingly smaller pixel-to-inch conversion factor.

An appropriate *padding* approach must be determined for the convolution of the $\mathtt{E}'_{\mathtt{xx}}$ and $\mathtt{D}'_{\mathtt{xx}}$ images. As the GSD increases or as the convolution kernel size increases, the coverage area of the kernel within the boundaries of the image decreases if not allowed to extend beyond the image boundary. One option is to not pad the images and simply use the data that is contained within the boundaries of the largest GSD size. However, this results in a significant loss of information at the smaller GSD sizes, where statistics are available over the majority of the image. For this reason, a decision was made to pad the images with content from the adjacent areas in the image, thus providing the same number of data points irrespective of the GSD kernel size. This was done by replicating the contents of the adjacent areas, and adding a "corner" of the right size. Figure 6.4 illustrates the padding. Figure 6.4 also illustrates why a one foot GSD is a practical limit for the variability data, as a significant fraction of the image starts to be replicated.

A final point regarding the padding is that the statistics of the padded regions have some natural deviation from the native image as a whole. This manifests itself when examining the mean values of the $\vec{f}$ and $\vec{\epsilon}$ components as a function of GSD. The changing mean value is minimal, and typically less than 0.1% for the f_{00} and ϵ_0 components. It is for this reason that the mean values are determined using the native images, and not an inherent by-product of the variability calculation as shown in Figure 6.3. Examples of this change are given in the extended data set, provided as part of Appendix A.

So the variability data is generated by the $\vec{f}$ and $\vec{\epsilon}$ images from equations 6.2 and 6.3 as a function of GSD using $\mathtt{E}'_{\mathtt{xx}}(GSD)$ and $\mathtt{D}'_{\mathtt{xx}}(GSD)$ images which result from the convolution with a `RECT` kernel which has pixel dimensions corresponding with that GSD. The $\vec{f}(GSD)$ and $\vec{\epsilon}(GSD)$ are further processed to produce the appropriate DOP and χ images and statistics according to

$$DOP(GSD) = \frac{\sqrt{f_{10}^2(GSD) + f_{20}^2(GSD)}}{f_{00}(GSD)} \tag{6.5}$$

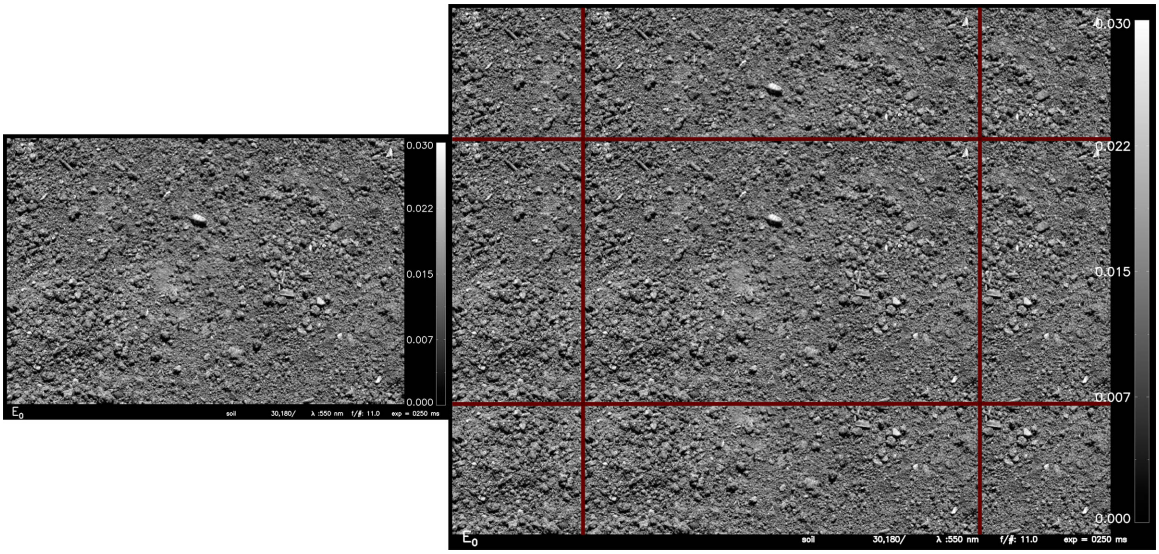

Figure 6.4: The $\mathtt{E}_{\mathtt{xx}}^{'}$ and $\mathtt{D}_{\mathtt{xx}}^{'}$ images must be padded prior to the convolution. At left is an original $\mathtt{E}_{\mathtt{xx}}^{'}$ image at the native size, along with the padded image for a case where $GSD = 12$ `in` (*right*). An equivalent of 6 `in` must be added to the image perimeter, shown by the dark red lines. (This image is $\mathtt{E}_{\mathtt{0}}^{'}$ of topsoil at 550 `nm` with $\theta_i = 23.3°$, $\theta_r = 30°$ and $\phi = 180°$).

and

$$\chi = \frac{1}{2}\tan^{-1}\left[\frac{f_{20}(GSD)}{f_{10}(GSD)}\right] \ , \tag{6.6}$$

with similar expressions using the $\vec{\epsilon}$ components to determine the downwelled sky result. The variability is quantified by the standard deviation of the data.

6.2.2 Data Output

The data resulting from the pBRVF algorithm is output in several formats. At each band for each scattering location or camera position, a standard data set is generated which captures the behavior of the material for that orientation. A standard set of four GSD sizes are used for all the data: 0.5", 3.0", 6.0" and 12.0". In addition, calculations are performed with a native resolution image and one filtered with a 5×5 pixel convolution kernel. This 5×5 kernel data is used to produce a high resolution data set, which is usually at $GSD \approx 0.07$", though it varies due to the variation in distance to the imaged surface. Each of the data elements resulting from the processing are described with examples provided. A significant number of qualitative images are produced, providing a visual representation of the numerical data.

6.2.2.1 Mean and Variability Output

The processing results are summarized by two sets of four text files for each wavelength, one set for the $\vec{f}$ BRDF data and one set for the $\vec{\epsilon}$ sky data. Each set contains a summary file, which summarizes the mean and variability output. An example of the summary file is shown below.

```
Data Set Information { Data/20050508_Grass/ 30,180/ grass 550 11.0 0150 0015
73.1400  0.0150000}_BRDF{ N Y Y N Y N      19765.7 N  0    1535     0 1023 }
Kernel Sizes (pixels)
          5         37        219        439        877
Equivalent GSD size (inches)
   0.0683620   0.5058792   2.9942577   6.0021877  11.9907026
Residual Energy from Registration
   0.0572607   0.0103939   0.0071458   0.0071132   0.0071911
S0  Mean, Std Dev, Skewness, Kurtosis
   0.0166094   0.0090140   1.6011703   5.0106888
   0.0166104   0.0040766   0.5525676   0.5965202
   0.0166180   0.0017481   0.5437287  -0.1169703
   0.0165713   0.0012175   0.9595386   0.0031123
   0.0165973   0.0007756   0.8129728  -0.3813481
S1  Mean, Std Dev, Skewness, Kurtosis
   0.0006589   0.0011991   2.5018150  19.9789341
   0.0006578   0.0003294   1.2999472   3.4198228
   0.0006582   0.0001342   0.9248016   1.7511740
   0.0006561   0.0000796   0.6469660   0.0960295
   0.0006607   0.0000395   0.1111674  -0.6996152
S2  Mean, Std Dev, Skewness, Kurtosis
  -0.0003548   0.0012339  -0.9124157  14.5992479
  -0.0003543   0.0002609  -0.5657478   1.9048358
  -0.0003545   0.0001560  -0.3204452   0.2708384
  -0.0003523   0.0001346  -0.3052895   0.3610795
  -0.0003582   0.0000915  -0.3335640   0.0855753
DOP  Mean, Std Dev, Skewness, Kurtosis
   0.0772946   0.0555669   2.3982752  14.0492791
   0.0458506   0.0158332   0.6786323   1.4717430
   0.0458446   0.0085645   0.3986163   0.1556489
   0.0457658   0.0066618   0.2921953  -0.1689830
   0.0456889   0.0041020   0.2470003  -0.8497894
Angle  Mean, Variance, Skewness, Kurtosis
  -6.99646001229.8257040   0.4779456   0.0640459
 -13.7265392  75.8694434   1.2383244  10.3249222
 -13.9023326  25.7786517   0.3237586   0.5526447
 -13.8850471  21.0678935   0.3188132   0.4167368
 -14.1132118  10.0025566   0.1875721   0.1167709
Reflectance Factor
```

```
0.0521801
```

The first two lines contain meta data, which provides information such as the material measured and scattering orientation, the camera exposure conditions, the required pixel-to-inch conversion factor, the equivalent DC to $\mathtt{sr}^{-1}$ conversion factor, the extent of the image used and other parameter settings from the algorithm. The `Kernel Sizes` line reports the actual pixel size used for the convolutions to obtain the `Equivalent GSD size` in inches, which is shown on the following line. Next, the mean value of the ΔE data, called the `Residual Energy from Registration` is reported which corresponds to the GSD sizes from the preceding line.

The next five sections provide the BRVF statistics for the Stokes elements and the resultant DOP and χ. Note that the labels are identical regardless of whether it is $\vec{f}$ or $\vec{\epsilon}$ data–it is only by the file name that a distinction is made between the two. So `S0` corresponds to f_{00} or ϵ_0, `S1` to f_{10} or ϵ_1, etc. Each line under the `S0, S1, S2, DOP` and `Angle` are the statistics for each of the GSD sizes from above. The first line corresponds to the 0.068 `in` data, the second line the 0.5 `in` data, etc. Each line contains the mean, standard deviation, skewness and kurtosis. (The higher-order statistics are never used, but were inherently computed by the technique, so they are also reported). Finally, the equivalent reflectance factor magnitude is reported, calculated using the mean S0 magnitude.

Note the changing mean value of S0 as the GSD size changes. This is the biasing resulting from the padding process, as discussed in §6.2.1. Also note the significant ΔE magnitude at 5×5 pixel GSD, and the resulting DOP magnitude.

6.2.2.2 Histogram Output

Accompanying each summary file are text files with the histogram data for f_{00} (or ϵ_0), DOP and χ. The binning of the data is dynamically scaled according to the data contents. As an example, the first part of a DOP histogram file is shown below.

```
Data Set Information { Data/20050508_Grass/ 30,180/ grass 550 11.0 0150 0015
73.1400   0.0150000}_BRDF{ N Y Y N Y N   19765.7 N   0    1535       0 1023 }
Equivalent GSD size (inches)
    0.06836    0.50588    2.99426    6.00219   11.99070
Minimum, Bin Size, Maximum
 0.00000000 0.00200000 1.50000000
Histogram Data
    "          "        "        "         "        "
   0.024000    25334    36237     4440        0        0
   0.026000    26927    45486    11269        0        0
   0.028000    28408    53435    17745      288        0
   0.030000    29733    62042    30019    18984        0
```

0.032000	30808	68980	49187	32131	0
0.034000	31285	73159	70782	45636	0
0.036000	32598	77510	89686	89733	22637
0.038000	33307	82191	129555	110124	70167
0.040000	33252	83704	131865	169990	244994
0.042000	33351	84121	133194	193931	297772
0.044000	33579	82079	164291	177952	273043
0.046000	33265	78329	153986	177885	134953
0.048000	33532	74042	137515	166773	218502
0.050000	33134	70328	100887	109242	187319
0.052000	32097	64330	79288	82506	80475
0.054000	32028	58334	55479	44136	22502
0.056000	31315	53120	49699	49372	595
0.058000	30443	48216	50045	47548	0
0.060000	29676	42070	30545	24662	0
0.062000	29106	35234	19951	9258	0
0.064000	28225	29985	10938	2808	0
0.066000	27524	25975	11518	0	0
0.068000	27006	22025	10317	0	0

As with the summary file, the first two lines contain metadata, followed by the applicable GSD. Next, the histogram minimum, bin size, and maximum value are given. Finally the histogram data is reported, where the first column is the magnitude of the quantity of interest, here DOP, and the next five columns correspond to the GSD of interest. Note that the first several rows are not shown for brevity.

A plot of the histograms is also generated for each of the f_{00}, DOP and χ quantities (or ϵ_0, DOP and χ in the case of the downwelled sky data), which show the change as a function of GSD. An example of the histograms from the BRDF (f_{00}) data is shown in Figure 6.5.

6.2.2.3 Qualitative Imagery

Qualitative imagery is produced of each of the three Stokes vectors or those corresponding to the $\vec{f}$ elements. In addition, the DOP and χ data are also written to image files. Each of these five images is produced for each of the four standard GSD units, as well as for the native and high-resolution 5×5 pixel kernel. The net result is a total of 30 images. These images are written out in `jpeg` format with an embedded scale corresponding to the appropriate units for the data. The $\vec{f}$ or Stokes data are shown in terms of $[\mathtt{sr}^{-1}]$ and are kept as grayscale images. The DOP ranges from 0.0–1.0 and χ is scaled from -90–90°. A color index is used for both the DOP and χ data which greatly improves the visual contrast and absolute magnitude determination.

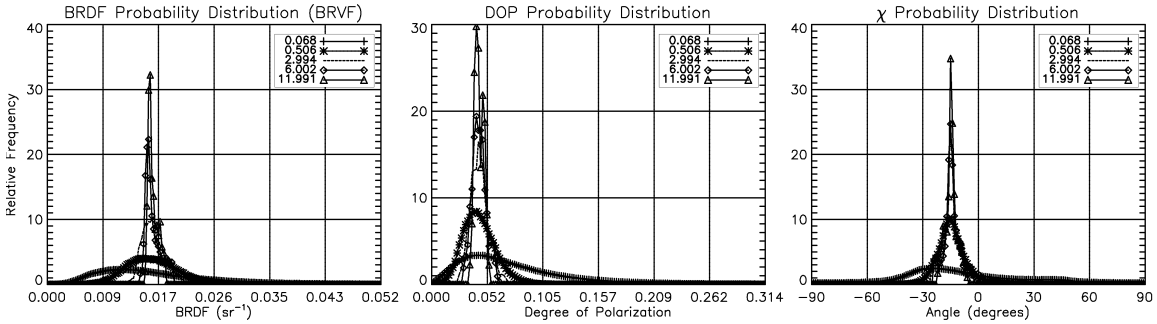

Figure 6.5: An example of the BRVF histograms generated for each hemispherical sampling location. Shown are the BRDF or f_{00} (*left*), *DOP* (*middle*) and χ (*right*) distributions as a function of GSD, shown in the legend in units of inches. These data are for lawn grass at 550 nm, with $\theta_i = 27.7°$, $\theta_r = 30°$ and $\phi = 180°$.

The dynamic range of these images are scaled such that the same range is present for all GSD sizes, facilitating a comparison. The maximum scale value for the f_{00} and *DOP* images is set such that 99.5% of the pixels are less than the maximum scale value, or in other words the "brightest" 0.5% of all pixels are saturated. This maximum magnitude is determined from the data processed with the 5×5 kernel. Using this maximum value, the magnitude of the Stokes or f_{10} and f_{20} images are set to ± 0.25 of the maximum magnitude.

Finally, the ΔE data is written out using the native resolution data, the 5×5 data, and at the 0.5 and 3 in GSD level. This scale is consistently set to a maximum of 0.1, which provides a consistent means of inter-comparison of all data sets, to include different materials. Examples of the qualitative imagery may be seen in Figure 6.6.

6.3 Measurement Results

The data produced from the measurements are extensive, making a succinct presentation of the results difficult. The complete data set accompanies this document on a DVD ROM, with a description of the archiving method and file naming convention provided in Appendix A.

The data presented in this section are limited to three primary materials which had an adequate number of measurements: top soil, asphalt and lawn grass. For these materials, the following measurement results are presented for each scattering or imaging location. Note that only mean values are presented here. The variability data are included in §A.1.

1. pBRDF The f_{00}, f_{10}, f_{20} pBRDF Mueller matrix components per equation 4.19. These are the inherent quantities the measurement is intended to quantify.

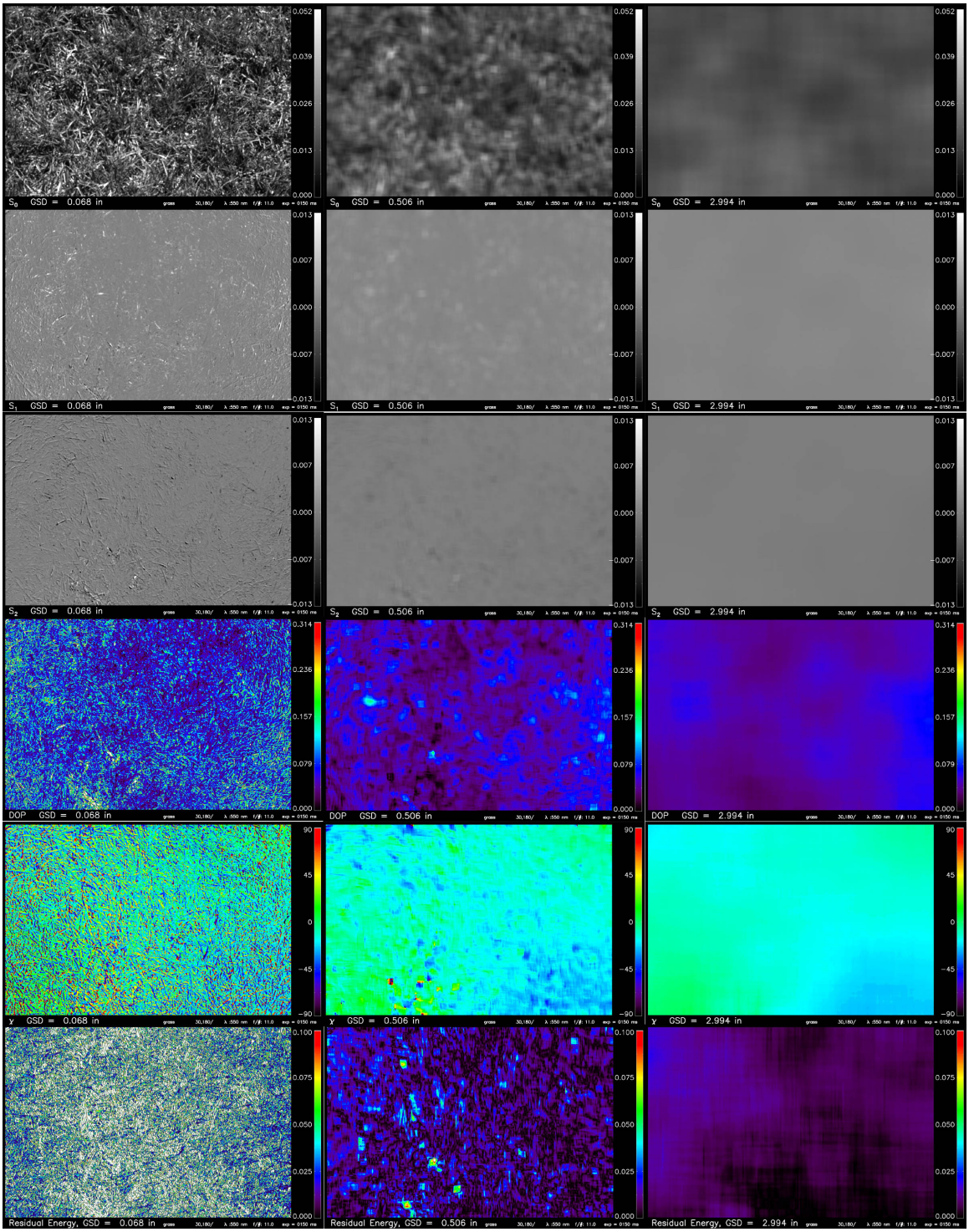

Figure 6.6: Examples of the images written out as part of the data processing for visual reference. From top to bottom are f_{00}, f_{10}, f_{20}, DOP, χ and ΔE, with an increasing GSD from left to right of 0.07 `in` (the 5×5 high resolution data), 0.5 and 3.0 `in`. These data are for lawn grass at 550 `nm`, with $\theta_i = 27.7°$, $\theta_r = 30°$ and $\phi = 180°$, and may be compared with the histograms shown in Figure 6.5. Note the considerable ΔE magnitude and resulting error in the high-resolution DOP and χ images. The spatial registration of grass is particularly challenging, as there is often some movement of the blades between successive images (*cf.* §6.3.3).

2. Sky Contribution The mean ϵ_0, ϵ_1 and ϵ_2 values or the "sky" contribution ($\vec{L}_d$) to the signature per equation 4.19. The $\vec{\epsilon}$ data change depending upon the sky condition, and as such are only representative of the weather conditions at the time of the measurement.

3. Total Stokes The S_0, S_1 and S_2 mean Stokes radiance measured with both the sun ($\vec{L}_r$) and sky ($\vec{L}_d$) radiance contributions—or the signal as it would be measured by a remote sensor. This is equivalent to $f_{xx} + \epsilon_x$.

4. *DOP* Two degree of polarization quantities are given, that resulting from the BRDF, or solar-only ($\vec{f}_{xx}$) contributions and the total, or that from $\vec{S}$.

5. ΔE The residual signal left by the difference between the two cross polarization measurements, as shown by equation 5.40. This quantity is given for $GSD = 3$ `in`.

The units for the $\vec{\epsilon}$ and $\vec{S}$ quantities are a bit confusing. They are given in units of [$\mathtt{sr}^{-1}$] such that they remain relative in magnitude to the $\vec{f}$ pBRDF quantities. However, it is not proper to consider these as true BRDF magnitudes since the scale factor is provided by the solar-only illumination magnitude.

A description of the measured materials and their results follow. All measurements were made in Rochester, New York. Additional data analysis is in Chapter 7, which presents much of the GSD-dependent variability data.

6.3.1 Topsoil Results

The topsoil measurements were made on May 20, 2005, and spanned from 12:24–4:01 PM, Eastern Standard Time. This duration made it possible to acquire data at solar incident angles ranging from 23.3° to 53.6°. The topsoil data is the most extensive measurement made, with ten scattering positions measured at both 550 and 750 `nm`. The soil was not *in situ*, but dug up and spread on a plastic tarp to a depth of a few inches such that no effects of the tarp were present. The soil was raked to provide a relatively uniform surface, then allowed to dry for several hours to reach an equilibrium state so that further changes would not impact the measurement results. An overview of the measurement area and the soil surface is shown in Figure 6.7. The topsoil measurement results are summarized in Table 6.1.

The average f_{00} magnitude for the soil measurements is 0.02468 $\mathtt{sr}^{-1}$ at 550 `nm` and 0.04364 $\mathtt{sr}^{-1}$ at 750 `nm`, which is equivalent to reflectance factors of $\rho(550) = 0.0775$ and $\rho(750) = 0.1371$ (Table 6.1). There is an appreciable range in f_{00} magnitude, reaching a maximum near the retroreflection or "hot spot" orientation and having a minimum in

Table 6.1: The BRDF measurement results for top soil. The variability data are presented in Table A.1.

Orientation [°]			BRDF (Sun Only) [$\mathtt{sr}^{-1}$]			SKY (Sky Only) [$\mathtt{sr}^{-1}$]			TOTAL (Sun + Sky) [$\mathtt{sr}^{-1}$]			DOP		ΔE
θ_i	θ_r	ϕ	f_{00}	f_{10}	f_{20}	ϵ_0	ϵ_1	ϵ_2	S_0	S_1	S_2	(BRDF)	(Total)	(GSD=3")
550 nm														
27.4	0	0	0.02873	0.00061	-0.00017	0.00405	0.00004	-0.00012	0.03279	0.00065	-0.00029	0.02200	0.02172	0.18%
48.0	0	0	0.02400	0.00155	0.00019	0.00513	0.00025	-0.00004	0.02913	0.00180	0.00015	0.06497	0.06205	0.37%
29.5	30	40	0.04273	0.00034	-0.00010	0.00619	0.00000	-0.00009	0.04892	0.00034	-0.00019	0.00837	0.00804	0.29%
45.5	30	80	0.02715	-0.00111	0.00041	0.00731	-0.00011	-0.00009	0.03446	-0.00122	0.00032	0.04370	0.03658	0.24%
53.6	30	135	0.01797	0.00025	0.00204	0.00796	0.00011	0.00041	0.02593	0.00036	0.00245	0.11462	0.09555	0.14%
23.3	30	180	0.02042	0.00132	-0.00029	0.00412	0.00019	0.00000	0.02454	0.00151	-0.00029	0.06606	0.06269	0.32%
30.8	45	0	0.04125	0.00023	0.00003	0.00638	0.00002	0.00002	0.04763	0.00025	0.00005	0.00570	0.00533	0.16%
24.3	45	180	0.01675	0.00184	-0.00026	0.00423	0.00040	-0.00007	0.02099	0.00224	-0.00033	0.11109	0.10781	0.51%
33.4	63	180	0.01500	0.00232	-0.00050	0.00595	0.00085	-0.00021	0.02095	0.00317	-0.00070	0.15794	0.15488	0.66%
51.2	68	180	0.01276	0.00235	-0.00050	0.00724	0.00128	-0.00013	0.02000	0.00363	-0.00063	0.18839	0.18408	1.02%
750 nm														
27.4	0	0	0.04957	0.00067	-0.00005	0.00638	-0.00004	-0.00010	0.05595	0.00063	-0.00015	0.01351	0.01160	0.34%
48.0	0	0	0.04305	0.00149	0.00012	0.00817	-0.00019	0.00006	0.05122	0.00130	0.00018	0.03467	0.02554	1.18%
29.5	30	40	0.07045	0.00036	-0.00001	0.01183	-0.00001	-0.00007	0.08229	0.00035	-0.00008	0.00512	0.00437	0.59%
45.5	30	80	0.04886	-0.00135	0.00036	0.01098	-0.00010	0.00012	0.05985	-0.00145	0.00047	0.02860	0.02546	0.52%
53.6	30	135	0.03550	0.00032	0.00251	0.00807	-0.00007	0.00032	0.04357	0.00026	0.00283	0.07126	0.06521	0.35%
23.3	30	180	0.03682	0.00143	-0.00035	0.00915	0.00027	0.00003	0.04596	0.00170	-0.00032	0.03990	0.03763	0.73%
30.8	45	0	0.06891	0.00005	0.00020	0.01577	-0.00003	0.00005	0.08468	0.00002	0.00026	0.00303	0.00304	0.26%
24.3	45	180	0.03121	0.00215	-0.00007	0.01099	0.00029	-0.00009	0.04220	0.00245	-0.00016	0.06907	0.05812	0.42%
33.4	63	180	0.02784	0.00233	-0.00059	0.02167	0.00096	-0.00013	0.04951	0.00329	-0.00072	0.08651	0.06805	0.13%
51.2	68	180	0.02419	0.00247	-0.00049	0.02562	0.00184	-0.00007	0.04981	0.00431	-0.00056	0.10407	0.08734	0.58%

Figure 6.7: The measurement area and close-up of the topsoil.

the forward scattering direction. This magnitude change is characteristic of most natural materials, where self-shadowing reduces the signature away from the solar angle and conversely near the solar angle the signature is a maximum due to minimal self-shadowing. The maximum for both bands is 60–70% above the mean, with the minimum being $\approx 55\%$ of the mean.

It is interesting to examine the ratio between the f_{00} magnitudes at 550 and 750 nm for the same orientation. This ratio stays relatively constant, between 0.53 and 0.61 indicating the BRDF "shape" does not change appreciably between the two bands, but is scaled by the total brightness. This concept will become instrumental in extrapolating these results to other spectral bands, to be addressed in Chapter 7 on the Background Model.

The f_{00} images could easily be mistaken for those made on the lunar surface, or other planetary body without an atmosphere. The effect of removing the downwelled sky radiance is dramatic and results in completely dark shadowed regions with significant contrast. The hot-spot phenomena is also visually evident in one of the measurements, where an overall brightness change is noted within an image frame. These effects are seen in Figure 6.8.

The DOP reaches a maximum of 0.1883 at 550 nm and 0.1041 at 750 nm. These results are consistent with Umov's law, or the fact that DOP is inversely proportional to reflectance. The polarization effects are examined in detail with the development of the Background Model, Chapter 7.

Interpretation of $\vec{\epsilon}$ resulting from the downwelled sky is more difficult. To first order, one would expect the magnitude of ϵ_0 to be relatively constant with respect to scattering orientation, assuming similar sky conditions. However, there appears to be more variability than can be accounted for from varying sky conditions.

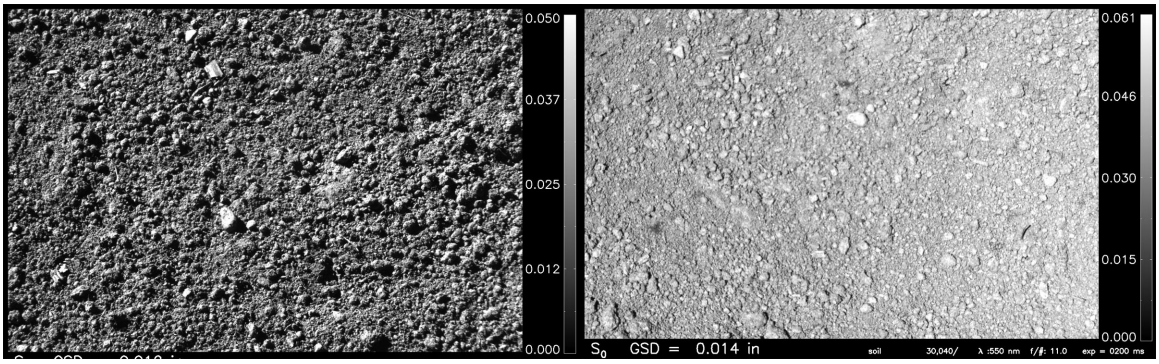

Figure 6.8: The dramatic shadow contrast resulting from removal of the downwelled sky radiance is noted in this f_{00} image at left, where $\theta_i = 53.6°$, $\theta_r = 30°$ and $\phi = 135°$. At right, a gradual increase in the f_{00} signal is noted going from the left of the image to the right, or approaching the retroreflection position. $\theta_i = 29.5°$ with the scattering orientation at the center approximately $\theta_r = 30°$ and $\phi = 40°$. Both images are at $\lambda = 550$ nm.

It is also observed that the ratio of ϵ_0 to the average f_{00} is consistently much higher than the same ratio for the calibration panel data (not shown in the Table). For instance, the cosine-adjusted sky radiance fraction from the calibration panel measurements had a mean of 10.0% at 550 nm with minimal variability. However, the average ϵ_0 to mean f_{00} magnitude was 23.7%. This indicates that the sky is responsible for a larger fraction of the total signal compared to a smooth Lambertian surface. This effect is understood by considering the significant self-shadowing and resulting radiance reduction.

6.3.2 Lawn Grass Results

The lawn grass measurements were made on May 8, 2005, and spanned from 12:57–3:05 PM, Eastern Standard Time, resulting in incident solar angles from 27.7° to 45.2°. A total of nine scattering positions were measured at 550 and 750 nm, but one of the 550 nm measurements was not useful due to the tripod being bumped between images. The grass was very healthy and had been mowed five days prior to the measurement; however, there were no visually discernable "mow" patterns remaining. An overview of the area and a close-up of the region measured are shown in Figure 6.9.

The grass measurements impose an additional constraint—there must be minimal wind. Movement of the individual grass blades by the wind results in spatial misregistration among the eight images. This particular day was relatively calm, and care was used to image during calm periods. The summary of the grass measurement results are shown in Table 6.2.

The average f_{00} magnitude for the grass measurements is 0.02167 sr^{-1} at 550 nm and

Table 6.2: The BRDF measurement results for lawn grass. The variability data are presented in Table A.2.

Orientation [°]			BRDF (Sun Only) [$\mathtt{sr}^{-1}$]			SKY (Sky Only) [$\mathtt{sr}^{-1}$]			TOTAL (Sun + Sky) [$\mathtt{sr}^{-1}$]			*DOP*		ΔE
θ_i	θ_r	ϕ	f_{00}	f_{10}	f_{20}	ϵ_0	ϵ_1	ϵ_2	S_0	S_1	S_2	(BRDF)	(Total)	(GSD=3")
550 nm														
45.2	0.0	0.0	0.01874	0.00062	-0.00005	0.00222	0.00004	-0.00001	0.02096	0.00066	-0.00006	0.03320	0.03161	0.49%
36.7	30.0	45.0	0.02384	-0.00011	0.00004	0.00267	-0.00006	0.00000	0.02650	-0.00016	0.00004	0.00479	0.00636	0.43%
34.5	30.0	90.0	0.01903	-0.00001	0.00048	0.00261	0.00002	0.00006	0.02163	0.00000	0.00055	0.02538	0.02531	0.35%
27.7	30.0	180.0	0.01661	0.00066	-0.00035	0.00242	0.00009	-0.00003	0.01903	0.00075	-0.00038	0.04506	0.04439	0.72%
32.5	45.0	0.0	0.03153	0.00012	-0.00001	0.00407	0.00000	0.00001	0.03560	0.00011	0.00000	0.00369	0.00321	0.35%
38.2	45.0	50.0	0.02516	-0.00015	0.00053	0.00394	-0.00002	0.00009	0.02910	-0.00016	0.00063	0.02203	0.02229	0.22%
29.3	45.0	180.0	0.01630	0.00084	-0.00034	0.00353	0.00019	-0.00006	0.01983	0.00103	-0.00040	0.05582	0.05590	0.68%
43.0	61.0	180.0	0.02212	0.00104	-0.00021	0.00508	0.00029	-0.00015	0.02720	0.00134	-0.00035	0.04811	0.05083	0.49%
750 nm														
31.2	0.0	0.0	0.12306	0.00088	-0.00074	0.01214	0.00003	-0.00023	0.13520	0.00090	-0.00097	0.00932	0.00982	0.40%
45.2	0.0	0.0	0.13291	0.00108	0.00045	0.01280	-0.00012	-0.00033	0.14571	0.00096	0.00011	0.00876	0.00662	0.33%
36.7	30.0	45.0	0.13998	-0.00072	-0.00008	0.01703	0.00014	0.00018	0.15700	-0.00058	0.00010	0.00517	0.00375	0.35%
34.5	30.0	90.0	0.12604	-0.00077	0.00093	0.01745	0.00072	-0.00012	0.14349	-0.00005	0.00081	0.00958	0.00569	0.30%
27.7	30.0	180.0	0.11903	0.00032	-0.00026	0.01598	0.00031	0.00000	0.13501	0.00063	-0.00026	0.00348	0.00504	0.20%
32.5	45.0	0.0	0.16125	-0.00017	0.00009	0.02380	-0.00007	0.00023	0.18506	-0.00024	0.00031	0.00118	0.00213	0.55%
38.2	45.0	50.0	0.15190	-0.00042	0.00031	0.02463	-0.00035	-0.00002	0.17653	-0.00078	0.00029	0.00345	0.00470	0.44%
29.3	45.0	180.0	0.12235	0.00057	-0.00038	0.02121	-0.00001	0.00014	0.14357	0.00055	-0.00024	0.00557	0.00420	0.27%
43.0	61.0	180.0	0.14561	0.00100	0.00012	0.03038	0.00008	-0.00018	0.17599	0.00108	-0.00006	0.00690	0.00615	0.25%

Figure 6.9: An overview of the lawn grass area with a close-up of the region measured.

0.13579 $\mathtt{sr}^{-1}$ at 750 nm, which is equivalent to reflectance factors of $\rho(550) = 0.0681$ and $\rho(750) = 0.4316$ (Table 6.2). As with the topsoil data, the maximum signature is in the retroreflection position, with a minimum in the forward scattering location. However, there is much greater variability in the f_{00} ratios between the two spectral bands at a given orientation compared to the topsoil. The ratios range from 0.140 to 0.196, with the smallest value being in a forward scattering location ($\theta_i = 27.7°, \theta_r = 30.0°, \phi = 180.0°$) and the highest near the retroreflection position ($\theta_i = 32.5°, \theta_r = 45.0°, \phi = 0.0°$). It is hypothesized that this results from considerable "secondary" illumination of the grass by itself at 750 nm, which is approximately six times more reflective than at 550 nm. BRDF images at the forward scattering orientation of $\theta_i = 27.7°, \theta_r = 30.0°, \phi = 180.0°$ support this premise, as shown in Figure 6.10.

As previously mentioned, movement of the grass by the wind poses a unique challenge, and is most problematic at 550 nm. At 550 nm there is greater contrast, enhancing any grass movement or misregistration. In addition, a slight change in a grass blade orientation may result in a significant change in the magnitude of a specular reflection from that blade, even though there may be good spatial registration. This potentially contributes to significant DOP calculation uncertainties. However, examination of the ΔE data and imagery demonstrate these effects are mitigated once the minimum processing GSD is reached or $GSD = 0.5$ in—see Figure 6.11.

The grass DOP is examined after having satisfied concerns that meaningful calculations may be made from the measurements. The DOP for the grass at 750 nm is negligible, and at 550 nm the measured maximum was 0.056, occurring in the forward scattering orientation of $\theta_i = 29.3°, \theta_r = 45.0°, \phi = 180.0°$. As anticipated, the minimum DOP was measured in

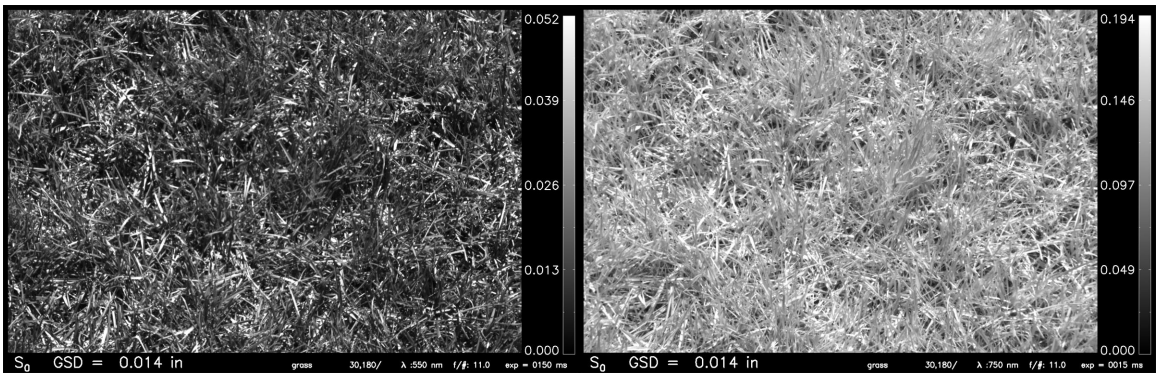

Figure 6.10: The appearance of grass between 550 `nm` and 750 `nm` is significantly different (left and right), beyond a simple reflectance magnitude change—note the change in the $\mathtt{sr}^{-1}$ scale between the images. At 550 `nm`, significant contrast results from shadowing, while at 750 `nm` secondary reflections "self illuminate" solar shadowed regions. ($\theta_i = 27.7°, \theta_r = 30.0°, \phi = 180.0°$).

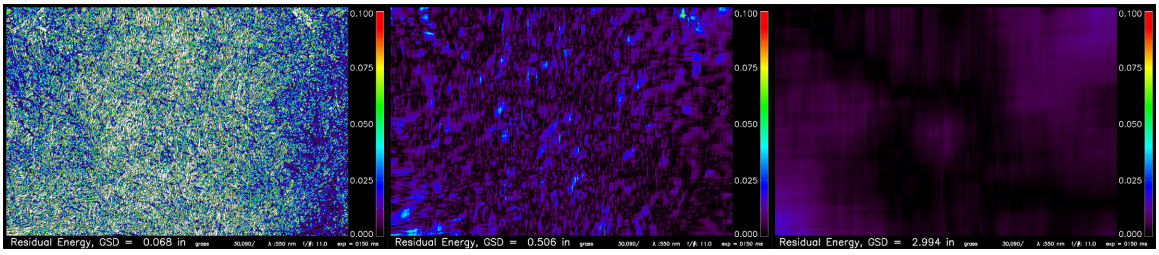

Figure 6.11: For the grass measurements, a significant ΔE magnitude is present at $GSD = 0.068$ `in` (*left*, a 5×5 pixel averaging) but quickly diminishes with increasing GSD as seen from the $\Delta E(GSD = 0.5")$ (*middle*) and $\Delta E(GSD = 3.0")$ (*right*). The mean ΔE values are 0.057, 0.010 and 0.007, respectively, with a maximum magnitude scale of 0.1 for all images. (Compare with the typical ΔE data from the topsoil, Figure 5.20).

Figure 6.12: An overview of the asphalt area with a close-up of the asphalt surface. The close-up is approximately 18 `in` across.

the orientation closest to the retro-reflection position, at $\theta_i = 32.5°, \theta_r = 45.0°, \phi = 0.0°$.

6.3.3 Asphalt Results

The asphalt measurements were made on April 21, 2005, and spanned from 10:18–11:26 AM, Eastern Standard Time, resulting in incident solar angles from 39.3° to 32.5°. The asphalt area measured was highly uniform, and rather than imaging a common area by repositioning the camera, the camera head was simply rotated to obtain different azimuth views. The only negative consequence is that in a few of the images, relatively dark asphalt regions were present. However, these dark regions were eliminated from the analysis. The measurement area and asphalt surface are shown in Figure 6.12.

The scattering angles are also limited in this data set, with only one $\theta_r = 45°$ measurement, the rest being $\theta_r = 0, 30°$. The limitation in high θ_r data was a consequence of the solar obscuration or shadow panel being too small, which was later enlarged. (High θ_r angles cover a larger ground region, thus requiring a larger shadow area). Another difference with this data set is that both spectral bands were not collected at the same hemispherical position. A total of six hemispherical measurement positions were made at 550 `nm` and five at 750 `nm`. The summary of the asphalt measurement results are shown in Table 6.3.

The average f_{00} magnitude for the asphalt measurements is 0.04231 $\mathtt{sr}^{-1}$ at 550 `nm` and 0.05021 $\mathtt{sr}^{-1}$ at 750 `nm`, with equivalent reflectance factors of $\rho(550) = 0.1329$ and $\rho(750) = 0.1577$. As with the topsoil and grass, the minimum reflectance is in the forward scattering orientation with a maximum noted toward the retroreflection position. However, the change in the BRDF magnitude is not as dramatic for the asphalt as observed with the

Table 6.3: The BRDF measurement results for asphalt. The variability data are presented in Table A.3.

Orientation [°]			BRDF (Sun Only) [$\mathtt{sr}^{-1}$]			SKY (Sky Only) [$\mathtt{sr}^{-1}$]			TOTAL (Sun + Sky) [$\mathtt{sr}^{-1}$]			*DOP*		ΔE
θ_i	θ_r	ϕ	f_{00}	f_{10}	f_{20}	ϵ_0	ϵ_1	ϵ_2	S_0	S_1	S_2	(BRDF)	(Total)	(GSD=3")
550 nm														
35.4	0.0	0.0	0.04188	0.00063	-0.00031	0.00430	0.00013	-0.00015	0.04618	0.00076	-0.00046	0.01677	0.01924	0.45%
35.9	30.0	40.0	0.05073	0.00023	-0.00004	0.00646	0.00005	0.00011	0.05719	0.00028	0.00007	0.00460	0.00505	0.53%
37.0	30.0	90.0	0.04449	-0.00012	0.00137	0.00620	0.00006	0.00007	0.05069	-0.00006	0.00144	0.03091	0.02843	0.17%
37.8	30.0	135.0	0.03947	0.00209	0.00136	0.00559	0.00026	0.00017	0.04506	0.00235	0.00153	0.06318	0.06223	0.33%
38.4	30.0	180.0	0.03859	0.00271	-0.00048	0.00550	0.00035	-0.00010	0.04409	0.00306	-0.00058	0.07132	0.07064	0.21%
39.3	45	180	0.03869	0.00465	-0.00176	0.00650	0.00043	-0.00024	0.04519	0.00508	-0.00200	0.12851	0.12081	0.43%
750 nm														
34.3	0	0	0.05044	0.00065	-0.00071	0.00397	0.00011	0.00004	0.05441	0.00076	-0.00067	0.01908	0.01862	0.35%
32.5	30	40	0.05863	0.00014	0.00004	0.00591	0.00024	0.00005	0.06454	0.00038	0.00009	0.00248	0.00605	0.40%
32.9	30	90	0.05126	0.00011	0.00166	0.00584	-0.00002	0.00001	0.05710	0.00009	0.00167	0.03245	0.02929	0.32%
33.2	30	135	0.04537	0.00277	0.00161	0.00537	-0.00005	-0.00016	0.05074	0.00272	0.00145	0.07062	0.06075	0.70%
33.8	30	180	0.04536	0.00297	-0.00101	0.00520	0.00020	-0.00008	0.05056	0.00317	-0.00109	0.06916	0.06630	0.63%

topsoil and grass. For both the 550 nm and 750 nm data, the maximum f_{00} magnitude is approximately 30% greater than the minimum magnitude.

A direct one-to-one comparison of the relative f_{00} magnitudes between 550 and 750 nm is not possible due to the geometry differences. However, from the similar scattering geometries it is noted that the ratio of the 550 nm to 750 nm stays relatively constant ranging from 0.83 to 0.87. As with the topsoil results, the BRDF shape appears to be maintained between the two bands, and simply scaled by the total magnitude.

As with the other measurements, the DOP is observed to follow Umov's law, with $DOP(550)$ generally greater than $DOP(750)$ for similar orientations. The maximum DOP is noted in the forward scattering orientation.

6.3.4 Additional Results

Additional measurements of asphalt and grass as well as landscape mulch were completed on other days, but the data sets are incomplete or have considerable error due to the presence of high cirrus clouds. Some of these data are presented in Appendix A.

A critical element of the measurements, the GSD dependent variability, has not been presented here. These data are discussed as part of the BRDF model development in Chapter 7. All the variability data is also presented in tabular form in Appendix A.

Chapter 7

Background pBRDF Model

Having obtained experimental data on materials which constitute the polarized background or "clutter" environment, a means to model and represent these materials is needed. An appropriate model enables extrapolation of the results to arbitrary illumination and sensor orientations, as well any VNIR spectral band. The only known existing pBRDF model for background material, that used in support of the POLDER program (*cf.* §2.2.6.2), provides only crude estimates of the signature given two generic material classes. Furthermore, there is no ability to account for the natural variability present in naturally-occurring materials.

Unlike the target material pBRDF model, the background model is highly empirical with only a few physics-based underpinnings. The end objective is not a high-fidelity representation of specific materials, but a means to quantify the pBRDF behavior and variability for materials. Having accomplished this, synthetic image generation programs may realistically represent the polarimetric behavior of background materials. This in turn provides the means to fully explore algorithms exploiting spectral-polarimetric signatures.

As discussed in Chapter 5, the experimental data only enable derivation of the first column of the pBRDF Mueller matrix, or the f_{00}, f_{10} and f_{20} components. This results in the inability to formally handle incident polarized radiance, such as that from portions of the sky. However, it will be shown that the impact from this lack of fidelity is negligible.

The background pBRDF model directly provides *i*) f_{00} or the intensity component of the BRDF, *ii*) DOP (degree of polarization) and *iii*) χ, the polarization orientation. These quantities are needed for all permutation of illumination orientations (θ_i) and sensor

orientations (θ_r, ϕ_r). From these values, f_{10} and f_{20} may be determined from

$$f_{10} = \frac{DOP f_{00}}{\sqrt{1+\tan^2(2\chi)}} \qquad \begin{cases} +f_{10} & \text{if } -\frac{\pi}{4} \le \chi \le \frac{\pi}{4}, \\ -f_{10} & \text{if } -\frac{\pi}{2} \le \chi < -\frac{\pi}{4} \text{ or } \frac{\pi}{4} < \chi \le \frac{\pi}{2} \end{cases} \tag{7.1}$$

$$f_{20} = \frac{DOP f_{00} \tan(2\chi)}{\sqrt{1+\tan^2(2\chi)}} \qquad \begin{cases} +f_{20} & \text{if } 0 \le \chi \le \frac{\pi}{2}, \\ -f_{20} & \text{if } -\frac{\pi}{2} \le \chi < 0\ , \end{cases} \tag{7.2}$$

which is similar to that given previously, but with the Stokes components in place of the f_{xx} elements, see (5.23) and (5.24).

Discussion of the background model proceeds by first examining the data at the two measured spectral bands. After characterizing the behavior of the average f_{00}, DOP and χ quantities, a means to quantify the variability of these parameters as a function of GSD is developed. A spectral extrapolation technique is derived bringing all the model elements together, followed by a summary of the calculations. A comparison of the model to the measurements is made, and finally known shortcomings of the model are addressed. The implementation and validation of this model into a high-fidelity synthetic image simulator, DIRSIG, will be addressed in Chapter 9.

7.1 Mean Values

7.1.1 Scalar BRDF (Intensity) Component

The Roujean BRDF model (*cf.* §2.2.4) was selected to model the intensity-only or f_{00} BRDF component. The Roujean model is a popular BRDF model for landcover materials and has been shown to provide a good representation of a wide range of materials [93, 39]. Recall that the Roujean model has only three parameters, $\mathtt{k_0}$, $\mathtt{k_1}$ and $\mathtt{k_2}$, given by

$$f_{00}(\theta_i, \theta_r, \phi) = [\mathtt{k_0} + \mathtt{k_1} f_1(\theta_i, \theta_r, \phi) + \mathtt{k_2} f_2(\theta_i, \theta_r, \phi)] \left(\frac{1}{100\ \pi}\right)\ . \tag{7.3}$$

The model is most commonly used to provide a "reflectance factor," resulting in the $\mathtt{k}$ parameters being proportional to reflectance. Equation 7.3 is actually the Roujean model multiplied by $\frac{1}{100\ \pi}$, which results in a proper BRDF having units of $[\mathtt{sr}^{-1}]$. Used in this manner, the $\mathtt{k}$ parameters are still derived in reflectance units, which facilitates a comparison with other published values. The f_1 and f_2 functions are strictly driven by the geometry of the incident and reflected directions, and were previously given by (2.93) and (2.94).

Even though all materials have azimuthal symmetry, the background BRDF model

requires the azimuth angle to be specified over the full azimuth range of $0 \leq \phi < 2\pi$. This is necessary to provide the correct polarization angle, χ, which in turns provides the correct f_{10} and f_{20} ratios. However, the Roujean model restricts the azimuth angle to $0 \leq \phi \leq \pi$, with symmetry accounting for the other half of the scattering azimuth angles. This requirement forces conditioning of ϕ such that it is in the proper range when $\phi > \pi$. One such statement providing this is `IF` $\phi > \pi$ `THEN` $\phi = 2\pi - \phi$.

Determination of the $\mathtt{k_0}$, $\mathtt{k_1}$ and $\mathtt{k_2}$ Roujean parameters providing the best fit to the data is accomplished via a least squares fit. Having more than three measurements results in an overdetermined system of linear equations. Consider a set of n measurements made on a material. This experimental data may be expressed using (7.3) as

$$\vec{f_{00}} = \vec{\mathtt{k}}\ \mathbb{F} \tag{7.4}$$

where $\vec{f_{00}}$ is a $1 \times n$ row vector of measured values, $\vec{\mathtt{k}}$ is the 1×3 vector of Roujean parameters sought, $[\mathtt{k_0}, \mathtt{k_1}, \mathtt{k_2}]$ and $\mathbb{F}$ is a $3 \times n$ matrix consisting of column vectors of $\begin{bmatrix} 1 \\ f_1^n \\ f_2^n \end{bmatrix}$ for each of the n measurements or

$$\mathbb{F} = \begin{bmatrix} 1 & \cdots & 1 \\ f_1^0 & \cdots & f_1^{n-1} \\ f_2^0 & \cdots & f_2^{n-1} \end{bmatrix} . \tag{7.5}$$

The least squares solution for $\vec{\mathtt{k}}$ is therefore found by

$$\vec{\mathtt{k}} = \vec{f_{00}}\ \mathbb{F}^{\#} \tag{7.6}$$

where $\mathbb{F}^{\#}$ is the pseudo-inverse of $\mathbb{F}$ given by

$$\mathbb{F}^{\#} = \mathbb{F}^T \left(\mathbb{F}\ \mathbb{F}^T \right)^{-1} . \tag{7.7}$$

Therefore the three Roujean parameters $\mathtt{k_0}$, $\mathtt{k_1}$ and $\mathtt{k_2}$ may be determined for each material at each wavelength measured, which in turn provides the f_{00} BRDF component at arbitrary illumination and reflection orientations per (7.3). Table 7.1 provides an example of the model performance for "lawn grass" at 550 `nm`, where the model results are compared to the measurements. Also shown in Table 7.1 is the Lambertian BRDF estimate determined by RMSE minimization. The Lambertian estimate results in significant error at some geometries, although at one orientation is does provide a better result. The Roujean model results for all materials at both wavelengths is included in §A.2 of the extended measurement

Table 7.1: Measured vs. Roujean-modelled BRDF for grass at 550 nm where $[k_0, k_1, k_2] = [6.8702, 0.3881, 29.0824]$. The RMSE for this data set is 0.001022. The best Lambertian estimate is 0.01956 sr^{-1}, resulting in considerable error at some geometries. The same comparisons with the additional data sets are included in §A.2.

θ_i [°]	θ_r [°]	ϕ [°]	**Measured** [sr^{-1}]	**Modelled** [sr^{-1}]	**Modelled Error** [%]	**Lambertian Error** [%]
45.2	0	0	0.01874	0.01927	2.84	4.38
36.7	30	45	0.02384	0.02464	3.37	-17.95
34.5	30	90	0.01903	0.01971	3.56	2.79
27.7	30	180	0.01661	0.01586	-4.5	17.76
32.5	45	0	0.03153	0.02957	-6.23	-37.96
38.2	45	50	0.02516	0.02659	5.67	-22.26
29.3	45	180	0.01630	0.01558	-4.42	20.00
43.0	61	180	0.02212	0.02211	-0.02	-11.57

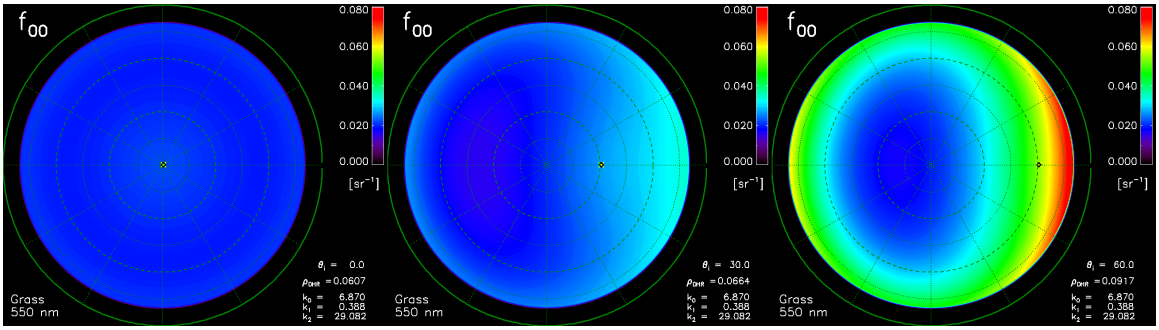

Figure 7.1: The Roujean-modelled BRDF of grass at 550 nm using $[k_0, k_1, k_2] = [6.8702, 0.3881, 29.0824]$. The incident illumination is at $\theta_i = 0°$ (*left*), $\theta_i = 30°$ (*middle*) and $\theta_i = 60°$ (*right*). Note that the maximum θ_r calculated is 80°. The complete set of hemispherical results are included in §A.2.

results Appendix.

Figure 7.1 provides the Roujean results of the lawn grass at 550 nm throughout the scattering hemisphere for incident illumination angles of $\theta_i = 0°, 30°$ and 60°.

7.1.2 Degree of Polarization (*DOP*)

The *DOP* has been shown to be highly correlated with the phase angle, ξ, or the total angular extent between the illumination source and receiver. ξ was previously given in

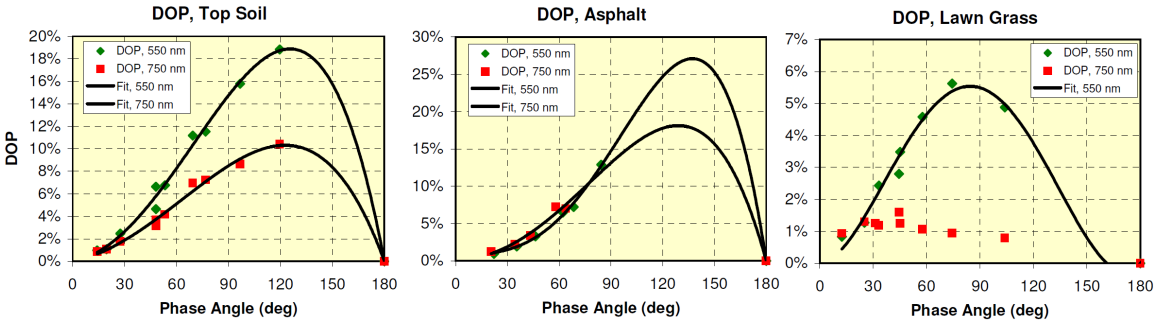

Figure 7.2: The DOP versus the phase angle, ξ for top soil, asphalt and lawn grass at 550 and 750 nm. Fourth-order polynomial fits are shown with the data. No fit is made for the grass data at 750 nm, as the DOP is minimal and subject to measurement uncertainty as discussed in §5.3.7.2.

(2.95), but is also given here for reference as[1]

$$\cos\xi = \cos\theta_i \cos\theta_r + \sin\theta_i \sin\theta_r \cos\phi \ . \tag{7.8}$$

It is in ξ-space that the DOP is extrapolated for a given set of θ_i, θ_r and ϕ. A fourth order polynomial was found to provide a good fit to the experimental data. It is via this polynomial that the DOP is determined as a function of ξ according to

$$DOP(\xi) = \mathtt{p}_1\ \xi + \mathtt{p}_2\ \xi^2 + \mathtt{p}_3\ \xi^3 + \mathtt{p}_4\ \xi^4 \ , \tag{7.9}$$

where it is noted that there is no zero order coefficient since $DOP(0) = 0$. The $\mathtt{p}_1$ through $\mathtt{p}_4$ coefficients are given for ξ in radians. Figure 7.2 demonstrates the correlation by showing the measured DOP versus ξ for top soil, asphalt and grass at 550 and 750 nm. For the asphalt data there is some uncertainty in the actual maximum DOP, as there are a lack of measurements at high ξ conditions. These fits are simply scaled versions of polarization from Fresnel reflectance (recall Figure 2.1), but for the total scatter angle ξ instead of the half angle. From this basis, it is also known that as $\xi \rightarrow 180°$ that $DOP \rightarrow 0.0$; therefore this data point has been added to all measured data sets.

The DOP in the scattering hemisphere is therefore determined by mapping the phase angle, ξ, and corresponding DOP into the scattering hemisphere. For the grass measurements at 550 nm, the results are shown as Figure 7.3.

[1]N. B. For the numerical calculation of ξ, caution is required when $\theta_i = \theta_r$ and $\phi = 0$ or π. Floating point round error can easily result in a $\cos^{-1}$ argument magnitude that is > 1.0.

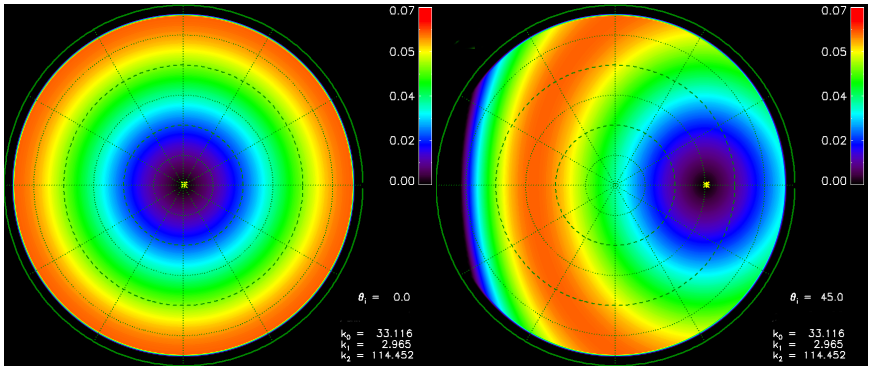

Figure 7.3: *DOP* of grass at 550 nm as determined by the polynomial fit to the phase angle from Figure 7.2. $\theta_i = 0°$ (left) and $\theta_i = 45°$ (right).

7.1.3 Polarization Orientation (χ)

The mean value of the polarization orientation, which relates the ratio of the f_{10} and f_{20} magnitudes is determined strictly by geometry. Assuming all polarization is attributed to front-surface, single event reflectance, then χ is uniquely determined from the required orientation of the microfacet needed to specularly reflect radiance in the sensor direction. In theory, there is some deviation in the actual polarization angle from the "front surface only" reflectance due to contributions from p-polarized volumetric scattering being transmitted through the surface, but it is not measurable to within the tolerance of the measurement system. The measurement technique only supports determining the mean χ to within $\pm 15°$ (*cf.* §5.3.1.1).

Consider two vectors originating at the microfacet surface—one directed toward the incident illumination source, $\hat{i}$, and another directed along the sensor or reflection direction, $\hat{r}$ (see Figure 7.4). In terms of the material surface normal coordinates, or the *macro*facet coordinate system, these vectors are given in Cartesian coordinates as

$$\hat{i} = \begin{bmatrix} i_x \\ i_y \\ i_z \end{bmatrix} = \begin{bmatrix} \sin\theta_i \\ 0 \\ \cos\theta_i \end{bmatrix} \tag{7.10}$$

and

$$\hat{r} = \begin{bmatrix} r_x \\ r_y \\ r_z \end{bmatrix} = \begin{bmatrix} \sin\theta_r \cos\phi_r \\ \sin\theta_r \sin\phi_r \\ \cos\theta_r \end{bmatrix} . \tag{7.11}$$

The Cartesian coordinate reference frame is such that $+x$ is toward the source ($\phi = 0°$),

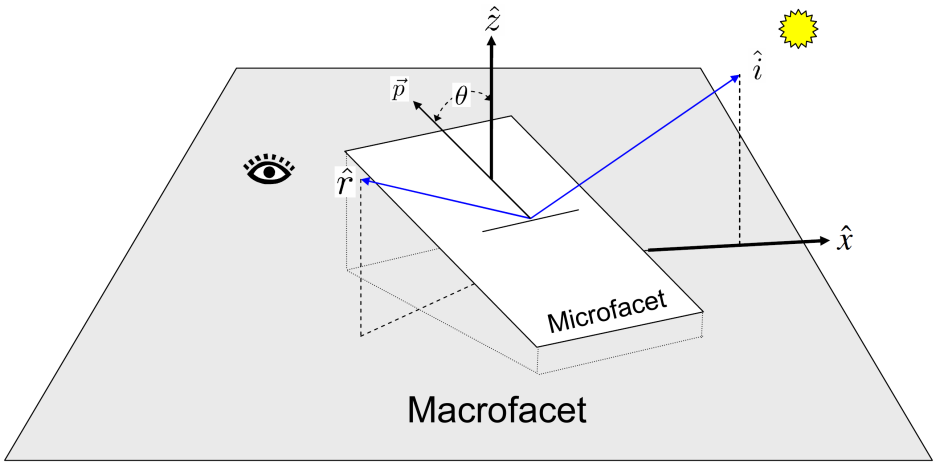

Figure 7.4: The geometry of the polarization angle determination is illustrated by presenting a single microfacet above the plane of the macrofacet or material surface.

with $+z$ aligned with the macrofacet or material surface normal vector. The $+y$ orientation is defined such that a right-hand coordinate system is satisfied, or in the $\phi_r = 90°$ direction.

The cross product of $\hat{r}$ with $\hat{i}$ results in a vector $\vec{p}$ orthogonal to the plane of incidence, and oriented in the *micro*facet plane:

$$\vec{p} = \hat{r} \otimes \hat{i} \ . \tag{7.12}$$

The polarization orientation relative to the sensor may be determined from the angle between $\hat{p}$ and the *macro*facet surface normal, or $\hat{z}$ direction. The angle between these two vectors is

$$\theta = \cos^{-1}\left(\frac{\vec{p}}{|\vec{p}|} \cdot \hat{z}\right) \ , \tag{7.13}$$

recognizing that the normalized surface normal direction is $\hat{z} = \begin{bmatrix} 0 \\ 0 \\ 1 \end{bmatrix}$.

Having obtained the angle θ relative to $\hat{z}$, one only needs to subtract $\frac{\pi}{2}$ to express the angle relative to the x-y plane as viewed by the sensor, or the reference frame from which the polarization orientation χ relative to the macrofacet is defined,

$$\chi = \theta - \frac{\pi}{2} \ . \tag{7.14}$$

This results in $-\frac{\pi}{2} < \chi \leq \frac{\pi}{2}$. Assembling the terms into a single expression provides

$$\chi = \cos^{-1}\left[\frac{\hat{r} \otimes \hat{i}}{|\hat{r} \otimes \hat{i}|} \cdot \hat{z}\right] - \frac{\pi}{2} \,. \tag{7.15}$$

7.1.4 Establishing Statistical Independence of the Mean Values

For the f_{00}, DOP and χ selection process, there has been an implicit assumption of statistical independence. However, there are phenomenological reasons to argue that f_{00} and DOP should be inversely correlated via Umov's effect, as discussed in §2.2.1. However, examination of the data demonstrate that f_{00} and DOP are in fact highly independent. One explanation of this is that each image is composed of the same material, but with f_{00} and DOP variability driven by the orientations of constituent materials. That is, variations in "brightness" and DOP result from different orientations of common materials.

Figure 7.5 demonstrates the statistical relationship between f_{00} and DOP by examining their joint probability distribution for a particular data set—forward scattering of "lawn grass" at 550 `nm`. The top of the figure presents the joint histograms between f_{00} (x-axis) and DOP (y-axis) for $GSD = 0.5$ `in` (left) and $GSD = 3.0$ `in` (right). On the bottom are the standard distribution statistics, as previously presented in Figure 6.5. The joint probability statistics may be better understood by realizing the univariate distributions on the bottom result from integrating the joint probability density. Integration along the y- or DOP-axis results in the f_{00} probability. Similarly, integration of the joint probability density along the x- or f_{00}-axis results in the DOP probability. The key element to note in Figure 7.5 is that there is not a pronounced asymmetry with the f_{00} and DOP joint probability distributions. This suggests these quantities are ill-correlated and the independent selection of f_{00} and DOP values is justified. In stark contrast, the statistical *dependence* of f_{00} with DOP will later be demonstrated in §10.3 for an image containing many material types.

7.2 Variability—BRVF

Having determined the mean value for f_{00}, DOP and χ throughout the scattering hemisphere, or equivalently f_{00}, f_{10} and f_{20} via (7.1) and (7.2), it is now appropriate to discuss the GSD-dependent variability of these quantities, or the BRVF. Recall the measured variability in the f_{00}, DOP and χ parameters as a function of GSD previously presented in Figure 6.5. The data were processed to generate statistics for GSD sizes of 0.5, 3.0, 6.0 and 12.0 `in`. Processing the data at $GSD < 0.5$ `in` may potentially become contaminated by spatial registration errors. Trying to obtain meaningful information for $GSD > 12$ `in` is

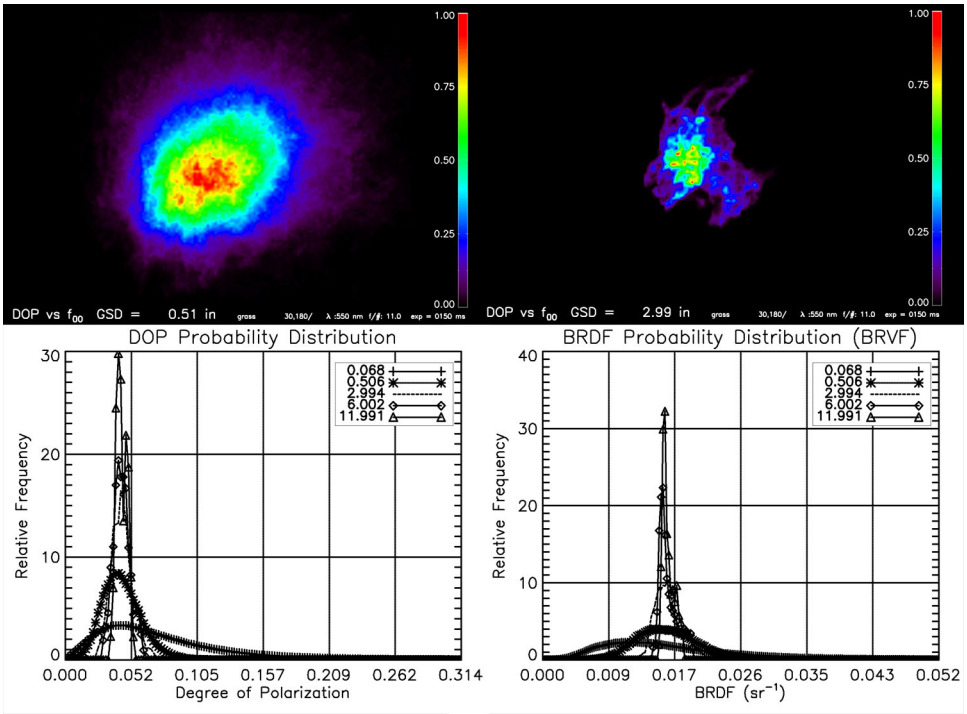

Figure 7.5: The joint probability density of f_{00} and DOP for $GSD = 0.5$ `in` and $GSD = 3.0$ `in`, *top left* and *top right*, respectively. The integrated univariate probabilities are shown on the bottom for DOP and f_{00}, *bottom left* and *bottom right*.

not possible due to the significant image padding required.

Note that *the variability need only be determined for strong illumination sources, which in the VNIR will usually mean the sun.* The radiance leaving the surface reflected from the sky is adequately averaged by the hemispherical extent of the sky illumination, and only the mean values for f_{00}, f_{10} and f_{20} are needed.

The variability is primarily a function of GSD, but is also dependent upon the solar-target-sensor geometry. An efficient means to include both sources of variability was not found, and as such the orientation dependency is not captured. The variability for a given GSD is computed by averaging the variability for each scattering geometry captured in the measurement series. The geometry-dependent variability is generally secondary to that of the GSD dependence. It is therefore a reasonable compromise in attempting to represent this complex, multi-dimensional parameter.

7.2.1 Intensity Variability

The f_{00} variability for each of the processed GSD values is determined by averaging all the f_{00} standard deviations from each hemispherical position for that GSD value. The standard deviations are first normalized by the mean f_{00} magnitude, resulting in a relative or percentage standard deviation of f_{00} given by $\sigma^{\%}_{f_{00}}$. To this data, a fit is made in the form of

$$\sigma^{\%}_{f_{00}} = \mathtt{a}\ GSD^{-\mathtt{b}}\ . \tag{7.16}$$

The absolute intensity variability, $\sigma_{f_{00}}$, is therefore given by

$$\sigma_{f_{00}} = f_{00} \cdot \sigma^{\%}_{f_{00}}\ . \tag{7.17}$$

For each material, `a` and `b` fit parameters are supplied, which in turn provides the percentage standard deviation as a function of the GSD, expressed in inches. Examples of fits to this data are provided in Figure 7.6. Note that the net reflectance does not apparently play a significant role, as for soil $\rho(550) \approx 7.8\%$ and $\rho(750) \approx 13.8\%$, grass $\rho(550) \approx 6.8\%$ and $\rho(750) \approx 43\%$, and finally asphalt $\rho(550) \approx 13.3\%$ and $\rho(750) \approx 15.8\%$. The f_{00} variability will be further explored when spectral extrapolation is considered in §7.3.1.2.

Determination of the f_{00} value proceeds as follows. The mean value is obtained via (7.3), strictly from the Roujean parameters and geometry. The variability as a function of GSD is determined by a normal distribution having a standard deviation of $\sigma_{f_{00}}$. Note that in rare instances, the random draw from the distribution function may result in $f_{00} < 0$, in which case f_{00} is set equal to zero.

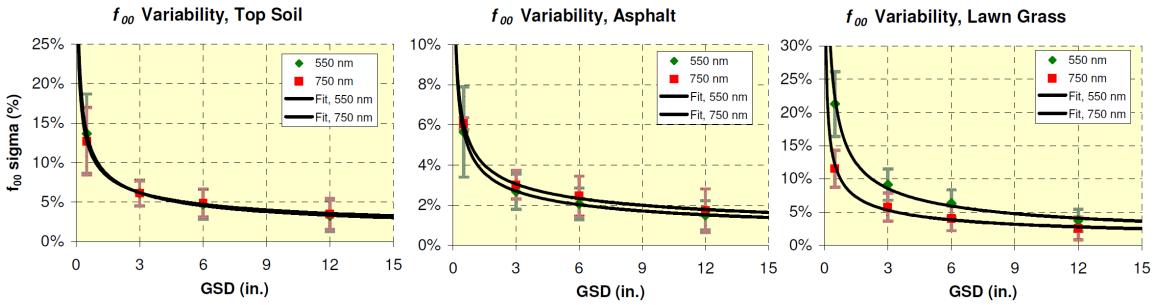

Figure 7.6: The f_{00} variability as captured by $\sigma^{\%}_{f_{00}}$ as a function of GSD. The fits to the data are made with a function of the form of (7.16). The error bars represent a $\pm\sigma$. Top soil (*left*), asphalt (*middle*) and lawn grass (*right*).

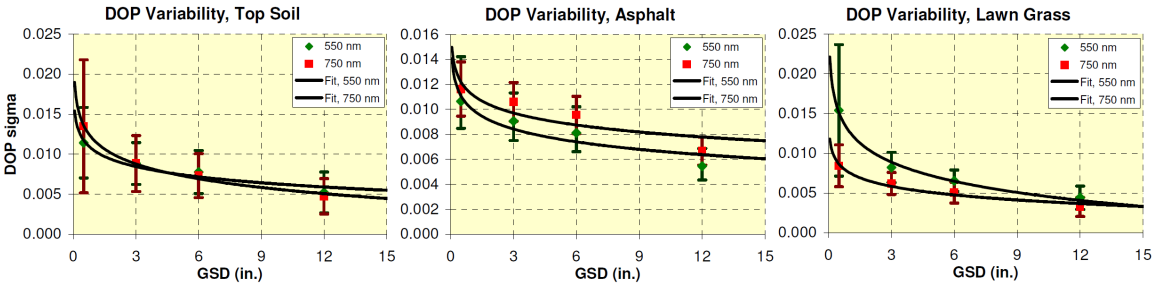

Figure 7.7: The DOP variability expressed by σ_{DOP} as a function of GSD for top soil (*left*), asphalt (*middle*) and lawn grass (*right*). The error bars represent $\pm 1\sigma$.

7.2.2 DOP Variability

In a similar manner, the DOP variability is determined by considering the behavior as a function of GSD. The function describing the relationship between the σ_{DOP} and GSD is a natural log fit, expressed as

$$\sigma_{DOP} = -\mathtt{c}\ln(GSD) + \mathtt{d}\ . \tag{7.18}$$

Figure 7.7 demonstrates the fit of equation 7.18 to the experimental data.

It must be remembered that $0.0 \leq DOP \leq 1.0$, so that if a random draw returns a value outside this range, it must be set to either 0 or 1.

7.2.3 Orientation Variability

The variability in the polarization orientation angle, χ, is highly correlated with DOP. This is realized by considering the following hypothetical cases. For the first scenario,

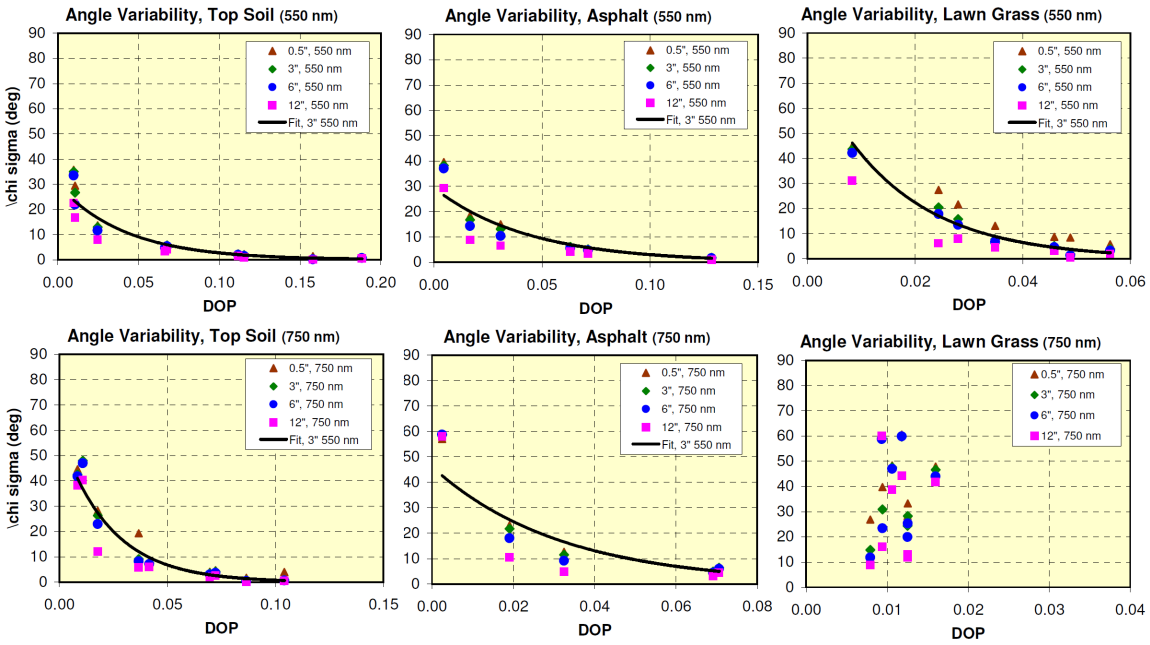

Figure 7.8: The standard deviation of the χ component, σ_χ, as a function of DOP for top soil (*left*), asphalt (*middle*) and lawn grass (*right*). The 550 nm data are on top, with the 750 nm data on bottom. A fit to all the $GSD = 3$ in data is made in the form of equation 7.19. No meaningful fit is made to the 750 nm grass data, since the low DOP results in considerable χ error as noted in §5.3.7.3.

the image-wide $DOP = 1.0$. For this to be realized, each pixel in the image must also have $DOP = 1.0$ and furthermore have identical polarization orientations. At the opposite extreme, each individual pixel may have a $DOP = 1.0$, but with a random pixel-to-pixel polarization orientation. In this case, the net image-wide result is depolarization, resulting in $DOP = 0.0$.

Upon this basis and the observations of the experimental data, the χ variability is fit as a function of DOP. An exponentially decaying function was selected, based upon a reasonable fit to a variety of materials. The function is given as

$$\sigma_\chi = \mathtt{e}e^{-\mathtt{f}DOP} \tag{7.19}$$

where $0.0 \leq DOP \leq 1.0$. The domain of polarization orientation angles is limited to $\frac{\pi}{2} \geq \chi > -\frac{\pi}{2}$. For instances where a random draw returns χ outside this domain, the resulting angle must be "unwrapped" back to the appropriate domain. An example of equation 7.19 fit to experimental data is presented in Figure 7.8.

It is seen that σ_χ has some correlation with GSD, with σ_χ decreasing with increasing

GSD. However, the data demonstrate a better correlation with DOP. For materials having no appreciable polarization, *e.g.* $DOP < 0.01$ for all illumination and sensor orientations, the angular orientation is highly random. The 750 nm grass data in Figure 7.8 demonstrates this.

7.3 Spectral Extrapolation

Spectral extrapolation of the data from only the two measured bands, 550 ± 6 nm and 750 ± 12.5 nm to throughout the VNIR region presents a significant challenge. Unlike the target material generalized microfacet model, the background model is completely empirically based and as such there is no direct means of incorporating physics into the extrapolation. However, the physics of polarization phenomenology, such as Umov's law, may still be used to guide the technique. The only input required in addition to the experimental data is a spectral reflectance factor $\rho(\lambda)$ measurement.

7.3.1 Total Intensity Extrapolation

7.3.1.1 Mean Total Intensity

Oddly enough the most basic BRDF component, the total intensity or f_{00} value is the most difficult to extrapolate. As will be seen, phenomenology-based techniques may be used to determine the DOP and χ spectral dependence. However, it is difficult to incorporate phenomenology in extrapolating the spectral variation of f_{00}. Several approaches were pursued which directly scaled the k_0, k_1 and k_2 Roujean parameters. However, these techniques would ultimately fail when tested at the limits of the spectral reflectance factor, that is when $\rho = 0$ or $\rho = 1$.

One approach that has proven effective is to linearly scale f_{00} by $\rho(\lambda)$ using the Roujean-modelled f_{00} of the measured bands and their resulting total reflectance, ρ_{DHR}. This establishes a simple linear equation where the slope is the difference between the measured f_{00} quantities and their associated total reflectance. The equation is therefore

$$f_{00}(\lambda) = \left[\frac{f_{00}(\lambda_b) - f_{00}(\lambda_a)}{\rho_{DHR}(\lambda_b) - \rho_{DHR}(\lambda_a)}\right] \rho(\lambda) + b \ , \tag{7.20}$$

where $f_{00}(\lambda_a)$ and $f_{00}(\lambda_b)$ are the Roujean-modelled f_{00} values from measurements and b is the intercept value. $\rho_{DHR}(\lambda_b)$ and $\rho_{DHR}(\lambda_b)$ are the total reflectance obtained by integration of the Roujean-modelled λ_a and λ_b bands.

The intercept, b, is determined by substituting a set of the known values of $\rho_{DHR}(\lambda_x)$

for $\rho(\lambda)$ and $f_{00}(\lambda_x)$ for $f_{00}(\lambda)$ such as

$$b = f_{00}(\lambda) - \left[\frac{f_{00}(\lambda_b) - f_{00}(\lambda_a)}{\rho_{DHR}(\lambda_b) - \rho_{DHR}(\lambda_a)}\right] \rho(\lambda) \tag{7.21}$$

$$= f_{00}(\lambda_a) - \left[\frac{f_{00}(\lambda_b) - f_{00}(\lambda_a)}{\rho_{DHR}(\lambda_b) - \rho_{DHR}(\lambda_a)}\right] \rho_{DHR}(\lambda_a) \ . \tag{7.22}$$

The intercept must be calculated during the model execution, as it depends upon the calculated f_{00} value derived from the Roujean model.

For this particular case where only two spectral bands were measured, the 550 `nm` and 750 `nm` bands may be directly equated with "band a" and "band b", respectively. However, in the most general approach where n bands are measured and Roujean modelled, the a and b bands should correspond to those having a total reflectance just spanning the reflectance factor of the wavelength of interest, as it is presumed the BRDF anisotropy between the two bands should be most representative of that at the unknown wavelength.

The $f_{00}(\lambda_a)$ and $f_{00}(\lambda_b)$ quantities are Roujean-modelled and obtained by the appropriate Roujean parameters supplied as one of the model inputs. They are given explicitly as

$$f_{00}(\lambda_a) = [\mathtt{k_{0a}} + \mathtt{k_{1a}}\ f_1 + \mathtt{k_{2a}}\ f_2]\left(\frac{1}{100\ \pi}\right) \tag{7.23}$$

$$f_{00}(\lambda_b) = [\mathtt{k_{0b}} + \mathtt{k_{1b}}\ f_1 + \mathtt{k_{2b}}\ f_2]\left(\frac{1}{100\ \pi}\right) \tag{7.24}$$

after the Roujean model from (7.3).

The ρ_{DHR} values for (7.20) are determined via integration of (7.23) with an incident angle of $\theta_i = 45°$. This angle represents a typical day time imaging scenario, and more importantly a typical geometry for the collection of $\rho(\lambda)$ spectral data. It is noted that there is minimal ρ_{DHR} variability over the range from $0° \leq \theta_i \leq 60°$. The integration limit for θ_r is set to 80°, as the Roujean model is ill-behaved as $\theta_r \to 90°$. This has a minimal impact on the ρ_{DHR} calculation, as a 100% reflecting Lambertian surface evaluates to $\rho_{DHR} = 0.9727$ when limiting θ_r to 80°. $\rho_{DHR}(\lambda_a)$ and $\rho_{DHR}(\lambda_b)$ are explicitly supplied as model parameters, though they could equivalently be computed from the Roujean parameters.

One note of caution when using this technique is that the Roujean-modelled f_{00} may result in negative values for some orientations. In these cases, the magnitude is set to zero. However, when performing the interpolation from (7.23), it is important to maintain any negative values such that an appropriate interpolation is made. Any negative values after the interpolation are then set to zero.

This approach toward spectral extrapolation of the total intensity may be summarized

as modulating the anisotropic "shape" of the BRDF according to the "shape" difference between the a and b bands. The required assumption is that changes in the BRDF anisotropy for a given $\rho(\lambda)$ follow the same trend as those observed between the measured bands, in this case the 550 and 750 nm Roujean-modelled measurements.

7.3.1.2 Total Intensity Variability

The relative f_{00} variability may be treated as identical for all spectral bands. For this to be strictly true requires all the constituents of a background material to have the same spectral "shape", which is only modulated in intensity for a given illumination and observation orientation. This representation is highly accurate when all constituent materials are identical, in which case the variability arises from varying surface orientations ($\cos(\theta_i)$ variations) and shadowing. This assumption should still remain accurate as long as the smallest GSD size at which the data is processed contains a distribution of materials which are statistically representative of other GSD elements in the image.

Perhaps the most significant breakdown in this approximation are for materials such as grass, which has appreciable radiance resulting from *transmittance* which alters the statistics. It is also likely that spectral bands with very low reflectance have increased variability, since a larger percentage of the surface-leaving radiance is from front surface reflectance. Figure 7.6 shown earlier supports this notion, as the variability differences between the soil and asphalt data are minimal. However, the difference in the grass f_{00} variability between the 550 and 750 nm bands is more significant.

Figure 7.9 provides a fit to the f_{00} variability by combining both the 550 and 750 nm data sets for the materials. Error bars represent a single standard deviation from all the measurements. Most significant is the fact that the error for the grass f_{00} variability is not appreciably higher than that of the soil and asphalt, in spite of a greater difference between the two spectral bands for grass. Treating the f_{00} variability may be considered a significant assumption and simplification, but the experimental data provide support for this approximation.

7.3.2 DOP Spectral Extrapolation

7.3.2.1 DOP Mean Value

As discussed in the polarization orientation derivation, it is hypothesized that all polarization is due to front-surface Fresnel reflectance. Furthermore, it is assumed that the index of refraction does not appreciably change over the VNIR range. Under these conditions, the magnitude of the measured f_{10} and f_{20} components are spectrally independent per the

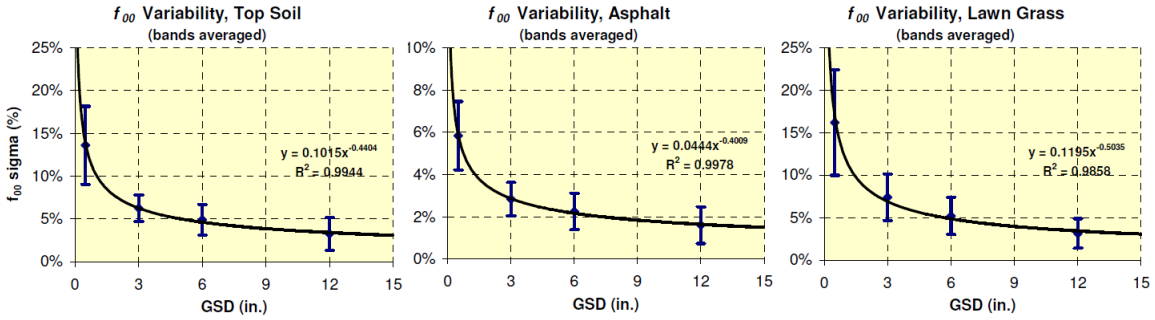

Figure 7.9: f_{00} variability as a function of GSD derived from the average of all 550 and 750 nm variability data; top soil (*left*), asphalt (*middle*) and lawn grass (*right*).

Fresnel equations as seen in §2.1.2.2. This is equivalent to saying that the polarized fraction of the total f_{00} component, f_{00}^{p} should remain constant, independent of wavelength. The polarized fraction is given by

$$f_{00}^{p} = DOP \cdot f_{00} = \sqrt{f_{10}^{2} + f_{20}^{2}} \ , \tag{7.25}$$

with the resulting unpolarized fraction, f_{00}^{u} given by

$$f_{00}^{u} = (1 - DOP) \cdot f_{00} \ . \tag{7.26}$$

This hypothesis is tested by examining the top soil data set. The top soil data is well-suited for this analysis as there is appreciable, but a markedly different DOP at 550 and 750 nm. Figure 7.10 presents f_{00}^{p} of the 550 nm data plotted against the 750 nm data for the same geometric orientation. It is seen that there is reasonable agreement between the two sets of spectral data, as noted by the slope equal to 1.09 from the fit equation. The error bars with these data should not be considered a true uncertainty, but are uncertainty estimates based upon propagating the ΔE parameter discussed in §5.3.2.

The data may be further scrutinized by considering f_{00}^{p} as a function of the phase angle, ξ. As before, under the assumption that all polarization is attributable to front-surface reflectance, the quantities should be equal so long as the refractive index is the same. The f_{00}^{p} quantity is similar to a scaled version of the DOP from Fresnel reflectance. Figure 7.11 provides f_{00}^{p} as a function of ξ for the three materials. Very good agreement is obtained with all but the lawn grass data at 750 nm. Grass at 750 nm has negligible polarization, which results in a large relative error in the polarization, which in turn results in a high f_{00}^{p} uncertainty per (7.26).

Figures 7.10 and 7.11 provide strong evidence supporting Umov's effect. This results in

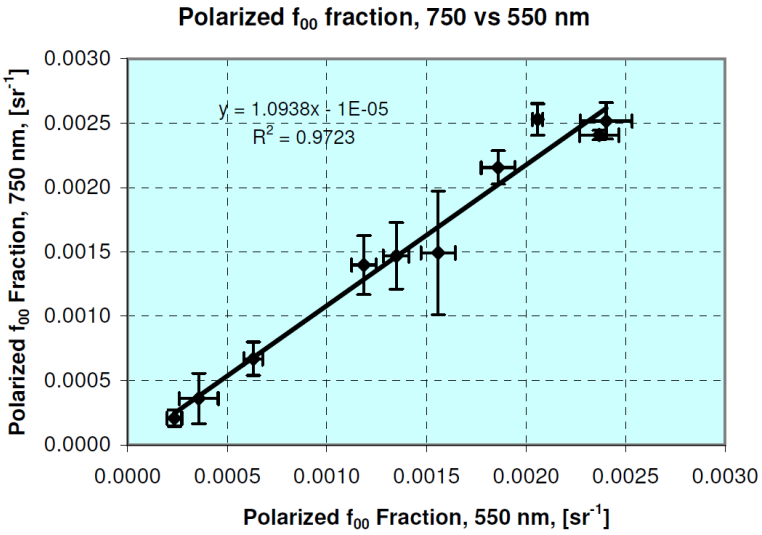

Figure 7.10: The polarized f_{00} BRDF component "top soil" at 750 nm versus that at 550 nm. The data supports the hypothesis that this quantity is spectrally independent.

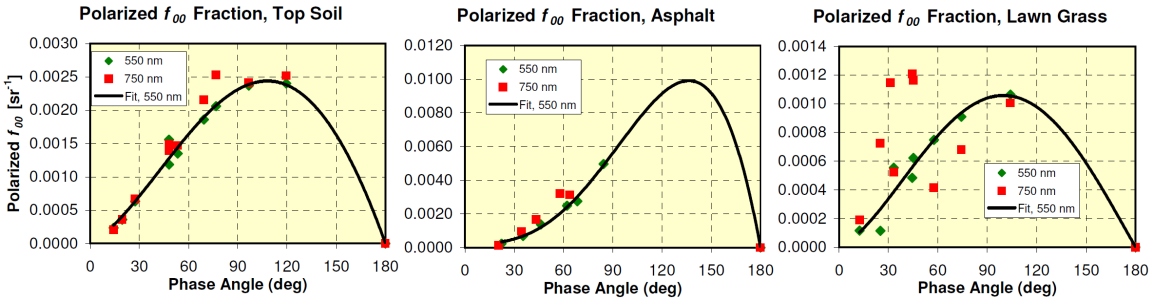

Figure 7.11: The polarized f_{00} BRDF component as a function of the phase angle ξ for top soil (*left*), asphalt (*middle*) and lawn grass (*right*). A fourth-order polynomial fit to the band having the highest *DOP* is also provided (*cf.* Figure 7.2).

the polarization being inversely proportional to total reflectance, as the measurement data already illustrates. It is upon this tenant that the polarization extrapolation is based.

Directly pursuing this approach would lead one to quantify f_{00}^{p} as a function of ξ, then obtain the DOP by simply dividing f_{00}^{p} by the f_{00} magnitude at that orientation, as given by the Roujean model output. Although this directly follows the physics of the phenomenology, it is not the most robust approach, as it is highly dependent upon how well the spectrally-extrapolated Roujean model represents f_{00}. Given that the spectral extrapolation of the Roujean parameters is already an estimate driven by the best fit parameters at two discrete wavelengths, further calculations based on this parameter may likely propagate substantial error.

Instead, a proportionality scale factor is derived based upon Umov's effect. The scale factor may not simply be the inverse ratio between the reflectance magnitudes, though this agrees well with the data collected. A simple inverse ratio approach results in the $DOP \rightarrow \infty$ as $\rho(\lambda) \rightarrow 0$. An appropriate ratio is constructed by considering the f_{00}^{p} component along with the unpolarized component, f_{00}^{u}. The total intensity is therefore the sum of these two components. It has been established that f_{00}^{p} is λ independent; the f_{00}^{u} component contains all the volumetric scatter, and is therefore proportional to the spectral reflectance factor, $\rho(\lambda)$.

To implement this scaling, a "base" DOP or DOP_0 is defined as $DOP(\xi)$ from the measured spectral band having the highest DOP. This band is chosen as it has the least error in the DOP measurement. Variables referring to this base band are denoted by the "$_0$" subscript. From the preceding discussion, the expression to spectrally scale the DOP from DOP_0 is seen to be given as

$$DOP(\lambda) = \left[\frac{f_{00_b}^{u} + f_{00}^{p}(\xi)}{f_{00}^{u}(\lambda) + f_{00}^{p}(\xi)} \right] DOP_0(\xi) \tag{7.27}$$

Application of (7.27) directly from spectral reflectance data which is typically in units of reflectance is enabled by replacing $f_{00}^{u}(\lambda)$ with $\rho(\lambda)$, and converting $f_{00}^{p}(\xi)$ to a polarized reflectance factor, $\rho_{pol}(\xi)$. This conversion is made by simply taking the product with π or

$$\rho_{pol}(\xi) = f_{00}^{p}(\xi)\ \pi\ . \tag{7.28}$$

The final expression for the conversion for spectrally scaling DOP is therefore

$$DOP(\lambda) = \left(\frac{\rho_0 + \rho_{pol}(\xi)}{\rho(\lambda) + \rho_{pol}(\xi)} \right) DOP_0(\xi) \tag{7.29}$$

$$= \gamma \cdot DOP_0(\xi) \tag{7.30}$$

with γ representing the scale factor. Just as $DOP_0(\xi)$ is determined by a fourth-order polynomial, the spectrally-independent $\rho_{pol}(\xi)$ magnitude is also determined by a fourth-order polynomial fit, as seen from Figure 7.11. This fit is given by

$$\rho_{pol}(\xi) = \mathtt{pf}_1 \; \xi + \mathtt{pf}_2 \; \xi^2 + \mathtt{pf}_3 \; \xi^3 + \mathtt{pf}_4 \; \xi^4 \; . \tag{7.31}$$

A sample calculation is provided for extrapolating the DOP from 550 nm to 750 nm at a single phase angle for the top soil data. In this case, $\rho(550) = 0.078341$ and $\rho(750) = 0.137600$. The two fourth order polynomials, which provide DOP_0 and ρ_{pol} are given by

$$DOP_0(\xi) = 2.5881 \times 10^{-4} \; \xi + 2.2020 \times 10^{-5} \; \xi^2 - 1.8179 \times 10^{-8} \; \xi^3 - 6.2297 \times 10^{-10} \; \xi^4 \tag{7.32}$$

$$\rho_{pol}(\xi) = 2.4413 \times 10^{-3} \; \xi + 4.7223 \times 10^{-3} \; \xi^2 - 2.4952 \times 10^{-3} \; \xi^3 + 2.3711 \times 10^{-4} \; \xi^4 \tag{7.33}$$

The $DOP(\lambda)$ is calculated for $\xi = \frac{\pi}{2}$ or 90°, noting that the polynomial coefficients are given for ξ in units of radians. The base DOP or DOP_0 is calculated as 0.1475 using (7.32) and similarly $\rho_{pol}(\xi) = 0.007259$. From equation 7.29, the resulting DOP is

$$DOP(\lambda = 750, \xi = \frac{\pi}{2}) = \left(\frac{0.078341 + 0.007259}{0.137600 + 0.007259} \right) 0.1475 \tag{7.34}$$

$$= 0.0872 \; . \tag{7.35}$$

This value may be compared to the best estimate provided directly from the experimental for soil at 750 nm. The best estimate is given by a fourth order polynomial fit to the data, as previously shown in Figure 7.2. The best estimate is 0.0850, which compares favorably to 0.0872 determined using the extrapolation technique.

A better understanding of the approach's effectiveness is demonstrated by considering all the measured data for all three materials, and determining the DOP for one of the bands via (7.29). All three materials happen to have the 550 nm as the "base" DOP band, or that having the highest DOP. Therefore the 750 nm DOP will be determined. The only knowledge of the 750 nm measurements used in this extrapolation per equation 7.29 is the reflectance factor, $\rho(750)$. Figure 7.12 provides results for all three materials, and demonstrates the effectiveness of the approach. The estimated 750 nm DOP is in close agreement with the experimental data for all three materials. The lawn grass at 750 nm has no appreciable

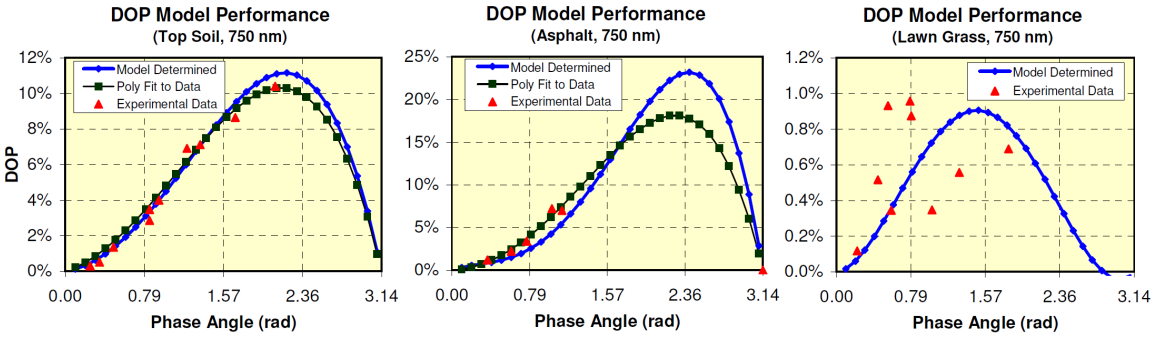

Figure 7.12: Performance of the DOP spectral extrapolation is demonstrated by comparing the model-determined DOP to that actually measured. The "base" DOP in all cases is the 550 nm band, as this band had the highest DOP (and lowest ρ). The model-predicted DOP is shown by the blue diamonds, the experimental data by red triangles and the best-fit to the experimental data by black squares (*cf.* Figure 7.2). Left to right are top soil, asphalt and lawn grass.

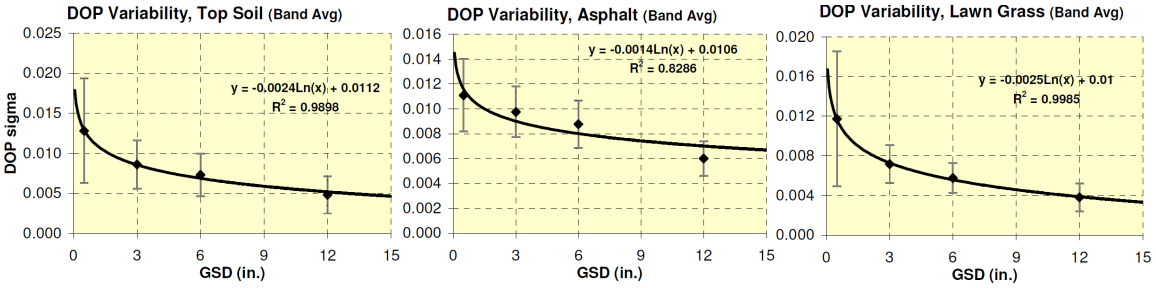

Figure 7.13: The band-averaged DOP standard deviation σ_{DOP} as a function of GSD. From left to right are top soil, asphalt and lawn grass. The error bars represent a $\pm\sigma$ from all the data.

polarization, and the measured DOP is greatly influenced by measurement uncertainty.

7.3.2.2 DOP Variability

As with the f_{00} variability, the DOP variability is treated as spectrally independent. This assumption is justified based upon the similar behavior of the DOP variability for both spectral bands as shown in Figure 7.7. The function parameters from equation 7.18 are developed by performing a fit to the average of all the data. Figure 7.13 presents the results for the three materials.

7.3.3 Polarization Orientation Spectral Extrapolation

Using the hypothesis that all polarization is attributable to front-surface microfacet reflectance results in the polarization orientation χ being spectrally independent. It is ac-

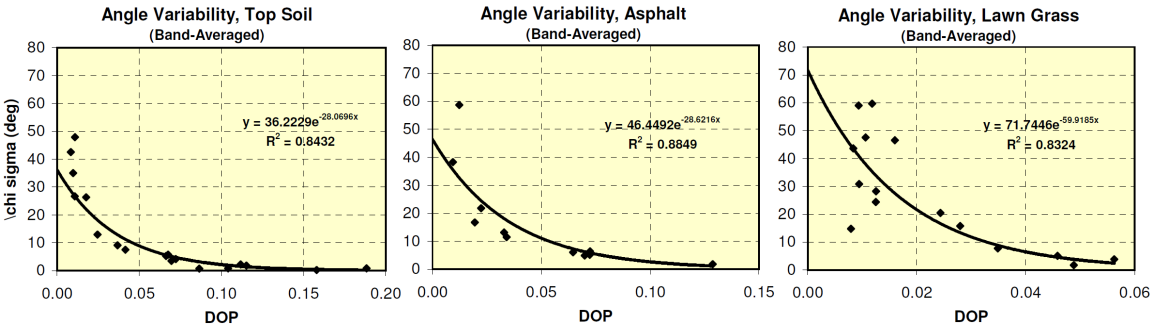

Figure 7.14: The variability of χ expressed as the standard deviation as a function of DOP for top soil (*left*), asphalt (*middle*) and lawn grass (*right*). A fit to the data of the form of equation 7.19 is also presented.

knowledged that volumetric scattering does impart some minor polarization, and as previously discussed is minimal and not captured. Volumetric scatter is proportional to the overall material reflectance, and provides a small p-polarization contribution to the signature. However, high volumetric scattering materials are inherently very depolarizing. The minor spectrally-dependent volumetric scattering impact to the net polarization angle is not significant—in particular for the clutter materials this model is intended to represent.

The spectral-dependence of the χ variability, σ_χ is already captured by the fact that it is a function of the DOP, which in turn is dependent upon the spectral reflectance factor. As seen from Figure 7.8, the difference between σ_χ at 550 and 750 `nm` is not appreciable. σ_χ is therefore treated as independent of $\rho(\lambda)$, other than the inherent spectral dependence of the DOP which is required to determine σ_χ (equation 7.19). The fit to σ_χ is made using all the $GSD = 3$ `in` data from each data set. The 3 inch data is sufficiently large that spatial registration errors are minimal compared to other error sources. Figure 7.14 presents the data along with equations fit to the data.

7.3.4 Spectral Correlation

To this point there has been no consideration of spectral correlation, that is, the f_{00}, DOP and χ values relative to those for the same pixel but at a different λ. If the total intensity or f_{00} parameter were allowed to have different band-to-band variance, without any input from the variance of adjacent bands, the results would be a spectral reflectance vector with a lot of unrealistic high frequency "ripple." In order to avoid this artifact, the f_{00} variability is determined only once per pixel location, and the same percentage variance applied to each spectral band. This results in a realistically behaved spectral reflectance vector, which is systematically higher or lower than the mean spectral reflectance or f_{00} value.

For the practical implementation, this means that f_{00} for a given pixel is determined by first making a random draw from a zero-mean normal distribution of width $\sigma^{\%}_{f_{00}}$ (equation 7.16). The value resulting from the random draw will be referred to as $\Delta f^{\%}_{00}$, which may either be positive or negative. The random draw is only performed once for a given pixel or GSD element, and then applied to all $f_{00}(\lambda)$. This is given by

$$f_{00}(\lambda) = \overline{f_{00}}(\lambda) + \Delta f^{\%}_{00} \cdot \overline{f_{00}}(\lambda) \ , \tag{7.36}$$

where $\overline{f_{00}}(\lambda)$ is the mean-value f_{00} resulting from the Roujean model interpolation from equation 7.20.

As previously discussed and demonstrated, there is no significant f_{00} to DOP correlation (*cf.* §7.1.4). Upon this basis there is not a requirement to explicitly provide any band-to-band correlation of the DOP. The appropriate level of correlation is already provided by virtue of the DOP being a function of the spectral reflectance factor for that λ, per equation 7.29. Since f_{00} and DOP are independent, it is therefore possible to use "texture maps" to provide spatially-correlated f_{00} placement [189]. However, this technique may not be applied to materials exhibiting f_{00} and DOP correlation.

The spectral independence of χ does not require any consideration of band-to-band correlation.

7.4 Spectral Reflectance Factor Measurements

The material spectral reflectance $\rho(\lambda)$ data is taken from field spectrometer measurements made by the Digital Imaging and Remote Sensing Measurements Team. An Analytical Spectral Devices (ASD) FieldSpec Pro Spectroradiometer is used by the Measurements Team to obtain the spectral reflectance following well-established protocols [190]. The ASD has a resolution of 1 `nm` and covers 350–2500 `nm`. Unfortunately, the ASD spectral measurements were not concurrent with the pBRDF measurements. Figure 7.15 presents the ASD-measured spectral reflectance factor compared to the calculated ρ_{DHR} derived from the Roujean-modelled measurements.

Table 7.2 provides direct comparison of the data shown in Figure 7.15. Strictly speaking, the ASD spectral value at the central wavelength should be determined using a weighted average of the actual bandpass of the 550 and 750 `nm` filters. However, the reflectance factor variability within the bandpass is minimal, so a simple average over the FWHM of the filter bands were used. Each of the material reflectance results are now discussed.

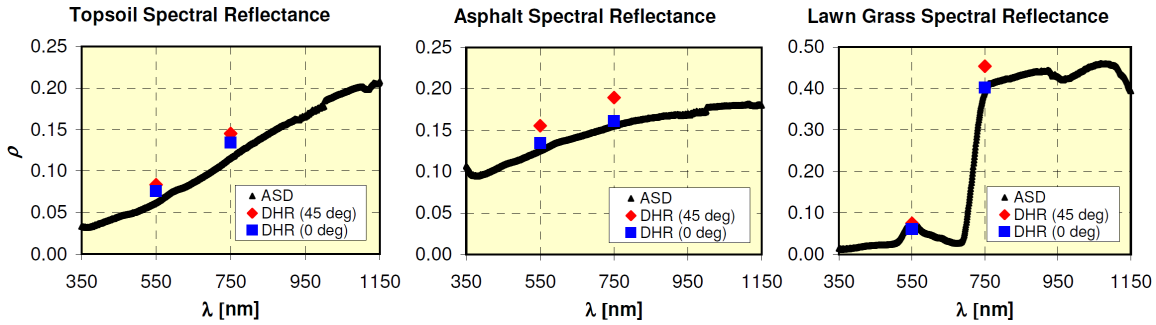

Figure 7.15: The spectroradiometer results for topsoil, asphalt and lawn grass compared with the Roujean model-derived ρ_{DHR} from the BRDF measurements, where ρ_{DHR} is given for $\theta_i = 0°, 45°$.

Table 7.2: The spectral reflectance factor as measured with a spectrometer compared to the total reflectance or ρ_{DHR} with $\theta_i = 0°$ and $\theta_i = 45°$.

Mat'l, λ	ρ	$\rho_{DHR}(0°)$	$\rho_{DHR}(45°)$
topsoil			
550	0.0622	0.0758	0.0838
750	0.1162	0.1339	0.1454
asphalt			
550	0.1255	0.1345	0.1554
750	0.1553	0.1607	0.1893
lawn grass			
550	0.0740	0.0607	0.0752
750	0.3892	0.4022	0.4533

Topsoil The topsoil measurements were made on the same sample as that used for the pBRDF measurements. As with the pBRDF measurements, it was ensured that the soil was adequately dry. A total of 29 measurements were made using the 3° FOV foreoptic, at a $\theta_r = 0°$ with $\theta_i = 35.5°$. The measurements were highly repeatable, as the standard deviation over the 350–1150 nm range covered in Figure 7.15 was less than 0.2% of the total magnitude measured.

As seen from Table 7.2, the model-determined ρ_{DHR} is consistently greater than the measured reflectance factor for both the 550 and 750 nm bands. When considering ρ_{DHR} at $\theta_i = 0°$, ρ is 18% less than ρ_{DHR} at 550 nm and 13% less at 750 nm (or about 1.8 and 2.9 reflectance units). A similar bias is also noted with the asphalt data.

It is difficult to reconcile the differences in the measurements, though this is not of considerable concern. The ASD spectral reflectance factor measurement does not actually measure ρ_{DHR}, but a pseudo-BRDF measurement taken at a given geometry. (It is not truly a BRDF measurement since the downwelled sky radiance is also present). The additional unknown factor is that the surfaces measured were not identical to that measured by the pBRDF measurement technique. In spite of these differences, the relative agreement is reasonable and corroborates the BRDF measurement results.

Asphalt The asphalt reflectance factor measurements were made concurrent with the topsoil measurements. The surface measured was visually very similar to the asphalt for which the pBRDF measurements were made. As with the topsoil data, the spectral reflectance factor is lower than ρ_{DHR}. The total reflectance of the asphalt or ρ_{DHR} also exhibits a larger increase with increasing zenith angle, which is also noted from Table 7.2.

Lawn Grass Finally, the lawn grass measurements are taken from an archived spectral measurement file for "healthy grass." At 550 nm the spectral reflectance factor is in good agreement and lies between ρ_{DHR} at 0° and 45°. There is more disparity at 750 nm, where the $\theta_i = 0°$ total reflectance is similar to the reflectance factor, but at $\theta_i = 45°$ the total reflectance is notably higher.

The ASD spectral reflectance factor measurements demonstrated reasonable agreement with the Roujean model BRDF which was used to derive the total reflectance or ρ_{DHR}. A better comparison would have been possible if the spectral measurements were made on the identical materials at the same time. The background model is directly dependent upon spectral reflectance factor measurements. Perhaps a different measurement protocol could be developed which would provide data closer approximating an actual ρ_{DHR}; *e.g.*, taking measurements at a sampling of θ_r and ϕ locations then averaging the results.

7.5 Downwelled Sky Radiance

Proper treatment of linearly polarized downwelled sky radiance requires a complete 3×3 Mueller matrix, which is not given with the background pBRDF model. It is suggested that the effects of the polarized component of the downwelled sky is negligible for background materials under solar illumination conditions. The $\vec{\epsilon}$ data from the measurement results provide a direct means to test this hypothesis. However, as previously discussed the $\vec{\epsilon}$ have uncertainty resulting from forward solar scatter adjacency effects.

Examination of the measurement data in §6.3 demonstrates a consistent *depolarization* of the sensor-reaching radiance when the sky radiance component $\vec{L}_d$ is included. A strong argument for the negligibility of sky polarization may be made by considering the reciprocity principal in conjunction with the fact that background materials aren't appreciably specular. From the reciprocity principal, it is known that the $\vec{L}_d$ component results from integration of the skydome radiance in the same proportion as the BRDF signature when the sensor is replaced with the source.

Therefore, the intensity-only or first Stokes component of the downwelled sky radiance is adequate for modelling the $\vec{L}_d$ contribution of the polarimetric signature from background materials. This is certainly not the case for target materials or materials which exhibit appreciable specularity. Increasingly specular surfaces enable significant portions of the sensor-reaching radiance to come from the skydome, and the majority of that portion from a relatively small solid angle which under the right orientation may have considerable polarization.

7.6 Model Summary and Material Parameters

Implementation of the model is summarized with a few tables and figures. First, a summary of all model input parameters previously discussed is shown in Table 7.3, along with references to the applicable equations and figures. An overview of the model and the use of all parameters which ultimately results in the first column of the pBRDF Mueller matrix, $\mathbf{F}_r$, is shown in Figure 7.16. Finally, the background pBRDF model parameters derived for the top soil, asphalt and lawn grass are shown in Figure 7.17.

From a practical standpoint, it's of interest to discuss the amount of data required by the model, and the manner in which the data was processed and the time required for this particular implementation. First, the minimum number of hemispherical sampling conditions is considered. The model parameters may be derived with a minimum of three sampling locations, driven by the three-parameter Roujean model, though in practise at

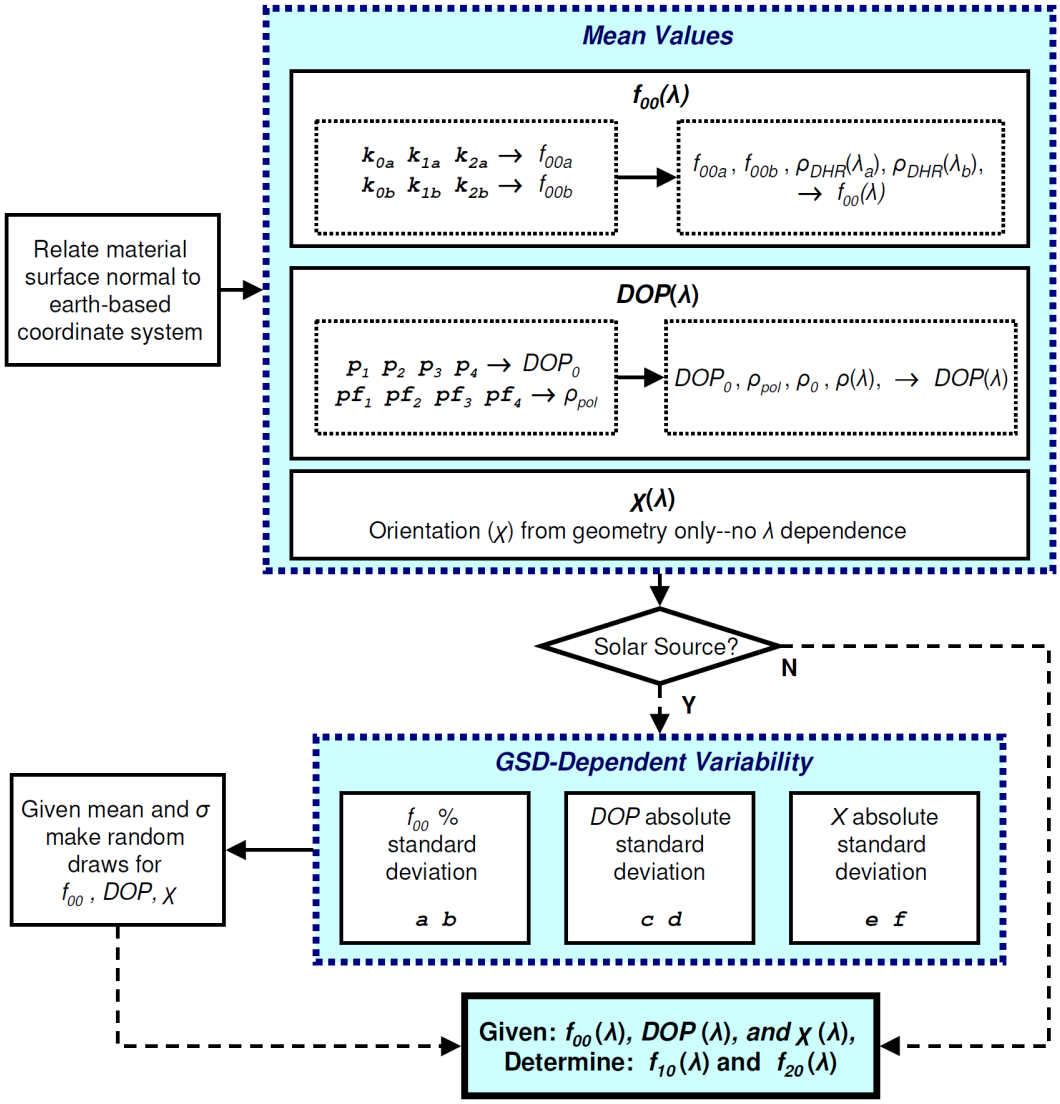

Figure 7.16: An overview of the model showing the input parameters and intermediate calculations. This process is completed for each λ. For all values, geometry information $(\theta_i, \theta_r, \phi_r)$ is required. GSD (in units of inches) must also be supplied for the variability calculations.

Top Soil Model Parameters				
Roujean Parameters				
	k_0(a/b)	k_1(a/b)	k_2(a/b)	
550 (a)	12.263763	5.168339	33.280293	
750 (b)	20.670481	7.950837	48.848812	
Total Reflectance				
	$\rho_{DHR}(\lambda a)$	0.083782	$\rho_{DHR}(\lambda b)$	0.145391
"Base" DOP Polynomial Coefficients				
	p_1	p_2	p_3	p_4
	1.4829E-02	7.2287E-02	-3.4192E-03	-6.7136E-03
"Base" DOP Reflectance Factor				
	ρ_b	0.083782		
Polarized Reflectance Factor Polynomial Coefficients				
	pf_1	pf_2	pf_3	pf_4
	2.4413E-03	4.7223E-03	-2.4952E-03	2.3711E-04
f_00 sigma %				
	a	b		
	0.101504	0.440410		
DOP sigma				
	c	d		
	0.002434	0.011249		
chi sigma				
	e	f		
	0.632208	28.069577		

Asphalt Model Parameters				
Roujean Parameters				
	k_0(a/b)	k_1(a/b)	k_2(a/b)	
550 (a)	14.257988	0.007507	40.263191	
750 (b)	16.17038	-1.105021	51.471607	
Total Reflectance				
	$\rho_{DHR}(\lambda a)$	0.155364	$\rho_{DHR}(\lambda b)$	0.189269
"Base" DOP Polynomial Coefficients				
	p_1	p_2	p_3	p_4
	4.7393E-02	-9.6926E-02	1.3496E-01	-3.4666E-02
"Base" DOP Reflectance Factor				
	ρ_0	0.155364		
Polarized Reflectance Factor Polynomial Coefficients				
	pf_1	pf_2	pf_3	pf_4
	3.6901E-03	-7.0599E-03	1.3223E-02	-3.6128E-03
f_00 sigma %				
	a	b		
	0.044429	0.400938		
DOP sigma %				
	c	d		
	0.001438	0.010589		
chi sigma				
	e	f		
	0.810692	28.621621		

Lawn Grass Model Parameters				
Roujean Parameters				
	k_0(a/b)	k_1(a/b)	k_2(a/b)	
550 (a)	6.8702	0.3881	29.0824	
750 (b)	40.9686	-1.6822	93.1120	
Total Reflectance				
	$\rho_{DHR}(\lambda a)$	0.075211	$\rho_{DHR}(\lambda b)$	0.453327
"Base" DOP Polynomial Coefficients				
	p_1	p_2	p_3	p_4
	1.9582E-03	9.8206E-02	-6.6807E-02	1.1251E-02
"Base" DOP Reflectance Factor				
	ρ_b	0.075211		
Polarized Reflectance Factor Polynomial Coefficients				
	pf_1	pf_2	pf_3	pf_4
	9.4574E-04	2.9314E-03	-1.7853E-03	2.4078E-04
f_00 sigma %				
	a	b		
	0.119524	0.503486		
DOP sigma				
	c	d		
	0.002465	0.009992		
chi sigma				
	e	f		
	1.252179	59.918513		

Figure 7.17: The background model BRDF parameters for top soil, asphalt and lawn grass. These parameters, along with the material spectral reflectance, provide the f_{00}, f_{10} and f_{20} polarimetric BRDF Mueller matrix components and their variability as a function of GSD for arbitrary illumination and reflection orientations.

Table 7.3: A summary of the input parameters to the background pBRDF model, along with references to the associated equations and figures.

Parameters	Application	Equations & Figures
$\rho(\lambda)$	material spectral reflectance (spectrometer-measured reflectance factor)	(7.20), (7.29)
$\mathtt{k_{0a}}, \mathtt{k_{1a}}, \mathtt{k_{2a}}$	Roujean parameters for wavelength a (in this case 550 nm)	(7.20), (7.23)
$\rho_{_{DHR}}(\lambda_a)$	the total reflectance for wavelength a	(7.20)
$\mathtt{k_{0b}}, \mathtt{k_{1b}}, \mathtt{k_{2b}}$	Roujean parameters for wavelength b (in this case 750 nm)	(7.20), (7.23)
$\rho_{_{DHR}}(\lambda_b)$	the total reflectance for wavelength b	(7.20)
ρ_0	the "base" wavelength reflectance factor for DOP spectral interpolation (equal to one of the $\rho_{_{DHR}}(\lambda_x)$ quantities)	(7.29)
$\mathtt{p_1}, \mathtt{p_2}, \mathtt{p_3}, \mathtt{p_4}$	$DOP_0(\xi)$ polynomial coefficients for "base" band, or that having the highest DOP	(7.9), Figures 7.2, 7.3
$\mathtt{pf_1}, \mathtt{pf_2}, \mathtt{pf_3}, \mathtt{pf_4}$	polynomial coefficients for determining the polarized reflectance fraction $\rho_{pol}(\xi)$	(7.29), (7.31), Figure 7.11
a, b	f_{00} relative (%) variability as a function of GSD	(7.16), (7.17), Figure 7.9
c, d	DOP variability as a function of GSD	(7.18), Figure 7.13
e, f	χ variability as a function of GSD	(7.19), Figure 7.14

least five are recommended. Careful selection of the scattering locations helps maximize the information from a minimal data set. Multiple measurements in the plane of incidence are highly useful—for a given θ_r, the phase angle ξ is maximized when in the plane of incidence (equation 2.95). Ideally measurements would be made at a phase angle larger than the maximum peak in the DOP (Figure 7.2). These data are instrumental in accurately determining the maximum DOP via fitting the fourth-order DOP polynomial (equation 7.9). At least one measurement in a "side-scattering" or $\phi = 90°, 270°$ orientation, and one near a "retroreflection" orientation is recommended ($\theta_r \approx \theta_i$ with $\phi = 0°$).

All scattering measurements are usually completed within a three hour period, not including setup of the instrumentation. The total raw data set consists of 12 images of each spectral band at each hemispherical location, with each image sized at 3 MB for this system. This translates to a total of 144 or approximately 432 MB of raw data for a notional two-band measurement at six hemispherical positions. After pre-processing and writing out intermediate images and data, the total data set roughly doubles, resulting in a full data set on the order of 1 GB.

Processing the data proceeds by the manual look-up of the solar incident angles based upon the time of each measurement. The calibration panel data is then processed, such

Table 7.4: Comparison of the background pBRDF model output to experimental data for lawn grass at 550 nm, with $\theta_i = 27.7°$, $\theta_r = 30°$ and $\phi = 180°$ for $GSD = 0.5$ in.

Quantity	Measurement	Model
f_{00} [sr^{-1}]	0.01661 ± 0.00408	0.01586 ± 0.00267
DOP	0.0458 ± 0.0158	0.0449 ± 0.0117
χ [rad]	-0.2463 ± 0.1520	$-6.921 \times 10^{-8} \pm 0.0849$

that a DC value is obtained, which may then be used for the $\cos(\theta_i)$ adjustment for the measurement data (equation 5.46). The adjusted DC magnitude, along with the camera exposure times are then provided as inputs to the algorithm (Figure 6.3), which writes out an ASCII text file having the mean and variability data as a function of GSD (p. 146).

Further use of this data was never automated, so it is manually entered into a spreadsheet where the variability fit parameters and fourth-order polynomial fits are derived. The measured f_{00} magnitudes with their corresponding geometries are assembled as an ASCII text file which serves as the input to the Roujean parameter determining algorithm. The Roujean algorithm also provides the hemispherical BRDF integration which in turn supplies the ρ_{DHR} model parameters.

Summarizing, it requires around five hours to set up, acquire the data, and break down the equipment; with another five hours to process the data and derive the model parameters. The five hour processing period could be automated significantly, and easily reduced to one hour.

7.7 Model Comparison with Empirical Data

The Background pBRDF model was implemented in an algorithm, the results of which may be directly compared to the empirical data. The model was used to replicate specific data sets from the measurements, with model parameters taken from Figure 7.17. The model output was constructed into an image simulating a full frame of data collected, with a sampling of both the model and measured results at the GSD of interest.

The first modelled result is of lawn grass at 550 nm, with $\theta_i = 27.7°$, $\theta_r = 30°$ and $\phi = 180°$. Comparison of the empirical measurements to the model results are shown in Figure 7.18. The synthetic data demonstrate good visual agreement between the model and the empirical data. Quantitative analysis of the data is shown in Figure 7.19 which presents the histograms and Table 7.4, which has the mean and standard deviations.

The data compare favorably, with the exception of χ, which is noted to off by 0.25 rad or 14°. However, this error is commensurate with the measurement uncertainty in χ. More

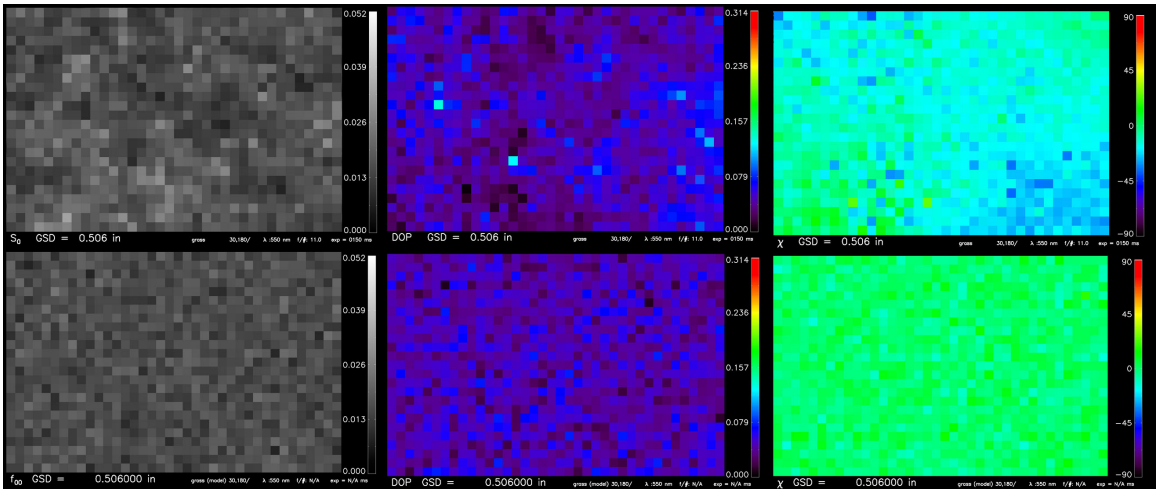

Figure 7.18: A comparison of empirical data (*top*) to synthetic data generated by the Background pBRDF model (*bottom*). Left to right are f_{00}, DOP and χ. These data are for "lawn grass" at $GSD = 0.5$ `in` at 550 `nm`, with $\theta_i = 27.7°$, $\theta_r = 30°$ and $\phi = 180°$. The scales for both sets of data have been set to identical ranges. Histograms for these data are shown in Figure 7.19.

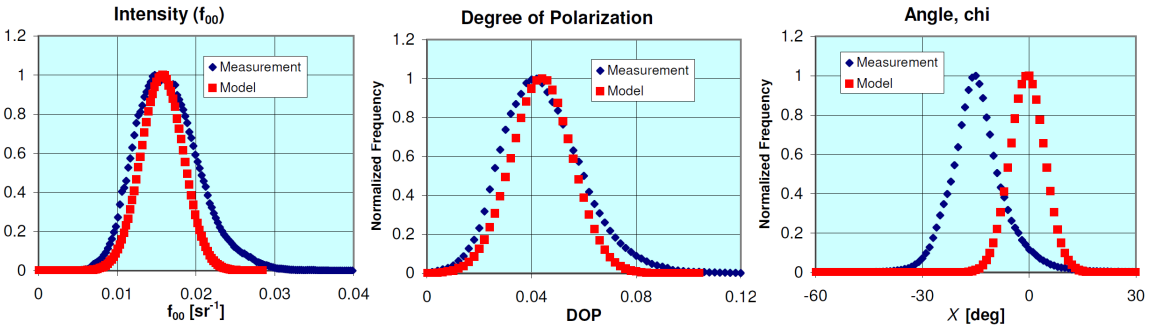

Figure 7.19: The histograms of the data from Figure 7.18 provide a direct comparison between the measurement and model results. The bias in the χ determination is evident, and the model distributions compare favorably with the data. (Note that this data is for the full convolved image set, a sample size which is close to 1536×1024 rather than the more limited population shown in Figure 7.18).

Table 7.5: Comparison of the background pBRDF model output to experimental data for top soil at 750 nm, with $\theta_i = 53.6°$, $\theta_r = 30°$ and $\phi = 135°$ for $GSD = 0.5$ in. The significant discrepancy in the polarization orientation (χ) is attributed to the camera angular accuracy about the optical axis, or the reference frame error as discussed in 5.3.1.1.

Quantity	Measurement	Model
f_{00} [sr^{-1}]	0.03550 ± 0.00662	0.03069 ± 0.00418
DOP	0.0723 ± 0.0135	0.0712 ± 0.0129
χ [rad]	0.7203 ± 0.0834	0.2967 ± 0.0858

significant is the difference in the f_{00} and χ variability, which is underestimated by the model. This is likely caused by the illumination-surface-reflection orientation dependency of the variability, which is not captured by the model.

Another modelled measurement is that of top soil at 750 nm, with $\theta_i = 53.6°$, $\theta_r = 30°$ and $\phi = 135°$. Comparison of the empirical measurements to the model results are shown in Table 7.5. Again, the results compare quite favorably. The model underestimates f_{00} and as before the χ bias is noted. The DOP data are particularly satisfying.

7.8 Background Model Limitations & Future Work

The limitations of the background pBRDF model and future improvements are briefly discussed.

GSD First is the GSD size limitation. As it stands, the model only accommodates a unimodal distribution of f_{00}, DOP and χ values. Obviously, as the GSD decreases to a size commensurate with the spatial extent of individual elements comprising a material (*e.g.*, blades of grass, individual stones in an aggregate), multimodal distributions are expected. The multimodal distributions are not captured by the single normal distribution and hence will not be accurately represented by the model. Techniques have been developed which successfully quantify multi-modal data and their spectral correlation [191, §5], but the geometric extrapolation of these results would likely prove difficult.

More significant is the other GSD extreme—how are the data extended to a GSD of the order of 1–3 m, a spatial resolution typical of many systems. The variability equations are well-behaved for increasing GSD sizes, but it is difficult to estimate when reality breaks down. It is thought the variability should be reliable up to 18 or 24 in, but beyond that other questions enter into the equation. It is suggested that there is a larger "macro" texture scale for all materials, and that the mean and variability values have some changes at a scale larger than that measured in these experiments.

In other words, there is a natural variability and mixture of background materials, dependent upon the local conditions of the material in question. For instance, in picking a suitable measurement region for the "lawn grass", areas with weeds and other anomalies were avoided in order to best capture the behavior of "just" grass. Realistic surface will have larger scale variability, such as from groupings of weeds, or soil exposure in sparsely covered grass regions, etc. A direct technique to extend the results to a larger GSD is to increase the stand-off distance of the measurement system, thereby increasing the GIFOV. However, it is thought an equally justified technique would be to use a mixed-pixel approach.

Complementary measurements of similar materials could be made to provide a linear mix of properties. For instance, continuing with the lawn grass example, measurements could be made of a "weedy" area as well as another area with some bare surface exposure, etc. In extending the results to a larger GSD size, one could then linearly mix the results from these individual subclasses.

Spatial Correlation Another shortcoming of the model is the lack of spatial correlation with adjacent pixels. Each GSD element has the pBRDF Mueller matrix generated independent of adjacent GSD elements. The spatially-correlated "texturing" is evident in some of the empirical data, in particular for the data processed at $GSD = 0.5$ `in`. One approach toward implementing realistic texture is via "texture maps", which are used in high-fidelity synthetic image generation programs such as DIRSIG. The inherent correlation of spatial features could be quantified using the imagery derived in the measurement process. The f_{00} variability could be applied in a traditional texture map fashion, as long as f_{00} and DOP are uncorrelated.

Variability Representation The variability of parameters have only been correlated with GSD, with the exception of χ which has been correlated with DOP. However, as previously stated, these distribution standard deviation parameters were generated by averaging the standard deviations from multiple incident solar angles and viewing angles. The result is that the illumination-sensing geometry dependence on the variability is not captured. Note the discrepancy in variability data presented by Figure 7.18.

It is thought that some of the noise characteristics of the system are influencing the model. The DOP measurement noise floor is difficult to understand on a per image basis. Some attempts have been made to remove known system artifacts when fitting the data, but undoubtedly some of the system is being modelled rather than the phenomenology.

Polarization Phenomenology Finally, a subtle polarization phenomena is not captured by the model—the so called "negative-branch" effect [118]. As the phase angle ξ decreases, there is a point at which the polarization should go to zero, then rise again before returning to zero at $\xi = 0$. The polarization angle is actually reversed in this small angular region, and may be attributed to multiple scattering events responsible for polarization at near-backscatter conditions. Recent data taken during the 2003 opposition of Mars by the Hubble Space Telescope demonstrate this phenomena [192]. The same phenomena is present in a transmissive medium as well—the polarization orientation near the sun also goes through this transition. The impact of the model not handling this effect is deemed to be negligible, as the DOP in this region of ξ is always minimal.

Also lacking is the ability to capture the small changes to the polarization orientation which result from volumetric polarization contributions. While these contributions are thought to be minimal, they nonetheless exist and are not represented by the model. A significant increase in the accuracy of the absolute polarization filter orientation with respect to the global coordinate system is required to explore these effects.

Total Intensity BRDF The model may be improved by exploring other f_{00} BRDF models. In particular, the Roujean model may be segmented into a four parameter model, which eliminates the assumption that protruding surface elements are equally transmissive and reflective. Data should also be acquired with at least three spectral bands. This enables testing the validity of some of the spectral extrapolation techniques.

Further improvements to the existing 3-parameter Roujean f_{00} model can also likely be achieved by weighting the experimental data samples. As currently implemented, the f_{00} BRDF fit parameters are derived with the measurements equally weighted. However, this presumes the measurements have been made at locations which best represent the overall behavior of the BRDF. An iterative approach could consider the variability of the measured BRDF magnitude relative to the model results, then provide a higher weight to those samples.

7.9 Conclusions

The background pBRDF model is a highly empirical means of incorporating the polarized signatures of background materials. The model's *forte* is the ability to accurately replicate the natural variability of the polarized signatures, a prerequisite for the eventual exploration of algorithms using polarization information. Many simplifications are made in order to extrapolate the results for arbitrary illumination and reflection orientations and also for

extending the results spectrally. However, the model represents a significant advance given the current lack of a realistic polarimetric background representation. It provides a meaningful step toward a clutter representation in which spectral-polarimetric algorithms must operate.

Chapter 8

Target pBRDF Model

A new polarimetric BRDF (pBRDF) model suitable for homogeneous or "target" materials is proposed. The basis of the model follows from the polarization of a microfacet BRDF model presented by Priest and Germer in [96], which was more broadly published by Priest and Meier in [97]. Many BRDF models may be segregated into components which represent *i*) surface or *specular* scattering and *ii*) *volumetric* scattering. Furthermore, many of those, such as Torrance-Sparrow and Maxwell-Beard, may be further decomposed into a *micro-facet* representation. The microfacet representation treats the specular scattering as that resulting from the orientation of individual facets on a material surface. The decomposition of a BRDF model into the microfacet representation thus enables polarization of the model via the Fresnel reflectance off the microfacets. To first order, the volumetric scattering component is usually considered completely depolarizing.

The most general representation of the model may be given by

$$f_r = f_{spec} + f_{vol} \ , \tag{8.1}$$

where f_{spec} is the BRDF attributed to front-surface, specular or Fresnel reflectance and f_{vol} is that due to internal scattering and re-emergence. The specular component of the BRDF is generalized as

$$f_{spec} = \frac{R_F(\beta)}{4\cos(\theta_i)\cos(\theta_r)} p(\theta_N) S \ , \tag{8.2}$$

where $R_F(\beta)$ is the Fresnel reflectance off a *micro*facet, with an angle of incidence β relative to the microfacet surface normal. The microfacets are oriented at an angle θ_N relative to the *macro*surface normal. The orientation of the microfacets is given by the probability density function, $p(\theta_N)$. Finally, a shadowing term, S, accounts for shadowing effects when the observation angle is not equal to the illumination angle. This term is bound from

$0 \leq S \leq 1.0$ and serves to attenuate the specular reflectance.

The angle of incidence on the microfacet may be given in terms of the macrofacet coordinate system. Note that β is simply half the phase angle ξ previously given by (7.8). β is therefore

$$\beta = \tfrac{1}{2}\cos^{-1}\left[\cos\theta_i\cos\theta_r + \sin\theta_i\sin\theta_r\cos\phi\right] \ . \tag{8.3}$$

Given β, θ_N is determined as [97, eq. 12]

$$\theta_N = \cos^{-1}\left[\frac{\cos\theta_i + \cos\theta_r}{2\cos\beta}\right] \ . \tag{8.4}$$

Note that the specular component as presented by (8.2) differs from that given by Priest. The Priest-Germer model also contains a $\cos(\theta_N)$ term in the denominator (*cf.*, [97, eq. 9, 11]). Priest does not derive the specular component representation, but cites other publications as the source of the equation. However, at least one of the cited sources, Maxwell, conforms to the form of the model given by (8.2), and also agrees with that given by He.[1] Priest also does not include a shadowing function, as the paper's emphasis was on the polarized Fresnel reflectance representation of the model.

When the Fresnel reflectance is cast in the form of a Mueller matrix, $\mathbf{F}_r$, then any microfacet model may be "polarized". Determining the Fresnel reflectance requires the complex refractive index for the material, $\tilde{n}_t$, and therefore $\tilde{n}_t$ is another required model parameter. With the Fresnel reflectance Mueller matrix, the polarized model representation is given by

$$\begin{aligned}\mathbf{F}_r &= \mathbf{F}_r^{spec} + \mathbf{F}_r^{vol} \\ &= \frac{\mathbf{R}_F(\beta)}{4\cos(\theta_i)\cos(\theta_r)}p(\theta_N)S + \mathbf{F}_r^{vol} \ .\end{aligned} \tag{8.5}$$

Usually the volumetric contribution is considered completely depolarizing, in which case $\mathbf{F}_r^{vol}$ may be represented by only the f_{00}^{vol} element, or equivalently the scalar intensity quantity f_{vol}. Microfacet BRDF models employ different functional forms of $p(\theta_N)$, S and $\mathbf{F}_r^{vol}$. Maxwell and Beard developed a protocol to empirically approximate each of these functions. It is this empirical determination of these parameters that in part motivates what will be referred to as a *generalized* microfacet pBRDF model. It is generalized by the fact that different functional forms of $p(\theta_N)$, S and $\mathbf{F}_r^{vol}$ may be used which provide the best fit to experimental data.

[1] In any event, the impact of $\cos(\theta_N)$ in the denominator is minimal; with most materials the BRDF magnitude rapidly decreases with increasing θ_N, such that division by a decreasing $\cos(\theta_N)$ quantity is negligible.

The final motivation for the model is the fact that an extensive database of hundreds of materials already exists with Maxwell-Beard model parameters. The NEFDS, as described in §2.2.2.6, may therefore be "polarized" by the application of the Priest-Germer microfacet polarization technique. Furthermore, the raw data used to derive the NEF Maxwell-Beard model parameters may be used to derive parameters providing optimal fits for the polarimetric BRDF signature, rather than just the overall f_{00} intensity component.

On a philosophical note, many argue that models should incorporate all the possible physics of the interaction, which then provides a validated basis for making predictions. While this is a noble effort, it is extremely difficult if not impossible to incorporate all the physics of optical scattering into a tractable model providing results within a meaningful computational time. On that note, the microfacet model is one in the domain of geometric optics; that is, strictly speaking the surface roughness and microfacet dimensions must be large relative to λ. However, the microfacet representation has demonstrated the ability to accurately model a wide range of materials from the UV to the LWIR, and is therefore considered as an adequate means to predict surface-leaving radiance.

This chapter begins with an overview of the generalized microfacet model, and presents different functional forms of $p(\theta_N)$, S and $\mathbf{F}_r^{vol}$ which may be used in the model. The coordinate transformation required to appropriately represent the Fresnel Mueller matrix reflectance are described. This is followed by a decomposition of the Maxwell-Beard BRDF model into the generalized microfacet representation, which enables application of the Maxwell-Beard model parameters and hence polarization of the Maxwell-Beard model. Next, the measurement protocol developed by Maxwell and Beard used to determine $\tilde{n}_t$, $p(\theta_N)$, S and $\mathbf{F}_r^{vol}$ is reviewed. The model is then implemented for six materials from the NEFDS and the results compared to raw lab data. These six materials were also made available for pBRDF measurements, which were completed using the imaging system described in §5.2. These measurement results are reviewed and compared with the model results. Finally the shortcomings of the model are discussed with future recommendations made.

8.1 Generalized Microfacet Model Overview

Each of the generalized microfacet model components as shown in (8.5) are presented. The presentation is primarily limited to the Maxwell-Beard form of the $p(\theta_N)$, S and $\mathbf{F}_r^{vol}$ functions, though a few others are mentioned and presented.

8.1.1 Microfacet Probability Distribution Functions, $p(\theta_N)$

The microfacet probability distribution function, $p(\theta_N)$, may be thought of as providing the "spread" of the specular microfacet reflections according to the surface roughness statistics. This distribution function uses two parameters: a surface roughness parameter σ, and a bias parameter B. A lower σ corresponds to a smoother or more specular surface. The B parameter provides an overall magnitude adjustment. The effect of $p(\theta_N)$ is to place a "peak" in the specular direction. This results due to the relationship of θ_N to the reflection coordinates θ_r and ϕ via equations 8.3 and 8.4. In θ_r space, the reflection coordinate space, the entire $p(\theta_N)$ function is translated according to θ_i, with placement of the peak at the specular reflectance orientation; that is at $\theta_r = \theta_i$ with an azimuth angle of 180°. This results from the mathematical relationship of θ_N to θ_i, θ_r and β. Two $p(\theta_N)$ functions will be examined—a Gaussian distribution function $p_G(\theta_N)$ and a modified Cauchy function $p_C(\theta_N)$.

8.1.1.1 Gaussian Probability Distribution Function

The Gaussian microfacet probability distribution function $p_G(\theta_N)$ is that used by the Priest-Germer model [97, eq. 9] and is given by

$$p_G(\theta_N) = \frac{B}{2\pi\sigma^2 \cos^3(\theta_N)} \exp\left[\frac{-\tan^2(\theta_N)}{2\sigma^2}\right] , \tag{8.6}$$

where σ^2 is the microfacet slope variance and B is the bias parameter. Note that Priest-Germer do not include a scaling factor, so $B = 1$ for their model. This distribution function is attractive, as integration over the 2π hemisphere evaluates to unity; it is based on the assumption of a Gaussian surface height distribution [97, §6]. Figure 8.1 provides output of $p_G(\theta_N)$ for a few values of σ and B for both in the plane of incidence ($\phi = 0, 180°$) and "cross-plane" ($\phi = 90, 270°$) scattering. The function is shown in terms of the dependency upon θ_r, or $p_G(\theta_N(\theta_r))$.

8.1.1.2 Modified Cauchy Distribution Function

The modified Cauchy microfacet probability distribution function $p_C(\theta_N)$ is adapted from that used by the more recent versions of the NEF Maxwell-Beard BRDF model. It is given by

$$p_C(\theta_N) = \frac{B}{\cos(\theta_N)\left[\sigma^2 + \tan^2(\theta_N)\right]} . \tag{8.7}$$

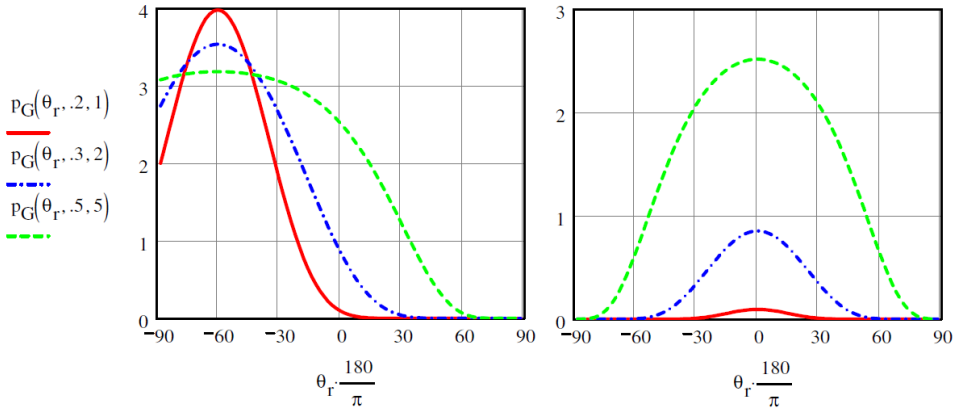

Figure 8.1: Results of the Gaussian distribution function for $\theta_i = 60°$. At left are results in the plane of incidence ($\phi = 0°$) and at right "cross-plane" ($\phi = 90°$). The bias and surface roughness parameters for each of the curves are $[\sigma, B] = [0.2, 1]$ (solid, red), [0.3, 2] (dash-dot, blue) and [0.5, 5] (dash, green). Note the change in scale between the left and right figures.

Note that this function differs from that given by the NEF [193, eq. 4.1-3], as this function has been transformed into the generalized microfacet representation. (This is further discussed in §8.2 when the Maxwell-Beard model is decomposed into the generalized microfacet components). Figure 8.2 provides output of $p_C(\theta_N)$ for a few values of σ and B for both in the plane of incidence and "cross-plane" scattering. As with the Gaussian function, $p_C(\theta_N)$ is shown in terms of the dependency upon θ_r, or $p_C(\theta_N(\theta_r))$.

8.1.2 Shadowing Function S

The shadowing function S plays an obvious physical role in the BRDF spectral reflectance component. When the observer is not coincident with the incident irradiance, there are shadowing effects which modify the signature. That is, some microfacet elements may not be illuminated due to others blocking the illumination source. It is also possible that some illuminated microfacet elements are not visible by the observer due to line-of-sight blocking by microfacets. These effects are respectively termed "shadowing" and "masking" by Torrance and Sparrow [77]. Furthermore, it is possible to have simultaneous shadowing and masking. The net result is an attenuation of the specular reflectance due to what is collectively referred to as shadowing effects.

Only the NEF Maxwell-Beard shadowing function is presented [193, p. 23]. This shadow function is a somewhat simplified form compared to that originally given by Maxwell [65,

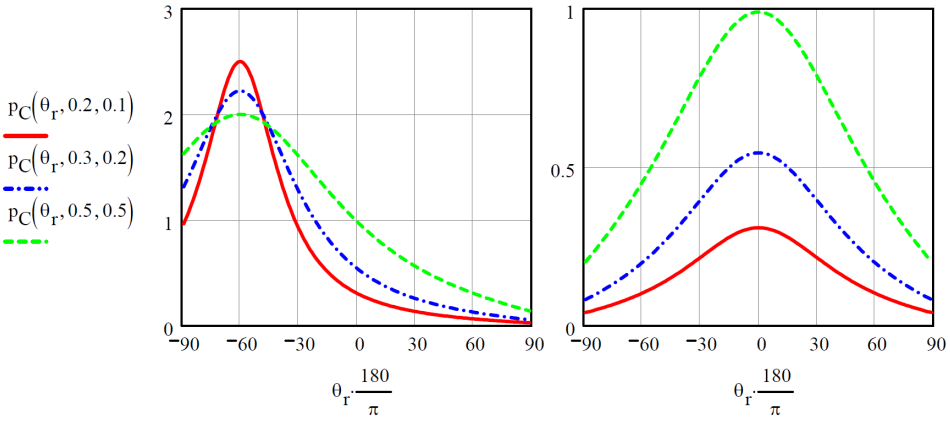

Figure 8.2: Results of the modified Cauchy distribution function for $\theta_i = 60°$. At left are results for in the plane of incidence ($\phi = 0°$) and at right "cross-plane" ($\phi = 90°$). The bias and surface roughness parameters for the presented values are $[\sigma, B] = [0.2, 0.1]$ (solid, red), $[0.3, 0.2]$ (dash-dot, blue) and $[0.5, 0.5]$ (dash, green). Note the change in scale between the left and right figures.

p. 10]. It is given by

$$S_{MB} = \frac{1 + \frac{\theta_N}{\Omega}\, e^{-2\beta/\tau}}{1 + \frac{\theta_N}{\Omega}} \,, \tag{8.8}$$

where Ω and τ are the fit parameters.

Maxwell and Beard found this function provided an improved fit to the data over that of the Torrance-Sparrow shadow function, but this comparison was primarily limited to paint samples. The behavior of S_{MB} is such that in the retroreflection orientation ($\theta_i = \theta_r, \phi = 0°$) the magnitude is one, thus providing no attenuation. Similarly, the magnitude of the function in the forward scattering specular direction ($\theta_i = \theta_r, \phi = 180°$) is also one. Figure 8.3 illustrates the behavior of S_{MB} for varying Ω and τ values.

8.1.3 Fresnel Reflectance

The Fresnel reflectance, $R_F(\beta)$ is an essential component of the microfacet model and provides the magnitude and polarization of the specular reflectance off the microfacets. Fresnel reflectance is usually represented as a scalar magnitude in terms of the incidence angle (or equivalently the reflectance angle) and the incident polarization state. All that is required to produce the Fresnel reflectance is the complex indices of refraction of the incident medium, $\tilde{n}_i$ and the medium which is reflecting the light, $\tilde{n}_t$, along with the incident angle (which via the law of reflectance is also the reflectance angle). The complex index is given by the real component, n, and the imaginary component κ such that $\tilde{n} = n - i\kappa$. Generally, the incident medium is air such that $n_i \approx 1.0 - i0.0$.

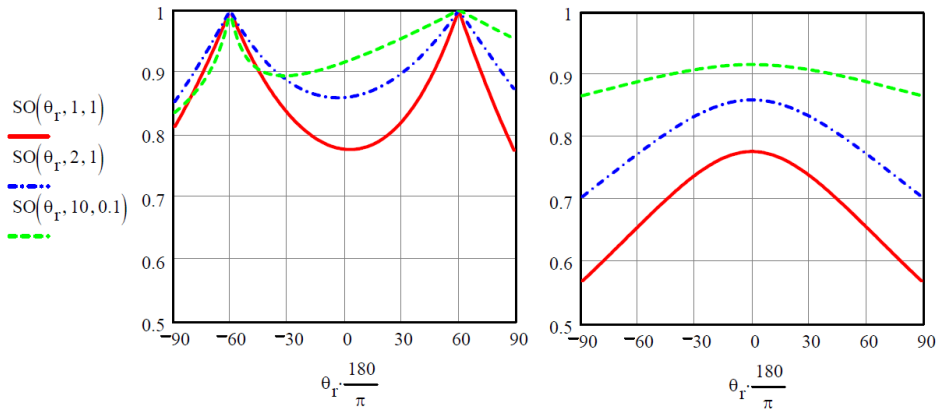

Figure 8.3: The Maxwell-Beard shadowing function as a function of θ_r for $\theta_i = 60°$. At left are results in the plane of incidence ($\phi = 0°$) and at right "cross-plane" ($\phi = 90°$). The parameters for the presented values are $[\tau, \Omega] = [1.0, 1.0]$ (solid, red), [2.0, 1.0] (dash-dot, blue) and [10.0, 0.1] (dash, green).

The usual values given by the Fresnel equations are the fraction of s-polarized and p-polarized reflectance, given the same incident polarization (see equations 2.10 and 2.12, and Figure 2.1). From these values, the total reflectance from an unpolarized source is easily determined, which is the manner in which the Maxwell-Beard model determines the specular reflectance magnitude. However, representing the Fresnel reflectance as a Mueller matrix $\mathbf{R}_F(\beta)$ enables polarization of any microfacet-based BRDF model, immediately transforming the scalar BRDF result, f_r or the f_{00} BRDF component into the full polarimetric BRDF Mueller matrix, $\mathbf{F}_r$. The process is complicated by the coordinate transformations necessary to relate the microfacet Fresnel reflectance to the *macro*facet coordinate system in which the pBRDF model operates.

Hence the material index of refraction $\tilde{n}_t$ is critical in providing an accurate polarimetric representation with the generalized microfacet model. The derivation of an appropriate $\tilde{n}_t$ value will be further discussed in §8.3.3. The coordinate transformations necessary to represent $\mathbf{R}_F$ and thus $\mathbf{F}_r$ in terms appropriate for the *macro*facet coordinate system by which BRDF is defined is now discussed.

8.1.4 Coordinate Transformation of the Fresnel Reflectance

The required coordinate transformations to properly represent $\mathbf{F}_r$ is one of the most complicated aspects of the model. However, it is easily captured by a closed-form solution presented by Priest [97]. The requirement may be summarized as needing to transform the Fresnel reflectance from an individual *micro*facet to the *macro*facet coordinate system,

given an illumination source at θ_i with the observer at θ_r and ϕ.

It is first noted that for a given θ_i, θ_r and ϕ geometry, that the orientation of the microfacet is uniquely determined. This is understood by visualizing the required orientation a small mirror must have on the macrosurface to specularly reflect the incident radiance toward the observer. This "fixes" the required microfacet orientation which contributes to the specular signature.

The required coordinate transformation is invoked by the development of a 2×2 Jones matrix, $\mathbf{T}$, which is similar to a Mueller matrix. A Jones matrix is an adequate means of transferring polarized energy when only polarized states are considered. Given a Jones matrix, an equivalent Mueller matrix may be developed, though the converse is not true since a Mueller matrix handles the more general case of depolarization. The Jones matrix transforms the incident electric field oriented in the s and p polarization states to the reflected s and p polarization states. This matrix transformation is given by

$$\begin{bmatrix} \mathcal{E}_s^r \\ \mathcal{E}_p^r \end{bmatrix} = \begin{bmatrix} r_s & 0 \\ 0 & r_p \end{bmatrix} \begin{bmatrix} \mathcal{E}_s^i \\ \mathcal{E}_p^i \end{bmatrix} , \tag{8.9}$$

where $\mathcal{E}_s^i$ and $\mathcal{E}_p^i$ are the incident s and p polarization electric field, r_s and r_p are the reflected field magnitudes, and $\mathcal{E}_s^r$ and $\mathcal{E}_p^r$ are the reflected s and p polarization electric field. This is equivalent to the Fresnel reflectance equation, but retaining the electric field magnitudes (*cf.* equations 2.10 and 2.12).

However, two coordinate transformations are required to properly relate the relative s and p polarization states incident upon the microfacet surface normal. The first coordinate transformation rotates the plane of incidence, or the plane containing the incident radiance and *macro*surface normal vector, to the plane containing the *micro*facet normal and the incident radiance. The rotation between these two planes is given by η_i. Similarly, a second transformation rotates the plane of reflectance, defined by the reflected direction and the *macro*facet surface normal to the *micro*facet surface normal, termed η_r. Both η_i and η_r are uniquely determined by the BRDF coordinate system or θ_i, θ_r and ϕ. They are given by [97, eq. 19]

$$\cos(\eta_i) = \frac{\frac{\cos(\theta_i)+\cos(\theta_r)}{2\cos(\beta)} - \cos(\theta_i)\cos(\theta_r)}{\sin(\theta_i)\sin(\beta)} \tag{8.10}$$

$$\cos(\eta_r) = \frac{\frac{\cos(\theta_i)+\cos(\theta_r)}{2\cos(\beta)} - \cos(\theta_r)\cos(\theta_r)}{\sin(\theta_r)\sin(\beta)} . \tag{8.11}$$

The coordinate transformation of the electric fields are accomplished by multiplying

the incident electric field, which is defined in terms of the macrofacet coordinate system relative to the incident illumination direction, by the η_i coordinate transformation before the Fresnel reflectance. After the Fresnel reflectance, the η_r coordinate transformation is accomplished, which produces the surface-leaving electric field components in terms of the sensor or observer's orientation in the macrofacet coordinate system. Therefore, the resulting electric field components, in terms of the coordinate system of the observer is given by [97, eq. 14]

$$\begin{bmatrix} \mathcal{E}_s^r \\ \mathcal{E}_p^r \end{bmatrix} = \begin{bmatrix} \cos(\eta_r) & \sin(\eta_r) \\ -\sin(\eta_r) & \cos(\eta_r) \end{bmatrix} \begin{bmatrix} r_s & 0 \\ 0 & r_p \end{bmatrix} \begin{bmatrix} \cos(\eta_i) & -\sin(\eta_i) \\ \sin(\eta_i) & \cos(\eta_i) \end{bmatrix} \begin{bmatrix} \mathcal{E}_s^i \\ \mathcal{E}_p^i \end{bmatrix} \tag{8.12}$$

$$= \begin{bmatrix} T_{ss} & T_{ps} \\ T_{sp} & T_{pp} \end{bmatrix} \begin{bmatrix} \mathcal{E}_s^i \\ \mathcal{E}_p^i \end{bmatrix} . \tag{8.13}$$

The resulting Jones matrix, $\mathbf{T}$ is formed from the coordinate transformations and the Fresnel reflectance, r_s and r_p. The sign convention needed for η_i and η_r is not clearly presented by Priest. It is ambiguous from (8.10) since the cosine is an even function; however when used as an argument for sine in (8.12) it must be defined. For $0° < \phi < \pi$ the sign of the η angles is negative, and for $\pi < \phi < 2\pi$ they are positive. Furthermore, in the plane of incidence or $\phi = 0°$ or 180°, both η_i and η_r are zero.

Now the Jones matrix components are used to construct the Fresnel reflectance Mueller matrix, $\mathbf{R}_F$. The complete 4×4 Mueller matrix may be reproduced from these elements, but only the 3×3 matrix components relevant to linear-only polarization are shown. As given by Priest and Meier [97, eq. 15], the resulting $\mathbf{R}_F$ component magnitudes (ρ_{xx}) are

$$\begin{aligned}
\rho_{00} &= \tfrac{1}{2}\left[|T_{ss}|^2 + |T_{sp}|^2 + |T_{ps}|^2 + |T_{pp}|^2\right] , \\
\rho_{01} &= \tfrac{1}{2}\left[|T_{ss}|^2 + |T_{sp}|^2 - |T_{ps}|^2 - |T_{pp}|^2\right] , \\
\rho_{02} &= \tfrac{1}{2}\left[T_{ss}T_{ps}^* + T_{ss}^*T_{ps} + T_{sp}T_{pp}^* + T_{sp}^*T_{pp}\right] , \\
\rho_{10} &= \tfrac{1}{2}\left[|T_{ss}|^2 - |T_{sp}|^2 + |T_{ps}|^2 - |T_{pp}|^2\right] , \\
\rho_{11} &= \tfrac{1}{2}\left[|T_{ss}|^2 - |T_{sp}|^2 - |T_{ps}|^2 + |T_{pp}|^2\right] , \\
\rho_{12} &= \tfrac{1}{2}\left[(T_{ss}T_{ps}^* + T_{ss}^*T_{ps}) - (T_{sp}T_{pp}^* + T_{sp}^*T_{pp})\right] , \\
\rho_{20} &= \tfrac{1}{2}\left[T_{ss}T_{sp}^* + T_{ss}^*T_{sp} + T_{ps}T_{pp}^* + T_{ps}^*T_{pp}\right] , \\
\rho_{21} &= \tfrac{1}{2}\left[(T_{ss}T_{sp}^* + T_{ss}^*T_{sp}) - (T_{ps}T_{pp}^* + T_{ps}^*T_{pp})\right] , \\
\rho_{22} &= \tfrac{1}{2}\left[(T_{ss}T_{pp}^* + T_{ss}^*T_{pp}) - (T_{ps}T_{sp}^* + T_{ps}^*T_{sp})\right] .
\end{aligned} \tag{8.14}$$

Again it is emphasized that the Fresnel Mueller matrix components given by 8.14 for a specified θ_i, θ_r and ϕ geometry are only a function of the material refractive index $\tilde{n}_t$. When

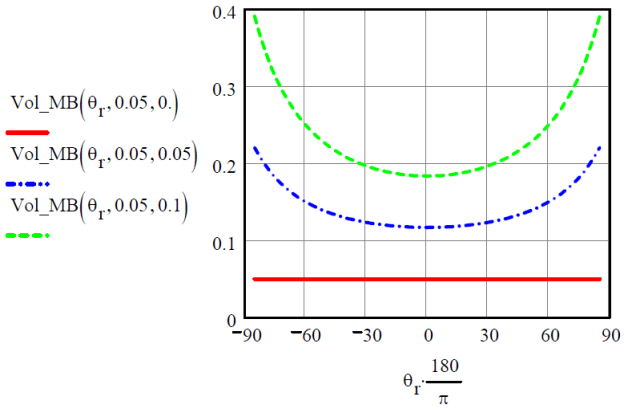

Figure 8.4: The Maxwell-Beard volume BRDF component as a function of θ_r for $\theta_i = 60°$. The parameters for each of the curves are $[\rho_D, \rho_V] = [0.05, 0.0]$ (solid, red), $[0.05, 0.05]$ (dash-dot, blue) and $[0.05, 0.1]$ (dash, green).

the volumetric BRDF component of the microfacet model is treated as a completely unpolarized term, then all model polarization is by virtue of the microfacet Fresnel reflectance.

8.1.5 Volume Component

Finally the volumetric scattering component of the generalized microfacet model is considered. The only representation given is that from the NEF Maxwell-Beard BRDF model. This term is completely randomly polarized and is expressed as

$$V_{MB} = \rho_D + \frac{2\rho_V}{\cos(\theta_i) + \cos(\theta_r)} \ , \tag{8.15}$$

where ρ_D and ρ_V are two free fit parameters. The nomenclature used is that from the NEF, and is an adaptation of that originally proposed by Maxwell, where ρ_D is the *diffuse* or Lambertian component and ρ_V is the *volumetric* scattering parameter [193, p. 22]. The nomenclature is somewhat confusing, as both are considered part of the overall volumetric scattering component in the generalized microfacet model given by (8.1).

Notice that (8.15) is equal to a simple Lambertian contribution when $\rho_V = 0$. The function also has azimuthal symmetry. Figure 8.4 provides some output for V_{MB}. The Maxwell-Beard model parameters allow non-physical negative values of ρ_D and ρ_V, which may provide a better fit to the empirical data.

It is acknowledged that volumetric scattering is not completely depolarizing. Subsurface radiance emerging through a microfacet is polarized via Fresnel transmittance. The net result is that volumetric scattering is preferentially p-polarized via Fresnel transmittance.

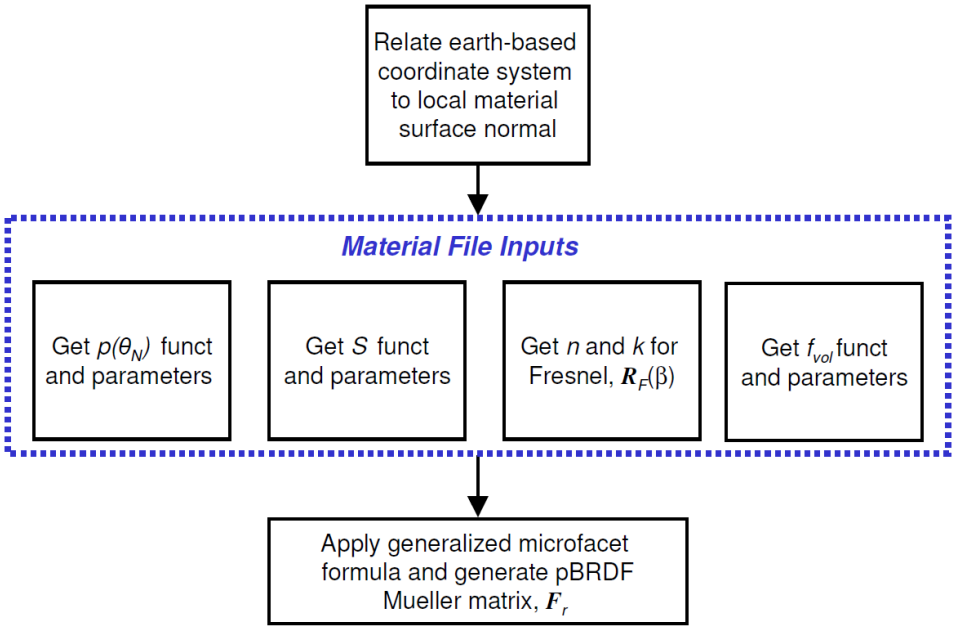

Figure 8.5: The process of generating the pBRDF Mueller matrix for a target material.

This effect was previously noted from the "magic 8-ball" imaging experiment in §5.2.3. A rigorous polarimetric BRDF model should include volumetric polarization.

Some insight into this phenomenon is provided by Ellis [101], who investigated a glossy white paint. Much like the surface of the white region on the 8-ball, the polarization from glossy white paint is predominantly p-polarization for view angles away from the specular lobe. A more rigorous treatment was recently provided by Germer [194].

8.1.6 Combining Components and Output

Generating a material polarimetric BRDF is therefore enabled by the selection of the appropriate microfacet components and fit parameters which best match experimental data. For a given material, the required data is therefore *i*) the functional form of $p(\theta_N)$ and the σ and B fit parameters, *ii*) the functional form of S and the associated fit parameters (here only S_{MB} was presented with τ and Ω fit parameters), *iii*) the functional form of $\mathbf{F}_{vol}$ and associated fit parameters and finally *iv*) the material refractive index, $\tilde{n}_t$. Figure 8.5 provides a high-level overview of the $\mathbf{F}_r$ generation process for such applications as synthetic image generation.

An overview of the individual components and the relevant equations are given in Table 8.1. It is reminded that additional functions may be used for these components that were

Table 8.1: Generalized microfacet model components and applicable equations.

Component	**Functions** (equations)
microfacet distribution, $p(\theta_N)$	$p_G(\theta_N)$ (8.6), $p_C(\theta_N)$(8.7)
shadow function, S	S_{MB}(8.8)
volumetric BRDF, f_{vol}	V_{MB} (8.15)

not explicitly discussed (*e.g.*, Torrance-Sparrow or He shadowing functions).

A key element yet to be addressed is the manner by which spectral interpolation of the model is made possible. For most BRDF measurement systems, there are typically only a few spectral bands for which the model parameters may be derived, termed *reference* bands. Spectral interpolation of the model between these reference bands is made possible by a high spectral resolution ρ_{DHR} data set. This is discussed in detail in §8.4.2. However, attention is first given to the Maxwell-Beard BRDF model and how it may be cast in the form of the generalized microfacet model given by (8.5).

8.2 Maxwell-Beard Decomposition into the Microfacet Model

The Maxwell-Beard model specular component is given by [65, eq. 9]

$$f_r^{spec}(\theta_i, \phi_i; \theta_r, \phi_r) = \frac{R_F(\beta)}{R_F(0)} \frac{f_{ZBS}(\theta_N) \cos^2 \theta_N}{\cos\theta_i \cos\theta_r} \left(\frac{1 + \frac{\theta_N}{\Omega}\ e^{-2\beta/\tau}}{1 + \frac{\theta_N}{\Omega}} \right) , \tag{8.16}$$

which was also reviewed in §2.2.3.3.2. Equation 8.16 seemingly has little resemblance with the generalized microfacet model specular component given by (8.5). However, further examination of the zero bistatic scan (ZBS) BRDF or $f_{ZBS}(\theta_N)$ from equation 2.70 demonstrates the model's conformity to the microfacet representation. Recall that $f_{ZBS}(\theta_N)$ is given by

$$f_{ZBS}(\theta_N) = \frac{R_F(0) p(\theta_N)}{4 \cos\theta_i \cos\theta_r} , \tag{8.17}$$

where $R_F(0)$ is the Fresnel reflectance at zero degree or normal incidence.

Substitution of (8.17) into (8.16) results in the specular component of the Maxwell-Beard model equal to

$$f_r^{spec} = \frac{R_F(\beta)}{R_F(0)} \frac{\cos^2 \theta_N}{\cos\theta_i \cos\theta_r} \left[\frac{R_F(0) p(\theta_N)}{4 \cos\theta_i \cos\theta_r} \right] S . \tag{8.18}$$

However, for the f_{ZBS} scan, $\theta_i = \theta_r = \theta_n$ so the product of $\cos\theta_i$ and $\cos\theta_r$ may be replaced

with $\cos^2\theta_N$ in the denominator of f_{ZBS}. Upon this substitution, (8.18) simplifies to

$$f_r^{spec} = \frac{R_F(\beta)p(\theta_N)}{4\cos\theta_i\cos\theta_r}S\ , \tag{8.19}$$

or the generalized microfacet specular representation.

In this manner, it is seen that the f_{ZBS} raw data taken for the Maxwell-Beard model provides a fit to (8.17), from which the actual microfacet distribution $p(\theta_N)$ is obtained. The $f_{ZBS}(\theta_N)$ fit function recently used by the NEF is a modified Cauchy distribution given by [193, eq. 4.1-3]

$$f_{ZBS}(\theta_N) \approx \frac{R_F(0)B}{4\cos^3(\theta_N)\left[\sigma^2+\tan^2(\theta_N)\right]}\ . \tag{8.20}$$

Therefore from (8.20) and (8.17) it is seen that

$$\frac{R_F(0)p(\theta_N)}{4\cos\theta_i\cos\theta_r} = \frac{R_F(0)B}{4\cos^3(\theta_N)\left[\sigma^2+\tan^2(\theta_N)\right]} \tag{8.21}$$

from which $p(\theta_N)$ may be solved for as

$$p_C(\theta_N) = \frac{B}{\cos(\theta_N)\left[\sigma^2+\tan^2(\theta_N)\right]}\ , \tag{8.22}$$

or the modified Cauchy microfacet distribution function previously given by equation 8.7 in §8.1.1.2.

8.3 Empirical Measurements & Parameter Determination

The generalized microfacet model parameters are determined according to the protocol established by Maxwell and Beard [65]. The only distinction made between the Maxwell and Beard method and the generalized microfacet method is the consideration of different functional forms for $p(\theta_N)$, S and f_{vol} which may be "mixed and matched" to provide the best fit to the experimental data.

An overview of the empirical data used to derive the parameters is presented, in conjunction with the parameter derivation process. The parameter fitting is mostly described qualitatively. Data relevant to understanding the polarization properties of the materials are emphasized. Much of the discussion parallels that found in [193].

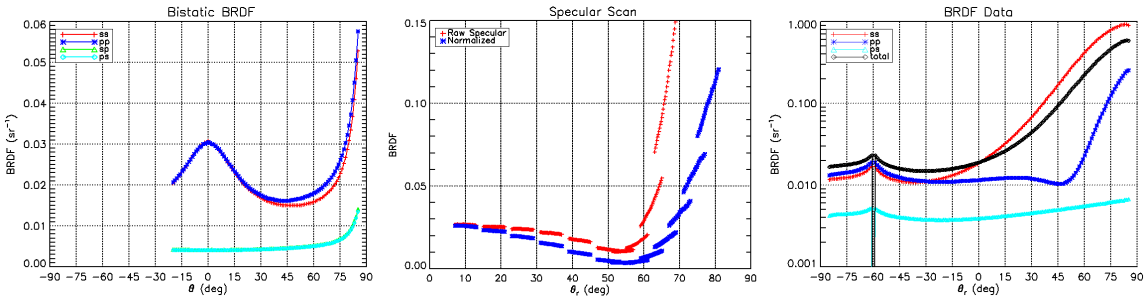

Figure 8.6: An example of the raw data used to derive the M-B BRDF model parameters. These data are for a green paint at 632.8 nm. Shown are the ZBS scan (*left*), the specular scan (*middle*) and the in-plane scan (*right*). Note that the specular scan data has the raw data (*red*) and the area-normalized raw data obtained by taking the product with $\cos\theta_i \cos\theta_r$ (*blue*). The in-plane scan graph also includes the derived intensity-only BRDF, shown in black.

8.3.1 Empirical Data Overview

There are three BRDF measurements made which enable derivation of the model parameters. They include: *i*) a near-zero bistatic or *ZBS* angle BRDF measurement $f_{ZBS}(\theta_N)$ previously discussed, *ii*) a *specular* scan BRDF measurement and *iii*) an *in-plane* BRDF scan with $\theta_i = 60°$. Each of the these BRDF measurements is completed with different combinations of source and receiver polarization orientations, or *ss*, *pp*, *sp* and *ps* where the first letter indicates the source polarization orientation and the second indicates the receiver polarization orientation. Examples of each the measurements is shown in Figure 8.6.

These measurements are made at discrete wavelengths, termed *reference* wavelengths. The reference wavelengths for the NEF material measurements include 0.325, 0.6328, 1.06, 3.39 and 10.6 μm and are made with laser sources. Spectral interpolation of the results is discussed in §8.4.2.

8.3.2 Zero-bistatic (ZBS) Angle BRDF

The zero bistatic or ZBS measurement consists of the source and detector positioned as close together as possible ($\theta_i \approx \theta_r$) and the BRDF measured as the source and detector are moved together in a plane which intersects the material surface normal. All four permutations of linear polarization states are measured in this manner: f_{ss}, f_{pp}, f_{sp} and f_{ps}, where the first subscripted letter indicates the incident polarization and the second the received polarization. Several examples of ZBS measurements are shown in [65, Appendix I].

The ZBS measurements enable determination of the microfacet density function, $p(\theta_N)$.

This is realized by considering the mechanisms of reflectance for when $\theta_i \approx \theta_r$. Since polarization is preserved for a zero incident angle, the like-polarization BRDF (f_{ss} and f_{pp}) is proportional to the microfacet distribution. However, the f_{pp} and f_{ss} data also contain radiance which has been volumetrically scattered; presuming the volume scattering is completely depolarizing, then equal amounts of s and p radiance are produced from the volume scattering. This volume contribution to the ss and pp data is easily corrected for as the cross-polarized or f_{sp} and f_{ps} data are direct measurements of the volumetric scattering. Therefore, the BRDF attributed to the microfacet distribution may be estimated by only considering the specular reflectance of the ZBS data, f_{ZBS}^{spec}. In order to provide the best estimate of f_{ZBS}^{spec} which is correlated to the microfacet distribution, the average of the like-polarization components are taken, from which the average of the cross-polarization components are subtracted which provides

$$f_{ZBS}^{spec} = \tfrac{1}{2}(f_{ss} + f_{pp} - f_{sp} - f_{ps}) \ . \tag{8.23}$$

Since f_{ZBS}^{spec} is only attributed to microfacet reflectance with surface normals oriented toward the source and detector, it is noted that $\theta_N \approx \theta_i, \theta_r$. Furthermore, this retroreflection orientation is a condition in which there is no shadowing, so $S = 1$.

With f_{ZBS}^{spec} in hand from (8.23), it is seen from (8.17) that the microfacet probability distribution is given by

$$p(\theta_N) = \frac{4\cos^2(\theta_N)\ f_{ZBS}}{R_F(0)} \ . \tag{8.24}$$

Various distribution functions, such as the Gaussian and modified Cauchy may then be used which provide a best fit to $p(\theta_N)$.

The ZBS data also provide another important signature—that of the volumetric scattering. The cross-polarized BRDF from f_{ZBS} are attributed to volume scattering. The f_{sp} and f_{ps} components of the f_{ZBS} data are those which result from the volumetric scattering—that is, all signal due to the cross polarized source and receiver conditions are due to radiance which is internally scattered and depolarized such that the opposite polarization is produced. For an unpolarized volume function, the average of the two cross-polarized components may be taken to approximate the volumetric scattering or

$$f_{ZBS}^{vol} = \tfrac{1}{2}(f_{sp} + f_{ps}) \ . \tag{8.25}$$

An example of some remarkable fits to the f_{ZBS}^{vol} data is seen in Figure 8.7 where the Maxwell-Beard volume function V_{MB} from equation 8.15 has been used.

Finally, it is observed that usually $f_{pp} \approx f_{ss}$ and $f_{sp} \approx f_{ps}$. However, often f_{pp} may

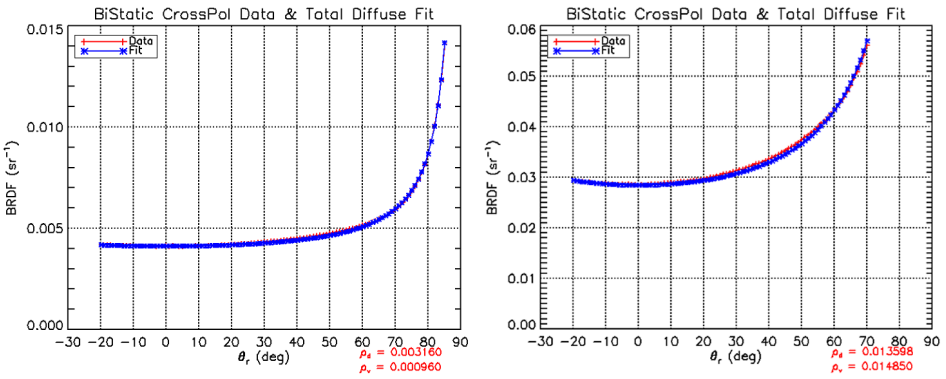

Figure 8.7: Two examples of remarkable fits made to the experimentally-measured f_{ZBS}^{vol} data and the Maxwell-Beard volume function V_{MB}. At left are the measurement and model fits for green paint at 632.8 nm and at right is the same for concrete, also at 632.8 nm. The modelled data (blue) virtually overlie the experimental data (red). The model parameters for the green paint are $\rho_D = 0.00316$, $\rho_V = 0.00096$ and for the concrete $\rho_D = 0.013598$, $\rho_V = 0.014850$.

exceed f_{ss}, such as noted in Figure 8.6. This provides some insight into the polarizing nature of volume scattering, and may be used in part to provide a fit to polarized volume scattering functions.

8.3.3 Specular scan

In Maxwell and Beard's original work, an index of refraction was used for their paint samples based upon past measurement programs, and was not directly derived for their model [65, p. 10]. However, they observe that the index may be determined experimentally by measuring the Brewster angle, θ_B (see equation 2.25). The specular scan provides data used to determine an effective Brewster's angle, from which $\tilde{n}$ may be estimated. As seen from §8.1.3, an accurate estimate of the refractive index is critical for accurately modelling the polarization nature of a material.

The specular scan data is taken by fixing the illumination source, then placing the detector at the approximate location of the specular lobe, that is, $\theta_r \approx \theta_i$ and $\phi_i = 0°$ and $\phi_r = 180°$. With the illumination source remaining fixed, the detector is scanned approximately $\pm 5°$ about the specular direction. This process is repeated for discrete values of the illumination angle, typically spanning $80° \leq \theta_i \leq 10°$ in $10°$ increments. The specular scan data are "area normalized" by taking the product with $\cos\theta_i$ and $\cos\theta_r$, as shown in Figure 8.6.

A few basic relationships are described which may be used in determining $\tilde{n}$. First, it is noted that at a normal angle of incidence, the specular reflectance magnitude from the

Fresnel equations may be shown to be

$$\rho_F(\beta = 0) = \left(\frac{\hat{n}_t - 1}{\hat{n}_t + 1}\right)^2 = \left(\frac{\hat{n}_t - 1}{\hat{n}_t + 1}\right)\left(\frac{\hat{n}_t - 1}{\hat{n}_t + 1}\right)^* , \tag{8.26}$$

assuming the incident medium is air such that $\hat{n}_i \approx 1.0 - i0.0$. In explicit terms of n and κ this is

$$\rho_F(\beta = 0) = \frac{(n^2 + \kappa^2 + 1) - 2n}{(n^2 + \kappa^2 + 1) + 2n} . \tag{8.27}$$

The angle from the specular scan data corresponding to the minimum reflectance or β_{min} may be approximated as Brewster's angle. From Brewster's equation, the minimum reflectance angle may therefore be given by

$$\tan(\beta_{min}) = \hat{n}_t = n + i\kappa . \tag{8.28}$$

Squaring (8.28) and substituting into (8.27) results in

$$\rho_F(\beta = 0) = \frac{(\tan^2(\beta_{min}) + 1) - 2n}{(\tan^2(\beta_{min}) + 1) + 2n} . \tag{8.29}$$

This establishes conditions which n and κ must satisfy. It is noted that there is no direct measurement of $\rho_F(\beta = 0)$, but it may be approximated from the microfacet distribution density function $p(\theta_N)$ obtained from the f_{ZBS} data, in conjunction with the illumination source divergence, distance to the sample, and the receiver solid angle and distance to the sample.

Earlier versions of the NEFDS used $\tilde{n}$ values that were very unrealistic. However, a realistic value of $\tilde{n}$ is not required by the model to obtain and accurate total intensity or f_{00} BRDF model fit. For instance, an unrealistically high magnitude of $\tilde{n}$ could be used, which increases the reflectance. But this may be compensated for by a lower magnitude in the $p(\theta_N)$ function, or a reduced bias parameter B for this function.

The most recent version of the NEFDS, version 9.5, improved the parameter fitting process such that more realistic estimates of n and κ are obtained. Indeed the fit algorithm is undergoing continued improvements, which should result in better n and κ estimates [195]. The accurate determination of $\tilde{n}$ from the empirical data is a complex process. Some of the governing equations from ellipsometry may be employed to provide a more robust fitting technique. A good review of applicable equations may be found in [196, Chap. 29]. Additional discussions on n and κ fitting techniques are given in [98].

8.3.4 In-plane BRDF scan

Finally, the in-plane BRDF measurement is considered. These data are taken with the source fixed at $\theta_i = 60°$ and the receiver scanned through the plane of incidence. This is a more "traditional" measurement, as it provides scattering as a function of θ_r for a fixed θ_i. These data are used to verify the model performance for the $p(\theta)$ and f_{vol} parameters and $\tilde{n}$ determination, and is also used to fit an appropriate shadowing function, S.

Presuming the $p(\theta_N)$, f_{vol} and $\tilde{n}$ are correct, then the modelled BRDF should match well with the experimental data with the exception of shadowing effects. Shadowing effects are manifested by a decreased magnitude in the f_{00} BRDF compared to the modelled results. Therefore the modelled results may be used in conjunction with different shadow functions, and parameters derived for a shadow function which provide the best fit to the data.

From the in-plane BRDF scan, the total intensity or f_{00} BRDF may be determined by taking the average of the s polarization received, and adding that to the average of the p polarization received or

$$f_{00} = \tfrac{1}{2}(f_{ss} + f_{ps} + f_{pp} + f_{sp}) \ . \tag{8.30}$$

The in-plane BRDF measurements are usually made with only one cross-polarized component, ps, as it is consistently found to be nearly identical to ps.

Similarly, the DOP may be determined from the raw in-plane data according to

$$DOP = \frac{f_{ss} - f_{pp}}{f_{ss} + f_{ps} + f_{pp} + f_{sp}} \ . \tag{8.31}$$

The DOP as expressed in (8.31) may actually be negative, and is a result of p polarization dominating over s polarization or χ changing from 0° to 90°.

8.3.5 Parameter fitting summary

A simplistic explanation of the microfacet model parameter fitting process has been described. For the proper polarimetric implementation of a generalized microfacet model, it is critical that the material refractive index is accurately determined. Trades between the refractive index magnitude and the microfacet distribution bias parameter are not allowed as is possible when optimizing the model for the f_{00} or intensity-only signature.

In reality, the fitting process is best accomplished via an iterative approach. For instance, the pp specular scan data should also consider how the surface shadowing impact the raw data. The first derivation of the S function may be used with the specular scan data to make an improved estimate for β_{min}, which in turn refines the refractive index, etc. It is also observed that shadowing effects are also present with volumetric scattering, primarily from

the "masking" effect previously described whereby re-emerging radiance from a microfacet is blocked from observation by a neighboring microfacet.

8.4 Model Implementation

Implementation of the generalized microfacet pBRDF model is accomplished by using the existing BRDF parameters directly from the NEF. In this manner, it is implemented as strictly a polarized Maxwell-Beard BRDF model. In theory, the model parameters may be further optimized providing an improved fit for the polarization signatures.

8.4.1 Materials and Parameters

The raw BRDF measurement data was supplied by the Air Force Research Laboratory at Wright-Patterson Air Force Base for six materials: *i*) a glossy white paint, *ii*) concrete, *iii*) flat tan paint, *iv*) flat green paint, *v*) polished aluminum and *vi*) flat black paint. The model parameters associated with these materials are shown in Table 8.2. These parameters, along with the spectral hemispherical reflectance $\rho_{DHR}(\lambda)$ measurements constitute all the data necessary to drive the model. The $\rho_{DHR}(\lambda)$ data are shown in Figure 8.8.

8.4.2 Spectral Interpolation

8.4.2.1 Intensity-only traditional approach

The NEF Maxwell-Beard model implements f_{00} spectral interpolation in a manner similar to the Background Model as described in §7.3.1. That is, the overall shape of the BRDF is scaled between two spectral bands for which model parameters are available from the raw measurements. In addition, an overall magnitude adjustment is made according to the ratio of the model-derived ρ_{DHR} (provided as a model parameter) compared to the actual ρ'_{DHR} measurement. (The prime ($'$) symbol is used to indicate the directly measured reflectance for that wavelength). In this manner, ρ'_{DHR} is considered the "truth" data which provides a small magnitude adjustment to the parameter-determined BRDF [195].

Mathematically, the BRDF desired at a wavelength λ is given as a linear interpolation of the BRDFs from two adjacent reference wavelengths for which BRDF parameters have been derived, λ_j and λ_k. Remember the NEF interpolation is only for the total intensity, or the f_{00} pBRDF component. The interpolation, adapted from [193, eq. 4.3-1], is given by

$$f_{00}(\lambda) = \rho'_{DHR}(\lambda)\left[\frac{f_{00}(\lambda_j)}{\rho_{DHR}(\lambda_j)}\left(\frac{\lambda_k-\lambda}{\lambda_k-\lambda_j}\right) + \frac{f_{00}(\lambda_k)}{\rho_{DHR}(\lambda_k)}\left(\frac{\lambda-\lambda_j}{\lambda_k-\lambda_j}\right)\right], \tag{8.32}$$

Table 8.2: The parameters for the target material BRDF model. No fit parameters for aluminum at 10.6 μm are available.

Sample	λ [μm]	n	κ	B	σ	τ	Ω	ρ_D	ρ_V	ρ'_{DHR}
White Paint	0.352	1.5810	0.0685	0.0040	0.0035	7.821E+01	6.125E-01	3.279E-03	2.201E-03	0.0358
	0.632	1.5150	0.1122	0.0222	0.0079	1.345E-01	1.459E+00	3.638E-01	-5.010E-02	0.9756
	1.06	1.4960	0.1169	0.0306	0.0081	1.710E-01	1.483E+00	3.761E-01	-4.860E-02	1.0300
	3.39	1.6270	0.1345	0.0011	0.0015	4.355E+01	1.847E+00	1.307E-04	6.875E-05	0.0064
	10.6	1.5990	0.1568	0.0007	0.0013	7.529E+02	3.439E+02	3.992E-04	2.343E-04	0.0071
Concrete	0.352	1.4830	0.0497	0.2033	0.8188	6.091E+01	4.920E-02	2.949E-03	6.431E-03	0.0610
	0.632	1.4980	0.4071	0.2644	0.8574	5.536E+01	6.060E-02	2.290E-02	2.250E-02	0.2113
	1.06	1.4330	0.0102	0.5742	0.8524	4.756E+01	7.410E-02	2.290E-02	3.100E-02	0.2426
	3.39	1.2850	0.2923	0.2356	0.8057	7.145E+01	1.960E-01	1.664E-03	6.500E-03	0.0606
	10.6	1.7730	0.4146	0.0706	0.7556	2.286E+02	2.092E+00	6.629E-04	2.812E-04	0.0513
Tan Paint	0.352	1.4380	0.3021	0.1368	0.7907	8.715E+01	4.160E+00	3.314E-03	4.052E-03	0.0593
	0.632	1.4300	0.3573	0.1093	0.8029	5.879E+01	5.239E+01	1.114E-01	2.310E-02	0.4801
	1.06	1.4330	1.0600	0.0990	1.0600	4.460E+01	4.580E+00	1.974E-01	1.580E-02	0.7245
	3.39	1.2480	0.2833	0.1216	0.5075	2.736E+01	3.365E+01	6.793E-03	9.894E-07	0.0546
	10.6	0.9823	0.4014	0.0415	0.2272	3.136E+00	2.601E+01	1.290E-02	-1.550E-03	0.0648
Green Paint	0.352	1.437	0.3106	0.0602	0.3755	4.230E+01	7.397E+01	4.167E-04	2.469E-04	0.0496
	0.632	1.390	0.3371	0.1048	0.4563	1.854E+01	3.657E+01	6.914E-03	1.552E-03	0.0790
	1.06	1.376	0.2895	0.1739	0.4683	2.210E+01	1.683E+01	4.210E-02	1.769E-03	0.1949
	3.39	1.366	0.2746	0.0235	0.1288	8.789E+01	1.499E+02	-9.450E-04	-1.285E-03	0.0317
	10.6	1.125	1.0000	0.0068	0.0742	1.471E+02	5.338E+01	4.108E-03	-1.645E-03	0.0716
Aluminum	0.352	0.088	20.9400	0.0034	0.0030	7.821E+01	3.837E+00	3.981E-03	-3.058E-03	0.3210
	0.632	5.920	0.3045	0.0129	0.0018	2.145E-01	4.639E+00	5.167E-03	3.466E-03	0.4829
	1.06	28.570	4.8650	0.0029	0.0010	1.705E+00	8.239E+00	7.808E-03	4.138E-04	0.2285
	3.39	1.544	3.1760	0.0015	0.0075	2.287E+00	1.605E+00	-2.284E-03	2.184E-03	0.0247
	10.6	—	—	—	—	—	—	—	—	—
Black Paint	0.352	1.449	0.2146	0.0603	0.3553	2.170E+00	1.470E+02	-1.063E-04	5.286E-04	0.0464
	0.632	1.405	0.2289	0.0556	0.3331	1.717E+00	1.193E+02	-1.762E-04	5.427E-04	0.0402
	1.06	1.383	0.2697	0.0478	0.2914	4.702E+02	4.664E-01	3.892E-05	-3.275E-05	0.0407
	3.39	1.318	0.2882	0.0410	0.2300	2.414E+02	1.625E+02	2.997E-03	-2.015E-03	0.0423
	10.6	1.426	0.4579	0.0116	0.0705	6.039E+01	3.803E+01	7.702E-03	-1.805E-03	0.0533

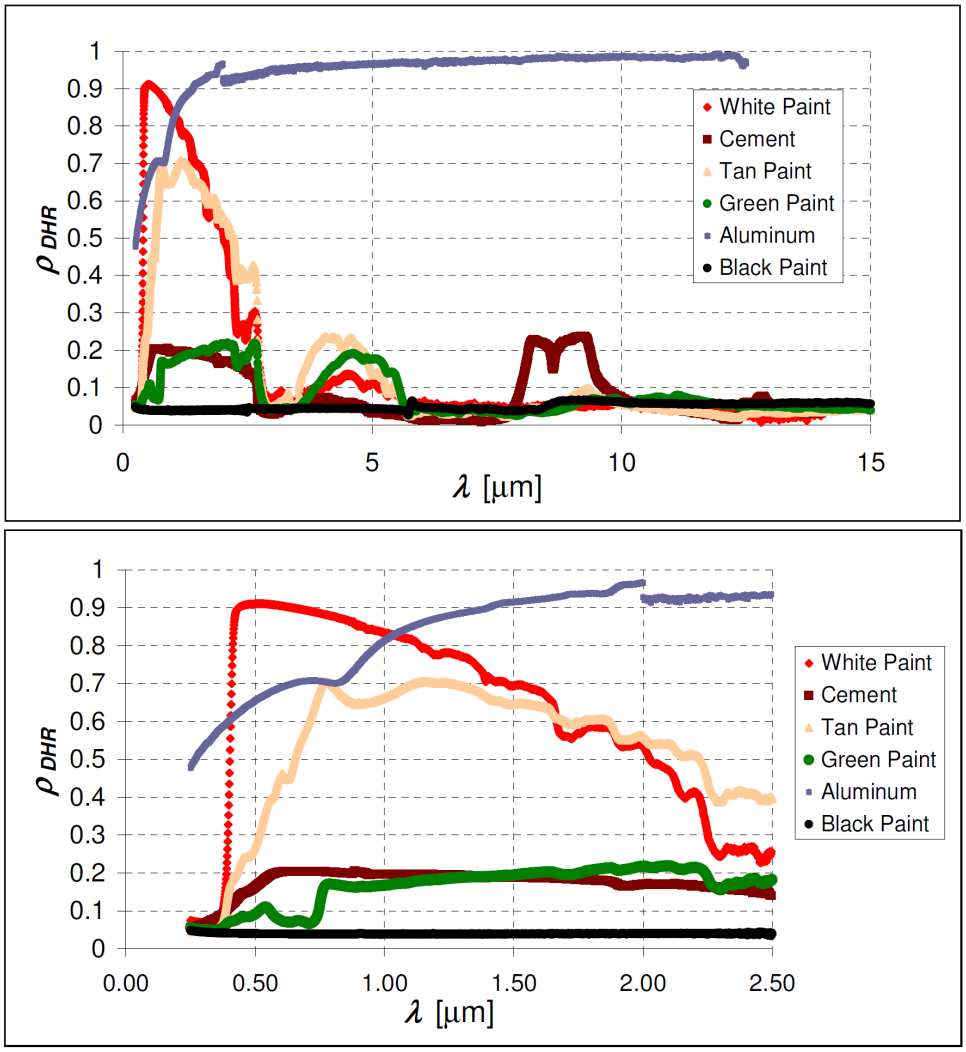

Figure 8.8: The target material $\rho_{DHR}(\lambda)$ measurements extend through the LWIR, with the full range shown on top. An expansion over the VNIR region is shown at bottom. (Note that an instrument transition point is visible for the aluminum sample at 2.0 μm).

where $\rho_{DHR}(\lambda_j)$ and $\rho_{DHR}(\lambda_k)$ are the total reflectance obtained by integration of the model-derived BRDF. Note that $\rho_{DHR}(\lambda_j)$ and $\rho_{DHR}(\lambda_k)$ are provided as model parameters, avoiding the need to perform the integration.[2] From (8.32) it is seen that when λ is equal to a wavelength for which fit parameters are derived (*e.g.*, $\lambda = \lambda_j$), the f_{00} magnitude is simply scaled according to the measured ρ'_{DHR} value or

$$f_{00}(\lambda = \lambda_j) = \frac{\rho'_{DHR}(\lambda_j)}{\rho_{DHR}(\lambda_j)} f_{00}(\lambda_j) \ . \tag{8.33}$$

However, this simple implementation is not possible with the polarized model. The specular component of the model, which is responsible for the polarization, must be scaled independent of the overall BRDF magnitude or f_{00} component. Furthermore, it is not possible to directly interpolate the specular component of the BRDF in a manner analogous with (8.32).

8.4.2.2 Specular component spectral interpolation

A logical means of scaling the specular component of the polarimetric microfacet model is developed by considering the physical basis for the individual specular component functions. It is suggested that both the microfacet probability density and shadowing functions ($p(\theta_N)$ and S) may be scaled directly via the model parameters taken from the adjacent λ_j and λ_k wavelengths. The parameters themselves are not scaled, as this would result in non-linear scaling between the spectral bands, but rather the total product of $p(\theta_N)$ and S are scaled. Both $p(\theta_N)$ and S are physically related to the surface microstructure, and their product will be denoted as μ (after microstructure). The same microstructure at one wavelength may appear different at other wavelengths, just as the required surface quality for LWIR optics are not as stringent as those for the UV. This is one basis for the wavelength-dependent $p(\theta_N)$ and S parameters supplied with the model. Therefore, the scaling of the microfacet distribution and shadowing function product, or μ, may be given by

$$\mu(\lambda) = \mu(\lambda_j) \left(\frac{\lambda_k - \lambda}{\lambda_k - \lambda_j} \right) \ + \ \mu(\lambda_k) \left(\frac{\lambda - \lambda_j}{\lambda_k - \lambda_j} \right) \ , \tag{8.34}$$

where $\mu(\lambda_j)$ is equal to the product of the microfacet density and shadowing functions for which parameters are given for λ_j or $\mu(\lambda_j) = p(B, \sigma, \lambda_j) \cdot S(\tau, \Omega, \lambda_j)$, with the same true

[2] For the six materials considered here, the model-determined ρ_{DHR} for each reference wavelength is provided. However, this is apparently not always the case, and the NEF algorithm performs a BRDF integration at run-time to produce ρ_{DHR} [195]. For materials without this parameter, it may be pre-computed and provided as a parameter, avoiding the need for a run-time generation.

for $\mu(\lambda_k)$. It is noted from (8.34) that when λ is either λ_j or λ_k, that the same value of μ is returned as that directly given by the parameters for that wavelength.

Having interpolated the microstructure related functions, the Fresnel reflectance is examined. As a reminder, the Mueller matrix Fresnel reflectance, $\mathbf{R}_f$ is completely determined by the incident and reflected angles and the material refractive index. Obviously, only the refractive index is λ dependent. As discussed in §5.3.1.3 with the water *DOP* experiment, the refractive index for many materials is relatively stable throughout the VNIR region. Therefore, the refractive index at λ is determined by a simple linear interpolation between the reference wavelengths for which the index was determined. This is admittedly an approximation which is subject to error, but is likely the best technique given the measured data. For large variations in $\tilde{n}$ between the two reference wavelengths there is more uncertainty in the validity of this approximation. The real and imaginary components of the index are each interpolated independently, or

$$n(\lambda) = n(\lambda_j)\left[\frac{\lambda_k - \lambda}{\lambda_k - \lambda_j}\right] \; + \; n(\lambda_k)\left[\frac{\lambda - \lambda_j}{\lambda_k - \lambda_j}\right] \; , \tag{8.35}$$

and similarly

$$\kappa(\lambda) = \kappa(\lambda_j)\left[\frac{\lambda_k - \lambda}{\lambda_k - \lambda_j}\right] \; + \; \kappa(\lambda_k)\left[\frac{\lambda - \lambda_j}{\lambda_k - \lambda_j}\right] \; . \tag{8.36}$$

With $\mathbf{R}_F$ and μ, the specular component of the model, or $\mathbf{F}_r$ is determined for arbitrary λ according to

$$\mathbf{F}_r^{spec} = \frac{\mu(\lambda)\,\mathbf{R}_F(\lambda)}{4\cos(\theta_i)\cos(\theta_r)} \; . \tag{8.37}$$

Summarizing, $\mu(\lambda)$ is the interpolated microstructure scaling factor, or the product of $p(\theta_N)$ and S given by (8.34), and $\mathbf{R}_F(\lambda)$ is the Fresnel reflectance Mueller matrix determined with the interpolated n and κ refractive index values per (8.35) and (8.36).

8.4.2.3 Volumetric component spectral interpolation

It's now time to return to the spectral interpolation of the total intensity or f_{00} component. The technique given by equation 8.32 is still considered the most viable approach, but now the specular f_{00} contribution must be taken into account. From equation 8.5 it was seen that the total f_{00} component is a sum of the specular, Fresnel reflectance and the volumetric contribution. Therefore, it is only the volumetric component which needs to be interpolated between the two measured spectral bands. However, the only truth data for this interpolation is the measured ρ'_{DHR} which includes both the specular and volumetric

contributions or

$$\rho^{'}_{DHR} = \rho^{spec}_{DHR} + \rho^{vol}_{DHR} \ . \tag{8.38}$$

It is therefore necessary to isolate the ρ^{vol}_{DHR} component for each λ to properly implement the spectral interpolation. This must be done for the reference spectral bands λ_j and λ_k used for the interpolation, and also the measurement-provided $\rho^{'}_{DHR}$ which scales the overall result. From (8.38) it is seen that the total volumetric reflectance, ρ^{vol}_{DHR} may be determined by simply subtracting the specular DHR contribution from the measurement-based DHR. This gives what will be termed a "measurement-based" $\rho^{vol^{'}}_{DHR}$ quantity, which is also denoted with a $(^{'})$ symbol or

$$\rho^{vol^{'}}_{DHR} = \rho^{'}_{DHR} - \rho^{spec}_{DHR} \ . \tag{8.39}$$

We are now faced with how to determine ρ^{spec}_{DHR}. Two options are apparent, the first of which is direct integration of the model-based f^{spec}_{00} component. However, this is computationally expensive, and for highly specular materials would require an adaptive sampling approach to converge on an accurate solution. The alternate and preferred technique is to estimate ρ^{spec}_{DHR} based upon the total *model*-based ρ_{DHR} which is provided as a model parameter at the reference wavelengths λ_j and λ_k. From this estimate, $\rho^{spec}_{DHR}(\lambda)$ for arbitrary λ may be determined. Recall that for small changes in the refractive index that Fresnel reflectance is very "gray" or color neutral, so the spectral-dependent magnitude change in ρ^{spec}_{DHR} is minimal.

So the specular reflectance for a reference wavelength j, $\rho^{spec}_{DHR}(\lambda_j)$, for which BRDF parameters are supplied is given by

$$\rho^{spec}_{DHR}(\lambda_j) = \rho_{DHR}(\lambda_j) - \rho^{vol}_{DHR}(\lambda_j) \ . \tag{8.40}$$

For clarification, recall that $\rho_{DHR}(\lambda_j)$ is the model-based reflectance which is supplied as one of the model parameters. $\rho^{vol}_{DHR}(\lambda_j)$ is determined by integration of the f_{vol} BRDF component, with an incident angle of 20°. This angle is used since it is the same incident angle for which the model-based DHR is solved; furthermore, this is the same angle at which $\rho^{vol^{'}}_{DHR}$ is directly measured.

For f_{vol}, ρ^{vol}_{DHR} is given by

$$\rho^{vol}_{DHR} = \int_{\Omega_r} f_{vol} \ \cos(\theta_r) \ d\Omega_r \ , \tag{8.41}$$

which for the Maxwell-Beard volume function (equation 8.15) is

$$\rho_{DHR}^{vol} = \int_{\Omega_r} \rho_D \cos(\theta_r)\ d\Omega_r + \int_{\Omega_r} \left(\frac{2\rho_V}{\cos(\theta_i) + \cos(\theta_r)} \right) \cos(\theta_r)\ d\Omega_r\ . \tag{8.42}$$

The first integral readily evaluates to $\pi \cdot \rho_D$. The second integral, evaluated with $\theta_i = 20°$ is expressed as and solved for by

$$2 \cdot \rho_V \int_{\Omega_r} \left(\frac{\cos(\theta_r)}{\cos(20°) + \cos(\theta_r)} \right) d\Omega_r \ \approx\ 2 \cdot \rho_V \cdot 2.0042 \ \approx\ 4 \cdot \rho_V\ . \tag{8.43}$$

Therefore, the total volumetric reflectance, ρ_{DHR}^{vol} is approximated by

$$\rho_{DHR}^{vol} \approx \pi \cdot \rho_D\ +\ 4 \cdot \rho_V\ . \tag{8.44}$$

So a convenient closed-form solution, in terms of the model-supplied ρ_D and ρ_V components is available. Now ρ_{DHR}^{vol} from (8.44) is available for use in (8.40) which in turn provides the model-based ρ_{DHR}^{spec} specular reflectance for the adjacent λ bands or $\rho_{DHR}^{spec}(\lambda_j)$ and $\rho_{DHR}^{spec}(\lambda_k)$. Given these two bounding values, the specular DHR for arbitrary λ is given by simple interpolation as

$$\rho_{DHR}^{spec}(\lambda) = \left[\frac{\rho_{DHR}^{spec}(\lambda_k) - \rho_{DHR}^{spec}(\lambda_j)}{\lambda_k - \lambda_j} \right] \lambda + b\ , \tag{8.45}$$

where as before the intercept value b is determined by substitution of λ with λ_j or λ_k for which ρ_{DHR}^{spec} is known. Having $\rho_{DHR}^{spec}(\lambda)$ then enables substitution into (8.39) to solve for $\rho_{DHR}^{vol'}$. Equation 8.39 is therefore given explicitly as

$$\rho_{DHR}^{vol'} = \rho_{DHR}^{'} - \left[\frac{\rho_{DHR}^{spec}(\lambda_k) - \rho_{DHR}^{spec}(\lambda_j)}{\lambda_k - \lambda_j} \right] \lambda + b \tag{8.46}$$

Now $\rho_{DHR}^{vol'}$ from (8.46) may be used in place of $\rho_{DHR}^{'}$ from (8.32) to spectrally-interpolate f_{vol}, or equivalently f_{00}^{vol}. This is given by

$$f_{00}^{vol}(\lambda) = \rho_{DHR}^{vol'}(\lambda) \left[\frac{f_{00}^{vol}(\lambda_j)}{\rho_{DHR}^{vol}(\lambda_j)} \left(\frac{\lambda_k - \lambda}{\lambda_k - \lambda_j} \right)\ +\ \frac{f_{00}^{vol}(\lambda_k)}{\rho_{DHR}^{vol}(\lambda_k)} \left(\frac{\lambda - \lambda_j}{\lambda_k - \lambda_j} \right) \right]\ , \tag{8.47}$$

where f_{00}^{vol} for the Maxwell-Beard case is determined by the ρ_D and ρ_V model parameters (eqs. 8.15 and 8.44).

8.4.2.4 Assembling the spectrally-interpolated components

With independently spectrally-interpolated specular and volumetric BRDF components, the total BRDF or $\mathbf{F}_r$ may now be given by

$$\mathbf{F}_r(\lambda) = \mathbf{F}_r(\lambda)^{spec} + \mathbf{F}_r(\lambda)^{vol} \ , \tag{8.48}$$

where $\mathbf{F}_r(\lambda)^{spec}$ is from (8.37) and $\mathbf{F}_r(\lambda)^{vol}$ is from (8.47). It is reminded that all $\mathbf{F}_r(\lambda)^{vol}$ matrix elements are zero, with the exception of the f_{00}^{vol} element.

Finally, it is noted that the method of interpolation supports different component functional forms for the different wavelengths. That is, $p(\theta_N)$ and S do not have to be of the same form for each wavelength. The same is generally true of the f_{vol} function, but a different means of determining ρ_{DHR}^{vol} than that described above would need developing.

8.4.3 Comparison to Empirical Data

Now for the moment of truth—how well is the polarization signature predicted by the model? The model was implemented with the NEFDS 9.5 material parameters, which used the modified Cauchy microfacet distribution function. The model data are examined in the plane of incidence, with an incident angle of 60°. This orientation enables a direct comparison to the laboratory results, per equation 8.31. Figure 8.9 compares the model results to the empirical data at 0.632 μm. The model results throughout the scattering hemisphere are also provided in Figure 8.10

The agreement of the model results with the empirical data vary significantly from material to material. The black paint data agree remarkably well, and the green paint also demonstrates a reasonable approximation. The other results are not as promising however. Volumetric scattering contributions to polarization are evident in the data.

In particular, the lab data for the glossy white paint reveals that p polarization dominates for most orientations. As earlier discussed, these effects were investigated by Ellis [101]. Front-surface microfacet reflectance from the white paint is confined to a small specular lobe, where the model provides a reasonable DOP prediction; away from this orientation volumetric scattering dominates. Since the surface is very smooth, transmitted and refracted radiance back through the surface has a significant p polarization component.

8.4.4 Shortcomings

It is clear from the laboratory measurements that volumetric polarization contributions are significant for some materials. A robust polarimetric BRDF model should incorporate

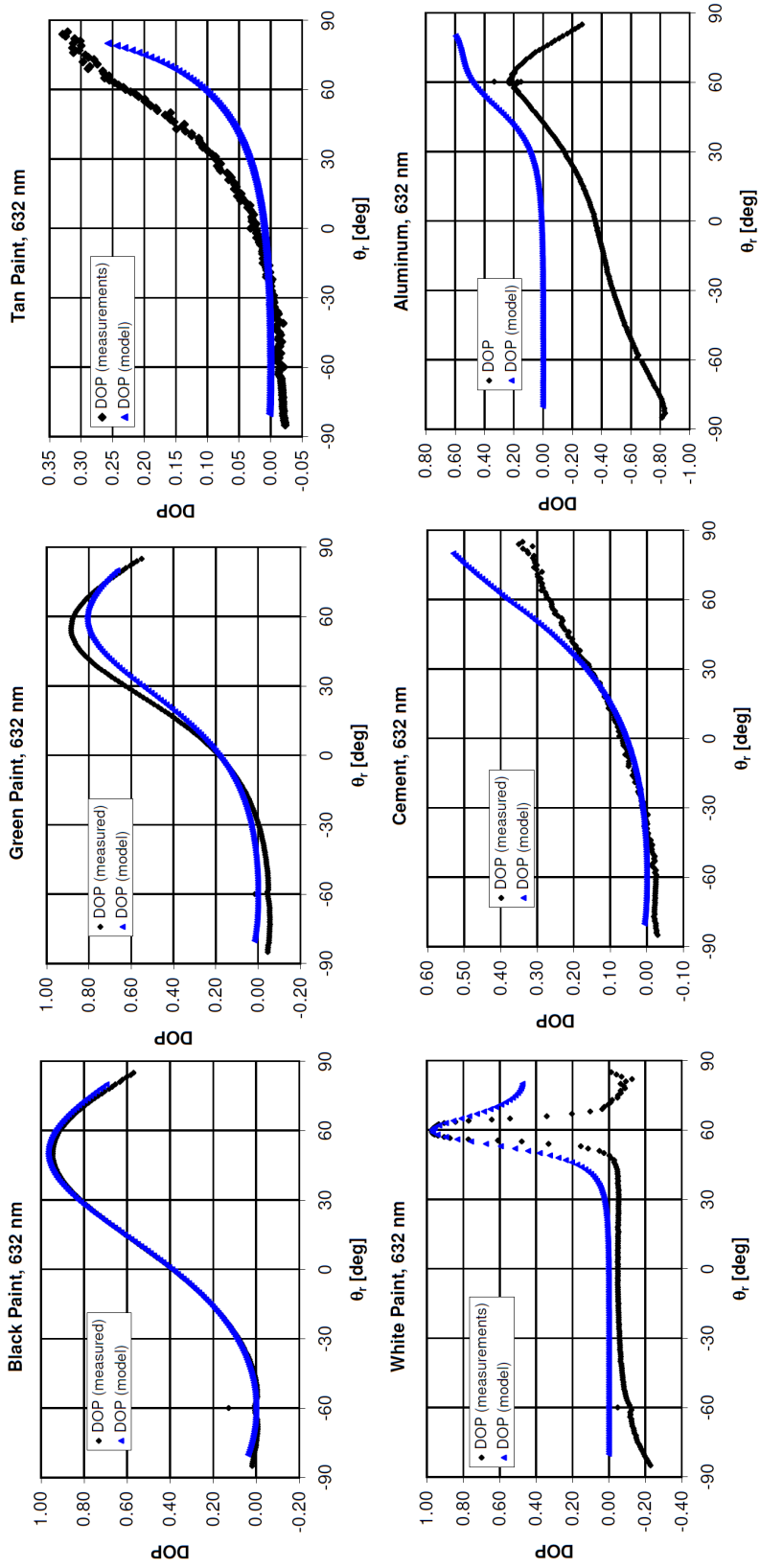

Figure 8.9: A comparison between the laboratory-measured DOP and the generalized microfacet model determined DOP at 0.632 μm.

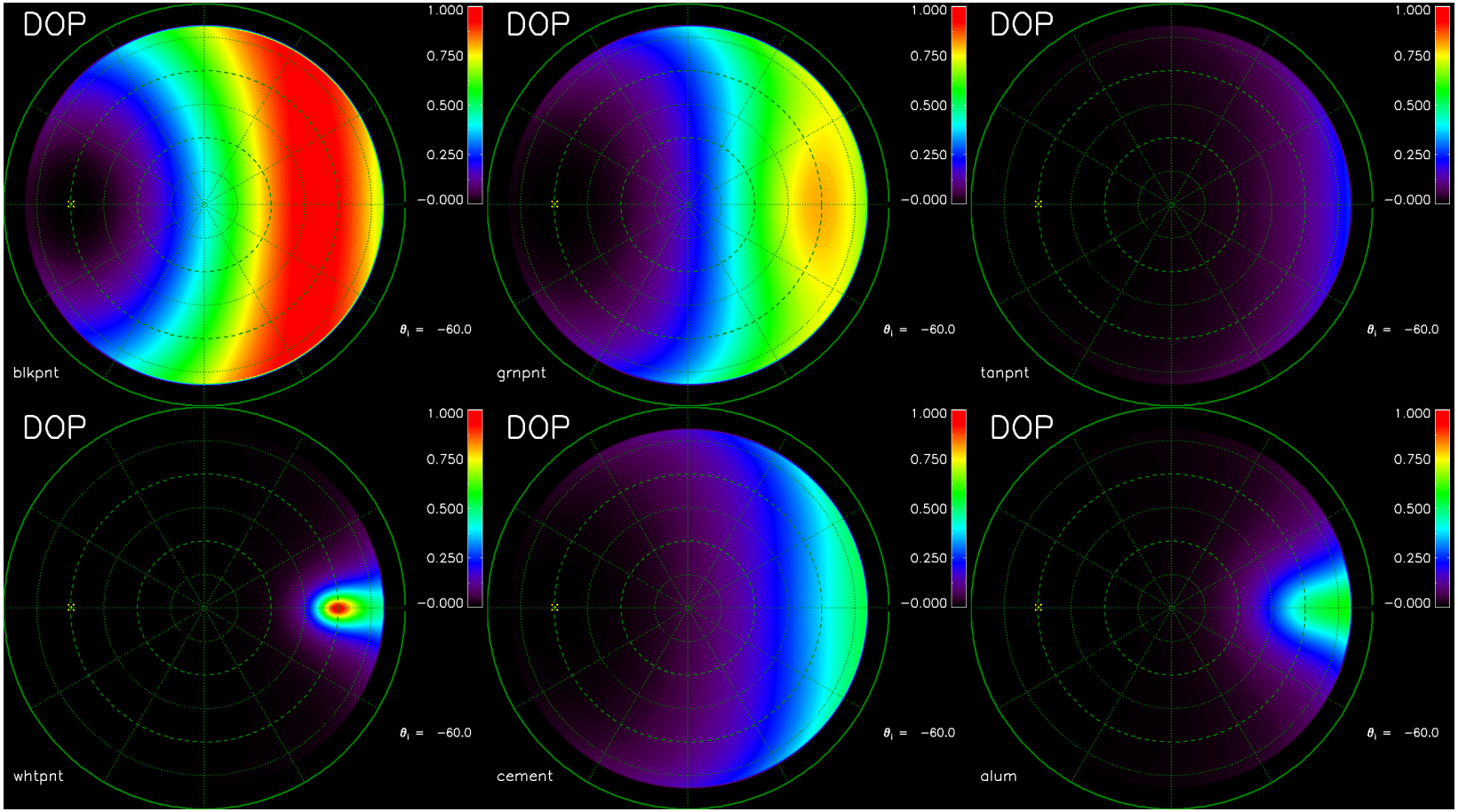

Figure 8.10: The pBRDF model-determined *DOP* throughout the scattering hemisphere (up to $\theta_r = 80°$) for the six materials at 632 μm with $\theta_i = -60°$. The results in the plane of incidence may be seen in Figure 8.9, which also provides a comparison to laboratory measurements. The order of the materials is the same as that in Figure 8.9: black paint (*top left*), green paint (*top middle*), tan paint (*top right*), white paint (*bottom left*), concrete (*bottom middle*) and aluminum (*bottom right*).

a polarized volume function. The raw lab data used to determine the microfacet functions and parameters contain significant data which may be used to incorporate volumetric polarization.

Perhaps a more significant challenge, and one not as easily overcome is an accurate refractive index determination over the spectral bands of interest. A reasonable estimate of $\tilde{n}$ is obtained at the reference wavelengths, however the linear extrapolation of $\tilde{n}$ between the reference bands requires a bit of faith. Many materials have a relatively stable refractive index over the VNIR region; however, absorption bands result in significant high frequency variability in κ which may not be captured by the model. One means of bridging the reference wavelength gaps is to derive the model parameters via hyperspectral BRDF measurements. Rather than using discrete λ measurements, a broad-band source and spectrometer may be used, such as discussed in [98].

8.5 Polarimetric Imaging Measurements of the Target Materials

A unique opportunity afforded itself late in this research effort. The materials from which the raw BRDF measurement data were taken were shipped to RIT. These samples included i) flat green paint, *ii*) flat black paint, *iii*) flat tan paint, *iv*) glossy white paint, *v*) polished aluminum and *vi*) concrete. The polarimetric imaging system described in §5.2, which was devised for the purpose of background material pBRDF measurements was used to measure the NEF material sample pBRDF. However, an additional spectral filter at 650 ± 6 `nm` was acquired, enabling measurements at 550, 650 and 750 `nm`.

8.5.1 Experiment Overview

The same approach and technique as that used for the background material measurements was employed for these samples. The experiment was conducted outdoors, whereby the sun provided a uniform and randomly polarized radiance source. As with the background material measurements, "shadow" or `D` images were made which provided removal of the downwelled sky radiance.

The samples were arranged such that all were measured in a single image frame. The camera distance was such that the x-axis 15° FOV had a GFOV of approximately 13.5 `in`, providing a minimum of 10,000 pixels on each material sample. This proved to be an efficient means to measure the samples, but provided a challenging dynamic range to obtain an adequate exposure for the range of signatures. For this reason two sets of different exposures were sometimes made for a given scattering angle. The samples were placed on the ground atop a blanket-covered cookie sheet, which provided a rigid surface that was

Figure 8.11: An overview of the experimental setup is shown at left, with a closeup of the sample placement at right. The sample placement is white paint (*top left*), concrete (*top middle*), polished aluminum (*top right*), tan paint (*bottom left*), black paint (*bottom middle*) and green paint (*bottom right*).

levelled. All samples were laid flat, with the exception of the concrete sample. The planar side of the concrete sample was faced upward, with material placed under the side such that the planar surface was approximately level. An overview of the measurement area and the sample placement is shown in Figure 8.11.

Only three hemispherical scattering locations were measured. Unlike the background material measurements, the objective was not to acquire many hemispherical samples to drive a pBRDF model. Instead, the goal is to acquire a few signatures which may be compared to existing measurements and the target model results. Two of the scattering orientations were approximately in the plane of incidence with $\theta_i = 34°$, $\theta_r = 0°$ and $\phi = 180°$ and $\theta_i = 29°$, $\theta_r = 51°$ and $\phi = 180°$. The other data set was acquired out of the plane of incidence, but still in a forward scattering orientation at $\theta_i = 24°$, $\theta_r = 43°$ and $\phi = 135°$.

8.5.2 Experimental Results

The results are presented according to the illumination and viewing orientations. A table and figure is provided for each of the three orientations measured. The tabular data include the f_{00}, DOP and χ averages as well as the standard deviation of those results. The figures provide the corresponding images of the same data. The DOP and χ data were derived

after low-pass filtering the raw images with a 5×5 convolution kernel, thus decreasing any errors attributable to residual spatial misregistration. The 5×5 convolution kernel corresponds to an effective ground sample distance (GSD) of approximately 0.044 inches. Note that the native resolution of the f_{00} images are presented for clarity.

Analysis of the data were completed using the "Region of Interest" tool in the popular software package ENVI. A minimum of 10,000 pixels were always used for each material, from which the statistics, to include a histogram, are generated and written out to a text file.

Some data is absent for instances where the sensor was saturated. Saturation was usually limited to the white and tan paint samples. When multiple exposure durations were used at the same orientation, the results from the longest exposure were used when possible, thereby improving the signal to noise.

The measurement technique is ill suited for highly specular materials, such as the polished aluminum sample. Any changes in the sky at the specular reflection location have dramatic impacts in the measurement result. In one instance, the panel used for occluding the sun was "visible" on the aluminum disc, rendering the results useless. (For semi-diffuse materials, these are never issues as no prominent signature is present from a confined direction). Although the glossy white paint is relatively specular, the large fraction of volumetric scattering present when away from the specular lobe results in an effective measurement of this material.

8.5.2.1 Measurement made with $\theta_i \approx 29°$, $\theta_r = 51°$ and $\phi = 180°$

For this measurement orientation, the phase angle ξ is 80°. The tabular results are shown in Table 8.3, with f_{00}, DOP and χ images given as Figure 8.12. No good data are available at 550 nm for the white and tan paints, as the camera was saturated for these materials.

As anticipated, the black paint sample has the highest DOP for all bands, since it has the lowest reflectance and the least volumetric scatter. The next highest DOP is present in the green paint, again consistent with that anticipated from the spectral reflectance magnitude. Most materials exhibit s polarization, such that $\chi \approx 0°$. However, the white paint and aluminum demonstrate p polarization, as previously seen in §8.4.3.

The polarization angle information demonstrates the effect of the time difference between successive images. The data were taken in the following chronological order: 750, 550 then 650 nm. With highly polarizing materials (*e.g.*, the black and green paint), a decreasing χ value is seen following this same order, which results from solar movement. This effect is also observed with the other data sets, thought the order of the acquisition may vary.

Table 8.3: Measurement results for the target materials for $GSD = 0.044$ `in`. For this geometry, $\theta_r = 51°$ and $\phi = 180°$. The images corresponding to these data are shown in Figure 8.12. The solar position was approximately the same for all measurements, but due to a small time difference there is meaningful change per spectral band. Therefore the incident solar angles are specified per band as $\theta_i(550) = 28.5°$, $\theta_i(650) = 30.0°$ and $\theta_i(750) = 27.7°$. Samples which were saturated in the measurement are indicated by "—".

Sample	λ [nm]	$f_{00} \pm \sigma$ [$\mathtt{sr}^{-1}$]		$DOP \pm \sigma$		$\chi \pm \sigma$ [°]	
Green Paint	550	0.0491	0.0009	0.3934	0.0147	-6.392	0.849
	650	0.0381	0.0009	0.5355	0.0201	-8.084	0.910
	750	0.0527	0.0011	0.3966	0.0172	-5.737	1.026
Black Paint	550	0.0292	0.0019	0.6666	0.0173	-5.862	0.646
	650	0.0285	0.0020	0.6748	0.0202	-7.679	0.735
	750	0.0370	0.0030	0.5315	0.0211	-4.934	0.824
Tan Paint	550	—	—	—	—	—	—
	650	0.1343	0.0018	0.0634	0.0086	-9.908	3.931
	750	0.1908	0.0023	0.0464	0.0080	-0.779	5.075
White Paint	550	—	—	—	—	—	—
	650	0.2423	0.0027	0.0846	0.0081	63.192	60.520
	750	0.2498	0.0034	0.0863	0.0072	82.121	24.402
Concrete	550	0.0498	0.0106	0.1512	0.0375	-5.429	4.221
	650	0.0535	0.0123	0.1376	0.0440	-5.738	6.031
	750	0.0625	0.0135	0.1317	0.0337	-4.945	6.247
Aluminum	550	0.0378	0.0083	0.0957	0.0404	34.177	72.097
	650	0.0335	0.0087	0.1264	0.0575	40.876	66.533
	750	0.0302	0.0065	0.1275	0.0430	31.913	74.756

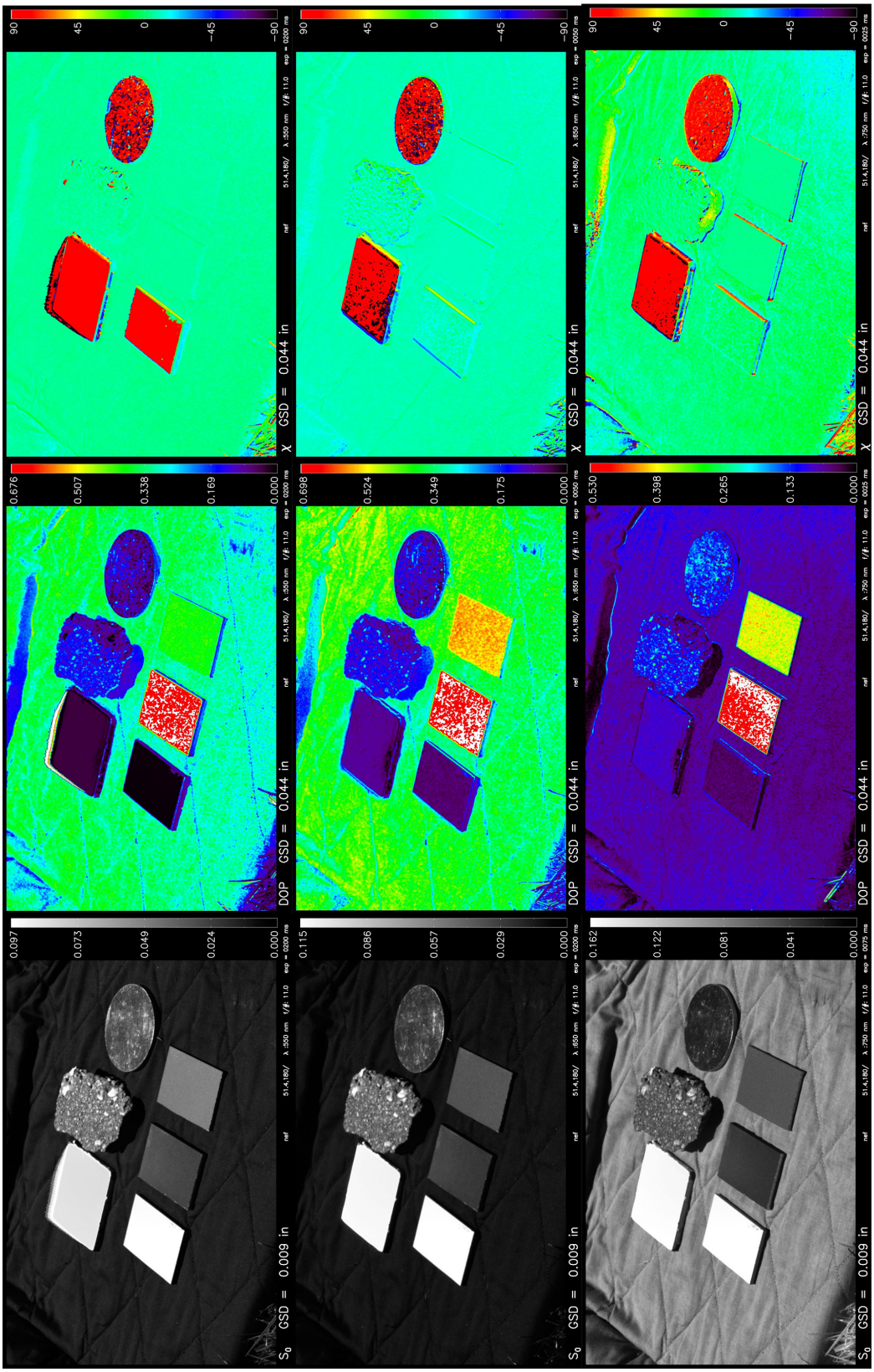

Figure 8.12: Target material results, $\theta_i \approx 29°$, $\theta_r = 51°$ and $\phi = 180°$. Shown left to right are f_{00} at the native resolution, and DOP and χ which have been downsampled to $GSD = 0.044$ in to improve spatial registration. From top to bottom are 550 nm, 650 nm and 750 nm. The tabular results for each material is given in Table 8.3, which also indicates which samples exceeded the camera dynamic range.

Table 8.4: Measurement results for the target materials for $GSD = 0.044$ `in`. For this geometry, $\theta_r = 0°$ and $\phi = 180°$. The images corresponding to these data are shown in Figure 8.13. The solar position was approximately the same for all measurements, but due to a small time difference there is meaningful change per spectral band. Therefore the incident solar angles are specified per band as $\theta_i(550) = 33.9°$, $\theta_i(650) = 32.9°$ and $\theta_i(750) = 34.5°$. Samples which were saturated in the measurement are indicated by "—".

Sample	λ [nm]	$f_{00} \pm \sigma$ [sr^{-1}]		$DOP \pm \sigma$		$\chi \pm \sigma$ [°]	
Green Paint	550	0.0314	0.0006	0.0410	0.0128	-13.819	9.317
	650	0.0216	0.0006	0.0544	0.0177	-8.507	9.323
	750	0.0373	0.0008	0.0444	0.0126	-13.419	7.295
Black Paint	550	0.0125	0.0009	0.0899	0.0157	-3.056	5.026
	650	0.0128	0.0009	0.0841	0.0181	0.375	5.162
	750	0.0198	0.0016	0.0644	0.0126	-3.646	4.723
Tan Paint	550	0.1050	0.0016	0.0141	0.0075	11.794	48.119
	650	—		—		—	
	750	—		—		—	
White Paint	550	—		—		—	
	650	—		—		—	
	750	—		—		—	
Concrete	550	0.0468	0.0102	0.0338	0.0153	2.413	17.875
	650	0.0510	0.0098	0.0329	0.0140	6.135	22.023
	750	0.0588	0.0119	0.0337	0.0174	-1.203	28.605
Aluminum	550	0.0292	0.0068	0.0572	0.0252	-34.443	59.859
	650	0.0261	0.0066	0.0536	0.0258	-30.699	61.300
	750	0.0266	0.0060	0.0543	0.0280	-32.698	66.070

8.5.2.2 Measurement made with $\theta_i \approx 34°$, $\theta_r = 0°$ and $\phi = 180°$

This orientation is the second in the plane of incidence, but now the phase angle is only ξ is 34°, with the camera in a nadir orientation. The tabular results are shown in Table 8.4, with f_{00}, DOP and χ images given as Figure 8.13. Saturation is present in all bands for the white paint, and all but the 550 `nm` band for the tan paint.

As anticipated, the DOP for all materials has decreased compared to the previous data set, which had a much larger phase angle. Note that the entire sample set is rotated significantly from the other in-plane data shown in Figure 8.12. This is a result of solar azimuth movement during this time. In the first data set, the solar position was approximately 224° east of north, while in this data set it is 239°.

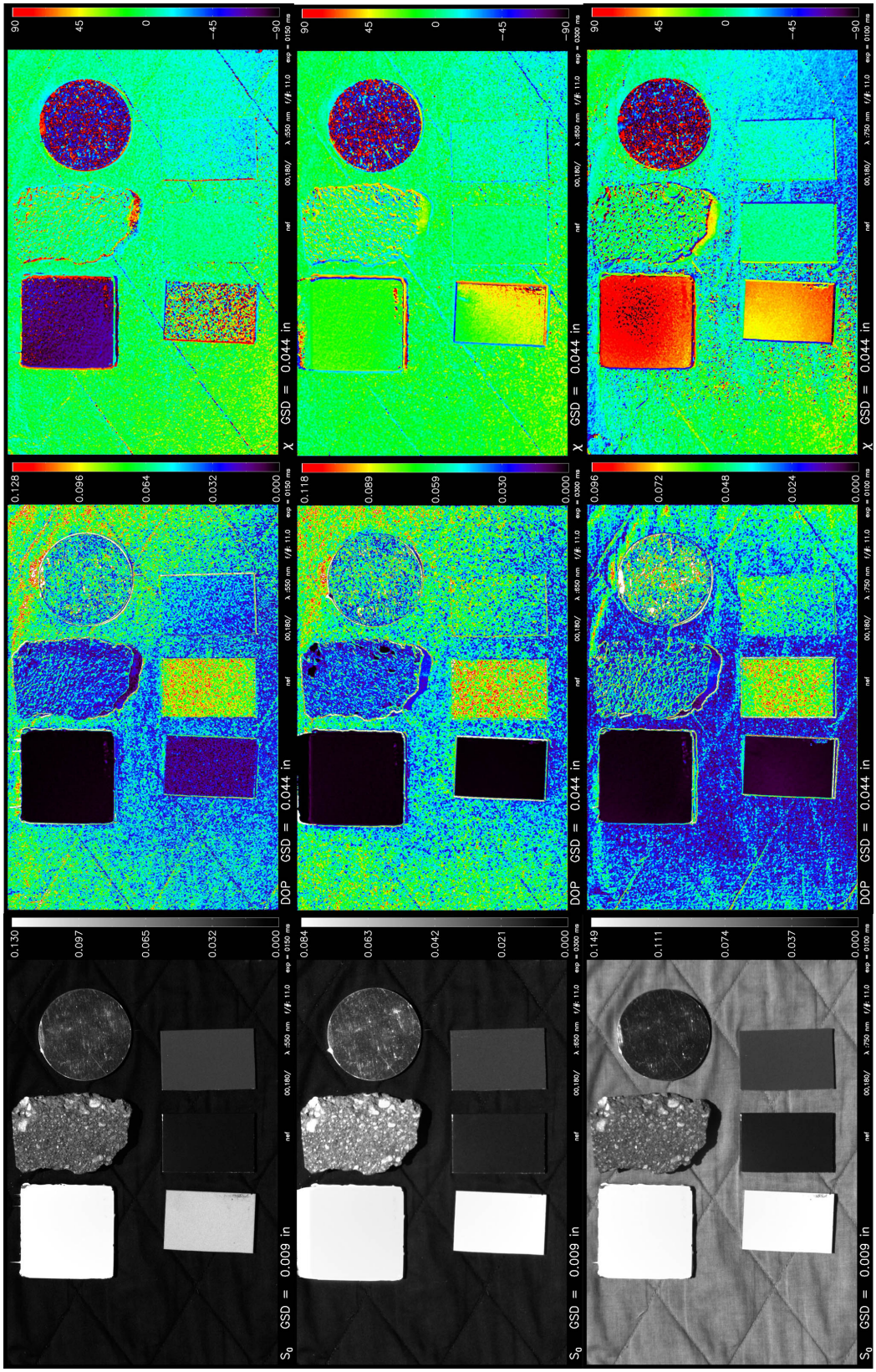

Figure 8.13: Target material results, $\theta_i \approx 34°$, $\theta_r = 0°$ and $\phi = 180°$. Shown left to right are f_{00} at the native resolution, and DOP and χ which have been downsampled to $GSD = 0.044$ in to improve spatial registration. From top to bottom are 550 nm, 650 nm and 750 nm. The tabular results for each material is given in Table 8.4, which also indicates which samples exceeded the camera dynamic range.

Table 8.5: Measurement results for the target materials for $GSD = 0.044$ `in`. For this geometry, $\theta_r = 43°$ and $\phi = 135°$. The images corresponding to these data are shown in Figure 8.14. The solar position was approximately the same for all measurements, but due to a small time difference there is meaningful change per spectral band. Therefore the incident solar angles are specified per band as $\theta_i(550) = 24.7°$, $\theta_i(650) = 24.4°$ and $\theta_i(750) = 23.7°$. Samples which were saturated in the measurement are indicated by "—".

Sample	λ [nm]	$f_{00} \pm \sigma$ [sr^{-1}]		$DOP \pm \sigma$		$\chi \pm \sigma$ [°]	
Green Paint	550	0.0395	0.0007	0.1624	0.0130	12.717	2.893
	650	0.0289	0.0007	0.2185	0.0158	13.170	2.658
	750	0.0442	0.0009	0.1552	0.0121	14.006	2.687
Black Paint	550	0.0217	0.0017	0.3186	0.0186	14.633	2.312
	650	0.0221	0.0016	0.2904	0.0155	15.015	2.206
	750	0.0284	0.0024	0.2286	0.0132	16.029	2.346
Tan Paint	550	0.1141	0.0014	0.0361	0.0113	21.390	11.262
	650	—	—	—	—	—	—
	750	0.1970	0.0023	0.0272	0.0093	32.445	13.587
White Paint	550	—	—	—	—	—	—
	650	—	—	—	—	—	—
	750	0.2619	0.0041	0.0399	0.0088	-17.180	82.972
Concrete	550	0.0562	0.0116	0.0862	0.0232	14.500	4.728
	650	0.0589	0.0056	0.0626	0.0330	14.358	22.478
	750	0.0705	0.0130	0.0709	0.0264	13.668	10.145
Aluminum	550	—	—	—	—	—	—
	650	0.0335	0.0051	0.0968	0.0253	58.956	10.963
	750	0.0329	0.0047	0.0959	0.0209	56.368	8.654

8.5.2.3 Measurement made with $\theta_i \approx 24.5°$, $\theta_r = 43°$ and $\phi = 135°$

Finally, the results for the measurement made out of the plane of incidence is presented. For this measurement orientation, the phase angle ξ is 62°. The tabular results are shown in Table 8.5, with f_{00}, DOP and χ images given as Figure 8.14. Camera saturation occurred for the white paint at 550 and 650 `nm`, and the tan paint at 650 `nm`.

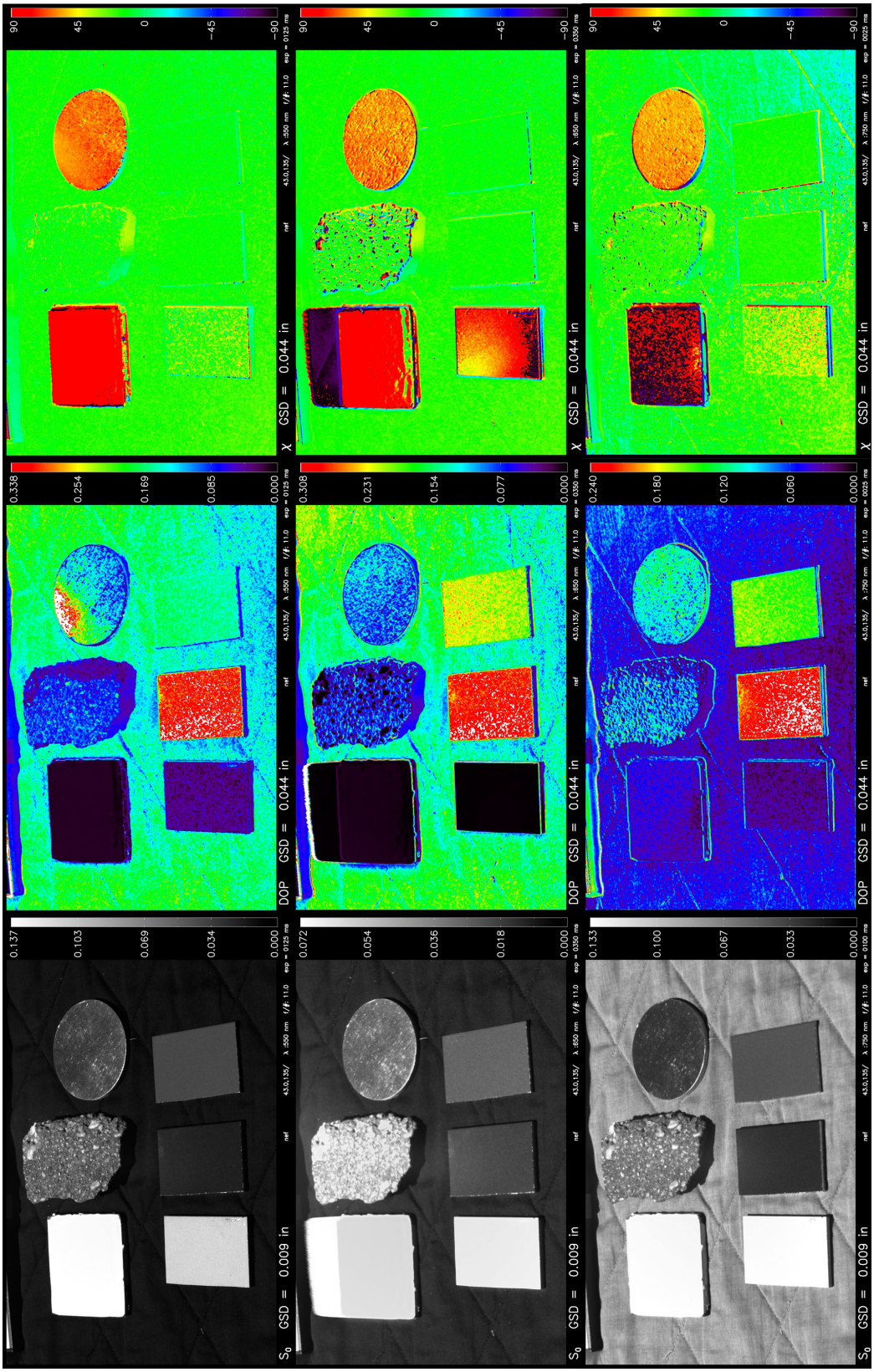

Figure 8.14: Target material results, $\theta_i \approx 24.5°$, $\theta_r = 43°$ and $\phi = 135°$. Shown left to right are f_{00} at the native resolution, and DOP and χ which have been downsampled to $GSD = 0.044$ in to improve spatial registration. From top to bottom are 550 nm, 650 nm and 750 nm. The tabular results for each material is given in Table 8.5, which also indicates which samples exceeded the camera dynamic range.

Table 8.6: A comparison is made between the measured DOP from the imaging experiments to that predicted by the generalized microfacet model. Samples which were saturated in the measurement are indicated by "—".

Sample	λ [nm]	$\theta_i, \theta_r, \phi =$ $29°, 51°, 180°$		$\theta_i, \theta_r, \phi =$ $34°, 0°, 180°$		$\theta_i, \theta_r, \phi =$ $24.5°, 43°, 135°$	
		Meas	Mod	Meas	Mod	Meas	Mod
Green Paint	550	0.3934	0.2348	0.0410	0.0258	0.1624	0.1079
	650	0.5355	0.4237	0.0544	0.0560	0.2185	0.2206
	750	0.3966	0.2554	0.0444	0.0284	0.1552	0.1194
Black Paint	550	0.6666	0.7275	0.0899	0.1350	0.3186	0.4635
	650	0.6748	0.6936	0.0841	0.1238	0.2904	0.4299
	750	0.5315	0.7217	0.0644	0.1281	0.2286	0.4519
Tan Paint	550	—	0.0261	0.0141	0.0028	0.0361	0.0122
	650	0.0634	0.0197	—	0.0021	0.0022	0.0091
	750	0.0464	0.0160	—	0.0017	0.0272	0.0075
White Paint	550	—	0.0221	—	0.0009	0.0116	0.0044
	650	0.0846	0.0288	—	0.0012	0.0072	0.0056
	750	0.0863	0.0315	—	0.0013	0.0399	0.0062
Concrete	550	0.1512	0.1017	0.0338	0.0123	0.0862	0.0503
	650	0.1376	0.1166	0.0329	0.0143	0.0626	0.0583
	750	0.1317	0.1261	0.0337	0.0153	0.0709	0.0628
Aluminum	550	0.0957	0.0561	0.0572	0.0012	—	0.0089
	650	0.1264	0.0766	0.0536	0.0058	0.0968	0.0240
	750	0.1275	0.0393	0.0543	0.0028	0.0959	0.0118

8.5.3 Results Comparison

The pBRDF measurement results from the imaging experiment are now compared to the pBRDF model. The DOP from the model is determined using the same illumination and reflectance geometries as the three scenarios from the experiment. The results are presented in Table 8.6. Overall the results are disappointing. One would hope that the black paint results, for instance, would have relatively good agreement with the imaging experiment given the excellent performance previously seen at 632 nm for $\theta_i = 60°$ (Figure 8.9). However, even this material has significant disparity in the results.

The model results were produced at the central wavelength of the spectral filters used in the measurements. If the actual sensor response were used, the results may marginally improve. However, it is clear that the disparity is not primarily attributed to this approximation.

The rank order correlation of the data presented in Table 8.6 is shown in Table 8.7. The model provides a good prediction of the relative DOP magnitude among the materials.

Table 8.7: A rank order correlation of the data presented in Table 8.6 demonstrates good model performance for the relative DOP magnitude among the materials. Measurements saturating detector have been eliminated from the analysis.

Sample	λ [nm]	$\theta_i, \theta_r, \phi =$ $29°, 51°, 180°$		$\theta_i, \theta_r, \phi =$ $34°, 0°, 180°$		$\theta_i, \theta_r, \phi =$ $24.5°, 43°, 135°$	
		Meas	Mod	Meas	Mod	Meas	Mod
Green Paint	550	3	3	3	4	4	4
	650	5	5	3	3	5	5
	750	5	5	2	3	5	5
Black Paint	550	4	4	5	5	5	5
	650	6	6	4	4	6	6
	750	6	6	4	4	6	6
Tan Paint	550	—	—	1	2	2	2
	650	1	1	—	—	1	2
	750	1	1	—	—	1	2
White Paint	550	—	—	—	—	1	1
	650	2	2	—	—	2	1
	750	2	2	—	—	2	1
Concrete	550	2	2	2	3	3	3
	650	4	4	1	2	3	4
	750	4	4	1	2	3	4
Aluminum	550	1	1	4	1	—	—
	650	3	3	2	1	4	3
	750	3	3	3	1	4	3

8.6 Target Model Summary and Recommendations

A generalized microfacet model has been derived, with results shown for the Maxwell-Beard implementation of the model using material parameters from the NEFDS. Using the NEF material parameters, the model provided reasonable performance for some materials.

It is clear that volumetric polarization contributions can be significant. The raw measurements prescribed by Maxwell-Beard contain information which may be used to approximate a polarized volumetric contribution. The spectral extrapolation of the results is also tenuous; primarily due to the approximations which must be made to the refractive index between the reference wavelengths. Hyperspectral BRDF measurements are one potential solution, whereby parameters may be derived directly for each wavelength.

Still of interest is derivation of the model parameters in a manner similar to that currently being done, but using DOP data as a criteria for the goodness of fit. Some sacrifices to the model output for the f_{00} BRDF component may likely be a good compromise in order to achieve more accurate polarimetric signatures. Along a similar vein, the use of different microfacet probability distribution functions, in conjunction with alternate shadowing representations may also improve the model using the existing raw data and measurement protocol.

Finally, it is acknowledged that often one would like the polarimetric signature of a material for which there have been no laboratory measurements. As seen from the basic phenomenology of material reflectance, some estimation of the polarimetric signature is possible based on rudimentary material properties. This approximation may be based upon *i*) whether the material is a dielectric or conductor, *ii*) a qualitative estimate of surface roughness and iii) a $\rho_{_{DHR}}$ measurement or estimate.

If a material is a dielectric, then the possibilities of volumetric (and hence depolarizing) scattering are greater since the imaginary portion of the index of refraction is near zero, $\kappa \approx 0$. Virtually no volumetric scattering will be present from a conductor. In addition, a conductor will have a lower DOP due to $\kappa > 0$ (with all things being equal) as seen in Figure 2.1.

From an estimate of surface roughness, a microfacet distribution function may be approximated. A notional shadowing function representative of other materials in the same materials class may be used.

A spectral $\rho_{_{DHR}}$ measurement or approximation is crucial. From this measurement, it should be possible to derive an approximation of the total reflectance due to that from the front surface facets. In dielectric materials, the majority of the spectral variability in the $\rho_{_{DHR}}$ is that due to the volumetric scattering (recall Umov's effect and the color neutrality of

Fresnel reflectance). The more reflectance attributed to first surface reflections, the higher the DOP.

The new Generalized Microfacet pBRDF model provides a flexible framework which is highly adaptable to many different materials. The ability to modularize varying microfacet distribution functions, shadowing functions and volumetric contributions enables a broad range of behaviors to fit material scattering properties. The decomposition of the Maxwell-Beard BRDF model into the microfacet representation enables a polarized version of this popular model. In particular, it enables the direct application of the NEFDS material parameters derived for the intensity-only or f_{00} BRDF component model, thus enabling polarization signature approximations to all the NEFDS materials.

Chapter 9

DIRSIG Implementation

As discussed in §4.4, synthetic imagery is an efficient and cost-effective means for guiding the development of algorithms and assessing their performance. Toward this end the Background and Target pBRDF models discussed in Chapters 7 and 8 were implemented in DIRSIG. (See §4.4 for a description of DIRSIG). In this chapter, the implementation and validation of the pBRDF models in DIRSIG is presented. Results from an independent stand-alone algorithm are compared to the DIRSIG results.

The DIRSIG implementation was completed by the Modelling Simulation Team of the Digital Imaging and Remote Sensing Group at RIT. This process practically occurred in three phases: *i*) communicating the model, *ii*) independent verification of results and *iii*) DIRSIG implementation.

Communication of the polarimetric models was accomplished by writing stand-alone documents describing the details of the Background and Target pBRDF models. These documents, in conjunction with meetings with the Modelling and Simulation Team conveyed the model concept and details. Independent verification was completed by matching the pBRDF model results from the original IDL code with stand-alone code from the Modelling and Simulation Team. A variety of illumination and scattering orientations were provided which exercised different model conditions. Finally, after successful independent verification of results, the code was implemented in DIRSIG.

9.1 DIRSIG Settings

Running DIRSIG with the atmosphere set to `SIMPLE` enables derivation of the BRDF from the DIRSIG-produced radiance data to within a close approximation. The `SIMPLE` atmosphere sets the solar irradiance to 0.2 $\frac{\mathtt{W}}{\mathtt{cm}^2 \cdot \mu\mathtt{m}}$, with a constant (and near zero) atmospheric attenuation for all spectral bands. Furthermore, the downwelled sky radiance is set to

1×10^{-3} $\frac{\mathtt{W}}{\mathtt{cm^2 \cdot sr \cdot \mu m}}$, resulting in an effective downwelled sky irradiance of approximately 3×10^{-3} $\frac{\mathtt{W}}{\mathtt{cm^2 \cdot \mu m}}$, or only 1.5% of the solar irradiance. Neglecting this contribution, the f_{00} BRDF component may be determined from a DIRSIG radiance image by noting that

$$L_0 \approx f_{00} \ \cos\theta_i \ E_s \ , \tag{9.1}$$

where L_0 is the first Stokes component of the surface-leaving radiance and E_s is the solar irradiance. f_{00} is therefore approximated by

$$f_{00} \approx \frac{L_0}{\cos\theta_i \ E_s} \ . \tag{9.2}$$

The `SIMPLE` atmosphere setting in DIRSIG also adds a spectrally-uniform upwelled radiance quantity of 0.2 $\left[\frac{\mathtt{W}}{\mathtt{cm^2 sr \mu m}}\right]$ which is simply subtracted off L_0 before calculating f_{00} in (9.2).

DIRSIG image generation was also completed using a realistic atmosphere, generated by the polarized version of MODTRAN, version 4 (MOD4P) [197]. The objective for these data with atmospheric effects was to enable a comparison to experimental data, where a net depolarization of the surface leaving radiance was consistently observed when the effect of the downwelled sky was included. It is noted for the Background Model that MOD4P is not required—the unpolarized MODTRAN is adequate as the polarization of incident radiance is not considered with the Background Model. That is, only the first column of the pBRDF Mueller matrix is present in the Background Model, with all other elements being zero.

Results obtained with realistic atmospheres were not consistent with the experimental data, and in some cases (particularly toward the blue), a *higher* DOP was observed when an atmosphere was present. Further investigation of this anomaly highlighted the manner in which DIRSIG 4.0 was configured for these renderings. The DIRSIG "generic rad solver", which is invoked by the pBRDF models was not configured to perform the sky hemisphere sampling which produces the downwelled radiance. Rather, it only provided a single solid angle sample of the sky in the direction corresponding to the specular reflectance. The net result is that no meaningful DIRSIG output was generated for realistic atmospheric conditions. Reconfiguration of the DIRSIG generic radiation solver is anticipated, which will enable atmospheric effects of the model to be explored and compared to experimental data.

9.2 Background pBRDF Model

Use of the model in DIRSIG required an additional consideration—properly relating the GSD from the model to an equivalent DIRSIG GSD. The measurements and model define the GSD as a linear, x-axis or horizontal dimension from the center of the imaging frame. The tangential increase in GSD for higher θ_r angles is not captured by this representation. For DIRSIG, this equivalent GSD is derived by projecting the solid angle of a sensor element, then calculating the diameter of that solid angle projection at the range of the surface. Using this technique, high look angle (*i.e.*, high θ_r) orientations have correspondingly larger GSD values associated with them.

9.2.1 Background pBRDF Model Verification

A set of verification data from the IDL version of the Background pBRDF model was provided to the Modelling and Simulation Team. The data, shown in Table 9.1, provided a variety of illumination conditions for the lawn grass measurements. The lawn grass Background pBRDF model parameters were given in Figure 7.17. To within floating point accuracy of the algorithms, the results shown in Table 9.1 were successfully replicated. Having obtained this agreement, the model was implemented in DIRSIG.

9.2.2 DIRSIG Background Model Configuration & Data Analysis

DIRSIG was configured to emulate the imaging conditions of the experiments. A simple "plate" of the appropriate background material was constructed and imaged at appropriate geometries. A framing array sensor was constructed, having the same focal length (50 mm) and dimensions as the SenSys camera CCD, but with significantly fewer elements. Rather than a 1536×1024 array, a 128×96 array was used with the photosites having a dimension of 108 μm. The 128×96 array provides a sufficient number of pixels to analyze the resulting statistics. The standoff distance to the plate was then varied to provide the appropriate GSD. For example, a 0.5 in GSD is achieved with a distance of 5.879 m.

The spectral range of the data was usually limited to $0.350\ \mu\text{m} \leq \lambda \leq 1.25\ \mu\text{m}$ with a spectral resolution of 0.025 μm. Spectral convolution of the data was not performed to provide a better match to the imaging system's 550 ± 6 nm and 750 ± 12 nm filter widths; however, there are no significant spectral features within the bandwidth of the filters so direct examination of the data at the 550 and 750 nm wavelength is adequate. DIRSIG currently does not support a sensor spectral response profile when producing Stokes output, so if a realistic sensor response is needed, it must be convolved in post-processing.

Table 9.1: Background pBRDF model verification results for lawn grass with $\rho = 0.04$, $\rho = 0.075211$ (the measured 550 nm band), $\rho = 0.20$ and $\rho = 0.60$. The variability data are for $GSD = 1.0$ in. The material file input parameters are provided in Figure 7.17.

θ_i [°]	θ_r [°]	ϕ [°]	$\overline{f_{00}}$ [sr^{-1}]	$\sigma^{\%}_{f_{00}}$	$\overline{DOP}$	σ_{DOP}	$\overline{\chi}$ [rad]	σ_{χ} [rad]	$\overline{f_{10}}$ [sr^{-1}]	$\overline{f_{20}}$ [sr^{-1}]
$\rho = 0.040000$										
30.0	0.0	180.0	0.010099477	0.0012071299	0.035673421	0.00999200	-4.3711390E-8	0.14769394	0.00036028289	-3.1496932E-11
45.0	60.0	90.0	0.012464409	0.0014897960	0.094614157	0.00999200	0.71372434	0.0043210606	0.00016847288	0.0011672137
45.0	60.0	270.0	0.012464410	0.0014897962	0.094614152	0.00999200	-0.7137244	0.0043210621	0.00016847259	-0.0011672138
$\rho = 0.075211$										
30.0	0.0	180.0	0.020179110	0.0024118880	0.019204699	0.00999200	-4.3711390E-8	0.39620172	0.00038753376	-3.3879279E-11
45.0	60.0	180.0	0.022506809	0.0026901039	0.049132650	0.00999200	-1.0249413E-7	0.065936040	0.0011058192	-2.2667996E-10
45.0	60.0	90.0	0.024095134	0.0028799469	0.051902859	0.00999200	0.71372434	0.055851613	0.00017865814	0.0012377793
45.0	60.0	270.0	0.024095136	0.0028799471	0.051902855	0.00999200	-0.71372447	0.055851623	0.00017865783	-0.0012377793
52.3	5.1	234.0	0.018439844	0.0022040039	0.043154157	0.00999200	-0.069179387	0.094340219	0.00078815142	-0.00010974887
$\rho = 0.200000$										
30.0	0.0	180.0	0.055901677	0.0066815920	0.0072852365	0.00999200	-4.3711390E-8	0.80925978	0.00040725694	-3.5603534E-11
45.0	60.0	90.0	0.065314824	0.0078066890	0.019963640	0.00999200	0.71372434	0.37858812	0.00018627461	0.0012905477
45.0	60.0	270.0	0.065314826	0.0078066892	0.019963639	0.00999200	-0.71372447	0.37858815	0.00018627428	-0.0012905477
$\rho = 0.600000$										
30.0	0.0	180.0	0.17040718	0.020367748	0.0024369828	0.00999200	-4.3711390E-8	1.0820581	0.00041527936	-3.6304876E-11
45.0	60.0	90.0	0.19744086	0.023598922	0.0067161142	0.00999200	0.71372434	0.83733224	0.00018943372	0.0013124347
45.0	60.0	270.0	0.19744087	0.023598922	0.0067161138	0.00999200	-0.71372447	0.83733226	0.00018943338	-0.0013124347

With this sensor configuration, a hypercube having dimensions of $128 \times 96 \times 148$ was produced with four spatial images for each spectral band corresponding to the S_0, S_1, S_2 and S_3 Stokes vectors. Note that no circular polarization is produced by the model, resulting in $S_3 = 0.0$ for all spectral bands. The DIRSIG output was analyzed by an IDL program which parsed the Stokes image hypercube, from which DOP and χ calculations were made on a spectral basis.

9.2.3 DIRSIG Background Model Results

Following is output produced by DIRSIG, which is compared with the experimental data and also the independent background model output. Note that some minor differences are present in the DIRSIG data. Achieving the exact orientation geometry is challenging; however, these differences are smaller than the FOV of the imaging system.

The results for grass are first presented. A "plate" of grass was used along with the spectral reflectance measurements given in §7.4. The pBRDF model parameters for lawn grass as shown in Figure 7.17 were used. Figure 9.1 illustrates DIRSIG output for lawn grass at 550 nm for a geometry of approximately $\theta_i = 29.3°$, $\theta_r = 49°$ and $\phi = 180°$, closely corresponding to one of the experiment orientations. The decreased variability for increasing GSD is readily apparent. Note that since a different GSD is achieved via the standoff distance of the sensor, that the same number of pixels are present in the images, but with coverage of a commensurately larger ground region.

Figure 9.2 provides an examination of the f_{00} and DOP statistics from 0.350 μm to 1.25 μm for the same orientation as the 550 nm shown in Figure 9.1. The reduced variability is apparent with increasing GSD in all spectral bands.

The DIRSIG results from the background model are compared to the IDL model in Figure 9.3. The experimental results are also presented.

9.3 Target pBRDF Model

Implementation of the Target Model proceeded with the same steps as those taken with the Background Model. A thorough verification of the IDL code output was completed against the output produced by the Modelling and Simulation Team, followed by implementation of the code into DIRSIG.

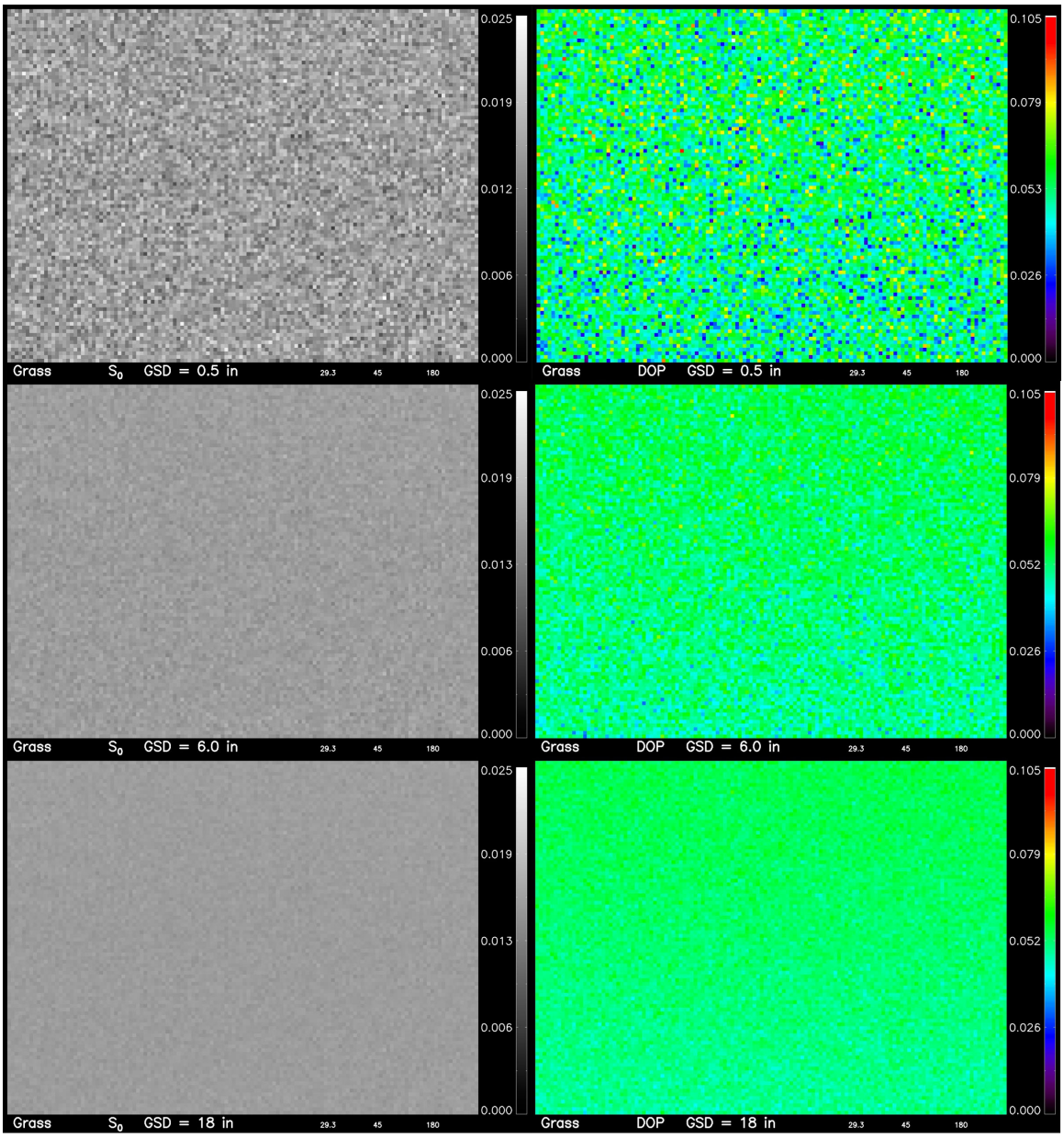

Figure 9.1: DIRSIG results for grass at 550 `nm` with a geometry approximately $\theta_i = 29.3°$, $\theta_r = 49°$ and $\phi = 180°$. At *left* is f_{00} and *right* DOP. The GSD size increases from top to bottom: $GSD = 0.5$ `in` (*top*), $GSD = 6.0$ `in` (*middle*) and $GSD = 18$ `in` (*bottom*). Note that the average DOP noticeably increases toward the top of the frame, which is a result of the increasing phase angle ξ.

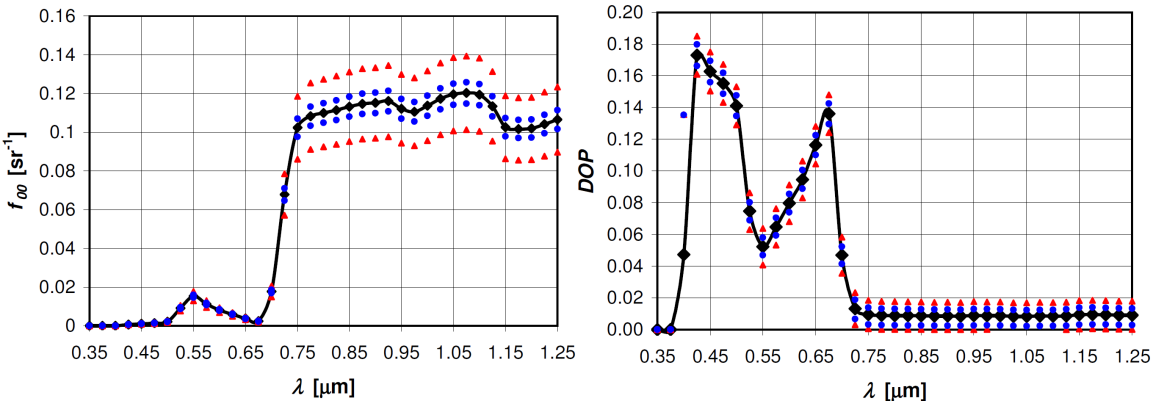

Figure 9.2: DIRSIG spectral results for grass with a geometry approximately $\theta_i = 29.3°$, $\theta_r = 49°$ and $\phi = 180°$ (see also corresponding 550 *nm* imagery from Figure 9.1). At *left* is the mean f_{00} (black, line) and $\pm\sigma$ results for $GSD = 0.5$ `in` and $GSD = 6.0$ `in` (red triangles and blue circles, respectively).

9.3.1 Target pBRDF Model Verification

A variety of geometries and material types were provided to the Modelling and Simulation Team. The initial verification was performed for a data set prior to implementing the spectral interpolation technique. After verifying these results against the independent IDL code, a set of spectral interpolation cases were tested, successfully replicated and coded into DIRSIG.

A sample of the verification output is shown below, where variable names are closely correlated to those presented in §8.4. These IDL results were matched to the Modelling and Simulation Team results to within floating point accuracy.

```
////////// SPECTRAL INTERPOLATION VERIFICATION DATA \\\\\\\\\\

Material: cement

Lambda (microns):        0.750000

linearly interpolated rho_lambda from rho LUT at lambda of interest
    0.203700
Geometry, th_i, th_r, phi
   24.000000   43.000000  135.000000
F_r_lambda
    0.056813    0.001408    0.003212
    0.002761   -0.001734    0.008264
    0.002163    0.007897    0.002417
```

				f_{00} [sr^{-1}]						*DOP*					
Material	λ [nm]	Orientation	GSD [in]	Meas.		IDL Code		DIRSIG		Meas.		IDL Code		DIRSIG	
				mean	std dev	mean	std dev	mean	std dev	mean	std dev	mean	std dev	mean	std dev
grass	550	29.3, 45, 180	0.5	0.01630	0.00329	0.01535	0.00260	0.01531	0.00242	0.05582	0.02227	0.05441	0.01170	0.05228	0.01150
grass	550	29.3, 45, 180	6.0	0.01630	0.00080	0.01535	0.00074	0.01531	0.00070	0.05582	0.00596	0.05441	0.00558	0.05237	0.00549
grass	550	29.3, 45, 180	18.0	n/a	n/a	0.01535	0.00043	0.01531	0.00039	n/a	n/a	0.05441	0.00287	0.05241	0.00283
grass	750	29.3, 45, 180	0.5	0.12235	0.01155	0.10299	0.01745	0.10231	0.01620	0.00557	0.01497	0.01062	0.01170	0.00945	0.00897
grass	750	29.3, 45, 180	6.0	0.12235	0.00242	0.10299	0.00499	0.10230	0.00468	0.00557	0.00499	0.01062	0.00558	0.00851	0.00533
grass	750	29.3, 45, 180	18.0	n/a	n/a	0.10299	0.00287	0.10230	0.00265	n/a	n/a	0.01062	0.00287	0.00846	0.00352
soil	550	24.3, 45, 180	0.5	0.01675	0.00229	0.01250	0.00173	0.01385	0.00205	0.11109	0.01682	0.13607	0.01286	0.10894	0.01576
soil	750	24.3, 45, 180	0.5	0.03121	0.00386	0.02641	0.00364	0.02852	0.00402	0.06907	0.03397	0.07588	0.01304	0.05731	0.01688

Figure 9.3: Tabular data are shown for DIRSIG output compared to the Background Model as implemented in IDL. Experimental results are also provided. The DIRSIG and Background Model results demonstrate good agreement; though a one-to-one comparison is not possible due to a small downwelled sky contribution in DIRSIG as well as a slight variation in geometry.

```
************** DIAGNOSTIC OUTPUT **************

Auxiliary angles: beta, theta_n, eta_i, eta_r (deg)
   30.918620   16.528177  -33.161810  -19.040004
-------------- SPECULAR COMPONENT -------
Interpolated refractive index
    1.480080   -0.297674
interpolated microstructure, mu
    0.437875
Fresnel Reflectance Mueller Matrix
    0.053283    0.008595    0.019603
    0.016848   -0.010582    0.050436
    0.013201    0.048197    0.014750
-------------- VOLUME COMPONENT --------
rho_vol_j
    0.161942
rho_vol_k
    0.195942
rho_spec_j
    0.049358
rho_spec_k
    0.046658
Interpolated rho_spec_lambda
    0.048613
rho_vol_prime
    0.155087
f_vol_j
    0.050257
f_vol_k
    0.060592

******** POLARIZATION INFO (not part of model) ******
Stokes incident
    1.000000    0.000000    0.000000
Stokes Out Magnitude
    0.056813
Normalized Stokes out
    1.000000    0.048590    0.038072
DOP
    0.061729
chi (deg)
   19.040004
Tue Aug 16 19:37:33 2005
```

9.3.2 DIRSIG Target Model Configuration & Data Analysis

The scene used for the Target model output is from the target material imaging experiment, described in §8.5. However, the six materials were placed on grass, which was in turn modelled using the Background model. Therefore concurrent Target and Background Model output is generated using the scene.

The DIRSIG sensor was designed to the same FOV and focal length as the SenSys camera used to acquire the data, but using a lower spatial resolution to help keep the file sizes manageable with high spectral resolution output. The overall focal plane dimensions were kept the same (thus preserving the FOV), while the focal plane detector sizes were increased. The resulting system had a 50 mm focal length, with a 308×205 array having 45 μm detectors.

An IDL program was written to analyze the DIRSIG output in a manner similar to the program used for the Background model output.

9.3.3 DIRSIG Target Model Results

DIRSIG was used to emulate the target material experiment for the $\theta_i \approx 29°$, $\theta_r = 51°$ and $\phi = 180°$ illumination and viewing conditions. Those results were presented in §8.5.2.1. The DIRSIG DOP output, compared to the field experiment DOP data is shown in Figure 9.4. As anticipated from Table 8.6, the results do not have good agreement with the field data. However, the discrepancy between the DIRSIG and field experiment results is greater than that between the IDL model and field results. Further investigation into the source of this anomaly is required to understand the problem. The sky sampling method, as currently implemented by DIRSIG's generic radiation solver may be in part the source of the discrepancy.

9.4 DIRSIG Summary

DIRSIG is a high fidelity physics-based synthetic imaging generation program with proven radiometric accuracy in simulating overhead sensing when used in conjunction with MODTRAN. It should be considered a leading candidate for continued application of pBRDF models toward the objective of developing and exercising polarization-based target detection and identification algorithms. The Background model has been successfully implemented in DIRSIG with results corroborated with external models and experimental data. A preliminary Generalized Microfacet Target model has also been implemented in DIRSIG, though the execution in DIRSIG requires further evaluation and validation.

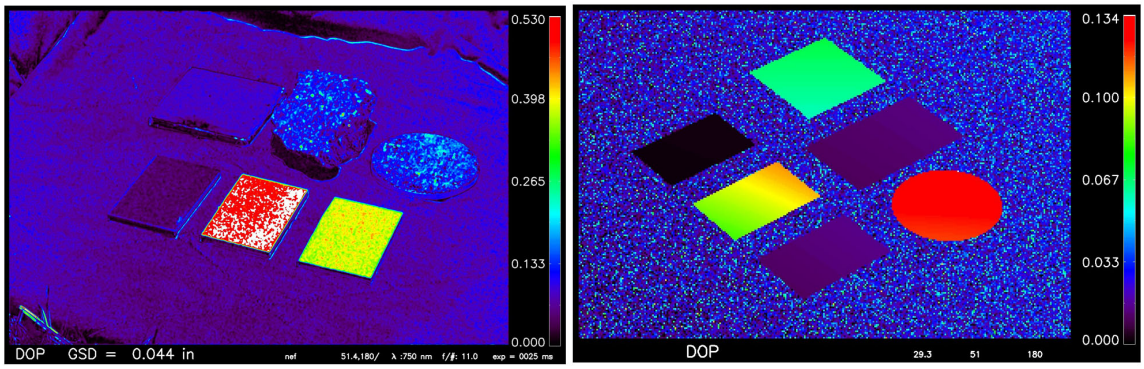

Figure 9.4: The field experiment *DOP* results (*left*) compared to DIRSIG results (*right*) at 550 nm. The DIRSIG output uses both the Target and Background pBRDF models, by placing the materials on grass instead of the cloth-covered sheet used in the field experiment. The DIRSIG output is for a similar illumination and viewing orientation as that of the field experiment: $\theta_i \approx 29°$, $\theta_r = 51°$ and $\phi = 180°$. The orientation difference between the images is from a different azimuthal positioning of the materials in the DIRSIG reference frame—the θ_i, θ_r and ϕ values are in fact similar.

Chapter 10

The Next Step

Now that the tools are in hand for estimating *a priori* polarized radiance from background and target materials, the question remains as to *how* to apply this knowledge. This chapter concludes the research by exploring a few additional areas, and making recommendations for future work. Three areas are briefly addressed: *i*) examination of polarimetric error sources throughout the imaging chain, *ii*) potential approaches toward spectral-polarimetric target detection algorithms, and *iii*) sources of polarimetric imagery which may be made available for future research.

10.1 Polarimetric Error Propagation

The importance of quantifying and bounding polarimetric errors in the image chain cannot be overestimated. If one discovers the uncertainty in the upwelled atmospheric polarized radiance contribution ($\vec{L}_u$) to be an order of magnitude higher than the polarimetric BRDF model used on a material, it would be ill-advised to expend resources on further refinement of the pBRDF model. Once the errors have been quantified, a means of minimizing and managing the errors is warranted. For instance, supporting data on atmospheric properties under which polarimetric imagery was acquired may provide substantial information toward atmospheric error reduction. Some of the uncertainties which may be investigated are shown in Table 10.1.

10.2 Polarimetric Image Investigation

In order to develop and test multispectral polarimetric algorithms, data must be made available. DIRSIG may adequately serve as the basis for many studies, but actual spectral polarimetric data is needed to thoroughly exercise algorithms. Next candidate sources of

Table 10.1: Polarization error sources.

Source	Potential Means of Investigation
$\vec{L}_d$, downwelled radiance	Coulson tables, MODTRAN4P, scattering phase functions, cloud cover impacts
$\vec{L}_u$, upwelled radiance	Coulson tables, MODTRAN4P, phase functions, POLDER images
Sensor/payload	quantify typical uncertainties for state-of-the-art imaging polarimeters
pBRDF	geometric (surface normal) uncertainties, pBRDF model departure from actual, pBRVF for target materials

Table 10.2: Polarimetric imagery sources.

Source	Attributes	Description
Quick Look Sensor	panchromatic, linear polarization	aircraft based, low altitude
AFRL/VS	multi-spectral, full polarization	tower collection efforts—scene content and spectral bands TBD
POLDER	3 spectral bands, linear polarization	GSD of 7 km
Space Shuttle	film-based pan & Ektachrome, linear polarization	calibration issues

polarimetric data are discussed, along with the preliminary analysis of some data which was obtained. The availability of this data is considered with respect to future research at RIT. A summary of the image data available is shown in Table 10.2.

10.2.1 Quick Look Sensor

In August 2002, General Dynamics of Ann Arbor, Michigan, led a collection of panchromatic linear polarization images in Alaska for the Bureau of Land Management (BLM). The Quick Look Sensor (QLS) instrument collected data using four bore-sighted DALSA 1M15 cameras having a 12-bit 1024×1024 silicon focal plane array mated with an f5.6, 100 mm focal length optics. This configuration provides an IFOV of 0.14 mrad producing a full angle FOV of 143.4 mrad or 8.2°. The linear polarization axes for the cameras are oriented at 0°, 45°, 90° and 135°. The raw imagery was processed and reportedly registered to within $\frac{1}{20}$ of a pixel [198], from which S_0, S_1 and S_2 imagery is derived. These images have been provided in a 940×940 single precision floating point format.

QLS is calibrated before each flight by imaging into an integrating sphere, enabling camera-to-camera response normalization. For noise correction, a dark current image is subtracted from each image and read-out noise corrections are made in the subsequent processing. With the BLM data collect, stray light is an issue for some camera look angles. The stray light is from internal reflective components near the focal plane (later corrected),

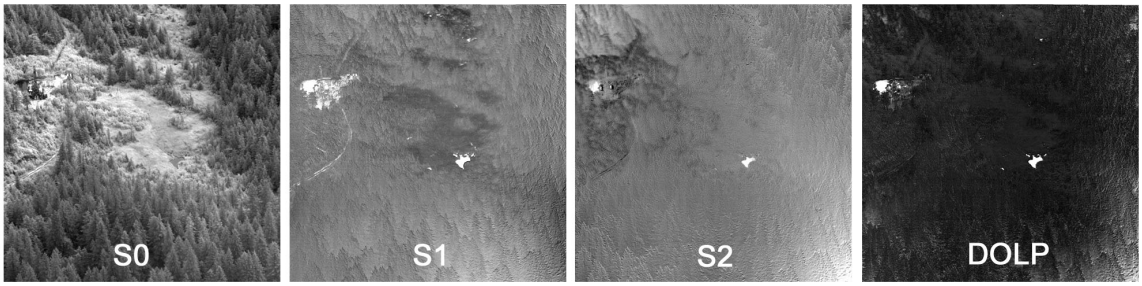

Figure 10.1: Stokes and derived DOLP images from the QLS BLM data—an oil drill pad area (03-010). As expected, a high DOLP signature from the water is evident. Note the artifacts in the bottom right of the frame from the camera flare.

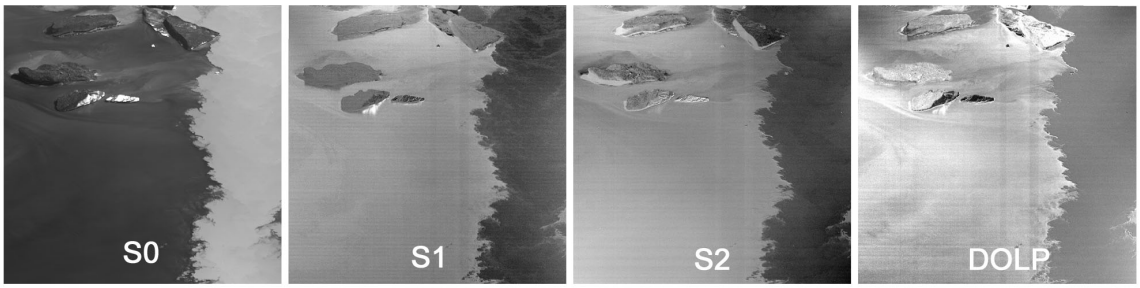

Figure 10.2: Stokes and derived DOLP images from the QLS BLM data–mouth of a river (08-073). A contrast reversal of the turbid versus relatively clear water is seen between the S_0 and linear polarization elements. Also of interest is the high S_1 signal from the reflection of the sea ice.

and is manifested by flare around the image periphery [199].

Four image sites were provided in the data set. A typical data set provides > 50 images acquired by the aircraft in a circular orbit about the target area. There is minimal meta-data supporting this collect, but the time, aircraft altitude, and aircraft latitude and longitude are provided. The target area latitude and longitude may be estimated from these data, and the solar position is easily obtained given the location and time. Image examples are shown in Figures 10.1 and 10.2, which have been linearly stretched to the full dynamic range.

Some predictions and observations of the QLS data are made. For example, much of the signal from water surfaces is specular reflection of the sky, which is also polarized. Given the derived solar and sensor orientation information some rudimentary predictions may be made and compared with that observed in the data. Figures 10.2 and 10.1 images were encoded into hue, saturation and value (HSV) color space representing the polarization angle (χ), DOLP, and S_0, respectively, according to the method proposed by Bernard [200].

Derivation of χ brings up another source of error in the images—the changing pitch of

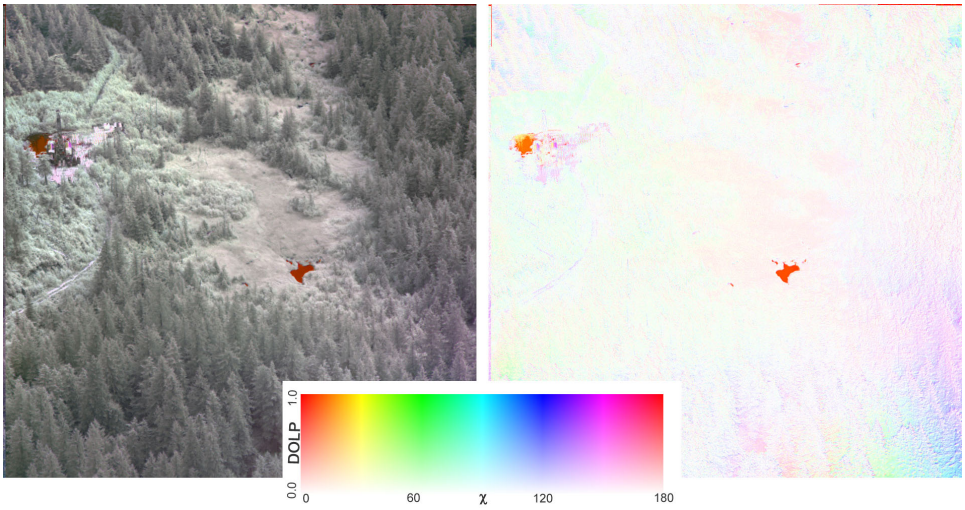

Figure 10.3: QLS image of Figure 10.1 encoded into hue, saturation and value (left). The image at right has the value set to 1.0 so that only the polarization information is visible. To increase visibility, the DOLP (saturation) has a 3× multiplier.

the aircraft. The derived Stokes images are in the camera reference frame, which may result in the S_1 axis not correlated to the local earth horizon for images generally taken 90° relative to the flight direction. This error has been estimated as ±5° [199], and is synonymous with the reference frame error previously discussed in §5.3.1.1.

An algorithm was written to encode the images into HSV space, with the results shown as Figures 10.3 and 10.4. Some interesting effects are visible in the HSV-encoded images. In the oil pad area image (Figure 10.3), the water surfaces have a high DOLP as anticipated, which is predominantly oriented in the $\chi \approx 0°$ or equivalently the 180°. However, notice the water area above and to the left of the oil drill—the reflection of the tree into the water is brought out as a change in the χ orientation, as opposed to the dominant sky-reflection area. It may also be concluded that the $\chi \approx 160°$ signal from around the base of the oil drill area is not water, but one would have likely made this conclusion looking at only S_0 imagery. The vegetation is largely randomly polarized, at least at this GSD. (The polarization present in the bottom right is attributed to the flare issue).

The water and ice scene of Figure 10.4 also has its share of interesting features. Perhaps the first observation is that of the predominant χ orientation. A χ histogram shows the distribution to be bimodal with means centered at $\chi_1 \approx 85°$ and $\chi_2 \approx 130°$. This is perhaps counter-intuitive, for if an unpolarized background were being reflected, one would expect $\chi \approx 0°$. Closer scrutiny provides some insight. The reflection of the sea ice in the water has a high DOLP, and is by definition at $\chi = 0°$, since the radiance leaving the sea ice is highly

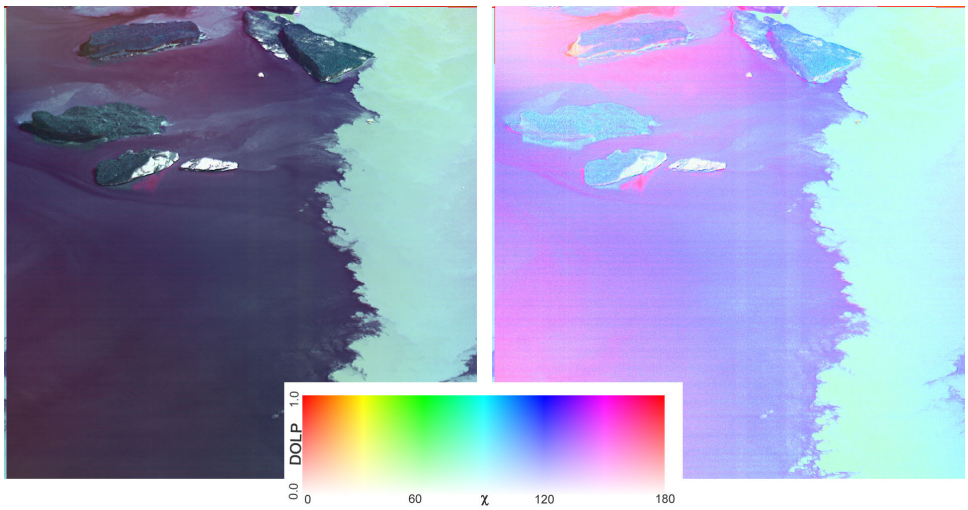

Figure 10.4: QLS image of Figure 10.2 encoded into hue, saturation and value (left). The image at right has the value set to 1.0 so that only the polarization information is visible. To increase visibility, the DOLP (saturation) has a 3× multiplier.

randomly polarized. However, the observed χ-orientation is approximately 170° or −10°. A logical conclusion is that the camera optical axis is rotated 10° from the true horizon, which may be from the pitch of the aircraft.

Other effects to note are the lower DOP in the turbid water to the right. This is expected since a larger fraction of the signal is from diffuse scattering under the water surface. Also, the multiple, diffuse scattering of the sea ice is seen to be highly randomly polarized, as expected. As for the bimodal χ distribution, some valid hypotheses may be errors resulting from the camera flare (in particular the $\chi \approx 160°$ regions near the corners. Other explanations could be the downwelled radiance of cumulus clouds being reflected, as opposed to the partially polarized diffuse sky radiance.

Phenomenology such as this may be explored in more detail with some quantitative analysis of the QLS data. In particular, for scenes with a broad expanse of water, the effects of the partial polarized sky radiance may be investigated. Doing so requires convolving the DALSA 1M15 CCD quantum efficiency (Figure 10.5) with the diffuse sky radiance.

10.2.2 AFRL Spectral-polarimetric Images

A series of spectral-polarimetric image collections have also been completed at AFRL/VS in Albuquerque, New Mexico. An example of an AFRL spectral polarimeter is seen in [202] which generates full Stokes images over 600 to 850 `nm` through sequential filtering. AFRL

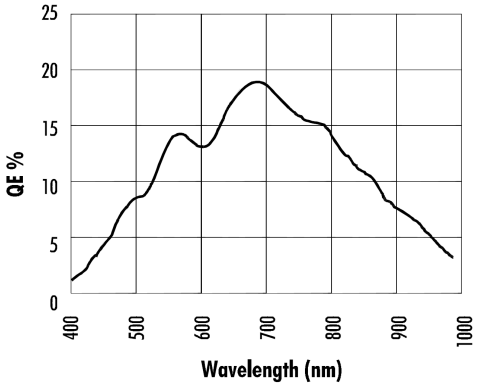

Figure 10.5: Quantum efficiency of the QLS Si-based CCD [201].

has been agreeable to the occasional use of their data by RIT.

10.2.3 POLDER

Data from the POLDER missions may also be obtained for this research. A description of POLDER with derived products was previously presented in §3.2.2.2. POLDER "Level-1" products are free of charge by signing and returning a user's agreement [203]. The Level-1 product includes radiometrically corrected images and for each pixel the viewing geometry, normalized radiance and Stokes vectors [204, 48]. While the POLDER GSD may not be adequate for detailed polarization analysis of surface properties, the data may prove beneficial for quantifying the polarized upwelled atmospheric radiance, $\vec{L}_u$, or at a minimum inter-comparison with Coulson-table or MODTRAN-derived $\vec{L}_u$ values.

10.2.4 Space Shuttle Missions

As discussed in §3.2.2.1, a series of mid-1980's Space Shuttle missions produced the first polarized images of the earth. However, most of the 1000+ images have not been digitized. Inquiries to NASA-Johnson on digitizing select images were met with an enthusiastic response. At my request, the Hawaiian island image previously analyzed by Egan [126] was digitized into an 8-bit RGB image at 4100×4100, corresponding to a ≈ 59 $\mathtt{mm}^{-1}$ sampling density, well into the grain for the 70 $\mathtt{mm}$ film.[1] Selection of the previously analyzed Hawaiian island image facilitates a comparison to Egan's results and helps validate this means of acquiring additional digitized imagery from NASA-Johnson.

[1] Mission STS51I: roll 50, frame 46 & roll 51, frame 141

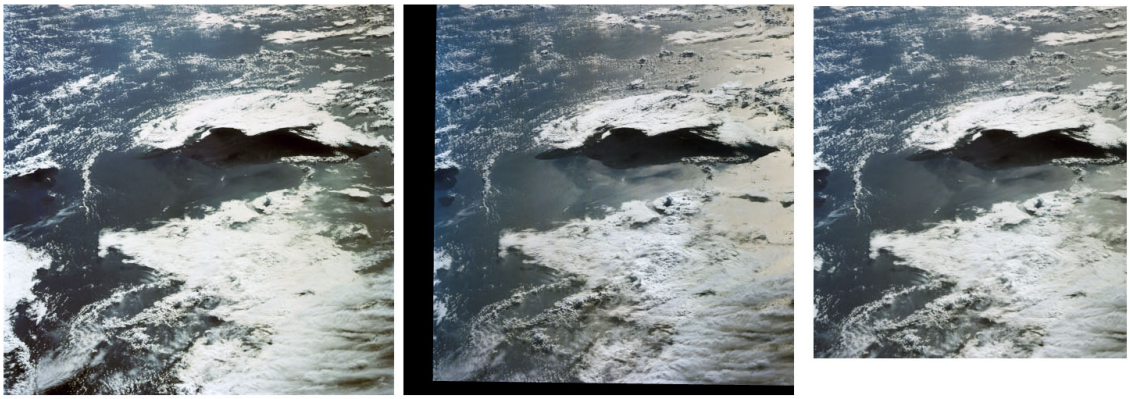

Figure 10.6: Space Shuttle polarization images of the Hawaiian islands with I_{min} (*left*), I_{max} (*middle*) and the intensity or $S0$ image (*right*) [205].

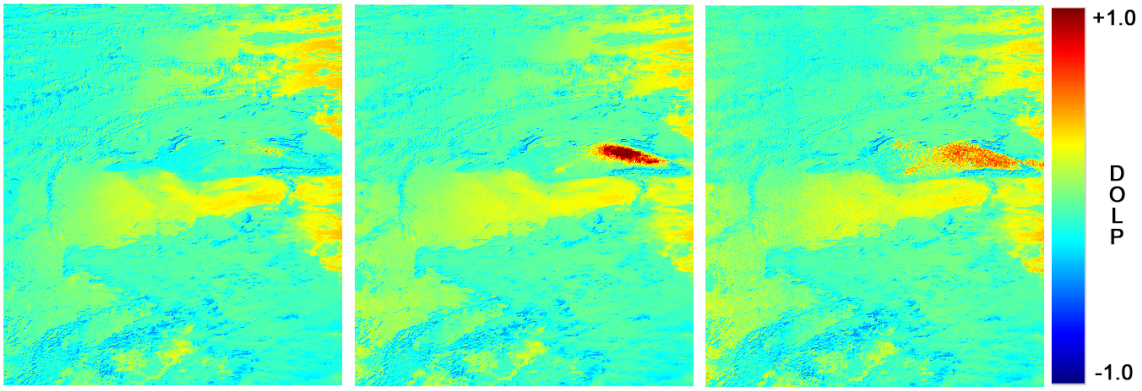

Figure 10.7: Hawaiian island DOLP for the R (*left*) G (*middle*) and B (*right*) image planes.

At the 4100×4100 format, the noise in the image was significant, and visually dominated by "salt-and-pepper" noise. A median filter was implemented to remove some of these artifacts, followed by a nearest-neighbor down sampling to 2000×2000. These images were then spatially registered with ENVI and a 2nd order polynomial fit. A common region between the two frames was then selected, followed by another down sampling to 500×500 thus further improving the registration accuracy. Figure 10.6 presents the registered images, as well as the total intensity $S0$ image calculated by $S0 = \frac{I_{max}+I_{min}}{2}$.

Using the registered images, the DOP estimation was made according to equation 3.2 for each of the RGB image planes. The results are shown as images in Figure 10.7. A DOLP histogram of the Figure 10.7 images provides another means of band-to-band comparison (Figure 10.8).

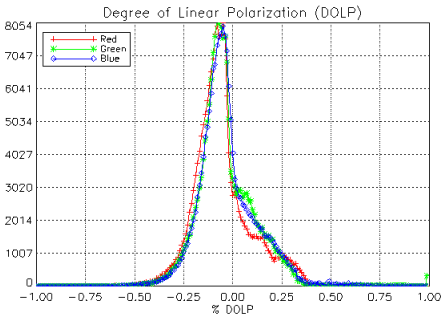

Figure 10.8: Hawaiian island image RGB DOLP distribution.

The results do not compare well with Egan's, which are best seen in [3, Ch. 20]. There is some agreement, such as the high positive $DOLP$ present over the island in the G and B channels, but in general the comparison is poor. Several factors may be responsible. For one, Egan used spectral filters when digitizing the film for the original work. The digitization provided for my images was completed using the native RGB response of the scanner coupled with the color film. Examining the RGB histograms of the digitized images also reveals dynamic range limitations with the scanning. In addition, the scanner exposure level was not fixed between the two images, resulting in a suspected mean-level brightness shift between the images.

In spite of these limitations, the shuttle images demonstrate meaningful polarization phenomenology. Further use of these images for this research effort should be accompanied by discussions with NASA-Johnson into an improved digitization process.

10.3 Target Detection Algorithms

Some observations and recommendations are made toward the development of spectral-polarimetric target detection algorithms. It should be realized that such algorithms require additional meta data that may not typically accompany similar spectral-only data. As a minimum, the incident solar angle θ_i and view angle θ_r, ϕ of the scene must be known. This is a prerequisite for predicting the pBRDF.

One simple means of incorporating polarization phenomenology into quantitative algorithms is to include information on the inverse correlation of the f_{00} to DOP. Some interesting observations were made from an image of a parking lot taken with the polarimetric imaging system previously described. An RGB image of the parking lot is shown in Figure 10.9, which may be compared to the 550 `nm` Stokes and DOP in Figure 10.10.

Figure 10.9: This RGB image of the parking lot may be used as a reference for examining the Stokes and DOP imagery in Figure 10.10.

The "usual" polarization phenomenology is evident in the data. The glass surfaces have a relatively high DOP as well as many of the vehicles. The vehicles with a high DOP are those which have a low reflectance at 550 nm. White vehicles have a relatively lower DOP, while the darker vehicles, to include red have a higher DOP. For the glass and vehicle surfaces, the polarization is attributed to specular reflectance from the sky in the background.

Examination of the joint probability function of f_{00} with respect to DOP brings out some interesting groupings as the GSD size is changed. The f_{00} and DOP were shown to be highly independent for a given material type, as demonstrated for the development of the background model (*cf.* Figure 7.5). However, for the parking lot scene the results are dramatically different, as shown in Figure 10.11.

Distinct groupings are evident from the joint probability distribution of S_0 and DOP as seen in Figure 10.11. Further analysis of the data was not made, but it is hypothesized that the relatively dark but high DOP grouping corresponds to vehicle and glass surfaces. Further analysis would likely reveal interesting results. Note that the convolution kernel used to produce the GSD data was of constant size over the entire image and approximated from the center of the image. This results in a significant error of the actual GSD in the foreground and background; a scene dependent convolution kernel size would likely result in a tighter grouping of the distributions seen in Figure 10.11.

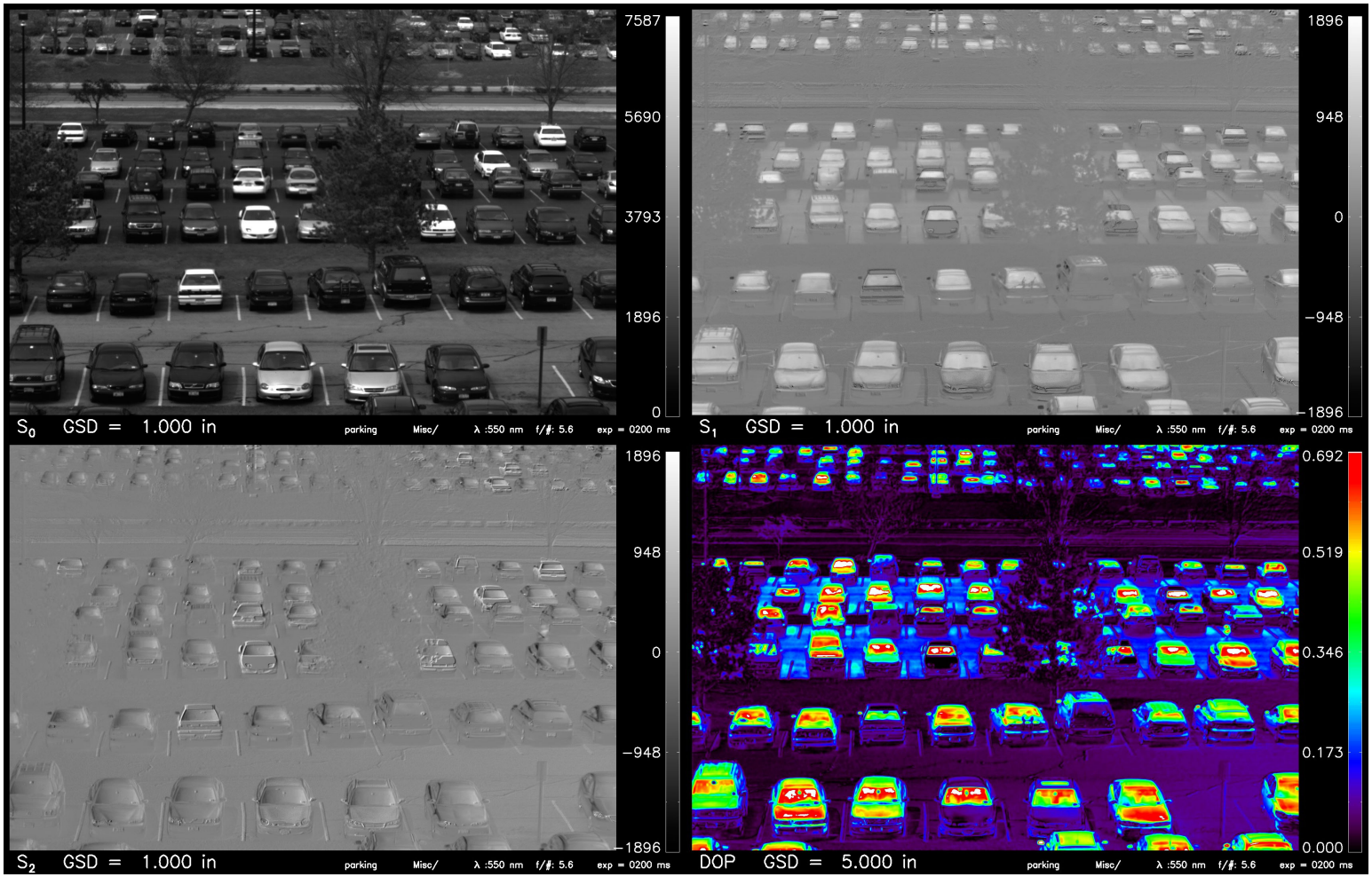

Figure 10.10: This image of a parking lot is at 550 `nm` and was made in the afternoon looking north such that the sun is positioned behind and to the left. The S_0 or total intensity image is *top left*, with S_1 and S_2 *top right* and *bottom left*, respectively. The Stokes image magnitude is given in terms of digital counts, where the S_1 and S_2 scale ranges from $\pm\frac{1}{4}$ the S_0 scale. Finally, the DOP image is *bottom right*, with a maximum scale value of 0.692. The GSD at the center of the image is approximately 1 `in`. The DOP image is composed of the Stokes images downsampled to 5 `in` to alleviate any spatial misregistration.

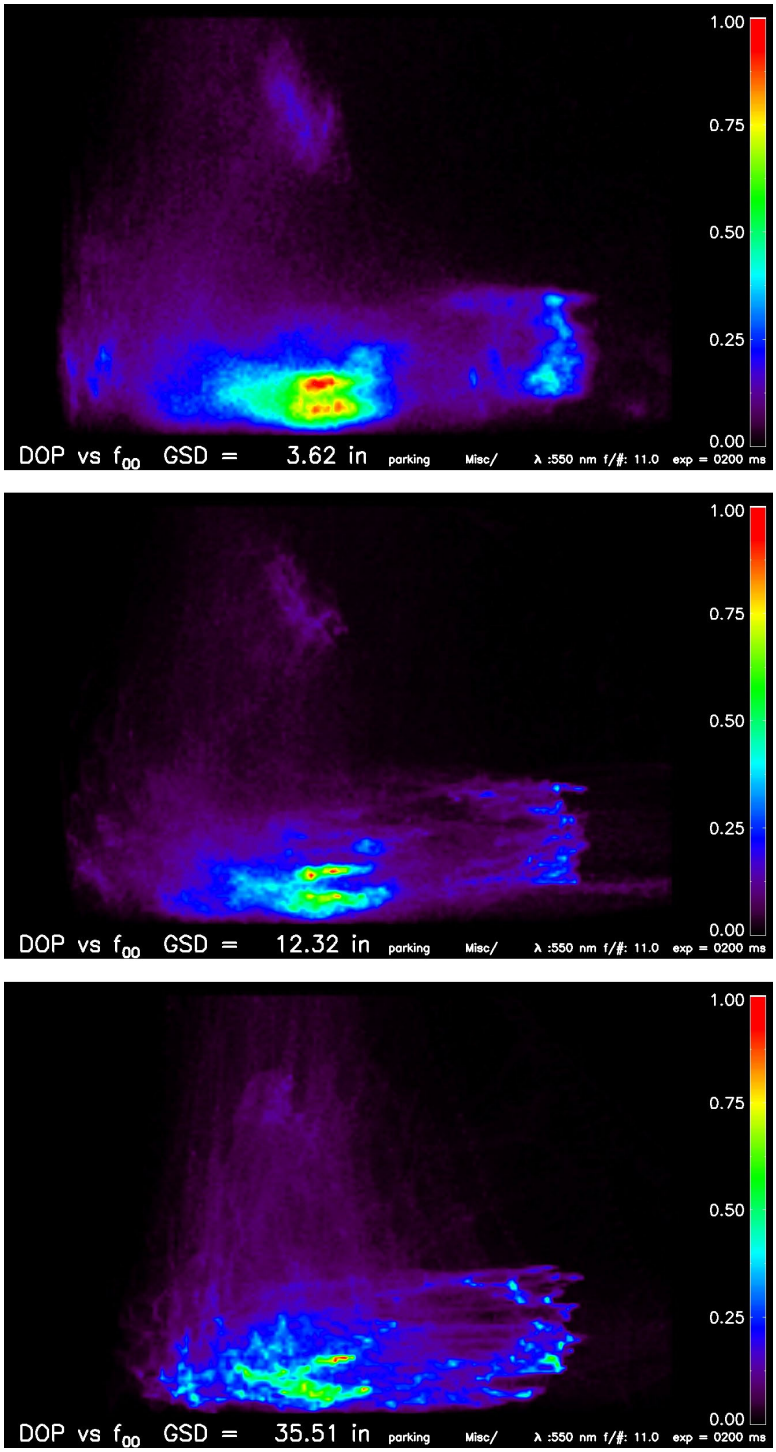

Figure 10.11: The joint probability distribution of f_{00} and DOP from the parking lot scene demonstrates significant correlation between the total brightness or S_0 (x-axis) component and the DOP (y-axis). From *top* to *bottom* are $GSD \approx 3.6, 12.3$ and 35.5 `in`. The evolution of the distribution as the GSD size is changed is particularly interesting. Note that the GSD sizes are specified as those relevant to the center of the image frame.

Appendix A

Extended Results

This appendix provides additional measurement results which were not practically included in the text. It also contains the Roujean-modelled BRDF results for the top soil, lawn grass and asphalt measurements. Finally, the DVD-ROM archival protocol and format for the experimental data is described.

A.1 Variability Results

Tables A.1–A.2 provide the measured variability of f_{00}, DOP and χ as a function of GSD.

Table A.1: The variability of the topsoil f_{00}, DOP and χ. The mean values for these quantities are presented in Table 6.1.

Orientation [°]			$\sigma_{f_{00}}$ [$\mathtt{sr}^{-1}$]				σ_{DOP}				σ_{χ} [°]			
θ_i	θ_r	ϕ	0.5”	3.0”	6.0”	12.0”	0.5”	3.0”	6.0”	12.0”	0.5”	3.0”	6.0”	12.0”
550 nm														
27.4	0	0	0.00274	0.00170	0.00143	0.00085	0.00981	0.00917	0.00804	0.00523	13.7427	12.9812	11.6395	8.0904
48.0	0	0	0.00396	0.00124	0.00078	0.00036	0.01079	0.00943	0.00793	0.00412	5.5533	5.2250	4.7745	3.4094
29.5	30	40	0.00431	0.00381	0.00362	0.00308	0.00807	0.00789	0.00729	0.00556	29.4248	26.6882	21.9784	16.8693
45.5	30	80	0.00399	0.00218	0.00196	0.00160	0.01156	0.01067	0.01031	0.00930	54.2348	53.5624	52.3950	37.2005
53.6	30	135	0.00370	0.00123	0.00074	0.00053	0.01556	0.01396	0.01262	0.00846	2.3138	1.8350	1.5889	1.0262
23.3	30	180	0.00234	0.00089	0.00061	0.00034	0.01047	0.00937	0.00833	0.00567	6.0361	5.7878	5.3995	4.2008
30.8	45	0	0.00266	0.00181	0.00162	0.00116	0.00473	0.00421	0.00356	0.00258	35.7277	35.0001	33.5033	22.6310
24.3	45	180	0.00229	0.00106	0.00086	0.00059	0.01682	0.00879	0.00765	0.00522	2.5400	2.2328	2.0407	1.5121
33.4	63	180	0.00237	0.00073	0.00040	0.00008	0.01341	0.00637	0.00436	0.00081	1.4898	0.2566	0.1637	0.0564
51.2	68	180	0.00289	0.00103	0.00075	0.00032	0.01974	0.00703	0.00540	0.00329	1.1041	0.8421	0.7750	0.6028
750 nm														
27.4	0	0	0.00433	0.00262	0.00215	0.00118	0.00927	0.00855	0.00738	0.00386	28.2160	26.3195	22.9218	12.1039
48.0	0	0	0.00655	0.00222	0.00146	0.00089	0.02064	0.00630	0.00484	0.00287	19.3368	9.1422	8.2273	5.7595
29.5	30	40	0.00673	0.00600	0.00573	0.00489	0.00917	0.00879	0.00803	0.00583	47.3849	47.9279	46.9176	40.3216
45.5	30	80	0.00678	0.00403	0.00369	0.00304	0.01020	0.00964	0.00927	0.00826	63.0371	61.6196	59.3071	55.9418
53.6	30	135	0.00662	0.00256	0.00181	0.00139	0.01354	0.01190	0.01056	0.00637	4.7772	4.1892	3.6685	2.5908
23.3	30	180	0.00398	0.00158	0.00109	0.00066	0.01151	0.00990	0.00846	0.00472	8.1618	7.5534	7.1194	5.8764
30.8	45	0	0.00468	0.00347	0.00313	0.00235	0.00505	0.00451	0.00360	0.00238	44.5554	42.5118	41.8099	38.1907
24.3	45	180	0.00386	0.00172	0.00134	0.00090	0.03397	0.01564	0.01050	0.00701	4.1290	3.4770	3.0263	2.0008
33.4	63	180	0.00403	0.00139	0.00084	0.00017	0.00796	0.00424	0.00309	0.00130	1.7096	0.7297	0.4373	0.1083
51.2	68	180	0.00486	0.00190	0.00144	0.00072	0.01410	0.00618	0.00521	0.00376	4.0180	0.8439	0.6777	0.4775

Table A.2: The variability of the lawn grass f_{00}, DOP and χ. The mean values for these quantities are presented in Table 6.2.

Orientation [°]			$\sigma_{f_{00}}$ [$\mathtt{sr}^{-1}$]				σ_{DOP}				σ_{χ} [°]			
θ_i	θ_r	ϕ	0.5”	3.0”	6.0”	12.0”	0.5”	3.0”	6.0”	12.0”	0.5”	3.0”	6.0”	12.0”
550 nm														
45.2	0.0	0.0	0.00553	0.00238	0.00166	0.00081	0.01316	0.00815	0.00667	0.00492	13.1065	7.7554	6.7157	4.5299
36.7	30.0	45.0	0.00511	0.00228	0.00178	0.00137	0.00910	0.00593	0.00482	0.00383	59.1041	57.3853	58.2065	53.9430
34.5	30.0	90.0	0.00471	0.00216	0.00164	0.00102	0.01273	0.00890	0.00816	0.00625	21.6972	15.8070	13.5388	7.9434
27.7	30.0	180.0	0.00408	0.00175	0.00122	0.00078	0.01583	0.00856	0.00666	0.00410	8.7103	5.0774	4.5902	3.1623
32.5	45.0	0.0	0.00473	0.00226	0.00156	0.00112	0.00710	0.00566	0.00463	0.00262	44.8747	43.6428	42.1865	31.1533
38.2	45.0	50.0	0.00473	0.00196	0.00135	0.00088	0.01068	0.00832	0.00815	0.00671	27.4780	20.4883	17.8281	6.1845
29.3	45.0	180.0	0.00329	0.00137	0.00080	0.00030	0.02227	0.00859	0.00596	0.00388	5.7515	3.8639	3.2249	1.9494
43.0	61.0	180.0	0.00349	0.00123	0.00071	0.00019	0.03242	0.01175	0.00732	0.00297	8.4048	1.7916	1.2450	0.5099
750 nm														
31.2	0.0	0.0	0.01577	0.00814	0.00616	0.00363	0.00909	0.00837	0.00720	0.00480	33.2716	28.2768	25.3046	11.7843
45.2	0.0	0.0	0.02283	0.01193	0.00735	0.00268	0.00792	0.00695	0.00572	0.00288	28.2547	24.4014	19.8872	13.0813
36.7	30.0	45.0	0.01812	0.01058	0.00895	0.00736	0.00707	0.00570	0.00461	0.00335	65.5744	67.1789	67.6092	69.4262
34.5	30.0	90.0	0.01722	0.01006	0.00801	0.00531	0.00859	0.00705	0.00590	0.00521	47.8713	46.5927	43.9910	41.6344
27.7	30.0	180.0	0.01324	0.00529	0.00282	0.00144	0.00825	0.00695	0.00584	0.00379	48.3048	47.5773	46.9262	38.6885
32.5	45.0	0.0	0.01328	0.00790	0.00652	0.00538	0.00594	0.00484	0.00358	0.00182	59.4992	59.0404	58.7825	60.0645
38.2	45.0	50.0	0.01594	0.00857	0.00661	0.00516	0.00699	0.00593	0.00480	0.00305	60.6053	59.7244	59.8415	44.2154
29.3	45.0	180.0	0.01155	0.00472	0.00242	0.00077	0.01497	0.00639	0.00499	0.00275	39.7794	30.8594	23.3559	15.9937
43.0	61.0	180.0	0.01334	0.00378	0.00206	0.00024	0.00707	0.00366	0.00279	0.00165	26.8589	14.8321	11.8123	8.9079

Table A.3: The variability of the asphalt f_{00}, DOP and χ. The mean values for these quantities are presented in Table 6.3.

Orientation [°]			$\sigma_{f_{00}}$ [sr^{-1}]				σ_{DOP}				σ_{χ} [°]			
θ_i	θ_r	ϕ	0.5”	3.0”	6.0”	12.0”	0.5”	3.0”	6.0”	12.0”	0.5”	3.0”	6.0”	12.0”
550 nm														
35.4	0.0	0.0	0.00280	0.00113	0.00071	0.00045	0.00746	0.00697	0.00611	0.00378	18.4198	16.7068	14.2720	8.8380
35.9	30.0	40.0	0.00290	0.00185	0.00167	0.00138	0.00609	0.00573	0.00501	0.00362	39.5596	38.2628	37.0324	29.3338
37.0	30.0	90.0	0.00278	0.00130	0.00104	0.00080	0.01067	0.01016	0.00949	0.00669	15.0502	13.1252	10.3856	6.5529
37.8	30.0	135.0	0.00298	0.00127	0.00092	0.00064	0.01193	0.01028	0.00933	0.00654	6.3873	6.1182	5.5830	4.0946
38.4	30.0	180.0	0.00047	0.00041	0.00036	0.00024	0.01163	0.00954	0.00842	0.00557	5.4580	5.1264	4.6956	3.4464
39.3	45	180	0.00251	0.00099	0.00072	0.00044	0.01612	0.01168	0.01030	0.00653	2.0535	1.8574	1.6310	1.0296
750 nm														
34.3	0	0	0.00303	0.00114	0.00063	0.00017	0.01016	0.00952	0.00857	0.00590	23.0651	21.7715	18.0000	10.4881
32.5	30	40	0.00344	0.00242	0.00223	0.00181	0.00914	0.00864	0.00755	0.00517	57.0360	58.6769	58.7390	58.0454
32.9	30	90	0.00294	0.00153	0.00135	0.00105	0.01107	0.01062	0.00978	0.00682	12.7047	11.4987	9.1727	4.7896
33.2	30	135	0.00292	0.00143	0.00129	0.00100	0.01393	0.01234	0.01117	0.00780	6.6945	6.4394	5.9671	4.4252
33.8	30	180	0.00286	0.00116	0.00079	0.00044	0.01384	0.01188	0.01067	0.00762	5.2162	4.9187	4.4755	3.1161

Table A.4: Measured vs. Roujean-modelled BRDF for topsoil at 550 nm where $[k_0, k_1, k_2] = [12.2638, 5.1683, 33.2803]$. The model RMSE for this data set is 0.00293 sr^{-1}. The best Lambertian estimate is 0.03065 sr^{-1}. Note that the RMSE minimization of the Lambertian estimate was driven by the two large values resulting from the "hot-spot" location.

θ_i [°]	θ_r [°]	ϕ [°]	**Measured** [sr^{-1}]	**Modelled** [sr^{-1}]	**Model Error** [%]	**Lambertian Error** [%]
27.4	0	0	0.02873	0.03236	12.63	6.68
48.0	0	0	0.02400	0.02532	5.51	27.71
29.5	30	40	0.04273	0.03651	-14.56	-28.27
45.5	30	80	0.02715	0.02710	-0.20	12.89
53.6	30	135	0.01797	0.01605	-10.71	70.56
23.3	30	180	0.02042	0.02301	12.70	50.10
30.8	45	0	0.04125	0.04202	1.86	-25.70
24.3	45	180	0.01675	0.01806	7.80	82.99
33.4	63.3	180	0.01500	0.01125	-25.03	104.33
51.2	68.3	180	0.01276	0.01510	18.31	140.20

A.2 Total Intensity Roujean-Modelled Results

The Roujean-modelled BRDF of the topsoil, asphalt and lawn grass are presented and compared to the measurements. In addition, the best Lambertian fit to the data is provided along with the resultant errors. Output from the Roujean model provides the f_{00} BRDF component throughout the scattering hemisphere for $\theta_i = 0°, 30°$ and $60°$. The topsoil model to measurements comparison is shown in Tables A.4 and A.5, with Figure A.1 providing the hemispherical results. The same data for asphalt is provided in Tables A.6 and A.7 and Figure A.2. Finally the lawn grass data and model results are shown in Tables A.8 and A.9 and Figure A.3.

Table A.5: Measured vs. Roujean-modelled BRDF for topsoil at 750 nm where $[k_0, k_1, k_2] = [21.6496, 4.7773, 37.1243]$. The model RMSE for this data set is 0.00460 sr^{-1}. The best Lambertian estimate is 0.05298 sr^{-1}. As with the 550 nm topsoil data, the RMSE minimization of the Lambertian estimate was driven by the two large values resulting from the "hot-spot" location.

θ_i [°]	θ_r [°]	ϕ [°]	**Measured** [sr^{-1}]	**Modelled** [sr^{-1}]	**Model Error [%]**	**Lambertian Error [%]**
27.4	0	0	0.04957	0.05561	12.18	6.88
48.0	0	0	0.04305	0.04485	4.17	23.07
29.5	30	40	0.07045	0.06167	-12.46	-24.80
45.5	30	80	0.04886	0.04742	-2.95	8.43
53.6	30	135	0.03550	0.03069	-13.56	49.24
23.3	30	180	0.03682	0.04153	12.80	43.89
30.8	45	0	0.06891	0.06978	1.26	-23.12
24.3	45	180	0.03121	0.03393	8.71	69.75
33.4	63.3	180	0.02784	0.02305	-17.22	90.30
51.2	68.3	180	0.02419	0.02788	15.25	119.02

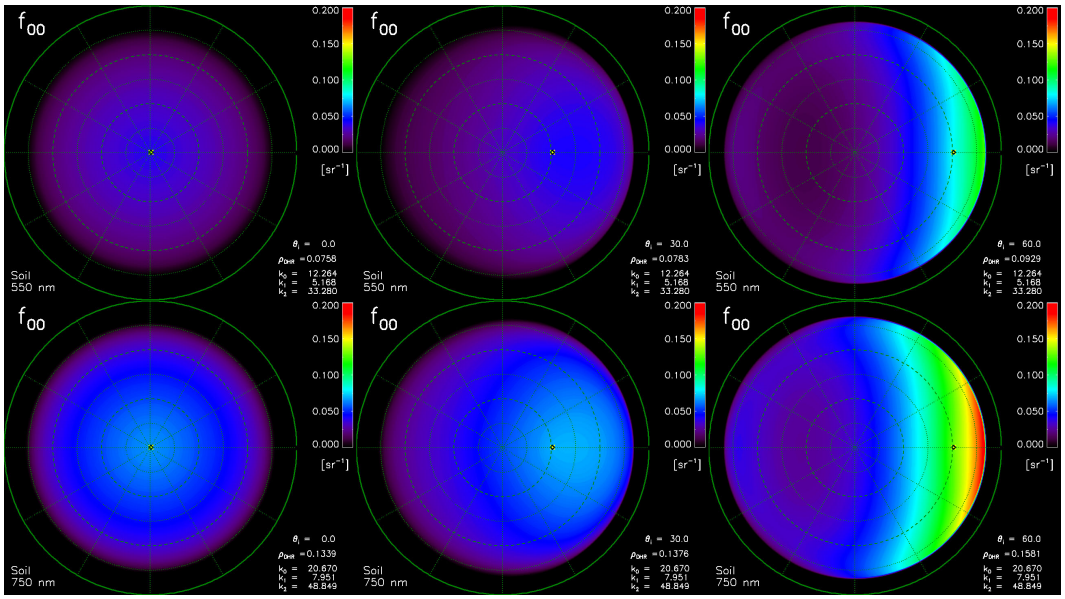

Figure A.1: The Roujean-modelled BRDF of topsoil at 550 nm (*top*) and 750 nm (*bottom*) for $\theta_i = 0°$ (*left*), 30° (*middle*) and 60° (*right*). Identical scales are used for both wavelengths, with a maximum of 0.20 sr^{-1}. Roujean parameters: $\vec{k}(550) = [12.2638, 5.1683, 33.2803]$ and $\vec{k}(750) = [21.6496, 4.7773, 37.1243]$. ($\theta_r$ has been limited to $\leq 80°$).

Table A.6: Measured vs. Roujean-modelled BRDF for asphalt at 550 nm where $[k_0, k_1, k_2] = [14.2580, 0.0075, 40.2632]$. The model RMSE for this data set is 0.00085 sr^{-1}. The best Lambertian estimate is 0.04414 sr^{-1}.

θ_i [°]	θ_r [°]	ϕ [°]	**Measured** [sr^{-1}]	**Modelled** [sr^{-1}]	**Model Error** [%]	**Lambertian Error** [%]
35.4	0	0	0.04188	0.04329	3.37	5.40
35.9	30	40	0.05073	0.05048	-0.49	-12.99
37.0	30	90	0.04449	0.04351	-2.21	-0.79
37.8	30	135	0.03947	0.03915	-0.82	11.83
38.4	30	180	0.03859	0.03787	-1.85	14.38
39.3	45	180	0.03869	0.03955	2.21	14.09

Table A.7: Measured vs. Roujean-modelled BRDF for asphalt at 750 nm where $[k_0, k_1, k_2] = [16.1704, -1.1050, 51.4716]$. The model RMSE for this data set is 0.00049 sr^{-1}. The best Lambertian estimate is 0.05142 sr^{-1}.

θ_i [°]	θ_r [°]	ϕ [°]	**Measured** [sr^{-1}]	**Modelled** [sr^{-1}]	**Model Error** [%]	**Lambertian Error** [%]
34.3	0	0	0.05044	0.05043	-0.03	1.94
32.5	30	40	0.05863	0.05861	-0.03	-12.30
32.9	30	90	0.05126	0.05111	-0.29	0.31
33.2	30	135	0.04537	0.04622	1.88	13.33
33.8	30	180	0.04536	0.04469	-1.48	13.36

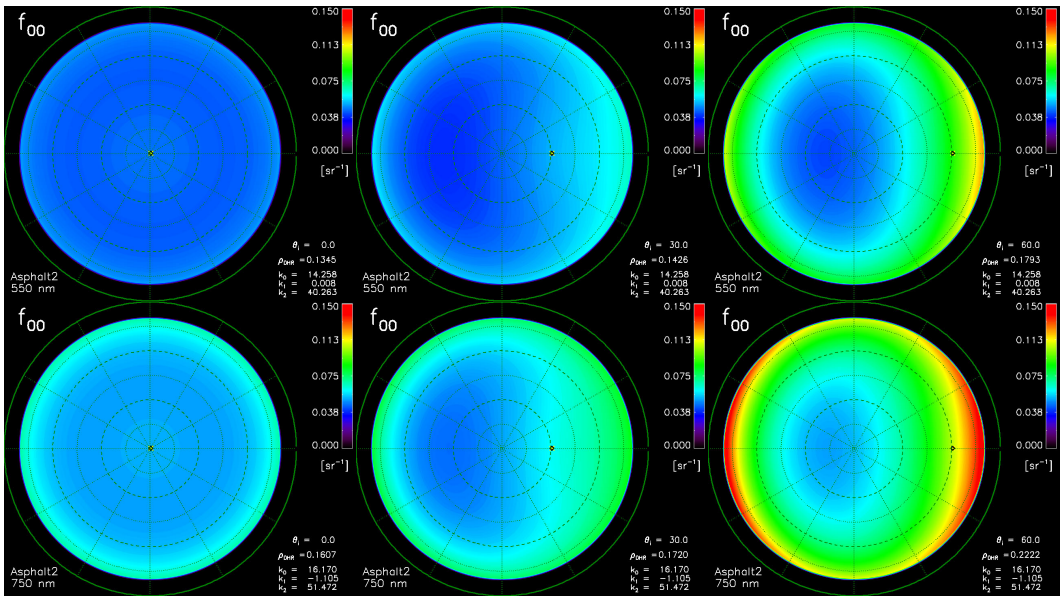

Figure A.2: The Roujean-modelled BRDF of asphalt at 550 nm (*top*) and 750 nm (*bottom*) for $\theta_i = 0°$ (*left*), 30° (*middle*) and 60° (*right*). Identical scales are used for both wavelengths, with a maximum of 0.15 sr^{-1}. Roujean parameters: $\vec{k}(550) = [14.2580, 0.0075, 40.2632]$ and $\vec{k}(750) = [16.1704, -1.1050, 51.4716]$. ($\theta_r$ has been limited to $\leq 80°$).

Table A.8: Measured vs. Roujean-modelled BRDF for grass at 550 nm where $[k_0, k_1, k_2] = [6.8702, 0.3881, 29.0824]$. The model RMSE for this data set is 0.001022 sr^{-1}. The best Lambertian estimate is 0.01956 sr^{-1}.

θ_i [°]	θ_r [°]	ϕ [°]	**Measured** [sr^{-1}]	**Modelled** [sr^{-1}]	**Model Error** [%]	**Lambertian Error** [%]
45.2	0	0	0.01874	0.01927	2.84	4.38
36.7	30	45	0.02384	0.02464	3.37	-17.95
34.5	30	90	0.01903	0.01971	3.56	2.79
27.7	30	180	0.01661	0.01586	-4.5	17.76
32.5	45	0	0.03153	0.02957	-6.23	-37.96
38.2	45	50	0.02516	0.02659	5.67	-22.26
29.3	45	180	0.01630	0.01558	-4.42	20.00
43.0	61	180	0.02212	0.02211	-0.02	-11.57

Table A.9: Measured vs. Roujean-modelled BRDF for grass at 750 nm where $[k_0, k_1, k_2] = [40.9686, -1.6822, 93.1120]$. The model RMSE for this data set is 0.00330 sr^{-1}. The best Lambertian estimate is 0.00436 sr^{-1}.

θ_i [°]	θ_r [°]	ϕ [°]	**Measured** [sr^{-1}]	**Modelled** [sr^{-1}]	**Model Error** [%]	**Lambertian Error** [%]
31.2	0	0	0.12306	0.12831	4.27	6.05
45.2	0	0	0.13291	0.12806	-3.65	-1.81
36.7	30	45	0.13998	0.14326	2.35	-6.77
34.5	30	90	0.12604	0.12931	2.59	3.54
27.7	30	180	0.11903	0.11771	-1.11	9.64
32.5	45	0	0.16125	0.15801	-2.01	-19.07
38.2	45	50	0.15190	0.15052	-0.91	-14.09
29.3	45	180	0.12235	0.11952	-2.31	6.66
43.0	61	180	0.14561	0.14741	1.24	-10.38

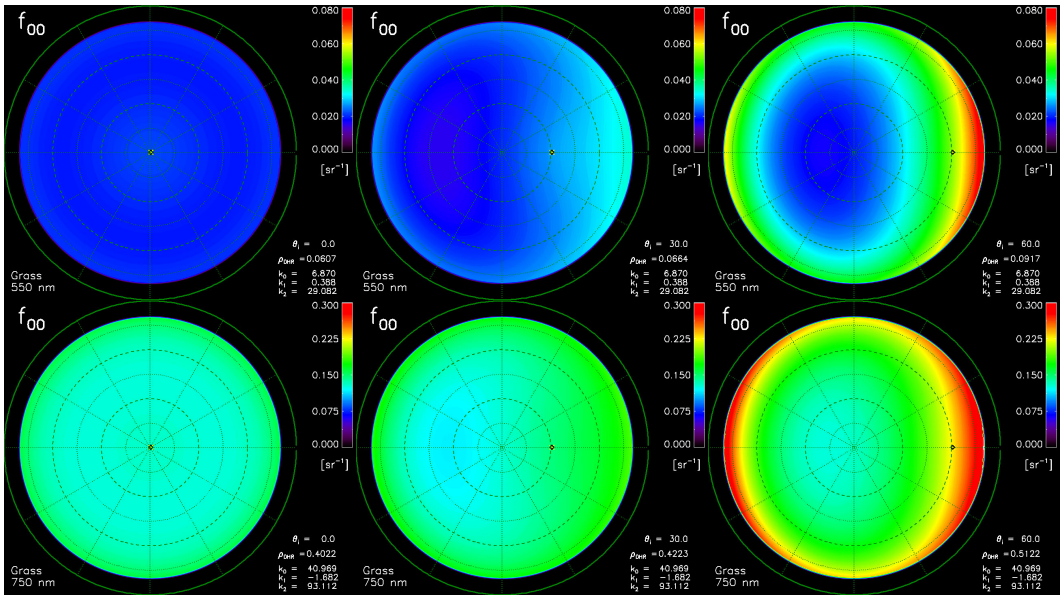

Figure A.3: The Roujean-modelled BRDF of lawn grass at 550 `nm` (*top*) and 750 `nm` (*bottom*) for $\theta_i = 0°$ (*left*), 30° (*middle*) and 60° (*right*). Different scales are used, with a maximum of 0.08 $\mathtt{sr}^{-1}$ at 550 `nm` and a maximum of 0.30 $\mathtt{sr}^{-1}$ at 750 `nm`. Roujean parameters: $\vec{\mathtt{k}}(550) = [6.8702, 0.3881, 29.0824]$ and $\vec{\mathtt{k}}(750) = [40.9686, -1.6822, 93.1120]$. ($\theta_r$ has been limited to $\leq 80°$).

A.3 Data Archive Protocol

All data from the measurements have been archived onto DVD-ROMs. The organization and file naming convention is described.

The subdirectories from the main directory are for each material measured. The directory name contains the year, month, date and material measured, *i.e.*, "`YYYYMMDD_material`". Within the material directory are the following files:

- An excel spreadsheet summarizing the measurements
- Photographs of the measurement setup and measured area
- A "metadata" `txt` file
- An animated `gif` file of the cloudcover over New York state during the measurement period.

The metadata text file contains a host of varying information. It includes information such as weather conditions, location of the measurements, unique camera positioning information for select angles. Also included is a list of the sample angle positions, along with the time the images were taken as well as the corresponding θ_i sun position. Following this list are the times for which the calibration panel images were taken, along with the corresponding θ_i sun position.

Figure serves as a good reference for the discussion of the directory contents. Under the main material directory are four different types of subdirectories, corresponding to *i*) each hemispherical measurement position, "`XX,YYY`" where `XX` is θ_r and `YYY` is ϕ, *ii*) Roujean-modelled f_{00} results for each wavelength, "`BRDF_ZZZ`" where `ZZZ` is λ, *iii*) calibration data, in "`Calibrate`" and *iv*) dark images in "`DarkImg`".

The hemispherical measurement position directories, `XX,YYY`, contain the raw `C` and `D` images, the preprocessed `C` and `D` images and directories for the results. The raw image file name contains the following, in this given order: the material name, whether the image is the `C` image ("`sun`") or a `D` image ("`sha`"), the spectral wavelength, the polarization filter orientation an finally the exposure time in `ms`.

The preprocessed data has a similar naming structure; after the material name, "`REG`" appears indicated the images are spatially registered, which is followed by "`BRDF`" or "`SKY`" indicating whether the images are the $\mathtt{C} - \mathtt{D}$ (BRDF) or `D` (sky) images.

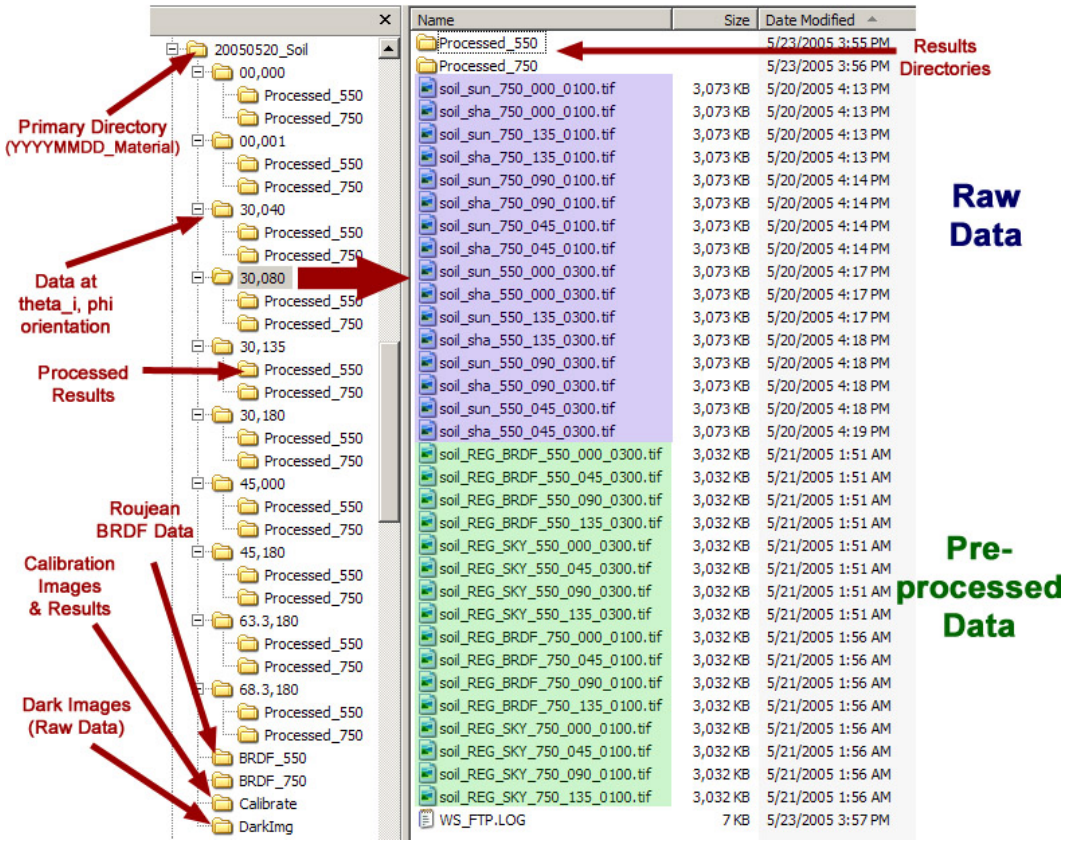

Figure A.4: The organization of the archived data is illustrated. The contents of the folder for the scattering angle of $\theta_r = 30°$ and $\phi = 80°$ are shown in the file list.

Bibliography

[1] V. S. Whitehead K. L. Coulson and C. Campbell. Polarized views of the earth from orbital altitudes. *SPIE Ocean Opt.*, 637:35–41, 1986.

[2] V. S. Whitehead and K. L. Coulson. Earth scenes in polarized light observed from the space shuttle. *Geocarto International*, 4:31–38, 1989.

[3] Walter G. Egan. *Optical Remote Sensing Science and Technology*. Marcel Dekker, Inc., 2004.

[4] John R. Schott. *Remote Sensing: The Image Chain Approach*. Oxford University Press, 1997.

[5] Kinsell L. Coulson. *Polarization and Intensity of Light in the Atmosphere*. A. DEEPAK Publishing, 1988.

[6] R. Walraven. Polarization imagery. In R. M. A. Azzam and D. L. Coffeen, editors, *Optical Polarimetry: Instrumentation and Applications*, volume 112 of *Proc. SPIE*, pages 164–167, 1977.

[7] Robert D. Guenther. *Modern Optics*. John Wiley & Sons, 1990.

[8] David J. Griffiths. *Introduction to Electrodynamics*. Prentice Hall, second edition, 1989.

[9] John David Jackson. *Classical Electrodynamics*. John Wiley & Sons, second edition, 1975.

[10] Nonconventional Exploitation Factors (NEF) Modeling. Technical Report ORD 257-96, ORD, August 1996. Limited distribution.

[11] G. G. Stokes. On the composition and resolution of streams of polarized light from different sources. *Trans. Cambridge Phil. Soc.*, 9:399, 1852.

[12] H. Mueller. The foundations of optics. *Journal of the Optical Society of America*, 38:661, 1948.

[13] Shih-Yau Lu and Russel A. Chipman. Interpretation of Mueller matrices based on polar decomposition. *Journal of the Optical Society of America A*, 13(5):1106–1113, May 1996.

[14] N. Umov. Chromatsche depolarisation durch lichtzerstreuung. *Physikalische Zeit.*, 6:674–676, 1905.

[15] F. E. Nicodemus. Reflectance nomenclature and directional reflectance and emissivity. *Applied Optics*, 9(6):1474–1475, June 1970.

[16] F. E. Nicodemus, J. C. Richmond, J. J. Hsia, I. W. Ginsberg, and T. Limperis. Geometrical considerations and nomenclature for reflectance; NBS Monograph 160. Technical report, Department of Commerce, National Bureau of Standards, 1977.

[17] John C. Stover. *Optical Scattering Measurement and Analysis*. SPIE Optical Engineering Press, second edition, 1995.

[18] Bruce Hapke, Dominick DiMucci, Robert Nelson, and William Smythe. The cause of the hot spot in vegetation canopies and soils: Shadow-hiding versus coherent backscatter. *Remote Sensing of Environment*, 58(1):63–68, October 1996.

[19] D. S. Flynn and C. Alexander. Polarized surface scattering expressed in terms of a bidirectional reflectance distribution function matrix. *Optical Engineering*, 34:1646–1650, 1995.

[20] W. Ni, C. E. Woodcock, and D. L. B. Jupp. Variance in bidirectional reflectance over discontinuous plant canopies. *Remote Sensing of Environment*, 69(1):1–15, July 1999.

[21] Kristin J. Dana, Bram van Ginneken, Shree K. Nayar, and Jan J. Koenderink. Reflectance and texture of real-world surfaces. *ACM Transactions on Graphics (TOG)*, 18(1):1–34, January 1999.

[22] Xiaofan Feng. Comparison of methods for generation of absolute reflectance factor measurements for BRDF studies. Master's thesis, Rochester Institute of Tchnology, 1990.

[23] S. R. Sandmeier and A. H. Strahler. BRDF laboratory measurements. *Remote Sensing Reviews*, 18(2–4):481–502, September 2000.

[24] K.J. Dana. BRDF/BTF measurement device. In *Eighth IEEE International Conference on Computer Vision*, volume 2, pages 460–466. IEEE, July 2001.

[25] Kristin J. Dana and Jing Wang. Device for convenient measurement of spatially varying bidirectional reflectance. *JOSA A*, 21(1):1–12, January 2004.

[26] Jefferson Y. Han and Ken Perlin. Measuring bidirectional texture reflectance with a kaleidoscope. *ACM Transactions on Graphics (TOG)*, 22(3):741–748, July 2003.

[27] Stephen R. Marschner, Stephen H. Westin, Eric P. F. Lafortune, Kenneth E. Torrance, and Donald P. Greenberg. Image-based BRDF measurement including human skin. In *Eurographics Workshop on Rendering*, 1999.

[28] Oliver Apel, Christian Goerling, Uwe Leinhos, Klaus R. Mann, and Bernd Schaefer. CHARISMA: a new way for angular-resolved scattering measurements. In *Laser-Induced Damage in Optical Materials*, volume 4347 of *Proc. SPIE*, pages 569–578, 2001.

[29] Charles Walthall, Jean-Louis Roujean, and Jeff Morisette. Field and landscape BRDF optical wavelength measurements: Experience, techniques and the future. *Remote Sensing Reviews*, 18:503–531, 2000.

[30] Stefan R. Sandmeier. Acquisition of bidirectional reflectance factor data with field goniometers. *Remote Sensing of Environment*, 73(3):257–269, September 2000.

[31] A. I. Lyapustin and J. L. Privette. A new method of retrieving surface bidirectional reflectance from ground measurements: Atmospheric sensitivity study. *Journal of Geophysical Research*, 104(D6):6257–6268, March 27 1999.

[32] G. F. Epema. Studies of errors in field measurements of the bidirectional reflectance factor. *Remote Sensing of the Environment*, 35:37–49, 1991.

[33] S. Sandmeier, W. Sandmeier, K.I. Itten, M.E. Schaepman, and T.W. Kellenberger. The Swiss field-goniometer system (FIGOS). In *International Geoscience and Remote Sensing Symposium*, volume 3 of *Proc. IEEE*, pages 2078–2080, 1995.

[34] S. R. Sandmeier and K. I. Itten. A field goniometer system (FIGOS) for acquisition of hyperspectral BRDF data. *IEEE Transactions on Geoscience and Remote Sensing*, 37(2):978–986, March 1999.

[35] Steve Schill. http://steve.schill.com/research.html.

[36] Stefan R. Sandmeier. e-mail correspondence, September 2004.

[37] Steve Schill. e-mail correspondence, July 2004.

[38] Gerard Serrot, Madeleine Bodilis, Xavier Briottet, and Helene Cosnefroy. Presentation of a new BRDF measurement device. In Adam D. Devir, Anton Kohle, Ulrich Schreiber, and Christian Werner, editors, *Atmospheric Propagation, Adaptive Systems, and Lidar Techniques for Remote Sensing II*, volume 3494 of *Proc. SPIE*, pages 34–40, December 1998.

[39] Yannick Boucher, Helene Cosnefroy, Alain D. Petit, Gerard Serrot, and Xavier Briottet. Comparison of measured and modeled BRDF of natural targets. In Wendell R. Watkins, Dieter Clement, and William R. Reynolds, editors, *Targets and Backgrounds: Characterization and Representation V*, volume 3699 of *Proc. SPIE*, pages 16–26, 1999.

[40] Donald W. Deering and Peter Leone. A sphere-scanning radiometer for rapid directional measurements of sky and ground radiance. *Remote Sensing of Environmen*, 19(1):1–24, February 1986.

[41] NASA MODIS land team, grassland PROVE (prototype validation exercise) internet site (MODIS land team), 2004. http://modarch.gsfc.nasa.gov/MODIS/LAND/VAL/prove/grass/prove.html.

[42] Michael H. Davis. A CCD based bidirectional spectral reflectance field instrument. Master's thesis, Rochester Institute of Tchnology, 1990.

[43] Prabal Nandy, Kurtis J. Thome, and Stuart F. Biggar. Laboratory characterization of a CCD camera system for retrieval of bi-directional reflectance distribution function. In Hiroyuki Fujisada and Joan B. Lurie, editors, *Sensors, Systems, and Next-Generation Satellites III*, volume 3870 of *Proc. SPIE*, pages 243–253, 1999.

[44] P. Nandy, K. Thome, and S. Biggar. Characterization and field use of a CCD camera system for retrieval of bidirectional reflectance distribution function. *Journal of Geophysical Research*, 106(D11):11957–11966, June 16 2001.

[45] Jeffrey S. Czapla-Myers, Kurtis J. Thome, and Stuart F. Biggar. Optical sensor package for multiangle measurements of surface reflectance. In Michael R. Descour and Sylvia S. Shen, editors, *Imaging Spectrometry VII*, volume 4480 of *Proc. SPIE*, pages 326–333, 2002.

[46] M. Radke, H. P. Roser, and A. Demircan. Bidirectional reflectance measurements using a CCD-line-camera on a rotating device. In *Geoscience and Remote Sensing Symposium*, volume 1 of *Proc. IEEE*, pages 589–591, 1999.

[47] A. Demircan, R. Schuster, M. Radke, M. Schnermark, and H. P. Rser. Use of a wide angle CCD line camera for BRDF measurements. *Infrared Physics & Technology*, 41:11–19, 2000.

[48] French Space Agency. Internet, http://smsc.cnes.fr/POLDER/, July 2004.

[49] Pierre-Yves Deschamps, François-Marie Bréon, Marc Leroy, Alain Podair, Annick Bricaud, Jean-Claude Buriez, and Geneviève Sèze. The POLDER mission: Instrument characteristics and scientific objectives. *IEEE Transactions on Geoscience and Remote Sensing*, 32(3):598–615, May 1994.

[50] M. Leroy, J. L. Deuzé, F. M. Bréon, O. Hautecoeur, M. Herman, J.C. Buriez, D. Tanré, S. Bouffiès, P. Chazette, and J. L. Roujean. Retrieval of atmospheric properties and surface bidirectional reflectances over the land from POLDER (processing algorithms). *Journal of Geophysical Research*, 102(D14):17023–17037, July 27 1997.

[51] F. Nadal and F.-M. Bréon. Parameterization of surface polarized reflectance derived from POLDER spaceborne measurements. *IEEE Transactions on Geoscience and Remote Sensing*, 37(3):1709–1718, May 1999.

[52] MODIS internet site, 2004. http://modis.gsfc.nasa.gov/.

[53] Crystal B. Schaaf, Feng Gao, Alan H. Strahler, Wolfgang Lucht, Xiaowen Li, Trevor Tsang, Nicholas C. Strugnell, Xiaoyang Zhang, Yufang Jin, and et al. Jan-Peter Muller. First operational BRDF, albedo nadir reflectance products from MODIS. *Remote Sensing of Environment*, 83(1–2):135–148, November 2002.

[54] MISR internet site, 2004. http://www-misr.jpl.nasa.gov/.

[55] William S. Bicket and Wilbur M. Bailey. Stokes vectors, Mueller matrices, and polarized scattered light. *Americal Journal of Physics*, 53(5):468–478, May 1985.

[56] David B. Chenault, J. Larry Pezzaniti, and Russell A. Chipman. Mueller matrix algorithms. In Dennis H. Goldstein and Russell A. Chipman, editors, *Polarization Analysis and Measurement*, volume 1746 of *Proc. SPIE*, pages 231–246, 1991.

[57] T. F. Schiff and Daniel J. Wilson Mark E. Southwood John C. Stover, Donald R. Bjork. Mueller matrix measurements with an out-of-plane polarimetric scatterometer. In Dennis H. Goldstein and Russell A. Chipman, editors, *Polarization Analysis and Measurement*, volume 1746 of *Proc. SPIE*, pages 295–306, December 1992.

[58] Diana M. Hayes. Error propagation in decomposition of Mueller matrices. In Dennis H. Goldstein and Russell A. Chipman, editors, *Polarization: Measurement, Analysis, and Remote Sensing*, volume 3121 of *Proc. SPIE*, pages 112–123, October 1997.

[59] S. R. Cloude. Conditions for the physical realisability of matrix operators in polarimetry. In *Polarization Considerations for Optical Systems II*, volume 1166 of *Proc. SPIE*, pages 177–185, 1989.

[60] James Q. Peterson, Gary L. Jensen, and Joseph A. Kristl. Imaging polarimetry capabilities and measurement uncertainties in remote sensing applications. In *Polarization Analysis, Measurement, and Remote Sensing III*, volume 4133 of *Proc. SPIE*, pages 221–232, 2000.

[61] Columbia-utrecht reflectance and texture database. Internet, 2004. http://www1.cs.columbia.edu/CAVE/curet/.

[62] Cornell university program of computer graphics. Internet, 2004. http://www.graphics.cornell.edu/online/measurements/reflectance/index.html.

[63] Susan H. C. P. McCall, Robert P. Breault, Rorik A. Henrikson, and et al. A globally accessible bidirectional scattering distribution function software data tool. In *Scattering and Surface Roughness II*, volume 3426 of *Proc. SPIE*, pages 303–309, July 1998.

[64] Surface optics corp optical properties library. Internet, 2004. http://www.surfaceoptics.com/brochures/SOC_Measured_Data_Doc.pdf.

[65] J. R. Maxwell, J. Beard, S. Weiner, D. Ladd, and S. Ladd. Bidirectional reflectance model validation and utilization. Technical Report AFAL-TR-73-303, Environmental Research Institute of Michigan (ERIM), October 1973.

[66] Harold B. Westlund and Gary W. Meyer. The role of rendering in the competence project in measurement science for optical reflection and scattering. *Journal of Research of the National Institute of Standards and Technology*, 107(3):247–259, May-June 2002.

[67] Harold B. Westlund and Gary W. Meyer. A BRDF database employing the Beard-Maxwell reflection model. In *Proceedings–Graphics Interface*, pages 189–200, 2002.

[68] Computer graphic rendering of material surfaces. Internet, 2004. http://math.nist.gov/~FHunt/appearance/nefdsimages.html.

[69] J. H. Lambert. Photometria sive de mensura et grabibus luminis, colorum et umbrae. Technical report, Augsberg, Germany, 1760.

[70] M. Minnaert. The reciprocity principle in lunar photometry. *Astrophysical Journal*, 93, 1941.

[71] Bruce W. Hapke. A theoretical photometric function for the lunar surface. *Journal of Geophysical Research*, 68(15):4571–4586, 1963.

[72] St. Sandmeier, Ch. Mller, B. Hosgood, and G. Andreoli. Sensitivity analysis and quality assessment of laboratory BRDF data. *Remote Sensing of Environment*, 64(2):176–191, May 1998.

[73] Stephen H. Westin and Kenneth E. Torrance James R. Arvo. Predicting reflectance functions from complex surfaces. In *ACM SIGGRAPH Computer Graphics, Proceedings of the 19th annual conference on Computer graphics and interactive techniques*, July 1992.

[74] Jan J. Koenderink, Andrea J. van Doorn, and Marigo Stavridi. Bidirectional reflection distribution function expressed in terms of surface scattering modes. In *Proceedings of the 4th European Conference on Computer Vision-Volume II*, pages 28–39. Springer-Verlag, 1996.

[75] M. Paulin L. Claustres, Y. Boucher. Spectral BRDF modeling using wavelets. In *Wavelet and Independent Component Analysis Applications IX*, volume 4738 of *Proc. SPIE*, pages 33–43, 2002.

[76] Szymon M. Rusinkiewicz. A new change of variables for efficient BRDF representation. In G. Drettakis and N. Max, editors, *Rendering Techniques, Proceedings of Eurographics Rendering Workshop*, pages 11–22. Springer Wien, 1998.

[77] K. E. Torrance and E. M. Sparrow. Theory for off-specular reflection from roughened surfaces. *Journal of the Optical Society of America*, 57(9):1105–1114, September 1967.

[78] John A. Conant and Jr. Frank J. Iannarilli. Development of a combined bidirectional reflectance and directional emittance model for polarized modeling. In Dennis Goldsteing, David Chenault, Walter Egan, and Michael Duggin, editors, *Polarization Analysis, Measurment, and Remote Sensing IV*, volume 4481 of *Proc. SPIE*, pages 206–215, 2002.

[79] James C. Jafolla, David J. Thomas, John W. Hilgers, William R. Reynolds, and Chris Blasband. Theory and measurement of bidirectional reflectance for signature analysis. In *Targets and Backgrounds: Characterization and Representation V*, volume 3699 of *Proc. SPIE*, pages 2–15, 1999.

[80] B. Sandford and L. Robertson. Infrared reflectance properties of aircraft paint. In *Proc. IRIS Targets, Backgrounds and Discrimination*, 1985.

[81] Petr Beckmann and Adndré Spizzichino. *The Scattering of Electromagnetic Waves from Rough Surfaces*. Pergamon Press, 1963.

[82] X. D. He, K. E. Torrance, F. X. Sillion, and D. P. Greenberg. A comprehensive physical model for light reflection. *Computer Graphics*, 25(4):175–186, July 1991.

[83] Xiao D. He, Patrick O. Heynen, Richard L. Phillips, Kenneth E. Torrance, David H. Salesin, and Donald P. Greenberg. A fast and accurate light reflection model. In *Proceedings of the 19th annual conference on Computer graphics and interactive techniques*, volume 26 of *ACM SIGGRAPH Computer Graphics*, pages 253–254, July 1992.

[84] N. S. Goel. Models of vegetation canopy reflectance and their use in estimation of biophysical parameters from reflectance data. *Remote Sensing Reviews*, 4:1–213, 1988.

[85] N. S. Goel and R. L. Thompson. A snapshot of canopy reflectance models and a universal model for the radiation regime. *Remote Sensing Reviews*, 18:197–226, 2000.

[86] A. H. Strahler. Vegetation canopy reflectance modeling–recent developments and remote sensing perspectives. *Remote Sensing Reviews*, 15:179–194, 1997.

[87] W. Luch and J. L. Roujean. Considerations in the parametric modeling of BRDF and albedo from multiangular satellite sensor observations. *Remote Sensing Reviews*, 18:197–226, 2000.

[88] Maria von Schönermark, Bernhard Geiger, and Hans Peter Röser (editors). *Reflection Properties of Vegetation and Soil—with a BRDF data base*. Wissenschaft und Technik Verlag, 2004.

[89] J. Roujean, M. Leroy, and P. Deschamps. A bidirectional reflectance model of the earth's surface for correction of remote sensing data. *Journal of Geophysical Research*, 97(D18):20,455–20,468, December, 20 1992.

[90] Mark A. Culpepper. Empirical bidirectional reflectivity model. In *Targets and Backgrounds: Characterization and Representation*, volume 2469 of *Proc. SPIE*, pages 208–219, 1995.

[91] Rupert M. J. Watson and Peter N. Raven. Comparison of measured BRDF data with parameterized reflectance models. In *Targets and Backgrounds VII: Characterization and Representation*, volume 4370 of *Proc. SPIE*, pages 159–168, 2001.

[92] James C. Jafolla, David J. Thomas, and John W. Hilgers. A comparison of BRDF representations and their effect on signatures. In *IRIS Proceedings*, 1998. Approved for public release.

[93] Olivier Hautecoeur and Marc Leroy. Intercomparison of several BRDF models for the compositing of spaceborne POLDER data over land surfaces. In *International Geoscience and Remote Sensing Symposium (IGARSS)*, volume 1, pages 204–208, 1996.

[94] M. Hess and R. Priest. Comparison of polarization bidirectional reflectance distribution function (BRDF) models. In *IEEE Aerospace Conference Proceedings*, volume 4, pages 95–102, 1999.

[95] Donald D. Duncan, Daniel V. Hahn, and Michael E. Thomas. Physics-based polarimetric BRDF models. In Leonard M. Hansse, editor, *Optical Diagnostic Methods for Inorganic Materials III*, volume 5192 of *Proc. SPIE*, pages 129–140, November 2003.

[96] Richard G. Priest and Thomas A. Germer. Polarimetric BRDF in the microfacet model: Theory and measurements. In *Proceedings of the 2000 Meeting of the Military Sensing Symposia Specialty Group on Passive Sensors*, volume 1, pages 169–181. Infrared Information Analysis Center, Ann Arbor, MI, 2000. Approved for public release.

[97] Richard G. Priest and Steven R. Meier. Polarimetric microfacet scattering theory with applications to absorptive and reflective surfaces. *Optical Engineering*, 41(5):988–993, May 2002.

[98] Matthew P. Fetrow, David L. Wellems, Stephanie H. Sposato, Kenneth P. Bishop, Thomas R. Caudill, Michael L. Davis, and Elizabeth R. Simrell. Results of a new polarization simulation. In *Polarization Analysis, Measurement, and Remote Sensing IV*, volume 4481, pages 149–162, 2002.

[99] Jason P. Meyers. *Modeling Polarimetric Imaging using DIRSIG*. PhD thesis, Rochester Institute of Technology, 2002.

[100] C. Acquista and R. Rosenwald. Multiple reflections in synthetic scenes. In *Proceedings of the Fifth Annual Ground Target Modeling and Validation Conference*, Houghton, MI, 1994.

[101] Kenneth K. Ellis. Polarimetric bidirectional reflectance distribution function of glossy coatings. *Journal of the Optical Society of America A*, 13(8):1758–1762, August 1996.

[102] G. Rondeaux and M. Herman. Polarization of light reflected by crop canopies. *Remote Sensing of Environment*, 38(1):63–75, 1991.

[103] F. M. Bréon, D. Tanré, P. Lecomte, and M. Herman. Polarized reflectance of bare soils and vegetation: measurements and models. *IEEE Transactions on Geoscience and Remote Sensing*, 33(2):487–499, March 1995.

[104] F. Massoumian, R. Jukaitis, M. A. A. Neil, and T. Wilson. Quantitative polarized light microscopy. *Journal of Microscopy*, 209(1):13–22, January 2003.

[105] L. B. Wolff. Polarization-based material classification from specular reflection. *IEEE Transactions on Pattern Analysis and Machine Intelligence*, 12(11):1059–1071, November 1990.

[106] L. B. Wolff and T. E. Boult. Constraining object features using a polarization reflectance model. *IEEE Transactions on Pattern Analysis and Machine Intelligence*, 13(7):635–657, July 1991.

[107] Lawrence B. Wolff. Polarization camera for computer vision with a beam splitter. *Journal of the Optical Society of America A*, 11(11):2935–2945, November 1994.

[108] Hany Farid and Edward H. Adelson. Separating reflections from images by use of independent component analysis. *Journal of the Optical Society of America A*, 16(9):2136–2145, September 1999.

[109] Silvano Fineschi, editor. *Polarimetry in Astronomy*, volume 4843 of *Proc. SPIE*, 2003.

[110] S. G. Demos, H. B. Radousky, and R. R. Alfano. Deep subsurface imaging in tissues using spectral and polarization filtering. *Optics Express*, 7(1):23–28, July 3 2000.

[111] Andreas H. Hielscher et al. Diffuse backscattering mueller matrices of highly scattering media. *Optics Express*, 1(13):441–453, December 22 1997.

[112] K. Messmer. *Orthogonal Polarization Spectral Imaging: A New Tool for the Observation and Measurement of the Human Microcirculation*, volume 24 of *Progress in Applied Microcirculation*. Karger, 2000.

[113] Aed M. El-Saba and Mohammad S. Alam. Polarization-encoded fringe-adjusted joint-transform correlator for fingerprint verification systems for high-security applications. In Anil K. Jain and Nalini K. Ratha, editors, *Biometric Technology for Human Identification*, volume 5404 of *Proc. SPIE*, pages 248–258, 2004.

[114] Wolfgang-Martin Boerner. Basic concepts of radar polarimetry and its application to target discrimination, classification, imaging and identification. Technical Report EMID-CL-82-05-18-02, Electromagnetic Imaging Division, University of Illinois at Chicago, 1982. Available at http://multisearch.dtic.mil/.

[115] Fawwaz T. Ulaby. *Radar polarimetry for geoscience applications*. Artech House, Norwood, MA, 1990.

[116] F. T. Ulaby, K. Sarabandi, and A. Nashashibi. Statistical properties of the Mueller matrix of distributed targets. *Radar and Signal Processing, IEE Proceedings F*, 139(2):136–146, April 1992.

[117] U. Wegmüller and C. Matzler. Rough bare soil reflectivity model. *Geoscience and Remote Sensing, IEEE Transactions on*, 37(3):1391–1395, May 1999.

[118] B. Lyot. Research on the polarization of light from planets and from some terrestrial substances. *Ann. Obs. Meudon VIII*, (1), 1929.

[119] Audouin Dollfus. Lunar surface imaging polarimetry: I. roughness and grain size. *Icarus*, 136:69–103, 1998.

[120] A. Dollfus. *Étude des planètes par la polarisation de la lumière*. PhD thesis, University of Paris, 1955.

[121] A. Dollfus. *Polarization Studies of Planets*, pages 343–399. University of Chicago Press, 1961.

[122] H. S. Chen and C. R. N. Rau. Polarization of light on reflection by some natural surfaces. *British J. Appl. Phys. (J. Phys. D)*, 1(2):1191–1200, 1968.

[123] William W. Burns. Airborne, remote sensing system that uses reflected polarized skylight to detect the presence of oil discharges into water. *IEEE Oceans*, 7:688–692, September 1975.

[124] Larry L. Stowe. Polarization of reflected sunlight as measured from a high-altitude balloon. In *Optical Polarimetry*, volume 112 of *Proc. SPIE*, pages 176–183, 1977.

[125] *Remote Sensing in Polarized Light*, volume 3014 of *NASA Conference Publication*, 1987.

[126] W. G. Egan, W. R. Johnson, and V. S. Whitehead. Terrestrial polarization imagery obtained from the space shuttle: characterization and interpretation. *Applied Optics*, 30:435–442, 1991.

[127] Walter G. Egan, Scott Israel, W. R. Johnson, and V. S. Whitehead. High resolution space shuttle polarimetry for farm crop classification. *Applied Optics-OT*, 31(10):1542–1548, April 1992.

[128] J. C. Roger, R. Santer, M. Herman, and J. L. Deuzé. Polarization of the solar light scattered by the earth-atmosphere system as observed from the U.S. shuttle. *Remote Sensing of Environment*, 48(3):275–290, June 1994.

[129] S. A. Israel and M. J. Duggin. Characterization of terrestrial features using space-shuttle-based polarimetry. In *IEEE International Geoscience and Remote Sensing Symposium*, volume 2, pages 1547–1549, 1992.

[130] Steven A. Israel, Mark H. Holly, and Victor S. Whitehead. Optimizing view/illumination geometry for terrestrial features using space shuttle and aerial polarimetry. In *Polarization and Remote Sensing*, volume 1747 of *Proc. SPIE*, pages 121–127, 1992.

[131] V. S. Whitehead. A summary of observations performed and preliminary findings in the space shuttle polarization experiment. In *Polarization and Remote Sensing*, volume 1747 of *Proc. SPIE*, pages 104–108, 1992.

[132] French Space Agency. POLDER images. Internet, http://smsc.cnes.fr/POLDER/GP_gallerie.htm, July 2004.

[133] V. N. Anjum and R. Ghosh. Angular and polarization response of vegetation, bare soil and water from ADEOS POLDER data over India. *International Journal of Remote Sensing*, 21(4):805–810, March 2000.

[134] D. P. Gibbs, C. L. Betty, A. K. Fung, and J. R. Irons. Automated measurement of polarized bidirectional reflectance for qualification of minerals and oxide coatings. In *IEEE International Geoscience and Remote Sensing Symposium*, pages 511–513, May 1992.

[135] D. P. Gibbs. *Measurement and model comparisons of polarized bidirectional reflectance: a new approach to advance understanding of light interaction with natural scenes.* PhD thesis, University of Texas at Arlington, 1992.

[136] Walter G. Egan. *Photometry and Polarization in Remote Sensing.* Elsevier, 1985.

[137] M. Herman and V. Vanderbilt. Polarimetric observations in the solar spectrum for remote sensing purposes. *Remote Sens. Rev.*, 15:35–57, 1997.

[138] V. C. Vanderbilt and L. Grant. Plant canopy specular reflectance model. *IEEE Transactions on Geoscience and Remote Sensing*, GE-23:722–730, 1985.

[139] V. C. Vanderbilt, L. Grant, and C. S. T. Daughtry. Polarization of light scattered by vegetation. *Proceedings of the IEEE*, 73:1012–1024, 1985.

[140] V. C. Vanderbilt, L. Grant, L. L. Biehl, and B. F. Robinson. Specular, diffuse, and polarized light scattered by two wheat canopies. *Applied Optics*, 24:2408–2418, 1985.

[141] V. C. Vanderbilt and K. J. de Venecia. Specular, diffuse, and polarized imagery of an oat canopy. *IEEE Transactions on Geoscience and Remote Sensing*, 26(4):451–462, July 1988.

[142] V. C. Vanderbilt, L. Grant, C. S. T. Daughtry, and L. L. Biehl. Polarized, bidirectional reflectance of sorghum bicolor. In *International Geoscience and Remote Sensing Symposium*, volume 3, page 1765, 1989.

[143] Michael J. Duggin and Gerald J. Kinn. Vegetative target enhancement in natural scenes using multiband polarization methods. In Dennis H. Goldstein, David B. Chenault, Walter G. Egan, and Michael J. Duggin, editors, *Polarization Analysis, Measurement and Remote Sensing IV*, volume 4481 of *Proc. SPIE*, pages 281–291, January 2002.

[144] Dennis H. Goldstein. Polarimetric characterization of federal standard paints. In *Polarization Analysis, Measurement, and Remote Sensing III*, volume 4133 of *Proc. SPIE*, pages 112–123, 2000. Also available in AFRL-MN-EG-TR-2003-7013 Technical Report, February 2003, pp 27-39 from DTIC http://multisearch.dtic.mil/.

[145] Neelam Gupta, Louis J. Denes, Milton Gottlieb, Dennis R. Suhre, Boris Kaminsky, and Peter Metes. Object detection with a field-portable spectropolarimetric imager. *Applied Optics-LP*, 40(36):6626–6632, December 2001.

[146] Neelam Gupta. Remote sensing using hyperspectral and polarization images. In James O. Jensen and Robert L. Spellicy, editors, *Instrumentation for Air Pollution and Global Atmospheric Monitoring*, volume 4574 of *Proc. SPIE*, pages 184–192, February 2002.

[147] Li-Jen Cheng, Mike Hamilton, Colin Mahoney, and George Reyes. Analysis of AOTF hyperspectral imagery. In A. Evan Iverson, editor, *Algorithms for Multispectral and Hyperspectral Imagery*, volume 2231 of *Proc. SPIE*, pages 158–166, 1994.

[148] Li-Jen Cheng, J. Mahoney, F. Reyes, and H. Suiter. Target detection using an acousto-optical tunable filter hyperspectral imager. In *Optical Pattern Recognition V*, volume 2237 of *Proc. SPIE*, pages 251–259, 1994.

[149] L. J. Denes, M. Gottlieb, B. Kaminsky, and D. F. Huber. Spectro-polarimetric imaging for object recognition. In *26th AIPR Workshop: Exploiting New Image Sources and Sensors*, volume 3240 of *Proc. SPIE*, pages 8–18, 1998.

[150] L. V. Katkovsky, B. I. Belyaev, Yu. V. Belyaev, T. M. Kurikina, A. I. Nesterovich, V. A. Sosenko, V. V. Veller, S. P. Zabirko, and V. A. Zaitseva. Spectropolarizational technique for detection of manmade objects in visible and near infrared spectral ranges. In *IEEE International Geoscience and Remote Sensing Symposium*, volume 2, pages 1381–1383, 1999.

[151] Melissa A. Sturgeon, Li-Jen Cheng, Philip H. Durkee, Michael K. Hamilton, John F. Huth, J. Colin Mahoney, Richard C. Olsen, and George F. Reyes. Spectral and polarimetric analysis of hyperspectral data collected by an acousto-optic tunable filter system. In A. Evan Iverson, editor, *Algorithms for Multispectral and Hyperspectral Imagery*, volume 2231 of *Proc. SPIE*, pages 167–176, July 1994.

[152] James D. Howe, Miranda A. Miller, Robert V. Blumer, Thomas E. Petty, Mark A. Stevens, David M. Teale, and Matthew H. Smith. Polarization sensing for target acquisition and mine detection. In *Polarization Analysis, Measurement, and Remote Sensing III*, volume 4133 of *Proc. SPIE*, pages 202–213, 2002.

[153] Miranda A. Miller, Robert V. Blumer, and James D. Howe. Active and passive SWIR imaging polarimetry. In *Polarization Analysis, Measurement, and Remote Sensing IV*, volume 4481 of *Proc. SPIE*, pages 87–99, 2002.

[154] R. Chandra and V. M. Bothle. Optical polarization to improve discrimination capability of remote sensing: a laboratory study. *International Journal of Remote Sensing*, 22(1):169–175, 2001.

[155] David S. Petri. Analysis of hyperspectral data using polarimetric characteristics. Master's thesis, Naval Postgraduate School, Monterey, CA, 1996. Approved for public release.

[156] Rulon Mayer, Richard Priest, Christopher Steliman, Geoffrey Hazel, and Alan Schaum. Detection of camouflaged targets in cluttered backgrounds using fusion of near simultaneous spectral and polarimetric imaging. Technical report, Naval Research Lab, Washington DC Optical Sciences Division, August 2000. Approved for Public Release.

[157] I. Reed and X. Yu. Adaptive multiple-band CFAR detection of an optical pattern with unknown spectral distribution. *IEEE Trans. on Acoustics, Speech, and Sig. Proc.*, 38:1760–1770, 1990.

[158] J. Halajian and H. Hallock. Principles and techniques of polarimetric mapping. In *Proceedings of the Eighth International Symposium on Remote Sensing of Environment*, volume 1, pages 523–540, October 1972.

[159] Dimitris Manolakis and Gary Shaw. Detection algorithms for hyperspectral imaging applications. *IEEE Signal Processing Magazine*, pages 29–43, January 2002.

[160] St. Sandmeier and D. W. Deering. Structure analysis and classification of boreal forests using airborne hyperspectral BRDF data from ASAS. *Remote Sensing of Environment*, 69(3):281–295, September 1999.

[161] Kinsell L. Coulson, Jitendra V. Dave, and Zdenek Sekera. *Tables Related to Radiation Emerging from a Planetary Atmosphere with Rayleigh Scattering*. University of California Press, Berkeley, CA, 1960.

[162] S. Chandrasekhar. *Radiative Transfer*. Clarendon Press, Oxford, 1950.

[163] Alexander A. Kokhanovsky. *Optics of Light Scattering Media*. Springer-Verlag, 2 edition, 2001.

[164] James R. Shell II and Thomas Schwarting. Derivation of atmospheric transmittance and diffuse sky irradiance fraction using ASD measurements. Technical report, Digital Imaging and Remote Sensing Laboratory, Rochester Institute of Technology, July 2, 2004.

[165] Alexander Berk, Lawrence S. Bernstein, and David C. Robertson. MODTRAN: A moderate resolution model for LOWTRAN 7. Technical Report GL-TR-89-C122, Air Force Geophysics Lab, April 1989. available at http://stinet.dtic.mil/index.html.

[166] A. Berk, G. P. Anderson, P. K. Acharya, J. H. Chetwynd, L. S. Bernstein, E. P. Shettle, M. W. Matthew, and S. M. Adler-Golden. *MODTRAN4 User's Manual*. Air Force Research Lab, Hanscom AFB, MA 01731-3010, June 1999.

[167] Brian Cairns, Larry Travis, Michael I. Mishchenko, and Jacek Chowdhary. Aerosol retrievals over land surfaces (the advantages of polarization). In *A Millennium Symposium on Atmospheric Chemistry: Past, Present, and Future of Atmospheric Chemistry*, American Meteorological Society, page Section 3.7, 2001.

[168] F. Maignan, F. M. Bréon, and R. Lacaze. Bidirectional reflectance of earth targets: Evaluation of analytical models using a large set of spaceborne measurements with emphasis on the hot spot. *Remote Sensing of Environment*, 90:210–220, 2004.

[169] DIRSIG internet site, 2004.

[170] J. R. Schott, S. D. Brown, R. V. Raque no, H. N. Gross, and G. Robinson. An advanced synthetic image generation model and its application to multi/hyperspectral algorithm development. *Canadian Journal of Remote Sensing*, 25(2), June 1999.

[171] Emmett J. Ientilucci and Scott D. Brown. Advances in wide area hyperspectral image simutaion. In Wendell R. Watkins, Dieter Clement, and William R. Reynolds, editors, *Targets and Backgrounds IX: Characterization and Representation*, volume 5075 of *Proc. SPIE*, pages 110–121, 2003.

[172] Scott D. Brown and John R. Schott. Characterization techniques for incorporating backgrounds into DIRSIG. In Wendell R. Watkins, Dieter Clement, and William R. Reynolds, editors, *Targets and Backgrounds VI: Characterization, Visualization, and the Detection Process*, volume 4029 of *Proc. SPIE*, pages 205–216, July 2000.

[173] Digitial Imaging and Remote Sensing Lab, Rochester Institute of Technology. *The DIRSIG User's Manual*, 3.5.3 edition, 2004.

[174] F. J. Iannarilli and J. A. Conant. Quantifying key trade-off between IR polarimetric discriminability versus pixel resolution against complex targets. In *Targets and Backgrounds: Characterization and Representation V*, volume 3699 of *Proc. SPIE*, pages 58–66, 1999.

[175] Matthew Fetrow. Personal correspondence, July 2004.

[176] David J. Thomas, Roger Evans, Jim Crosby, and James C. Jafolla. Surface reflectance variations in realistic targets. In *Targets and Backgrounds: Characterization and Representation IV*, volume 3375 of *Proc. SPIE*, pages 27–37, 1998.

[177] Gordon W. Lukesh, Susan M. Chandler, and James K. Boger. A laboratory experiment to demonstrate active non-imaging polarization distinction of materials. In *Polarization Analysis, Measurement, and Remote Sensing IV*, volume 4481 of *Proc. SPIE*, pages 126–136, 2002.

[178] J. R. Shell and J. R. Schott. A polarized clutter measurement technique based on the governing equation for polarimetric remote sensing in the visible to near infrared. In Wendell R. Watkins et al., editors, *SPIE: Targets and Backgrounds XI: Characterization and Representation*, volume 5811 of *Proc. SPIE*, pages 34–45, May 2005.

[179] Dennis H. Goldstein. Polarimetric characterization of spectralon. In *Polarization: Measurement, Analysis, and Remote Sensing II*, volume 3754 of *Proc. SPIE*, pages 126–136, 1999. Also available at http://multisearch.dtic.mil/ as part of technical report AFRL-MN-EG-TR-2003-7013, Feb 2003, pp. 15–26.

[180] Russell A. Chipman. *Handbook of Optics*, volume II, chapter 22. Optical Society of America, second edition, 2000.

[181] Jack D. Gaskill. *Linear Systems, Fourier Transformas, and Optics*. John Wiley and Sons, 1978.

[182] Photometrics synsys 1602e datasheet. Internet, 2004. http://www.photomet.com/pdfs/datasheets/sensys/ss1602e.pdf.

[183] Mark L. Mesenbrink. Complex indices of refraction for water and ice from visible to long wavelengths. Master's thesis, Florida State University, 1996. Air Force Institute of Technology Student, Report AFIT-96-037.

[184] Robert D. Fiete. Image quality and λfn/p for remote sensing systems. *Optical Engineering*, 38(7):1229–1240, 1999.

[185] Richard Hailstone. Basic Principles of Imaging Science I, 2002. Fall 2002 Course Notes, Rochester Institute of Technology course SIMG711.

[186] M. J. Duggin and R. S. Loe. Calibration and exploitation of a narrow-band imaging polarimeter. *Optical Engineering*, 41(5):1039–1047, May 2002.

[187] John R. Taylor. *An Introduction to Error Analysis: The Study of Uncertainties in Physical Measurements*. University Science Books, Oxford University Press, 1982.

[188] Hongjie Xie, Nigel Hicks, G. Randy Keller, Haitao Huang, and Vladik Kreinovich. An IDL/ENVI implementation of the FFT-based algorithm for automatic image registration. *Computers & Geosciences*, 29:1045–1055, 2003.

[189] J. R. Schott and S. D. Brown. Incorporation of enhanced texture/transition modeling tools into a synthetic image generation model. *IEEE International Geoscience and Remote Sensing Symposium Proceedings*, 3:1508–1511, 1998.

[190] Carl Salvaggio, Lon E. Smith, and Emily J. Antoine. Spectral signature databases and their application/misapplication to modeling and exploitation of multispectral/hyperspectral data. In Sylvia S. Shen and Paul E. Lewis, editors, *Algorithms and Technologies for Multispectral, Hyperspectral, and Ultraspectral Imagery XI*, volume 5806 of *Proc. SPIE*, pages 531–541, June 2005.

[191] J. R. Shell, C. Salvaggio, and J. R. Schott. A novel BRDF measurement technique with spatial resolution-dependent spectral variance. *2004 IEEE International Geoscience and Remote Sensing Symposium*, September 2004.

[192] Yu. Shkuratov, M. Kreslavsky, V. Kaydash, G. Videend, J. Bell III, M. Wolff, M. Hubbard, K. Noll, and A. Lubenowd. Hubble Space Telescope imaging polarimetry of Mars during the 2003 opposition. *Icarus*, 176:1–11, 2005.

[193] Nonconventional Exploitation Factors (NEF) Modeling. Technical Report v9.5, ORD, April 2005. Limited distribution.

[194] Thomas A. Germer. Polarized light diffusely scattered under smooth and rough interfaces. In *Polarization Science and Remote Sensing*, volume 5158 of *Proc. SPIE*, pages 193–204, 2003.

[195] Mike Metzler. Personal communication, 2005.

[196] Dennis Goldstein. *Polarized Light*. Marcel Dekker, Inc., second edition, 2003.

[197] Alexander Berk, Gail P. Anderson, et al. MODTRAN4 radiative transfer modeling for atmospheric correction. In Allen M. Larar, editor, *Optical Spectroscopic Techniques and Instrumentation for Atmospheric and Space Research III*, volume 3756 of *Proc. SPIE*, pages 348–353, October 1999.

[198] Andrew Fordham. personal communication, June 2004.

[199] Gary Stahl. personal communiction, June–July 2004.

[200] G. D. Bernard and R. Wehner. Functional similarities between polarization vision and color vision. *Vision Research*, 17:1019–1028, 1977.

[201] *DALSA 1M15 Camera Specifications*, December 2000. Available at http://www.imagelabs.com/pdf/dalsa1m15.pdf.

[202] Kenneth P. Bishop, Harold D. McIntire, Matthew P. Fetrow, and Lenore McMackin. Multispectral polarimeter imaging in the visible to near ir. In *Targets and Backgrounds: Characterization and Representation V*, volume 3699 of *Proc. SPIE*, pages 49–57, July 1999.

[203] Catherine Proy. personal e-mail correspondence, January 2004.

[204] F. M. Bréon. *POLDER Level-1 Product Data Format and User's Manual*. CNES, 2 edition, November 1997.

[205] Earth Sciences and NASA-Johnson Space Center Image Analysis. The gateway to astronaut photography of earth. http://eol.jsc.nasa.gov, August 2003.